Dynamics of Secondary Steady State Flows in a Combined Taylor-Couette and Escudier Vortex Breakdown Flow Field

by

Jordan K. Waldheim

A thesis submitted to the Graduate Faculty of
Auburn University
in partial fulfillment of the
requirements for the Degree of
Master of Science

Auburn, Alabama
02 May, 2022

Keywords: Taylor Vortices, Vortex Breakdown, Bifurcation, Instabillity, Taylor-Couette Flow

Approved by

Anwar Ahmed, Professor of Aerospace Engineering
Roy Hartfield, Walt and Virginia Woltosz Professor of Aerospace Engineering
Joe Majdalani, Francis Chair Professor of Aerospace Engineering
Brian Thurow, Department Chair, Associate Professor of Aerospace Engineering

Abstract

Confined Vortex flows are of a great practical significance in industrial processes and devices, especially within the fields of rheology and hydrodynamics. These confined swirling flows are characterized by a progression of instabilities that arise as Reynolds number, or Taylor number, increases. The growth of these small perturbations eventually result in secondary and even tertiary steady states with increasing spatio-temporal complexity. Eventually resulting in a fully turbulent flow field.

Effects of a varying height end-wall on the bifurcation and stability of secondary steady state flows within the annular gap of a Taylor-Couette cell were investigated. Experiments were conducted at four different end-wall aspect ratios of $\Gamma_{ew} = 0$, 0.5, 1.0, and 1.5 at Taylor numbers between T_a = 1,312 - 35,485. Co-rotation, counter-rotation, and stationary end-wall rotational conditions were investigated for the three larger aspect ratios, at end-wall Reynolds numbers between $R_{e_{ew}}$ = 944 - 2,926. Increases in Γ_{ew} were found to attenuate both the structural stability and vorticity of annular Taylor vortices. Co-rotation was found to dampen the effects of increases in Γ_{ew} while counter-rotation was found to enhance the effects of increases in Γ_{ew}. The changes in vortex stability and vorticity were found to result primarily from oscillatory axial flow within the annulus. This axial flow was found to be greatest at $\Gamma_{ew} = 1.0$, and 1.5 where a flow similar to the vortex breakdown bubble found by Escudier [24] was found to occur in the zone-2 region between the inner cylinder and upper end-wall. The presence of these zone-2 vortical structures was found to play a pivotal role in Taylor vortex stability and subsequent distortions at higher T_a numbers.

Acknowledgments

I would like to thank my committee members and the entire Auburn University Aerospace Engineering department. Especially my advisor and mentor Dr. Anwar Ahmed. Who's guidance, support, and great patience I could not have done this work without. Words alone can not express gratitude. I am forever grateful for all you have done for me and am truly blessed to have you as my mentor. I would also like to thank Mr. Andy Weldon for his expertise and guidance in machining the essential components needed to make this experimental investigation possible. I would like to thank Hamza Ahmed and Praveen Gambhir, for their help with the experimental setup. As well as A.J. Weiner, and Brian Davis for their encouragement of me pursing my graduate studies with Dr. Ahmed.

Last, but not least, I would like thank my family and friends.This journey has had many twist and turns; most of which I never could have predicted. I owe some much to my family and friends for all their emotional support, love, and encouragement. I could not have done this work and would not be where I am today without them.

Contents

List of Figures

Nomenclature

β	Eigenvector
$\boldsymbol{\epsilon}$	strain tensor
$\boldsymbol{\mathcal{V}}$	volume
$\boldsymbol{\tau}$	stress tensor
ϵ	elemental strain
η	R_I/R_O - cylinder gap ratio
η_{mag}	magnetic diffusivity
Γ_C	$L_I/\hat{\mathrm{d}}$ - inner cylinder aspect ratio
Γ_{ew}	H_{ew}/R_O - upper end-wall aspect ratio
$\hat{\mathrm{d}}$	gap width between inner and outter cylinders
λ	Eigenvalue
λ_i	*ith* energetic POD mode
ν	kinematic viscosity
Ω_I	angular velocity of inner cylinder
Ω_O	angular velocity of outer cylinder
Ω_{ew}	angular velocity of the rotating end-wall
Φ	POD basis function

ϕ	singular values of a matrix
$\Phi(\lambda_i)$	cumulative energy of POD modes
Ψ	flow domain / stream function
ρ	density
τ	elemental stress
ζ	Rayleigh's invisid centrifugal stability criterion
F	force
f	force per unit volume
H_{ew}	hight of rotating end-wall from the top of the inner cylinder
k	wavenumber
L_I	length of inner cylinder
L_O	length of outer cylinder
L_Ω	angular momentum
m	mass
P_{r_m}	Magnetic Prandelt number
R_I	outer radius of the inner cylinder
R_O	inner radius of the outer cylinder
R_r	radius of central axis rod
R_{e_c}	Reynolds number of inner cylinder
$R_{e_{ew}}$	Reynolds number of rotating end-wall

$R_{e_{tc-vb}}$	Reynolds number of inner cylinder in vortex breakdown form
R_{UW}	radius of the upper end-wall
T_a	Taylor number
$\mathbf{g}$	gravatational acceleration
$\mathbf{U}$	velocity vector / matrix
CCF	Circular Couette Flow
TCF	Taylor-Couette Flow
TV	Taylor Vortex / Vortices
TVF	Taylor Vortex Flow
VB	Vortex Breakdown
VBB	Vortex Bubble Breakdown
WVF	Wavy Vortex Flow

Chapter 1

Introduction

1.1 Motivation

Flow contained between two parallel boundaries is encountered in a variate of practical applications. Such bounded flows are found to occur in the motion of piston engine, the boundary layer between a wing and calm free-stream air, or the rotating motion of a turbine drive shaft; just to name a few. These bounded flows are what is known as Couette flow; defined as a shearing flow between two parallel boundaries where a relative velocity gradient exists. Classical Couette flow investigations have generally focused on the flow field contained between two concentric rotating cylinders. Where flow patterns that are produced in the gap between two concentric cylinders are dominated by the formation of instabilities that eventually result in the creation of stacked axisymmetric toroidal vortices. These instabilities are known as Taylor vortices, named after G.I. Taylor who first showed that the formation of such vortices are characterized by the ratio of centrifugal forces relative to the viscous forces present.

A Better understanding of the kinematics associated with the formation of Taylor vortices and other resulting steady state flows that exist in a closed rotating system is of particular interest in the field of rheology. With a special emphasis on the kinematics of entrained species. Most mixing processes involve some form of rotating impeller to achieve convection driven mass transport of one or more entrained species. Such processes result in an extremely chaotic flow field that stretches, folds and disperses the material in unpredictable ways. These uncertainties can prove to be extremely problematic in situations where the

mixing efficiency of entrained species are highly sensitive to flow anisotropy. The stretching of polymer chains in pharmaceutical production and chemical refinement processes are examples of such flows.

The stacked geometry of the counter rotating axisymmetric vortices present in Taylor-Couette flow is ideally suited for the extensional stretching of entrained species, such as polymer chains. However, there are limitations to the mixing potential of Taylor-Couette flow. This limitation stems from the fact that Taylor vortices are a secondary steady state that arises from centrifugal instabilities within laminar Couette flow. Which ultimately bounds their formation to a relatively small range of rotational frequencies. If the rotation rate of the inner cylinder is below a critical speed vortex formation does not occur. Conversely, If rotation is considerably increased beyond the critical rate Taylor vortices give way to higher order steady states. Eventually resulting in a completely chaotic and turbulent flow. These transitions between multiple steady states and the transition to turbulence have prompted numerous studies in an attempt to better understand the inherent physics and potentially gain control authority over the point at which such transitions occur.

While Taylor-Couette flow is one of the most studied flows in the fluids field it is by no means the only one. Another highly intriguing flow field of interest within rheology is that of the vortex breakdown. It is characterized by the formation of a recirculating zone, also known as a vortex bubble, that forms near the bottom of a vortex core as it begins to become unstable. While this phenomenon has been very well investigated and documented on the wings of highly swept delta plan-forms investigations into broader applications have been less pervasive. However, the formation of a vortex bubble is also found to occur in many confined cylinder mixing processes, such as bioreactor cell cultivation, and is thus an increasing topic of interest.

The formation of a recirculating region, and eventual breakdown of the vortex core, can be observed within a confined cylinder filled with fluid where either one or both of the cylinders end walls are rotated about the central axis. As with Taylor-Couette flow, the

point of transition where the vortex core begins to become unstable is of great interest. Many investigations have been undertaken in attempts to control the formation of vortex bubbles and delay the eventual breakdown of the central core [24], [9], [31], [7], [41]. Most of these control attempts have met with limited success, with the current solution for delta wing aircraft being to divert the vortex in order to mitigate the adverse effects of the breakdown when it does occur. However for mixing applications the diversion of a vortex core within a confined cylinder is not a practical solution. Especially when considering that for mixing to occur in such systems a central vortex is essential. Thus as with Taylor-Couette flow the possible methods for how to control and more fully understand the kinematics behind these transitions requires further investigation.

The objective of the present research was to investigate the kinematics of these two flow fields, first separately and later in a combined setup. The hope being that further insight can be ascertained that will lead to the development of methods that will give an increased level of flow control within mixing processes. A more complete model of the physics behind these steady state and turbulent transitions would not only aid in mixing processes but in control of vortex dominated flows over wings, bearing design, and weather modeling. Many different geometries have been tested in the past for both flow fields. However, no research into the combination of these two flows has been conducted. Thus this research will examine a very simple and traditional cylindrical geometry for these flows to allow for a more accurate comparison to preexisting investigations of the individual flows. Analysis of the differences present in the current research flow field configurations to that of previous investigations of the individual flow fields was performed in order to establish what effects these two flows have on steady state transitions when combined into a single domain.

1.2 Background

In order to establish a better understating of the key aspects of Taylor-Couette and vortex breakdown flows a brief history is presented. Development of the current physical

and kinematic understating of Taylor-Couette flow will be presented first, followed by the history and current understanding of the vortex breakdown phenomenon. It should be noted that the proceeding discussions will be heavily centered on Taylor-Couette flow, as that is the primary goal. While Vortex Breakdowns will be treated as a supplemental topic.

1.2.1 Taylor-Couette Flow; A Brief History

Interest in the flow between concentric rotating cylinders dates back to 1687 when Sir Isaac Newton used the geometric concept to describe the kinematics of rotational fluid motion in his famous work Principia. Newton was able to outline a key fluid dynamics principle with this example, using it to describe the resistance that arises in a fluid when fluid particles are separated from one another. Today this resistant force is more commonly known as viscous stress.

George Stokes was the next to investigate the flow between concentric rotating cylinders. Stokes' interest was in the velocity gradient that results from such a flow field, with a particular focus on the probable boundary conditions at the solid surface of the rotating wall. In 1848 he conceptually solved for the velocity gradients of three different arrangements, outer cylinder rotation, inner cylinder rotation, and counter rotation. The conclusions Stokes surmised were simple yet profound. First was his insight that boundary conditions at the wall were, in his time, unknowable and that highly accurate experimental measurements were needed in order to discover conditions that could be mathematically satisfied. Second, and probably his most brilliant conclusions, was the realization that rotation of the inner cylinder alone would ultimately result in highly unstable flow and eventually lead to eddy formations. This second conclusion was certainly ahead of its time, for it took another 75 years before evidence of Taylor vortices were experimentally found.

By the late 1880's scientific desire for further understanding of fluid viscosity and its effects was at the forefront of fluid dynamic research. However, there was a formidable barrier that existed since no accurate means of measuring fluid viscosity existed at the time. In 1888

two men, Henry Mallock and Maurice Couette, broke through this barrier by creating devices that used concentric cylinders where either the inner or outer cylinder was suspended from a torsion fiber. Interestingly, these men created their devices independent of one another with no knowledge of the other's work. Couette focused solely on the configuration where the inner cylinder was suspended while the outer cylinder rotated. Using this configuration Coutte was able to accurately measure torsion by observing the amount of deflection that was imposed on the inner cylinder. From these torsion measurements, he was able to show that the viscosity of water is constant up to $R_e \approx 2000$. After this discovery devices of such design became known as Couette viscometers, in recognition of his work. Mallock, on the other hand, designed his apparatus to function in such a way where either the inner or outer cylinder could be rotated. By utilizing both configurations He discovered that there is no linear relation between torque and angular velocity when the inner cylinder is rotated. This finding lead Mallock to come to the same, albeit incorrect, conclusion that Stokes had forty years earlier: any flow produced by the rotation of the inner cylinder would always be inherently unstable.

In 1920, Lord Rayleigh expanded upon Mallock's work in an attempt to better understand the stability of flow between two concentric cylinders. He did this by calculating the flow stability in the absence of viscous forces. "He showed that the flow is stable provided the square of the angular momentum per unit mass of the fluid increases monotonically outward" [22]. This result holds with Mallock's findings that inner cylinder rotation will cause the flow to be unstable while outer cylinder rotation will result in stable flow up to a critical point. While Rayleigh was correct in his calculations the exclusion of viscosity ultimately led him to an inaccurate generalization.

It was not until 1923 and the groundbreaking work of G.I. Taylor that the effects of viscosity on flow field stability were finally understood. Using experimental ink flow visualization and photographic recordings of the unstable flows resulting patterns, Taylor was able to extrapolate a theoretical stability diagram. Making him the first person to successfully

bridge the gap between stability theory and experimental observations. This success was due to his works reliance on the assumption of a no-slip boundary condition at a solid surface. The significance of Taylor's assumption and resulting observations was profound. His results were one of the strongest and most convincing pieces of evidence to support the accuracy of the Navier-Stokes equations and the importance of the no-slip boundary condition.

1.2.2 Instabilities and the Formation of Secondary States

Much of the research that followed Taylor's seminal work was concerned with the super-critical point at which Couette flow bifurcates into Taylor Vortex Flow, hereafter referred to as TVF. Initial research by Donnelly & Schwarz (1965), Chandrasekhar (1961), and Davey et al. (1968) focused on mathematically describing the eigenvalue problem and how to measure the transition at which TVF occurs more precisely [21], [11], [19]. Much of this early work in the 1960s was focused on what the effects of varying η and μ_Ω were on the critical Taylor number, where $\eta = \frac{R_i}{R_o}$ and $\mu_\Omega = \frac{\Omega_o}{\Omega_i}$.

By the mid 60's experimental observations by Coles (1965), Schwarz et al. (1964) as well as mathematical investigations by Coles, suggested that higher-order stable states beyond that of the initial bifurcation from Couette to TVF existed [15], [46]. Such results were inconsistent with Taylors original conclusion that "A moderate increase in the speed of the apparatus merely increased the vigor of the circulation in the vortices without altering appreciably their spacing or position, but a large increase caused the symmetrical motion to break down into some kind of turbulent motion" [52]. However, in 1965 Coles solidified these predictions of higher-order steady states when he experimentally observed the formation of azimuthal travailing waves within TVF. This additional bifurcation of the Couette flow field beyond TVF was described as Wavy Vortex Flow (WVF) [15]. Comparison between TVF and the WVF that Coles discovered can be seen in Fig 1.1. These results were later verified by Davey et al. (1968) and Krueger et al. (1966) [19], [32].

By the mid 1980s it was found by Synder that the assumption of a cylinder of infinite length that had been used since Taylor in the models and analysis of the instability of Circular Couette Flow, (CCF), was not as accurate as previously assumed. Andereck et al. (1986) cited Synder on this finding saying, "Synder (1969) also found that the finite length of the cylinders and the specific boundary conditions at the ends of the fluid column are important in determining how near a given system is to the ideal infinite-cylinder case" [2]. Snyder showed that in a finite length system boundary conditions at the stationary end walls result in the formation of Ekman cells near the top and bottom of the fluid column and that the effects of these cell formations become non-negligible when $L/d < 10$ [2], [14]. The formation of these Ekman cells, also known as Ekman vortices, were found to result from an imbalance between the pressure gradient and centrifugal forces that arises at the stationary end walls. This imbalance deforms stable CCF, causing a secondary circulation that forms into a stationary and rotationally symmetric base which differs from that of the infinite length case [17], [28]. Ironically this discovery partially validated Mallock and Stokes original assumption that any flow produced by inner cylinder rotation would be unstable. Later studies found that the formation of these end wall disturbances is not dependent on cylinder rotation rates but are in fact present at all instances of rotation [5], [17].

The Work done by Andereck et al. in the mid 1980s was fundamental in further expanding the known regimes of secondary steady state formations. Two separate studies were conducted by Andereck et al. (1983 & 86) that essentially mapped the vast majority of possible flow states that could be achieved within a Coutte cell. For both of these studies their system utilized a small gap ratio of $\eta \geq 0.8$ and independently rotating inner and outer cylinders, which allowed for as large of an experimental range as possible [2], [3]. Between these two studies, a large number of new secondary steady states were described, such as Modulated Wavy Vortices (MWV), Wavy Inflow Boundary (WIB), Wavy Outflow Boundary (WOB), Wavelets (WVL), etc. They mapped these different flow regimes as functions of inner and outer cylinder Reynolds numbers, which can be seen in Fig 1.2.

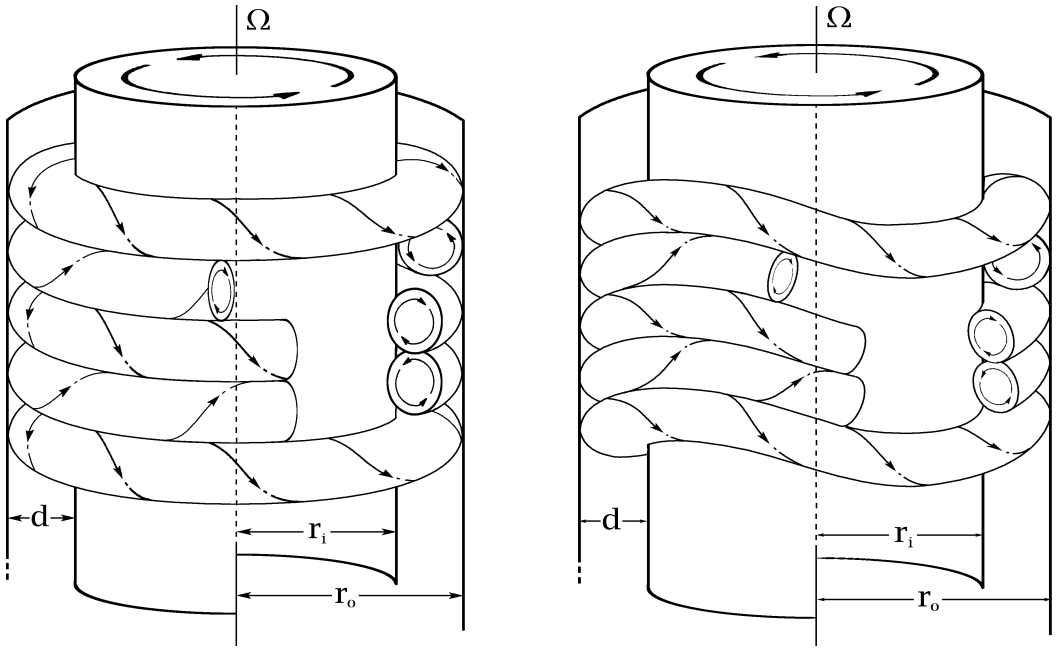

(a) Taylor Vortex Flow **(b)** Wavy Vortex Flow

Figure 1.1: Schematic representation of the counter-rotating toroidal vortices produced by TVF: (a) and WVF: (b), [37]

1.2.3 Methods of Control

Several investigations over the years have attempted to establish a means of control over the supercritical points at which Couette flow begins to bifurcate between the various stable states. These attempts can be separated into one of two categories, passive or active methods of control. Passive means have traditionally utilized some form of geometric modification to the system. Whereas active methods have generally used some type of external forcing, such as an induced magnetic field or through flow within the annulus. These methods are discussed in detail in the following sections.

Passive Flow Control

Flow stability, and control of the critical point at which flow bifurcation occurs, was first achieved by altering the geometric parameters of a Couette cell; namely the gap ratio η. Taylor (1923) performed a limited investigation on the effects of varying gap ratios on the stability of CCF in his seminal work. Although he did not discuss η specifically, his results

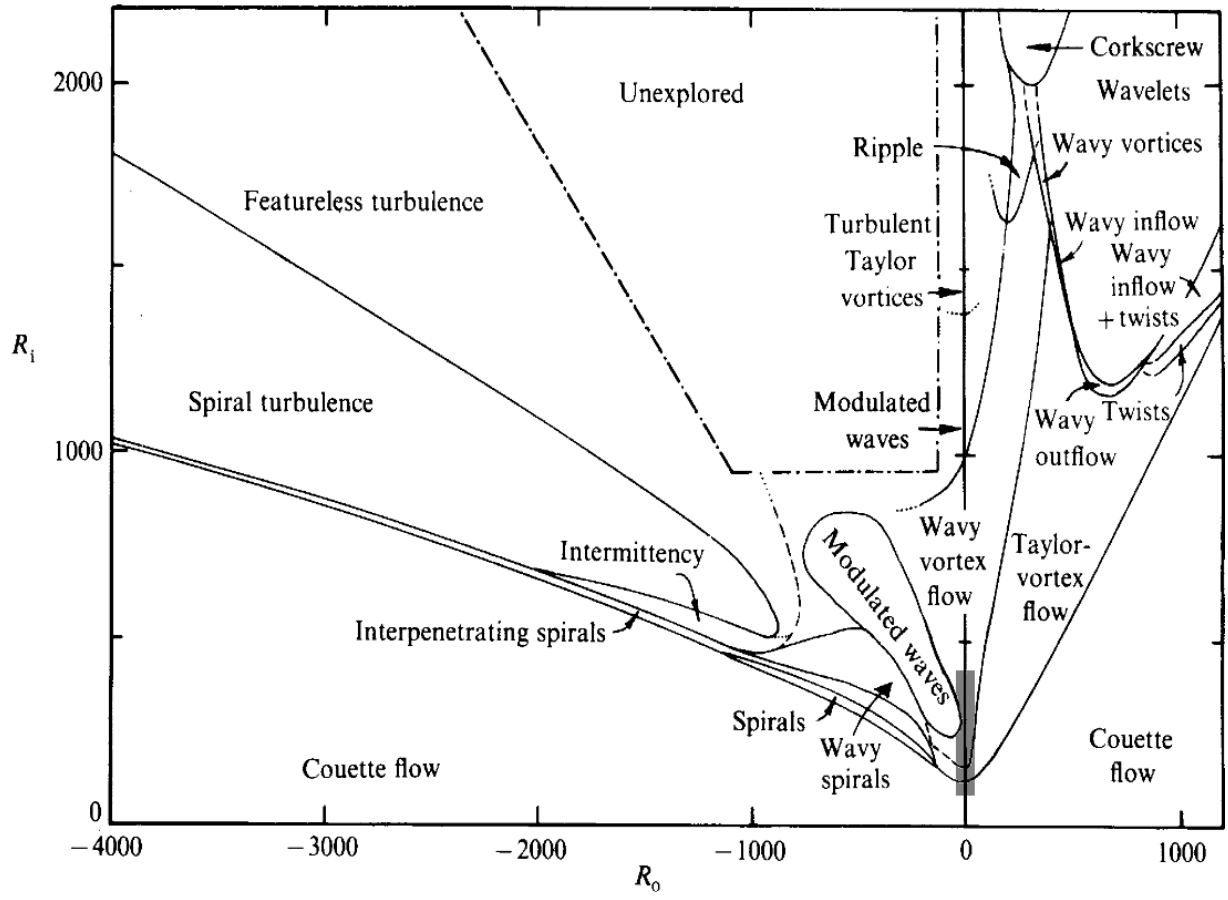

Figure 1.2: Taylor-Couette Flow Regime Chart; produced by Andereck, Lui and Swinney (1986) [2]. Here R_i & R_o represent the Reynolds number of the inner and outer cylinders respectively. $(---)$ indicate expected transition boundaries that were not firmly established by visual observations. $(\cdots)$ indicates expected continuations of unobserved boundaries. Gray area on the $R_o = 0$ line represents the approximate test domain of the current work.

show a general stabilizing effect on CCF as the gap ratio was increased [52]. These results were later expanded on by Coles (1967), and Sparrow et. al. (1964) to include wide gap ratios. They were able to analytically verify and show that stability of the flow is indeed increased as $\eta \to 1$ [16], [50]. A more recent investigation by Moussa et. al. (2014) further refined the current understanding of these effects. Their results showed that there is a critical point that exists at $\eta = 0.5$ and that the critical Reynolds number at which instability occurs had a direct and slightly indirect correlative relationship relative to an increase or decrease in η beyond 0.5 [38]. The effect of η on the transition between TVF and WVF was not as easily explained. A result that was altogether not surprising as a previous study by Jones (1984) showed that the transition between TVF and WVF was dependent on several variables including gap ratio, flow wavenumber, and the acceleration used to approach a given Re number [30].

Cole (1976) investigated the effects that annulus length had on flow stability. He utilized aspect ratios (Γ_C) in the range of 1-107 and found that annulus length had little to no effect on the primary transition from CCF to TVF. The transition between TVF to WVF however, was significantly affected by the length and resulted in an inverse relation between Γ_C and the point of $TVF \to WVF$ bifurcation. Indicating that shorter annuli stabilize TVF. These effects become most significant for $\Gamma < 40$, where the critical Re number for the transition to WVF increased by orders of magnitude [14].

Geometric changes to the topology of the cylinders have also been investigated. Ikeda & Maxworthy (1994) used sinusoidal modulations on the inner cylinder in-order to spatially force the flow [29]. They found that forcing did not effect the conditions at which bifurcation occurs for either the primary or secondary instability. However, it did artificially alter the wavelength of the vortices. Where a spatial amplitude of 10% the minimum gap width resulted in a 25% increase in wavelength compared to natural [29]. More recently Sprague et. al. (2008) utilized an axial step on the inner cylinder in the form of a spatial discontinuity located at the center [51]. Such an arrangement allowed for the simultaneous existence of

sub-critical CCF and supercritical TVF within the annulus. They noted that when one region was supercritical, while the other was sub-critical, moderately damped Taylor vortices weakly extended into the neighboring sub-critical region. However, if both regions were supercritical the resulting Taylor vortices produced in each region were dissimilar and differed in wavelengths [51].

One of the more interesting geometric alterations that has been studied is that of a conical Couette cell, investigated by both Wimmer (1995) and Noui-Mehidi et. al. (2001). In this geometric configuration, the two concentric cones lead to a centrifugal force that was varied in the axial direction. This variance, like that of the spatial discontinuity, resulted in sub-critical and supercritical flow regimes existing within the annulus simultaneously. Initial instability was found to occur in the presence of the cones larger radii, and slowly filled the annulus as R_e increased. This conical system also produced the rather interesting phenomenon of a periodic cycle of vortex travel whenever both sub and supercritical regions were present. This travel was characterized by the slow compression of the vortices that had the same rotational direction as that of the fixed end wall vortex near the cones larger radii. This compression continued until the upper most compressed vortex disappeared, at which point another vortex was generated out of the sub-critical region. Thus resulting in what appeared to be vortex travel from the smaller to lager radial end wall [56], [44].

Active Flow Control

Unlike passive control methods which are subjugated to changes in system geometry, active flow control incorporates numerous means by which to improve flow stability. Each of these means utilizes one or more external forces applied to the system. One such method is the use of through flows within the annulus.

Numerical simulations by Serre et al. (2008) addressed the effects of such a through flow [47]. Their study utilized both a radial outflow and radial inflow and found that relatively small radial outflows destabilized the system and enhanced the strength of the Taylor

vortices. A strong radial outflow or any radial inflow however, actually acted to stabilize the base CCF. They additionally state that the effects on the transition between TVF and WVF were less clear but did display a basic trend that showed that the transition to WVF was unaffected by the presence of a weak radial outflow. In the presence of a strong radial outflow, localized dislocations appeared in the wavy vortex structure but no discernible effect on the transition was found. However, when a radial inflow was applied a stabilizing effect that delayed the bifurcation to WVF was found to occur. [47].

More recently, Lalaoua (2015) simulated the effects of radial pulsation of the outer cylinder [33]. His results show a significant stabilization of the base CCF for ever increasing oscillating amplitude numbers, ϵ_{osc}; where $\epsilon_{osc} = \Delta R_o/R_i$ is radial strain. Lalaoua's model also showed a significant topological effect on Taylor vortices. Producing a flow pattern which tended towards those resembling the recirculating eddies produced behind a circular disc in a uniform flow, an effect which occurred at $\epsilon_{osc} \geq 7$ [33].

One of the more traditional methods of actively controlling the stability of TCF has been through the use of external applied magnetic fields. This is done by either entraining the working fluid contained with in the annular gap of the system with magnetic particles in such a way that the partials are suspended in the fluid, or by utilizing a liquid metal such as mercury or liquid sodium as the working fluid. Chandrasekhar (1953) first mathematically investigated this problem back in 1953 where he considered a TCF system with a weakly electrically conductive viscous working fluid in the presence of a uniform magnetic field applied in the axial direction [12]. He demonstrated that for $P_{r_m} << 1$, where $P_{r_m} = \frac{\nu}{\eta_{mag}}$, the presence of the magnetic field will act to stabilize the flow [12]. Donnelly and Ozima (1962) later verified Chandrasekhar's results experimentally and demonstrated that as magnetic field strength increased, torque measurements on the inner cylinder were reduced, and thus concluded that the flow was stable for some range beyond the critical speed [20].

More recent forays into the effects of an induced magnetic field on TCF stability have expanded upon the results of previous studies. Willis and Barenghi (2002) found that while

an axial field did stabilize the base CCF, the overall effect on the supercritical point of bifurcation to TVF was small when compared to the effects on the transition point to WVF [54], [55]. They showed that "A small field is capable of pushing the secondary instability from only a few percent above the first instability to several times the critical Reynolds number," [55]. While most of the studies conducted utilized an axially oriented magnetic field, other studies have additionally shown that both radial and azimuthal fields also have a stabilizing effect on the base CCF that delays the formation of Taylor vortices as well [43].

1.2.4 Vortex Breakdowns

Unlike Couette flow, investigations into the dynamics of vortex breakdowns are relatively new. While interest in fluid dynamics as a whole dates back to the ancient Greeks, vortical flows were historically treated more as a scientific curiosity than an actual topic of focus. That was until the mid-nineteenth century and the pioneering work of Hermann von Helmholtz (1867). In his 1867 paper "On Integrals of the Hydrodynamical Equations which Express Vortex Motion", Helmholtz established his three laws of vortex motion which ultimately sparked a new interest in the topic that continues to this day [27]. Since then, the study of vortical flows has matured into its own subfield of fluid dynamics that is known today as vortex dynamics. It took almost another 90 years from the time of Helmholtz's break through paper before the first vortex breakdown was recognized. In 1957 Peckham and Atkinson were the first to investigate the breakdown phenomena by qualitatively examining the leading edge vortices of highly swept delta wings [45]. J.K. Harvey (1962) was the first to study vortex breakdowns in a controlled laboratory setting [26]. In 1962 he utilized a setup where the swirl angle of a flow within a tube could be varied. With this setup Harvey was able to observe a bubble type vortex breakdown and estimated a critical swirl angle, defined as

$$S_{angle} = \tan^{-1} \frac{\text{axial velocity}}{\text{tangential velocity}} \tag{1.1}$$

to be approximately 50.5° [26]. He characterized this bubble type breakdown as an axisymmetric elongated sphere of stagnant fluid that the flow moves around until conditions downstream are similarly parallel to those upstream of the bubble. Since the flow downstream of the bubble was nearly identical to flow upstream, it lead Harvey to the conclusion that a vortex breakdown was not the result of flow instability. The early investigations predominantly utilized these swirling pipe flows to investigate the vortex breakdown phenomena. Vogel (1968) however, introduced the concept of using a closed geometry to investigate the breakdown and utilized a rotating end-wall in a closed cylindrical system to drive the flow. His results were later expanded upon by the seminal work of Escudier in 1984 [58], [24]. It is this closed geometry used by Vogel and Escudier that is of particular interest in the current work. While there is a large amount of overlap in the flow field characteristics within open and closed geometries, only the concepts of the later will be discussed.

1.2.5 Vortex Breakdown and Control

A vortex breakdown is defined by an abrupt change in the structure of a swirling flow. There are two main types of vortex breakdowns. Type 0, also known as a bubble breakdown or an axisymmetric breakdown, and type 2, also known as a spiral breakdown [39]. Within a closed geometry, only the bubble (type 0) breakdown is known to occur. This bubble is characterized by a limited region of recirculating flow that appears just downstream of an axial stagnation point. The stability limit at which this axial vortex bubble begins to form is determined by two parameters, the aspect ratio H/R_o, and the Reynolds number R_e [58]. Escudier's investigation expanded upon Vogel's work by using a larger variable range for these parameters. In doing so, he was able to detect up to 3 distinct breakdown bubbles with recirculating regions and noted that in some cases, when $Re > 2,500$ and $H/R_o > 1.5$, bubbles were found to oscillate in the axial direction. These results can be seen in Fig 1.3 [24]. Escudier's conclusions agree with those of Harvey in that the formation of vortex breakdown bubbles was not the result of flow instability, but was instead a transition from

one state to another. Any perturbations that existed in the flow would only result in a divergence from the axisymmetric geometry of the breakdown but would otherwise have no effect on its genesis. These basic results found by Escudier and Vogel for confined vortex breakdowns were later numerically verified by Lopez et. al. (1989 & 90) using the unsteady axisymmetric Navier-Stokes equation in an investigative series on axisymmetric breakdowns [34], [35], [8].

Increased understanding of the vortex breakdown phenomena has lead to many varied attempts at controlling its onset. Predominately this has involved the addition of a structural impedance, typically a rod, on the central axis. Cabeza et al. (2006) studied the effects of various sized rods placed along the central axis [9]. Utilizing radius ratios ranging from $R_r/R_o = 0.025 \rightarrow 0.125$, they found that as R_r was increased the critical Reynolds number at which vortex breakdown begins to occur also increased. Their results also show that for rod radii $R_r \geq 0.0625$, a vortex breakdown can occur at an aspect ratio of $H/R_O = 1$. This result differs from the open cylinder case studied by Escudier and other where no breakdown of any kind was found to occur at such a small aspect ratio; as noted in Fig 1.3.

Jørgensen, Sørensen and Aubry (2010) conducted a numerical study that also utilized a small axial rod to try and control vortex bubble formations [31]. However, unlike the passive stationary rod employed by Cebeza et al. they utilized a dynamic rotational rod in their model and conducted test for both co-rotation and counter-rotation cases. It should be noted that in this configuration, Jørgensen, Sørensen and Aubry's system was very similar in scope to that of a large gap Taylor-Coutte system, with the exception being that one of their end-walls was not stationary. Using constants for the end-wall Reynolds number,$R_{e_{ew}} = 2,200$, aspect ratio, $H/R_0 = 2.0$, and radius ratio, $R_r/R_O = 0.02$, they found that rod rotation results in the generation of a negative local vortex source near the fixed end-wall and a positive source near the rotating end-wall. Strength of these local sources was found to depend on the rotational direction of the rod, such that counter-rotation enhanced the positive source while co-rotation enhanced the negative source. Jørgensen et al. state that

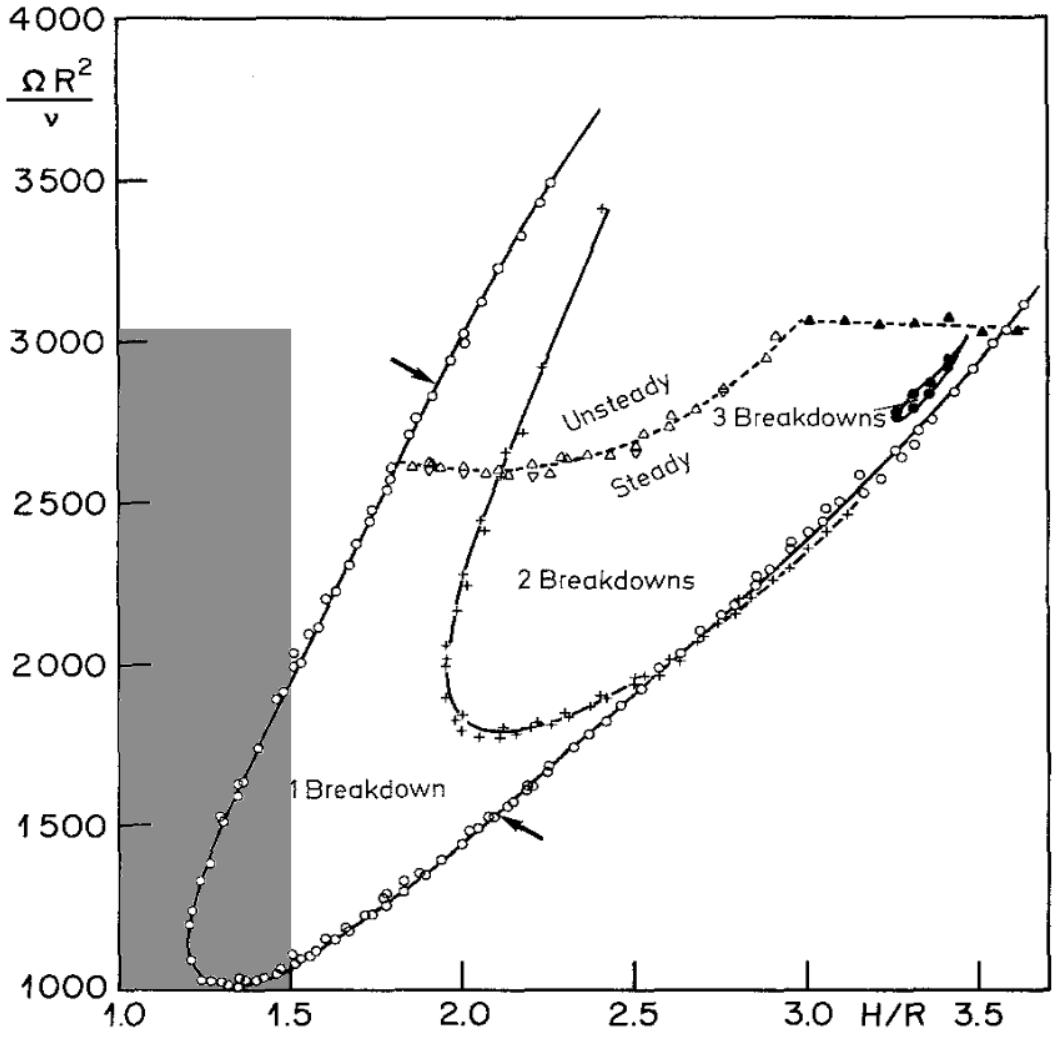

Figure 1.3: Stability boundaries for vortex breakdowns; produced by Escudier [24]. Here $R = R_o$, $\Omega = \Omega_{ew}$ the arrows represent the limits of Vogel's investigations, while the gray area represents the approximate test domain of the current work.

"it is the balance between the positive vorticity source near the rotating lid and the negative vorticity source near the fixed lid that controls the vortex breakdown" [31].

From their simulations, Jørgensen, Sørensen and Aubry (2010) found that when the positive source near the rotating end-wall was dominant, i.e. counter-rotation of the central rod relative to the rotating end-wall, vortex breakdowns were enhanced and resulted in larger and stronger breakdown bubbles. Domination of the negative source near the fixed wall however, i.e. co-rotation of the central rod relative to the rotating end-wall, was found to result in smaller weaker breakdown bubbles. In cases where the Reynolds number ratio was $R_{e_{rod}}/R_{e_{lid}} \geq 0.005$ vortex breakdown bubbles were seen to disappear completely. With these results Jørgensen et. al. showed that, even when utilizing a relatively thin axial rod, "Breakdown bubbles are either prevented by co-rotation or promoted by counter-rotation" [31].

Another method for actively controlling confined vortex breakdowns, that has been investigated over the past few decades, is the simultaneous rotation of both end-walls. Brøns, Voigt, and Sørensen (1999) performed a numerical investigation on the effects of co and counter-rotation of equally sized end-walls [7]. They conducted tests over a range of Reynolds numbers, $Re_{ew} = 800 - 2,500$, aspect ratios, $\Gamma_{ew} = 1 - 3.5$, and end-wall rotation ratios, $\frac{\Omega_{bottom}}{\Omega_{top}} = -0.02 - 0.05$, where positive and negative values of $\frac{\Omega_{bottom}}{\Omega_{top}}$ correspond to counter-rotation and co-rotation respectively. Their results showed that a delay in vortex breakdown bubble formation occurred for the counter-rotational end-wall cases. This, in turn, resulted in a stability graph $(\frac{R_e}{\Gamma_{ew}})$ where the bifurcation curves were shifted in the positive direction along both the vertical and horizontal axes. Counter-rotation was also found to result in a much narrower $(\frac{R_e}{\Gamma_{ew}})$ range, in which vortex breakdown bubbles were formed, when compared to the findings of Escudier and Vogel; displayed in Fig 1.3. For the co-rotational cases Brøns, Voigt and Sørensen (1999) observed the opposite tendencies, such that the bifurcation curve was shown to have a negative vertical and horizontal axial shift that was accompanied by a broader range between the upper and lower limits of the $(\frac{R_e}{\Gamma_{ew}})$ bifurcation curve. These

changes ultimately resulted in lower critical Reynolds numbers at which vortex bubbles were seen for a given Γ_{ew}; again, when compared to Escudier and Vogel's findings.

More recently Munumga et al. (2014) performed an experimental investigation similar to that of the numerical investigation conducted by Brøns, Voigt and Sørensen (1999) to determine the effectiveness of double end-wall rotation control on vortex breakdowns. However, unlike the previous numerical study Munumga et al. (2014) did not use equally sized rotating end-walls in their experimental system. Instead, their setup utilized a primary top rotating end wall, (of radius R_{ew}), with a partially rotating bottom end-wall where the outer most radius was stationary while the inner portion was made to rotate using various radial sized inserts (r_d).[41]. Their study employed a control disk to primary end-wall radius ratio range of approximately $r_d/R_{ew} = 0.05$ to 0.31 for a constant $\Gamma_{ew} = 2$. Experimental results showed a general agreement to the numerical analysis of Brøns et al. (1999) such that vortex breakdown was seen to occur at lower Reynolds numbers for co-rotation but was delayed to higher Reynolds numbers for counter-rotation. Additionally stating that, these higher and lower critical Reynolds number effects were, "amplified substantially by the use of larger control disks and higher rotation ratios" [41].

1.3 Fluid Dynamics

In this section a mathematical foundation of the physics within the two flow fields is presented. A more general formulation will be defined starting with Newton's second law and its application to fluids; better known as the Navier-Stokes equations. Followed by more specific examples and equations that pertain directly to the boundary conditions of the flow fields being presented here.

1.3.1 Navier-Stokes Equations

Newtons second law is one of the fundamental laws of physics. Simply stated, the second law says that the force acting on an object is equal to the object's time rate of change of momentum and is defined as [4].

$$F = \frac{d}{dt}(m\mathbf{U}) \tag{1.2}$$

Here the term $(m\boldsymbol{U})$ is known as the momentum of a body with mass m. When applying Eq. 1.2 to a system of fluid particles however, it is more convenient to work with density as opposed to mass. Thus, by dividing the momentum term by the volume of the system and reversing the terms for convenience Eq. 1.2 can be rewritten [53].

$$f = \rho\frac{d\mathbf{U}}{dt} \tag{1.3}$$

The term f in the equation above represents the applied force per unit volume on the fluid particles contained with a system. This term can be divided into two distinct components f_{body} and $f_{surface}$ [53]. Body forces are the macro scale forces, such as electromagnetic fields and gravity, which act at a distance on the entire volume of a system [4]. Surface forces on the other hand are those which act on the control surface of a fluid element. These forces arise from the stresses that are exerted on the sides of fluid elements and can be defined by the stress tensor written below; in Cartesian coordinates:

$$\boldsymbol{\tau_{ij}} = \begin{bmatrix} \tau_{xx} & \tau_{xy} & \tau_{xz} \\ \tau_{yx} & \tau_{yy} & \tau_{yz} \\ \tau_{zx} & \tau_{zy} & \tau_{zz} \end{bmatrix} \tag{1.4}$$

Contained within Eq. 1.4 are two distinct forms of stress: normal-stress and shear-stress. Normal stresses are the diagonal terms, where $i = j$. While shear stresses are the off diagonal terms, where $i \neq j$. Thus, since $\boldsymbol{\tau_{ij}}$ is a symmetric tensor, it follows that $\tau_{ij} = \tau_{ji}$

. If a fluid system is not at equilibrium the relative motion between fluid particles produces stress imbalances that result in net forces on the control surfaces of the fluid elements[18]. This net surface force can be written on a unit volume basis as:

$$f_i = \left[\frac{\partial \tau_{ii}}{\partial x_i} + \frac{\partial \tau_{ij}}{\partial x_j} + \frac{\partial \tau_{ik}}{\partial x_k}\right] = \frac{\partial \boldsymbol{\tau_{ij}}}{\partial x_j} = \nabla \cdot \boldsymbol{\tau_{ij}} \tag{1.5}$$

Where f_i is the force in the ith direction and i, j, and k are arbitrary coordinate place holders. Using this new definition of $f_{surface}$ from Eq. 1.5 and assuming that no external forces are applied to the system of interest, save for the ever-present force gravity, Eq. 1.3 can be rewritten.

$$\rho \frac{D\mathbf{U}}{Dt} = \rho \mathbf{g} + \nabla \cdot \boldsymbol{\tau_{ij}} \tag{1.6}$$

In-order to simplify Eq. 1.6 further the relationship between $\boldsymbol{\tau_{ij}}$ and $\boldsymbol{\epsilon_{ij}}$ needs to be established so that $\boldsymbol{\tau_{ij}}$ can be expressed in terms of fluid velocity $\mathbf{U}$. It is at this point that further manipulation of Newton's second law alone is of no use in advancing the mathematical description of fluid systems. Thus, additional theorems must be applied to Eq. 1.6. Introducing the fundamental law of conservation of mass and Newton's law of viscosity, combined with Stokes three postulates for the deformation of fluids, into Eq. 1.6 will allow for further discussion of the mathematical model. For conservation of mass the law simply states, that within any given system mass must be conserved, ie:

$$m = \rho \boldsymbol{\mathcal{V}} = \rho \frac{d\boldsymbol{\mathcal{V}}}{dt} + \boldsymbol{\mathcal{V}} \frac{d\rho}{dt} = constant \tag{1.7}$$

As previously mentioned, the goal is to express as many terms as possible as functions of fluid velocity. For the term $\frac{\partial \boldsymbol{\mathcal{V}}}{\partial t}$ in Eq. 1.7 this can be accomplished by utilizing the fact that the volumetric time rate of change of a fluid element is the result of total dilation caused by extensional forces acting on the element. By implementing this fact $\frac{\partial \boldsymbol{\mathcal{V}}}{\partial t}$ can now be rewritten in terms of normal-strain [53].

$$\frac{1}{\boldsymbol{\mathcal{V}}}\frac{d\boldsymbol{\mathcal{V}}}{dt} = \epsilon_{ii} + \epsilon_{jj} + \epsilon_{kk} = \frac{\partial u_i}{\partial x_i} + \frac{\partial u_j}{\partial x_j} + \frac{\partial u_k}{\partial x_k} = \nabla \cdot \boldsymbol{U} \tag{1.8}$$

Plugging the result of Eq. 1.8 into Eq. 1.7 and assuming fluid incompressibility where $\rho = constant$, which is an accurate assumption for the fluid used in the current work, the equation for the conservation of mass becomes:

$$\nabla \cdot \boldsymbol{U} = 0 \tag{1.9}$$

The resulting equation above can now be combined with Stokes' first and second postulates of fluid deformation. Respectively, these two postulates state that there must be a linear relationship between $\boldsymbol{\tau_{ij}}$ and $\boldsymbol{\epsilon_{ij}}$, and that the fluid must be isotropic. Applying these criteria allows for the normal-stress term $\frac{\partial \tau_{ii}}{\partial x_i}$ contained within Eq. 1.5 to be rewritten in terms of ϵ_{ij}. With the relationship between normal-stress and strain established, shear-stress must now be addressed so that it too can be rewritten in terms of ϵ_{ij}. This can be accomplished by using Newtons law of viscosity which states:

$$\tau_{ij} = \rho\upsilon\big(2\epsilon_{ij}\big) = \rho\upsilon 2\left(\frac{1}{2}\left[\frac{\partial u_i}{\partial x_j} + \frac{\partial u_j}{\partial x_i}\right]\right) \tag{1.10}$$

Equations 1.9 and 1.10 fulfill the first and second postulate of Stokes deformation law. The final postulate that needs to be satisfied is Stokes's third postulate, which states: when the fluid is at rest where $\boldsymbol{\epsilon_{ij}} = 0$, the deformation law must reduce to the hydrostatic equation. This implies that when a fluid is at rest normal-stresses must reduce to the hydrostatic pressure:

$$\tau_{ii} = -p \quad when \quad \tau_{ij} = 0 \quad \therefore \ \nabla p = \rho \mathbf{g} \tag{1.11}$$

Combining the concepts from Eqs. $\big(1.7$ - $1.11\big)$ descried above, stress terms can now be rewritten in terms of fluid velocity and pressure.

$$\tau_{ij} = -p\delta_{ij} + \rho\upsilon\left[\frac{\partial u_i}{\partial x_j} + \frac{\partial u_j}{\partial x_i}\right] + \lambda\Big(\nabla \cdot \boldsymbol{U}\Big)\delta_{ij} \tag{1.12}$$

Where δ_{ij} is the Kronecker delta and λ is the bulk viscosity coefficient. As previously stated the fluid of interest can be assumed to be incompressible. Thus, the third term on the right hand side in Eq. 1.12 goes to zero; leaving just the pressure and viscous terms. Using these results Eq. 1.6 can be rewritten.

$$\rho\left[\frac{\partial \boldsymbol{U}}{\partial t} + \big(\boldsymbol{U} \cdot \nabla\big)\boldsymbol{U}\right] \overset{\text{def}}{\equiv} \rho\frac{D\mathbf{U}}{Dt} = \rho\mathbf{g} - \nabla p + \rho\upsilon\nabla^2\boldsymbol{U} \tag{1.13}$$

The resulting equation presented in Eq. 1.13 is known as the Navier-Stokes equation and represents the fundamental foundation from which all viscous fluid systems are modeled.

Navier-Stokes: Cylindrical Coordinates

For the purpose of this work, it becomes convenient to transform Eq: 1.13 into a cylindrical coordinate system since the boundary conditions of the applicable geometry are, in-fact, a cylinder. Thus the following identities can be established between Cartesian (x, y, z) and cylindrical (r, θ, z) coordinates:

$$\begin{aligned} x &= r\cos\theta \qquad & y &= r\sin\theta \qquad & z &= z \\ r &= \sqrt{x^2 + y^2} \qquad & \theta &= \tan^{-1}\frac{y}{x} \qquad & z &= z \end{aligned} \tag{1.14}$$

Where $x = radial\ \ direction$, $\theta = azimuthal\ \ direction$ and $z = axial\ \ direction$. The dell operator must also be expressed in terms of the cylindrical system, taking the form:

$$\nabla = \hat{\mathbf{e}}_\mathbf{r}\frac{\partial}{\partial r} + \hat{\mathbf{e}}_\theta\frac{\partial}{\partial\theta} + \hat{\mathbf{e}}_\mathbf{z}\frac{\partial}{\partial z} \tag{1.15}$$

Here $\hat{\mathbf{e}}_\mathbf{r}$, $\hat{\mathbf{e}}_\theta$ and $\hat{\mathbf{e}}_\mathbf{z}$ are the unit vectors in the radial, azimuthal and axial directions respectively. Using the identities from Eq. 1.14 and Eq. 1.15, the vector form of the Navier-Stokes, from Eq. 1.13, can be rewritten in cylindrical coordinates using velocity components

with a vector field $\overrightarrow{U} = (v_r,\ \ v_\theta,\ \ v_z)$.

continuity:

$$\frac{1}{r}\frac{\partial}{\partial r}\Big(rv_r\Big) + \frac{1}{r}\frac{\partial v_\theta}{\partial \theta} + \frac{\partial v_z}{\partial z} = 0 \tag{1.16}$$

r-momentum:

$$\begin{gathered}\rho\left(\frac{\partial v_r}{\partial t} + v_r\frac{\partial v_r}{\partial r} + \frac{v_\theta}{r}\frac{\partial v_r}{\partial \theta} - \frac{v_\theta^2}{r} + v_z\frac{\partial v_r}{\partial z}\right) = \\ \rho g_r - \frac{\partial P}{\partial r} + \mu\left(\frac{1}{r}\frac{\partial}{\partial r}\left(r\frac{\partial v_r}{\partial r}\right) - \frac{v_r}{r^2} + \frac{1}{r^2}\frac{\partial^2 v_r}{\partial \theta^2} - \frac{2}{r^2}\frac{\partial v_\theta}{\partial \theta} + \frac{\partial^2 v_r}{\partial z^2}\right)\end{gathered} \tag{1.17}$$

θ-momentum:

$$\begin{gathered}\rho\left(\frac{\partial v_\theta}{\partial t} + v_r\frac{\partial v_\theta}{\partial r} + \frac{v_\theta}{r}\frac{\partial v_\theta}{\partial \theta} + \frac{v_r v_\theta}{r} + v_z\frac{\partial v_\theta}{\partial z}\right) = \\ \rho g_\theta - \frac{\partial P}{\partial \theta} + \mu\left(\frac{1}{r}\frac{\partial}{\partial r}\left(r\frac{\partial v_\theta}{\partial r}\right) + \frac{v_\theta}{r^2} + \frac{1}{r^2}\frac{\partial^2 v_\theta}{\partial \theta^2} - \frac{2}{r^2}\frac{\partial v_r}{\partial \theta} + \frac{\partial^2 v_\theta}{\partial z^2}\right)\end{gathered} \tag{1.18}$$

z-momentum:

$$\begin{gathered}\rho\left(\frac{\partial v_z}{\partial t} + v_r\frac{\partial v_z}{\partial r} + \frac{v_\theta}{r}\frac{\partial v_z}{\partial \theta} + v_z\frac{\partial v_z}{\partial z}\right) = \\ \rho g_z - \frac{\partial P}{\partial z} + \mu\left(\frac{1}{r}\frac{\partial}{\partial r}\left(r\frac{\partial v_z}{\partial r}\right) + \frac{1}{r^2}\frac{\partial^2 v_z}{\partial \theta^2} + \frac{\partial^2 v_z}{\partial z^2}\right)\end{gathered} \tag{1.19}$$

1.3.2 Vortex Dynamics

One of the most fundamental characteristics of any flow is the amount of angular deformation which acts on the fluid elements. Flow fields can be divide into two distinct classification, rotational and irrotational, dependent on whether angular deformation is present or not. Many viscous flows, including those presented in the present work, eventually produce some form of angular motion somewhere in the velocity field and are thus rotational. The loci where these rotationalities are present are known as eddies and their distribution within the flow is defined by the vorticity field $\boldsymbol{\omega}$:

$$\boldsymbol{\omega} \;=\; curl\, \boldsymbol{U} \;=\; \nabla \times \mathbf{U} \;=\; 2\boldsymbol{\Omega} \tag{1.20}$$

Here $\boldsymbol{\Omega}$ denotes the angular velocity of the flow field. Where, given a velocity field $\boldsymbol{U} = (u_i, u_j, u_k)$, the components of $\boldsymbol{\Omega}$ are defined as the rates of rotation about the axes (i, j, k) and are written in the form:

$$\Omega_i = \frac{1}{2}\left(\frac{\partial u_k}{\partial x_j} - \frac{\partial u_j}{\partial x_k}\right) \tag{1.21}$$

Eq. 1.21 is of a similar form as that of the shear strain term, ϵ_{ij}, from Eq. 1.10. This stems from the fact that ϵ_{ij} and $\boldsymbol{\omega}$ are not mutually independent of one another. Although ϵ_{ij} and $\boldsymbol{\omega}$ represent very different rates of measure, distortion and rotation respectively, they are both the result of the velocity gradient on individual fluid particles. Therefore, the velocity gradient itself can be thought of as a composition of ϵ_{ij} and $\boldsymbol{\omega}$. This relationship is most easily seen by comparing how ϵ_{ij} and $\boldsymbol{\omega}$ relate to the Laplacian and the velocity gradient:

$$\nabla^2 u_i \;=\; 2\frac{\partial \epsilon_{ij}}{\partial x_j} \;=\; -\big[\nabla \times \boldsymbol{\omega}\big]_i \tag{1.22}$$

$$\frac{\partial u_i}{\partial x_j} = \epsilon_{ij} + 2\Omega_k \tag{1.23}$$

"Thus, gradients in the strain field are related to gradients in vorticity. Note, however, that a uniform strain field can exist without vorticity while a uniform distribution of vorticity can exist without strain" [18]. While the former statement is mathematically true, it is only applicable for the special case of an inviscid flow. Although there are instances where such a model would be acceptable, this is not the case in the present work. Thus viscosity and its effects on the flow field, and more specifically on vorticity, must be addressed. This is most easily accomplished by first establishing a relationship between vorticity and angular moment (L_Ω). Given a small fluid element which is instantaneously spherical, and can thus be treated as a pseudo rigid body with a moment of inertia (I), the relationship between $\boldsymbol{\omega}$ and L_Ω can be written as:

$$L_\Omega = \frac{1}{2} I \boldsymbol{\omega} = I \boldsymbol{\Omega} \tag{1.24}$$

Since the element being considered is instantaneously spherical, at any one particular instant in time, pressure would be pointing inward at any given instant and thus have no significant effect on L_Ω. Therefore, any change in L_Ω would be a result of tangential surface stresses alone and the Lagrangian derivative of angular momentum can be written as:

$$\frac{DL_\Omega}{Dt} = T_\nu \quad \Longrightarrow \quad I\frac{D\omega}{Dt} = -\omega\frac{DI}{Dt} + 2T_\nu \tag{1.25}$$

Where T_ν is the viscous torque produced by the tangential surface stresses acting on the fluid element. This result leads to a very important implication. That being, to conserve momentum any change in the elements vorticity must result from either a change in viscous torque, a change in the elements moment of inertia, or some combination therein. In the latter case where viscous torque can be considered negligible any increase in $\boldsymbol{\omega}$ must result solely form a decrease in I; thus the fluid element must be elongated about its axis of rotation for an increase in vorticity to occur. These results are confirmed by comparing Eq. 1.25 with the Navier-Stokes equation (Eq. 1.13) from the previous section, where Eq. 1.13 can be rewritten in terms of $\boldsymbol{\omega}$ using the form:

$$\frac{\partial \boldsymbol{U}}{\partial t} = \boldsymbol{U} \times \boldsymbol{\omega} - \nabla\left(\frac{P}{\rho} + \frac{U^2}{2}\right) + \nu\nabla^2\boldsymbol{U} \tag{1.26}$$

Here $\left(\frac{P}{\rho} + \frac{U^2}{2}\right)$ is the Bernoulli function where $\frac{U^2}{2}$ is derived from the vector identity $\big(\boldsymbol{U} \cdot \nabla\big)\boldsymbol{U} + \boldsymbol{U} \times \boldsymbol{\omega}$. By taking the curl of Eq. 1.26 the equation can be further simplified:

$$\frac{D\boldsymbol{\omega}}{Dt} = \big(\boldsymbol{\omega} \cdot \boldsymbol{\nabla}\big)\boldsymbol{U} + \nu\nabla^2\boldsymbol{\omega} \tag{1.27}$$

From this, an analogy can be drawn from the terms on the right-hand side of Eq. 1.26 and 1.27 where:

$$-\boldsymbol{\omega}\frac{DI}{Dt} = \big(\boldsymbol{\omega} \cdot \nabla\big)\boldsymbol{U} \Rightarrow \text{Change in vorticity due to fluid stretching} \tag{1.28}$$

$$2T_\nu = \nu\nabla^2\boldsymbol{\omega} \Rightarrow \text{Change in vorticity due to viscous stresses} \tag{1.29}$$

These results reinforce the previously stated conclusions drawn from Eq: 1.25. At this point, a somewhat laconic mathematical base of vorticity has been established. However, it becomes more convenient to express the components of $\boldsymbol{\omega}$ in terms of cylindrical coordinates before moving on. As previously done with the Navier-Stokes equations of motion, $\boldsymbol{\omega}$ can be rewritten in terms of the r , θ and z coordinate system utilizing the form:

$$\omega_r = \left(\frac{1}{r}\frac{\partial u_z}{\partial \theta} - \frac{\partial u_\theta}{\partial z}\right) \qquad \omega_\theta = \left(\frac{\partial u_r}{\partial z} - \frac{\partial u_z}{\partial r}\right) \qquad \omega_z = \left(\frac{1}{r}\frac{\partial}{\partial r}\big(ru_\theta\big) - \frac{1}{r}\frac{\partial u_r}{\partial \theta}\right) \tag{1.30}$$

Taylor-Couette Flows

To fully understand the dynamics of Taylor-Couette flow and the formation of secondary steady states, one must first understand the dynamics of centrifugal instability. The basis for this concept was first developed by Lord Rayleigh in 1916. Rayleigh established a criterion

for the instability of a swirling flow where angular velocity $\Omega(r)$ has an arbitrary dependence on the radial distance from the axis of rotation. This criterion states that, for a swirling flow to be stable the following condition must hold:

$$\zeta(r) > 0 \quad \text{where} \quad \zeta = \frac{1}{r^3}\frac{d}{dr}\left(r^4\Omega^2\right) \tag{1.31}$$

It seems ironic, after such an important emphasis was placed on viscosity in the previous section, that to establish the basic concepts from which this criterion was derived the focus must be shifted and an inviscid azimuthal flow must now be considered. Rayleigh used a simple physical argument by considering two fluid elements of equal volume, (dV), rotating about a common axis at two separate radial distances, where:

$$u_\theta = r\Omega(r) \tag{1.32}$$

Since the flow is axisymmetric it is dependent only on r and z components. Thus the θ component of momentum from Eq. 1.18 can be rewritten:

$$\frac{DL_\Omega}{Dt} = \frac{D}{Dt}\left(ru_\theta\right) = 0 \tag{1.33}$$

This is of a similar form as that of Eq. 1.25, with the noted exclusion of the T_ν term due to inviscid conditions of Rayleigh's argument. Since viscous dissipation can not occur the angular momentum of each fluid element must remain constant. This angular momentum can be related to an element's kinetic energy per unit volume by the following:

$$E_i = \frac{1}{2}\rho u_{\theta_i}^2 = \frac{1}{2}\frac{\rho L_{\Omega_i}^2}{r_i^2} \tag{1.34}$$

Here i denotes a specific fluid element. Where $r_i = r_1$ and $r_i = r_2$ are the radial distances of the inner and outer elements, receptively, and are related by the identity $r_2 > r_1$. The combined kinetic energy of these two fluid elements can be written as:

$$\boldsymbol{E} = \frac{1}{2}\rho\left(\frac{L_{\Omega_1}^2}{r_1^2} + \frac{L_{\Omega_2}^2}{r_2^2}\right)dV \tag{1.35}$$

If the elements were to switch positions, such that *element* 1 is now at $r = r_2$ and *element* 2 is at $r = r_1$, and by virtue of Eq. 1.33 the angular momentum of each element is maintained, Eq: 1.35 would yield a different result for their combined energy. This change in kinetic energy can be expressed as:

$$\Delta\boldsymbol{E} \propto \left(L_{\Omega_2}^2 - L_{\Omega_1}^2\right)\left(\frac{1}{r_1^2} - \frac{1}{r_2^2}\right) \tag{1.36}$$

In the event that $\Delta\boldsymbol{E} < 0 \Rightarrow L_{\Omega_1}^2 > L_{\Omega_2}^2$ then such a swap would result in an energy release and thus cause an initially laminar base flow to become unstable. From this result it can be deduced that in-order for laminar flow stability to be maintained L_Ω^2 must decrease with decreasing r. Recalling that $L_\Omega = ru_\theta = r^2\Omega$ the connection to Rayleigh's stability criterion originally stated in Eq. 1.31 can now be seen.

$$\frac{dL_\Omega^2}{dr} \;=\; \frac{d}{dr}\left(r^4\Omega^2\right) > 0 \;\Rightarrow\; \text{for flow stability} \tag{1.37}$$

By applying Rayleigh's criterion to a flow between concentric cylinders the governing equations of Taylor-Couette flow can finally be established. For the given boundary conditions, and assuming cylinders of infinite length, the Navier-Stokes equations for an incompressible Newtonian fluid can also be applied. After which, the components of velocity and the pressure distribution in cylindrical coordinates become:

$$u_r = 0 \qquad u_\theta = Ar + \frac{B}{r} \qquad u_z = 0 \qquad \frac{\partial P}{\partial r} = \rho\frac{u_\theta^2}{r} \tag{1.38}$$

Where A and B depend on the radius ratio, $\eta = \frac{R_I}{R_O}$, and the rotational velocity ratio, $\mu_\Omega = \frac{\Omega_O}{\Omega_I}$, of the cylinders.

$$A = -\Omega_I \frac{\left(\eta^2 - \mu_\Omega\right)}{\left(1 - \eta^2\right)} \qquad B = \Omega_I R_I^2 \frac{\left(1 - \mu_\Omega\right)}{\left(1 - \eta^2\right)} \tag{1.39}$$

For cases such as those of the present work, where the outer cylinder is stationary, A and B reduce:

$$A = -\Omega_I \frac{\eta^2}{\left(1 - \eta^2\right)} \qquad B = \Omega_I \frac{R_I^2}{\left(1 - \eta^2\right)} \tag{1.40}$$

Applying Rayleigh's criterion from Eq. 1.37 to the boundary conditions described by Eq. 1.38 and Eq. 1.40, results in a linear stability limit of Taylor-Couette flow that is defined by:

$$\zeta = 4A^2\left(1 - \frac{B}{Ar^2}\right) \quad \text{where} \quad \zeta > 0 \quad \text{for flow stability} \tag{1.41}$$

While Eq. 1.41 describes the underlying physics of Taylor-Couette flow instability it is an oversimplification in reality. This stems from the fact that Eq. 1.37, from which Eq. 1.41 was derived, uses the assumption of inviscid flow. Thus Eq. 1.41 implies that if the outer cylinder is stationary Taylor-Coutte flow would always be unstable at any inner cylinder rotational rate. However, this is not the case in reality. When viscosity is reintroduced into the problem it acts as a stabilizing force which allows the flow to remain stable up to some critical point. Taylor was able to prove this in 1923 by using a linear stability analysis based on small perturbations of the velocity and pressure fields. Expressed as normal modes of the form:

$$\begin{gathered} u_r = 0 + u_r^{'} = u_r^*(r)\cos(kz)e^{qt} \quad u_\theta = \bar{u}_\theta + u_\theta^{'} = \bar{u}_\theta + u_\theta^*(r)\cos(kz)e^{qt} \\ u_z = 0 + u_z^{'} = u_z^*(r)\sin(kz)e^{qt} \quad P = \bar{p} + p^{'} = \bar{p} + p^*(r)\cos(kz)e^{qt} \end{gathered} \tag{1.42}$$

Here the superscript $(*)$ denotes amplitudes of component perturbation, k is the wavenumber, q is the growth rate of the perturbations and $\bar{u}_\theta$ and $\bar{p}$ are the steady-state solutions of azimuthal velocity and pressure respectively. By substituting the perturbations of Eq. 1.42

into the viscous axisymmetric form of the Navier-Stokes equation and then linearizing, a set of ordinary differential equations results:

Continuity:

$$\frac{1}{r}\frac{\partial}{\partial r}\left(ru_r^{'}\right)+\frac{\partial u_z^{'}}{\partial z} \implies \frac{1}{r}\frac{d}{dr}\left(ru_r^*\right)+ku_z^*(r)=0 \tag{1.43}$$

r-momentum:

$$\begin{aligned}\frac{\partial u_r^{'}}{\partial t}-2\Omega u_\theta^{'}&=-\frac{1}{\rho}\frac{\partial p^{'}}{\partial r}+\nu\left[\frac{\partial}{\partial r}\left(\frac{1}{r}\frac{\partial}{\partial r}\left(ru_r^{'}\right)\right)+\frac{\partial^2 u_z^{'}}{\partial z^2}\right]\\ \implies qu_r^*-2\Omega u_\theta^*&=-\frac{1}{\rho}\frac{dp^*}{dr}+\nu\left[\frac{d}{dr}\left(\frac{1}{r}\frac{d}{dr}\left(ru_r^*\right)\right)-k^2u_r^*\right]\end{aligned} \tag{1.44}$$

θ-momentum:

$$\begin{aligned}\frac{\partial u_\theta^{'}}{\partial t}+u_r^{'}\frac{d}{dr}\left(r\Omega\right)+u_r^{'}\Omega&=\nu\left[\frac{\partial}{\partial r}\left(\frac{1}{r}\frac{\partial}{\partial r}\left(ru_\theta^{'}\right)\right)+\frac{\partial^2 u_\theta^{'}}{\partial z^2}\right]\\ \implies qu_\theta^*+u_r^*\left(\frac{d}{dr}\left(r\Omega\right)+\Omega\right)&=\nu\left[\frac{d}{dr}\left(\frac{1}{r}\frac{d}{dr}\left(ru_\theta^*\right)\right)-k^2u_\theta^*\right]\end{aligned} \tag{1.45}$$

z-momentum:

$$\begin{aligned}\frac{\partial u_z^{'}}{\partial t}&=-\frac{1}{\rho}\frac{\partial p^{'}}{\partial z}+\nu\left[\frac{\partial}{\partial r}\left(\frac{1}{r}\frac{\partial}{\partial r}\left(ru_r^{'}\right)\right)+\frac{\partial^2 u_z^{'}}{\partial z^2}\right]\\ \implies qu_z^*&=-\frac{kp^*}{\rho}+\nu\left[\frac{1}{r}\frac{d}{dr}\left(r\frac{du_z^*}{dr}\right)-k^2u_z^*\right]\end{aligned} \tag{1.46}$$

By setting $q=0$ a critical wave number which corresponds to the flows marginal stability limit can be found. Letting $r=\tilde{x}\hat{\mathrm{d}}+R_I$, where $\hat{\mathrm{d}}=R_O-R_I$ and $\tilde{x}$ is a non dimensional parameter such that $0<\tilde{x}<1$, the azimuthal momentum, Eq. 1.45, can be written as:

$$2Au_r^*=\frac{\nu}{\hat{\mathrm{d}}^2}\left(\frac{d^2}{d\tilde{x}^2}-\left(k\hat{\mathrm{d}}\right)^2\right)u_\theta^* \tag{1.47}$$

Noting that $\left(\frac{d}{dr}\left(r\Omega\right)+\Omega\right)=\frac{1}{r}\frac{d}{dr}\left(ru_\theta\right)=2A$. The radial and axial components can also be reduced by combining Eq. 1.44 and Eq. 1.46, in order to eliminate the pressure terms:

$$2\big(k\hat{\mathrm{d}}\big)^2\frac{u_\theta}{r}u_\theta^* = \frac{\nu}{\hat{\mathrm{d}}^2}\Big(\frac{d^2}{d\tilde{x}^2} - \big(k\hat{\mathrm{d}}\big)^2\Big)^2 u_r^* \tag{1.48}$$

Some important relationships between the terms in Eq. 1.47 and Eq. 1.48 should be noted. Where the terms on the left-hand sides of equations 1.47 and 1.48 represent the Coriolis acceleration and tangential vorticity production, while the right-hand sides represent the tangential viscous force and viscous diffusion, respectively [16]. For steady flow to exist at a point just before instability occurs these forces must balance both locally and globally. Thus, the ratios of these forces must be of order unity. By setting $\Big(\frac{d^2}{d\tilde{x}^2} - \big(k\bar{\mathrm{d}}\big)^2\Big) = \gamma$ and $\Big(k\bar{\mathrm{d}} = \kappa\Big)$, and then combining Eq. 1.47 and Eq. 1.48, u_r^* and u_θ^* terms can be eliminated:

$$\frac{4A\Omega\hat{\mathrm{d}}^4}{\nu^2}\frac{\kappa^2}{\gamma^3} = 1 \tag{1.49}$$

Here $\big(\frac{4A\Omega\hat{\mathrm{d}}^4}{\nu^4}\big)$ relates the flows inertial forces to viscous forces and is defined, by convention, as the Taylor number $\big(T_a\big)$. Many different forms of T_a have been derived over the years, where different versions can yield different values of the T_a for the same flow. However, for every version of T_a there exist a critical limit where centrifugal forces begin to exceed viscous forces, which results in flow instability and the formation of TVF. For this work a small gap variation of the T_a, given by White, was used [53]:

$$T_a = \frac{\hat{\mathrm{d}}^3 R_I \Omega_I^2}{\nu^2} \tag{1.50}$$

From this form of the Taylor number a relationship to the more general dimensionless parameter of the Reynolds number can be shown:

$$T_a = R_{e_c}^2\left(\frac{1-\eta}{\eta}\right) \qquad \text{where} \qquad R_{e_c} = \frac{\Omega_I R_I \hat{\mathrm{d}}}{\nu} \tag{1.51}$$

Vortex Breakdowns

The last bit of mathematics that must be discussed are the governing equations of a confined vortex breakdown. As in section 1.2, the discussion on this subject matter will be much lighter than that of the previous section's discussion on Taylor-Couette flow. However, there are some fundamental mathematics that must be presented. There are 2 main parameters which characterize the onset of a vortex breakdown bubble at certain critical combinations:

$$R_{e_{ew}} = \frac{\Omega_{ew} R_O^2}{\nu} \qquad \Gamma_{ew} = \frac{H}{R_O} \tag{1.52}$$

Where $R_{e_{ew}}$ is the Reynolds number of the rotating end wall and Γ_{ew} is the aspect ratio of the confined vortex flow. The kinematics of the flow field can be similarly described as that of Taylor-Couette flow by using the axisymmetric form of the Navier-Stokes equations. Using a stream function and noting that the velocity field is depended only on (r, z) the components of velocity can be defined as such:

$$u_r = \frac{1}{r}\frac{\partial \psi}{\partial z} \qquad u_z = -\frac{1}{r}\frac{\partial \psi}{\partial r} \tag{1.53}$$

Thus the flow can be described by the swirling motion of the fluid (u_θ), and the isocurves of (ψ), which represent the intersections of the physical stream-surfaces with the meridional plane. Using Eq. 1.53 the azimuthal component of vorticity (ω_θ) can be found by expressing the Poisson equation in terms of the stream function.

$$\nabla^2 \psi = \frac{\partial^2 \psi}{\partial z^2} + \frac{\partial^2 \psi}{\partial r^2} + \frac{1}{r}\frac{\partial \psi}{\partial r} = r\omega_\theta \tag{1.54}$$

Incorporating Eq. 1.53 and Eq. 1.54 into the axisymmetric Navier-Stokes equations leads to the azimuthal velocity and vorticity transport equations given by:

$$\frac{\partial u_\theta}{\partial t} + \frac{\partial}{\partial r}(u_r u_\theta) + \frac{\partial}{\partial z}(u_z u_\theta) + \frac{2}{r}(u_r u_\theta) = \frac{1}{R_{e_{ew}}}\left[\frac{\partial}{\partial r}\left(\frac{1}{r}\frac{\partial (r u_\theta)}{\partial r}\right) + \frac{\partial^2 u_\theta}{\partial z^2}\right] \tag{1.55}$$

$$\frac{\partial \omega_\theta}{\partial t} + \frac{\partial}{\partial r}(u_r \omega_\theta) + \frac{\partial}{\partial z}(u_z \omega_\theta) - \frac{1}{r}\frac{\partial}{\partial z}(u_\theta^2) = \frac{1}{R_{e_{ew}}}\left[\frac{\partial}{\partial r}\left(\frac{1}{r}\frac{\partial (r \omega_\theta)}{\partial r}\right) + \frac{\partial^2 \omega_\theta}{\partial z^2}\right] \tag{1.56}$$

While equations 1.53 - 1.56 yield the velocity field and basic flow structure of a confined vortex breakdown flow they do not fully describe the actual physical means by which a vortex breakdown bubble forms. The exact physical mechanics which cause the formation of a breakdown bubble is still widely debated. Several theories have been proposed all of which can generally be categorized into one of three main ideas.

1. Hydrodynamic instability

2. Axial deceleration and flow stagnation

3. Transitions between critical flow states, generally due to wave phenomena

Chapter 2

Experimental Setup

Experimental tests were conducted in the Vortex Dynamics Laboratory at Auburn University. A Couette cell with a bottom-mounted inner rotating cylinder was constructed. The design utilized a gap ratio of $\eta = \frac{R_I}{R_O} = 0.815$ and an aspect ratio baseline of $\Gamma_c = \frac{L_I}{\hat{\mathrm{d}}} = 20$ at $\Gamma_{ew} = \frac{H_{ew}}{R_O} = 0$ for the inner cylinder. A positionally variable rotating upper end-wall was used as a means of flow control. The upper end-wall was designed so that an end-wall aspect ratio range of $\Gamma_{ew} = 0 - 1.5$ could be tested. The rotational frequency, direction and relative axial position of the upper end-wall and inner cylinder were made to vary over a range of experimental test cases.

2.1 Apparatus

A transparent acrylic tube was used to construct the outer cylinder of the Couette system. Acrylic sheets were assembled around the cylinder to make a square tank enclosure. To correct for the refractive index effects of the cylinder's curved surface, and to aid in temperature stability, the gap in between was filled with water. This fluid bath around the cylinder was designed to correct the optical path between the camera and the area of interest and ensure there were no distortions in the PIV images. A vertical support tower was constructed to mount the various components of the system. This tower was attached to the top of a steel table in-order to provide increased system stability. The tank assembly was attached to the front of the support tower using four bolts which were threaded into tapped mounting holes positioned at the four corners of the tank's rear plate. Two DC servo motors were mounted at the top and bottom rear of the tower in-order to drive the rotational components of the system.

2.2 Tank Geometry

The Couette cell/tank assembly, as seen in Fig. 2.1, consisted of a 61 cm (L_O) long acrylic outer cylinder with an inner diameter of 14.2 cm (2xR_O) and an outer diameter of 15.48 cm. Square end-plates were milled with a 15.5 cm diameter circular section drilled out of the center into which the top and bottom of the outer cylinder were placed. Weld-On #4 was utilized to chemically weld these end-plates to the outer cylinder, ensuring a watertight seal between components. This assembly was then enclosed using four pieces of 64 cm x 22.86 cm x 0.95 cm acrylic, these were attached to the side faces of the end-plates using a combination of threaded bolts and acrylic cement (Weld-On #4); resulting in a water tight bath around the outer cylinder. As previously stated this square outer tank aided in correcting the refractive index caused by the curved geometry of the outer cylinder which allowed for cleaner visual lines during PIV acquisition. The

The inner cylinder was constructed from a 26.0 cm (L_I) long, 11.60 cm (2xR_I) diameter, machined aluminum tube with two 11.20 cm diameter disks spot welded on to either end. The disks were machined so that one of the two had an 11.4 cm long rod at its center that was used to secure the assembly in a ball bearing insert at the center of an acrylic end-cap. This inner cylinder end-cap assembly was inserted and secured into the bottom of the outer cylinder using two circumferential O-rings. Variable height supports placed between the steel support table and the inner cylinder end-cap were additionally used to ensure a tight seal between the inner and outer cylinders. These supports also helped to support the load of the cantilevered tank.

The 14.15 cm (2xR_{UW}) diameter upper rotating end-wall was milled out of a 0.635 cm thick piece of aluminum stock. It was designed with a diameter slightly smaller than that of the outer cylinder, which resulted in a clearance of 0.05 cm, to allow for rotation. A 50 cm chrome-moly rod was secured to the top of the upper end-wall using a combination of tap hole/threading and tap welds and was used in facilitating end-wall adjustments in the vertical plane.

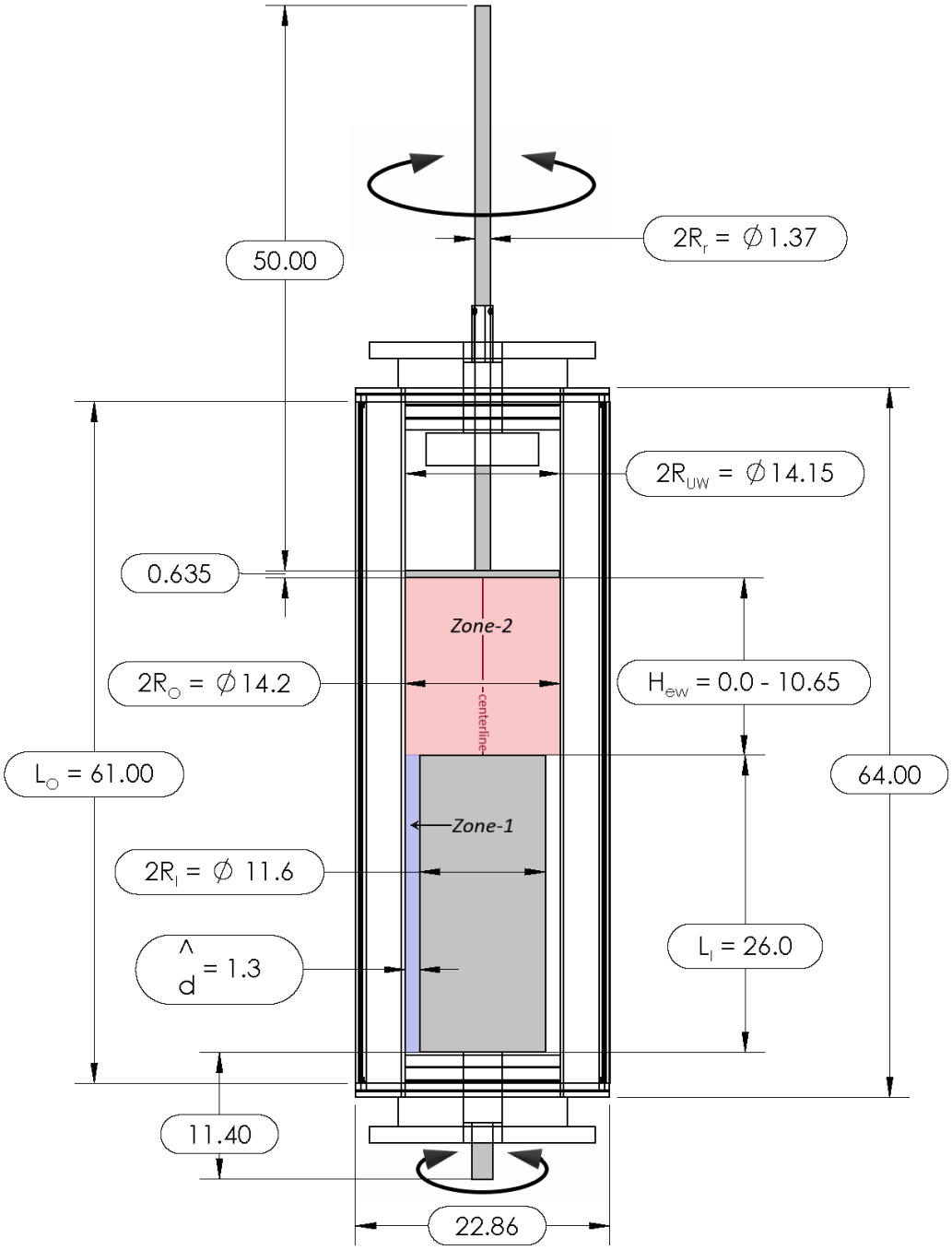

Figure 2.1: Details of the Couette Tank
(*all dimensions in cm*)

2.3 Rotation Control

Rotation of both the upper end-wall and inner cylinder was driven by a gear and belt system which utilized two high torque brushless motors, one for each rotational component. Each motor was connected to a BE15A series brush-less servo amplifier powered by a $50V$ DC power supply. Angular velocity of the rotating components was controlled by two separate 10 turn potentiometers connected to the servo amplifiers. Photo reflectors were built into the gears attached to both the upper end-wall and inner cylinder that allowed rotational rates to be verified through the use of a photo tachometer.

2.3.1 Working Fluid

The properties of the fluid that is used to fill the annulus of a Couette cell are extremely important in determining flow behavior and the onset of instabilities. For this investigation, the working fluid consisted of a 50% water 50% glycerin solution. Laboratory ambient temperature was maintained at $20.5°C \pm 0.5° \Leftrightarrow 68.9°F \pm 1.8°$. This temperature range resulted in a kinematic viscosity of $\approx 5.29e^{-6} \frac{m^2}{s}$ for the mixture. As previously mentioned the water bath that enclosed the Couette cell was used to insulate the working fluid from any changes in ambient temperature. To verify the stability periodic measurements were taken to ensure temperature consistency between tests. Aluminum microsphere seeding particles approximately $15\mu m$ in diameter were mixed into the working fluid prior to testing. Premixing of the particles was done to ensure that the seeding had a homogeneous distribution and suspension. These particles were used to seed the flow during testing so that PIV images could be captured.

2.3.2 Data Acquisition / Particle Imaging Velocimetry

Particle Imaging Velocimetry (PIV) is a very powerful experimental technique, especially when applied to fluid dynamic investigations. PIV provides instantaneous velocity vector measurements in a cross-section of a flow field by capturing images of entrained micron-sized

particles in a non-intrusive manner. For this reason, a 2D-2C PIV measurement technique was chosen as the data acquisition method for the current works experimentation. The experimental configuration of a PIV system generally consists of a light source, projected in the form of a planar sheet, a CCD camera and a dedicated PIV processor. While the exact setup of any given PIV system may differ, depending on the specific subject matter being investigated, it is typically configured to be of the form used by Mutabazi et al. as shown in Figure 2.2 [42]. For the current work, the experimental PIV setup that was used is noted to be exemplified best by this configuration (Fig. 2.2) as well.

A New Wave Research Solo III ND: YAG 50 mJ dual pulse laser was used in conjunction with a plano-concave lens attachment to create a $1.5\,mm$ thick light sheet. This light sheet was positioned on the left side of the Couette tank to intersect the systems vertical axis, resulting in an observable velocity field along the (r, z) plane that measured approximately $14.5cm$ x $15.5cm$. The laser was positioned approximately $85\,cm$ away from the apparatus resulting in a sheet that illuminated a vertical distance of approximately $34\,cm$. It should be noted that, due to the orientation, the sheet only illuminated one side of the annular gap. This was due to the presence of the opaque inner cylinder which prevented the light from illuminating the far side of the annulus. A Dantec 80C60 HiSense PIV/PLIF CCD camera, with a $60mm$ Nikon lens, was placed $114cm$ away from the system and oriented perpendicular to the light sheet plane. Both the laser and camera were connected to a Dantec FlowMap 2100 PIV processor to facilitate the simultaneous triggering. The laser was set to a trigger rate of $5.5\,Hz$ with a variable pulse duration (Δt) to allow for sufficient particle displacement between image captures. The interrogation window was set to a 32 x 32 pixel area with a 75% overlap criteria in both the vertical and horizontal directions. Triggering and acquisition were controlled through the Dantec Dynamics FlowManager software package. Post-processing of the PIV images was done using the Fluere 1.3 velocimetry analysis software and custom-built POD MATLAB code, both of which are discussed in the following sections.

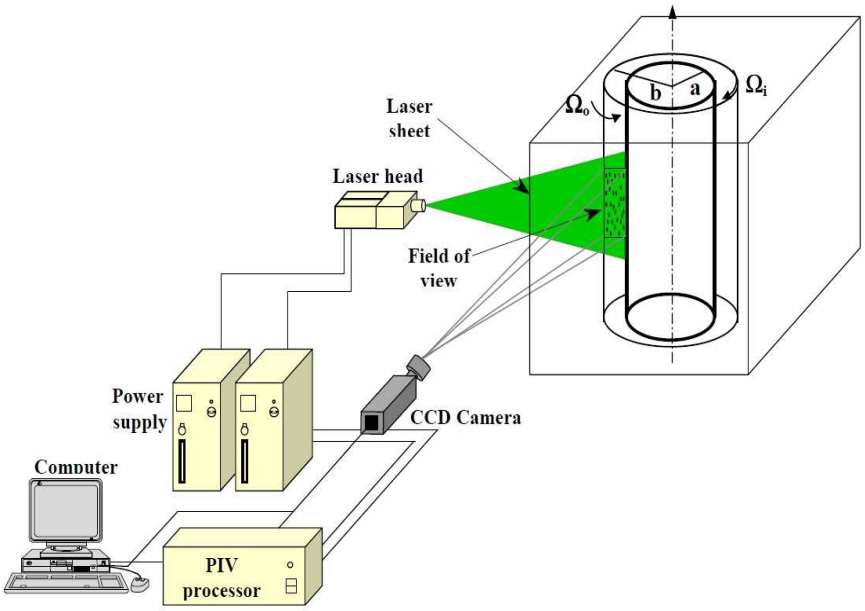

Figure 2.2: PIV System Setup [42]

2.4 Testing and Processing

Baseline tests were independently conducted for both flow fields. Taylor-Couette baseline tests were conducted over a R_{e_c} range of $74-387$ with a R_{e_c} step size of 15, corresponding to a T_a number range of $1,312-35,485$ and a $R_{e_{tc-vb}}$ of $314-1,631$ (where $R_{e_{tc-vb}} = \frac{\Omega_I R_I^2}{\nu}$). This range was tested at four values of Γ_{ew} by moving the stationary upperend-wall in increments of $\Delta\Gamma_{ew} = 0.5$ from $\Gamma_{ew} = 0 - 1.5$. For the two largest values of Γ_{ew} testing was be repeated, once for the upper flow domain and once for the lower domain, in order to capture the desired area of interest. Baseline measurements for the Vortex Breakdown flow field were conducted by modifying the system with a circular acrylic insert with two circumferential O-ring inlays. This insert was positioned on top of the rotational cylinder in-order to seal the inner cylinder and act as a non-rotating end-wall. The upper rotating end-wall was placed at three different values of Γ_{ew} : 0.5, 1 and 1.5. For each value of Γ_{ew} Reynolds numbers from $R_{e_{ew}} = 755$ to $R_{e_{ew}} = 3,020$ were tested in increments of $R_{e_{ew}} = 94$.

For the combined flow conditions, tests were conducted at the same Γ_{ew} values as those of the vortex breakdown baseline cases. Additionally, as with the Taylor-Couette baselines, tests were repeated for the $\Gamma_{ew} = 1$ and $\Gamma_{ew} = 1.5$ conditions to capture the upper and lower portions of the flow field. The range of Reynolds number and step size utilized for the inner rotating cylinder was the same as that used for the baseline test cases. R_e range for the upper end-wall was slightly modified from that used in VB baseline tests and ranged from $R_{e_{ew}} = 944 - 2,926$ with a step size of $R_{e_{ew}} = 94$. This reduced range was used to facilitate a more timely acquisition process. For all Γ_{ew} values utilized in the combined flow field investigations tests for both co-rotational and counter-rotational conditions of the upper end-wall and inner cylinder were conducted.

Images were processed using Fluere 1.3 velocimetry analysis software which uses an iterative image deformation algorithm to perform a Fast Fourier Transform (FFT) of image pairs to provide a cross-correlation of the velocity field. A Gaussian window with a 7 x 7 Sinc interpolation method with a total of four passes was chosen for calculation of image correlation. Due to the large amount of raw data that needed to be processed, an automated Matlab script was written utilizing the *java.awt.Robot* library and nested process loops to facilitate switching between the directories of the various test conditions. This allowed for continuous 24-hour processing of the PIV images on multiple computers and expedited the analysis of the experimental data.

2.5 Proper Orthogonal Decomposition

One of the most powerful techniques available for extracting coherent structures from a flow field is the Proper Orthogonal Decomposition (POD) method. POD allows for the acquisition of a low-dimensional approximations of higher-dimensional processes from experimental data and is often conducted to extract modal shapes, and basis functions [13]. POD is often reported under various names such as Principal Component Analysis (PCA), Kosambi-Karhunen-Loéve Transformation (KLT), Empirical Orthogonal Functions (EOF),

and Empirical Modal Analysis (EMA), just to name a few. POD was first introduced as a method of defining coherent structures within a fluid system by Lumeley (1967). He proposed that fluid structures could be defined in an unbiased manner with functions of the spatial variables that contain the maximum energy content. This is best described where given a flow field data matrix $\mathbf{D}$ a linear combination of POD basis vector $\Phi(x)$ can be found which maximize the following expression:

$$\max_{\Phi} \frac{\langle |[\Phi(\mathbf{x}), \mathbf{D}(\mathbf{x}, t)]^2| \rangle}{[\Phi(\mathbf{x}), \Phi(\mathbf{x})]} \tag{2.1}$$

Where x is an arbitrary variable representing spatial coordinates, t is an instantaneous time, or snapshots and $\langle \cdot \rangle$ is a time-averaging operation. To find the $\Phi(x)'s$ which maximize Eq: 2.1 it can be shown that a necessary condition which must be met is that $\Phi(x)$ is a solution of the Fredholm integral equation of the second type:

$$\int_{\Psi} \mathbf{K}(\mathbf{x}, \mathbf{x}^{'}) \Phi(\mathbf{x}^{'}) dx^{'} = \lambda \Phi(\mathbf{X}) \tag{2.2}$$

Where Ψ is the flow domain, and $\mathbf{K}$ is the space-correlation tensor, also known as the kernel:

$$\mathbf{K}(\mathbf{x}, \mathbf{x}^{'}) = \langle \mathbf{D}(\mathbf{x}, t), \mathbf{D}^{\mathbf{T}}(\mathbf{x}^{'}, t) \rangle \tag{2.3}$$

"According to the Hilbert-Schmidt theory, Eq: 2.3 has a denumerable set of orthogonal solutions $\Phi_n(\mathbf{x})$ with corresponding real and positive eigenvalues λ_n. The eigenvalue with the largest magnitude is the maximum which is achieved in the maximization problem Eq: 2.1" [10]. This implies that Eq: 2.1 can be implemented in the space orthogonal to $\Phi_n(x)$ in-order to find additional POD basis functions $\Phi_{n+1}(x)$. This procedure can be repeated such that a whole set of orthogonal functions representing coherent structures, and their corresponding relative energy levels, can be determined:

$$\Phi_1 \geq \Phi_2 \geq \Phi_3 ..... \geq \Phi_{n+1} \geq 0 \qquad \lambda_1 \geq \lambda_2 \geq \lambda_3 ..... \geq \lambda_{n+1} \geq 0 \tag{2.4}$$

Simply stated, Eq: 2.4 implies that if the flow field is projected along Φ_n the average energy content (λ_n) of the underlying flow structure is greater than that of flow field projections along Φ_{n+1}, i.e. ($\Phi_1 ..... \Phi_{n+1} \xrightarrow[\text{content}]{\text{energy}} \lambda_1 ..... \lambda_{n+1}$). In this way a flow fields coherent time-averaged structures can be extracted at various energy levels from a continuous data set of the flows velocity components.

At this point everything that has been outlined on the POD method above has dealt with it application on a continuous, or nearly unbounded temporally, data set for $\mathbf{D}$. However, in the present work $\mathbf{D}$ is discreet, both spatially and temporally, and can be more accurately defined as $\mathbf{D}(u, v, n)$ where $n = n^{th}$ PIV snapshot in the range $1 \rightarrow N$ and u and v are respectively the horizontal and vertical velocity components at a single grid point within the flow domain. Solving the Fredholm integral equation (Eq. 2.2) for $\mathbf{K}(\mathbf{x}, \mathbf{x}')$ directly would be very computationally expensive and, especially in the case of PIV data sets, is generally not a very practical approach. Thus the focus will now be shifted to describe POD methods which are better suited for discreet data set analysis and that are more applicable to the work here.

Given a data set ($\mathbf{D}$) is discreet and not continuous a simpler POD analysis method know as 'Snapshot' can be applied to solve for $\mathbf{K}(\mathbf{x}, \mathbf{x}')$. Lawrence Sirovich first introduced this method in 1987 as a way to efficiently determine the POD modes for large problems, particularly coherent structures in a turbulent flow field as this was the application for which he first developed it [48]. Sirovich's method of 'Snapshots' approach utilizes the ergodicity hypothesis and the fact that the eigenfunctions of the kernel are simply linear combinations of instantaneous solutions, or "Snapshot", such that the POD basis vectors can be written as:

$$\mathbf{K}(\mathbf{x},\mathbf{x}^{'}) = \lim_{n\to\infty}\sum_{n=1}^{N}\mathbf{D}_n(\mathbf{x}),\mathbf{D}_n^T(\mathbf{x}^{'}) \tag{2.5}$$

For Eq. 2.5 to be applicable, the time (dt) between snapshots ($\mathbf{D_n}(\mathbf{x}) = \mathbf{D}(\mathbf{x}, ndt)$) must be large enough such that the snapshots are uncorrelated and that there a finite number (N) of them large enough for a reasonable approximation of $\mathbf{K}(\mathbf{x},\mathbf{x}^{'})$. By substituting 2.5 into 2.2 results in a degenerate integral equation where the solutions are linear combinations of the snapshots, provided that the snapshots are linearly independent, i.e. ($M >> N$, where M = the number of data grid cells in a single snapshot). This criterion of $M >> N$ is typically true for most PIV data sets and was for the present work as well, where $N = 1000$ images, and $M = \frac{pixels}{window} = \frac{(1{,}224\times968)}{(32\times32)(1-0.75)} \approx 18{,}500$ grid points. Thus, the above substation is applicable here and the eigenvectors of K can be found as a linear combination of the snapshots utilizing the following equation:

$$\Phi(\mathbf{x}) = \sum_{n=1}^{N}\beta_n\mathbf{D_n}(\mathbf{x}) \tag{2.6}$$

Were $\mathbf{D_n}$ is the flow field vector map at time t_n, containing the flows u and v velocity vectors at each grid point for a given snapshot, and the coefficient β_n can be shown to satisfy the eigenvalue-eigenvector equation:

$$\mathbf{C}\beta = \lambda\beta \tag{2.7}$$

Here $\mathbf{C}$ is the correlation matrix ($\mathbf{C}_{ij} = \frac{1}{N}(\mathbf{D}_i(\mathbf{x}),\mathbf{D}_j(\mathbf{x}))$), defined as the inner product of the velocity perturbations of $\mathbf{D}$, β represents the eigenvectors and λ the corresponding eigenvalues. Thus the problem is reduced to finding the coefficients β_n of this linear combination, which can be accomplished by recognizing that the eigenfunctions Φ are orthogonal and can be normalized:

$$\langle\Phi_i,\Phi_j\rangle = \delta_{ij} \tag{2.8}$$

Such that Φ_i represents the eigenvectors of a symmetric $N \times N$ matrix, Φ_j represents the eigenvectors of a $M \times M$ matrix and δ^{ij} is the Kronecker delta. An approximation of the flow field can then be given as a linear combination of the eigenfunctions.

$$\mathbf{D}(\mathbf{x}) \approx \sum_{n=1}^{N} \alpha_n(t)\Phi_n(\mathbf{x}) \tag{2.9}$$

Here the coefficient $\alpha_n(t)$ is a function of time determined by $\alpha_n(t) = (\mathbf{D}(\mathbf{x}, t), \Phi_n(\mathbf{x}))$. Where $\alpha_n(t)^2$ represents the amount of energy in $\mathbf{D}(\mathbf{x}, t)$ in the direction of the n^{th} POD basis vector, Φ_n, and the total energy is the summation of the $\alpha_n(t)^2$ terms in the various directions of Φ_n. The coefficients of α_n are additionally noted to be uncorrelated and their mean values equal to the eigenvalues λ such that:

$$\langle \alpha_i(t), \alpha_j(t) \rangle = \delta_{ij}\lambda \tag{2.10}$$

By comparison of Eq. 2.7 - 2.10 it can be shown that the eigenfunctions Φ_i and Φ_j satisfy the eigenvalue-eigenvector equation such that:

$$\mathbf{D}\Phi_{i_n} = \lambda_n \Phi_{j_n} \quad \text{and} \quad \mathbf{D^T}\Phi_{j_n} = \lambda_n \Phi_{i_n} \quad \text{for } n = 1, ..., N \tag{2.11}$$

From the result above, where ^{T} indicates the matrix transpose, it is found that Φ_i and Φ_j are the eigenvectors (β) of $\mathbf{DD^T}$ and $\mathbf{D^TD}$, respectively, with eigenvalues $\lambda_n^2 \;\; n = 1, ..., N$. Given that $\mathbf{D}$ is an $N \times M$ data matrix, from Eq. 2.11 it can be deduced that:

$$D = U\Sigma V^T \tag{2.12}$$

Eq. 2.12 is known as the Singular Value Decomposition (SVD) and is an approximation of Eq. 2.5 commonly used for POD analysis of fluid field data matrices and was the approach used in the present work. Here V^T is an $M \times M$ orthogonal matrix, U is an $N \times N$ orthogonal matrix and Σ is an $N \times M$ of zeros except along the diagonal, which consist of $r = \min(N, M)$ non-negative numbers σ_n arranged in decreasing order. These diagonal values in Σ are known

as the singular values ($SV's$) of $\mathbf{D}$ (and $\mathbf{D}^T$), corresponding to real positive eigenvalues in the form $\sigma_n = \sqrt{\lambda_n}$. The number of $SV's$ present within Σ define the rank of $\mathbf{D}$, i.e (since $r = \min(N, M)$ the number of images within a PIV test case define the rank of $\mathbf{D}$, which in the present work was $N = 1000$).

Using Eq. 2.12 a POD analysis of the present works flow field data was conducted. From this analysis the flows turbulent kinetic energy (eigenvalues) was extracted. Modal plots of the decreasing energy content contained with the mode were constructed to analyze energy distribution variations between the test cases. For each test case flow field plots of the mean flows, (mode-0 σ_0), coherent structures were created. Additional field plots of the higher modal structures were subsequently produced after analysis of the energy distribution results. The application of POD, more specifically SVD, was a powerful tool that allowed the time-averaged flow field, and corresponding coherent structures, of the present work to found. These results and the subsequent comparison of their test case dependent differences are presented in the ensuing sections below.

Chapter 3

Results and Discussion

3.1 Independent Flow Fields

PIV measurements of the individual flow domains were taken in order to establish a baseline from which to compare the combined domain cases. A POD snapshot method was employed to extract various modes from the fluctuating velocity components, enabling the identification of smaller scale coherent structures contained within the more complex flow fields.

The eigenvalues of the first 15 POD modes were plotted for both Vortex Breakdown (VB) and Taylor-Couette Flow (TCF) cases and are presented in Figures 3.2, 3.13 and 3.23. These plots represent the cumulative sum of energy (Figures (a)) and the fraction of modal energy with respect to total energy (Figures (b)), contained within the flows at various conditions. In most cases flow energies (≥ 0.5) were typically found to be contained within the mean flow (mode-0). However, as evidenced by the $\Gamma_{ew} = 0.5, R_{e_{ew}} = 2077$ condition, presented in Figure 3.2 (a), this was not always true. In fact energy levels where found to be highly variable in each case depending on the specific flow conditions employed during tests. Drastic changes in modal energy content were typically found to occur between modes $1-4$. Mode-3 specifically was found to be a general point of inflection for the combined test cases (discussed in section 3.2). For this reason mode-3, in addition to mode-1, was used to reconstruct the velocity fields.

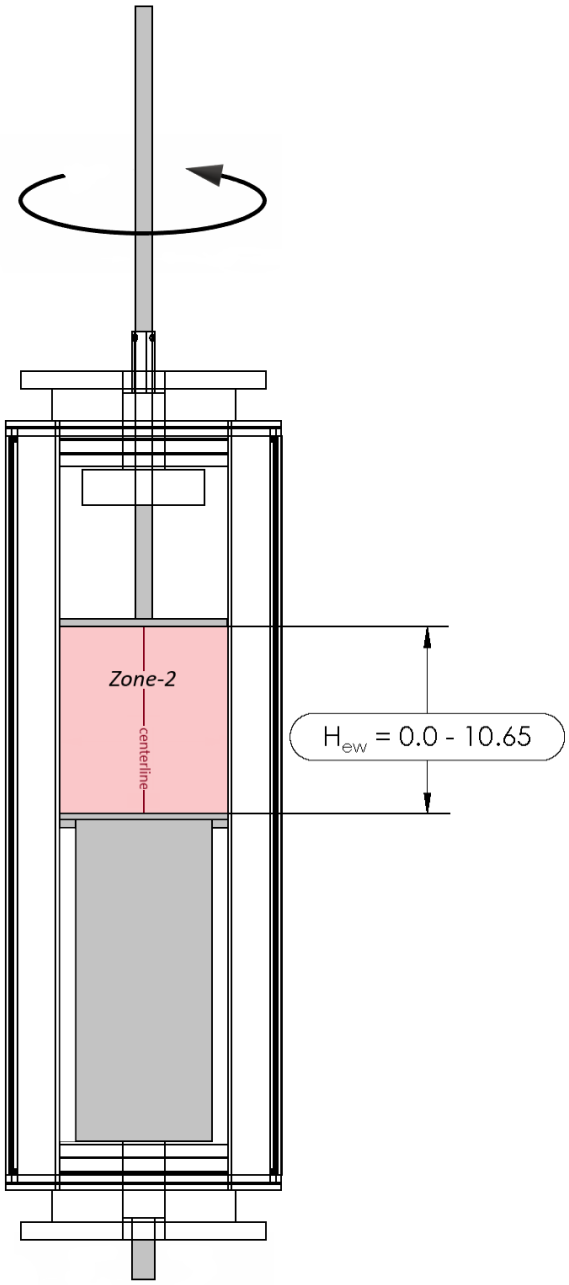

Figure 3.1: Configuration of VB - Zone-2 - rotationally independent upper end-wall test case

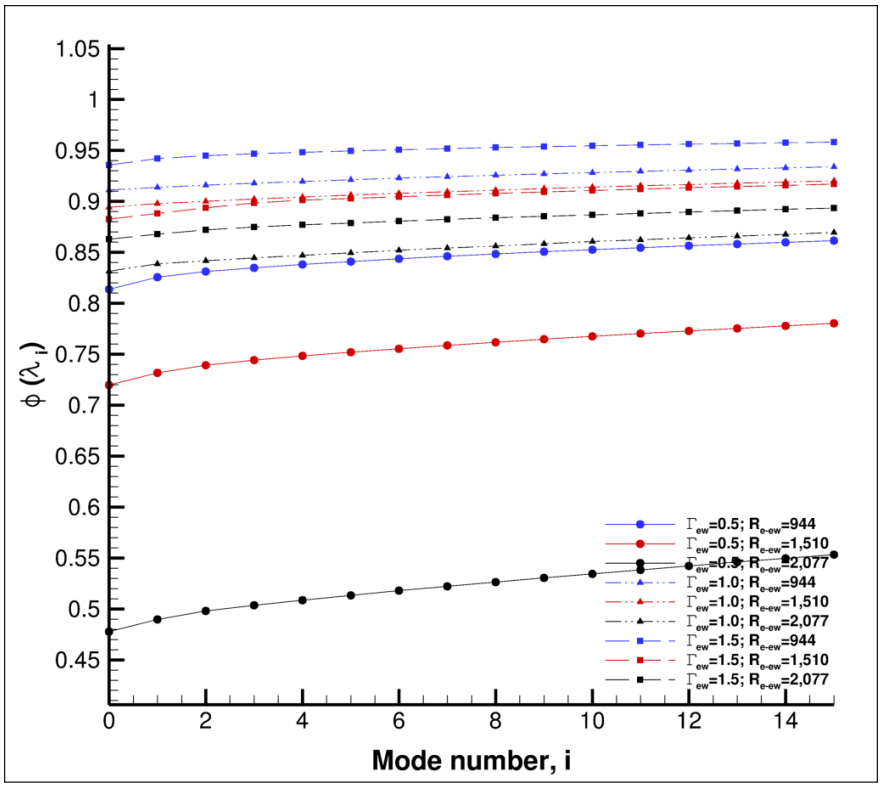

(a) cumulative distribution

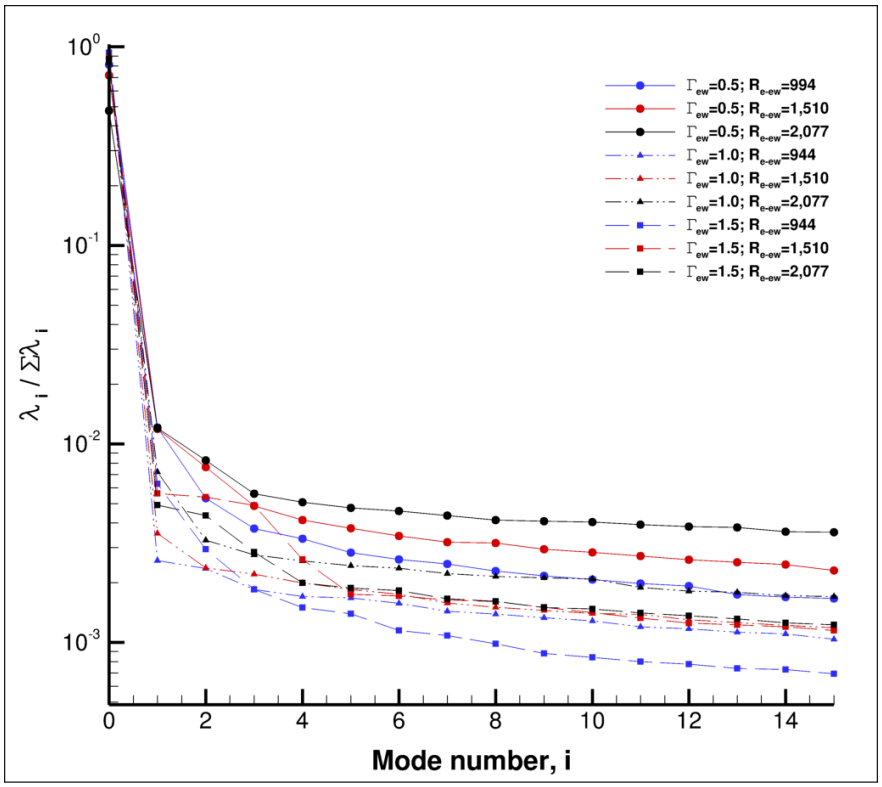

(b) POD spectrum, modes 0-15

Figure 3.2: Vortex breakdown - zone-2 - energy distribution

3.1.1 Vortex Breakdown - Zone-2 - Rotationally Independent Upper End-Wall

Streamlines and velocity contours for the Vortex Breakdown flow field are presented in Figures 3.3 - 3.11. Comparison of Figures 3.9, 3.8 and 3.3 reveals the effects of changes in aspect ratio on the mean flow. From the eight $\Gamma_{ew} = 1.5$ plots constituting Figure 3.3 flow structures typically indicative of a VBB seems to first appear at $R_{e_{ew}} = 1,133$. Indications of an earlier onset of the VBB were noted to occur at $R_{e_{ew}} = 944$, $z/\hat{d} \approx 6$ (Figure 3.3 (c) and (d)). Here streamlines in the vortex core are seen to exhibit an abrupt change in the radial direction coupled with reduced velocities in the same region. However, these changes did not result in the formation of a coherent recirculating VBB indicating that true onset lie some where between $R_{e_{ew}} = 944 - 1,133$. As $R_{e_{ew}}$ was increased from 944 to $1,888$ the breakdown bubble began to progressively migrate towards the lower stationary end-wall, increasing in width as it did so. Both of these effects were attributed, in part, to the central viscous core which also increased in diameter as $R_{e_{ew}}$ increased and distance from the rotating end-wall decreased. These results were found to be congruent with those of Escudier, Vogel and Gelfgat et al. [24] [58] [25].

Beyond $R_{e_{ew}} = 1,888$, initial results indicated that the VBB continued the aforementioned trends. This was a contradiction of Escudier's results, who found that for the case of $\Gamma_{ew} = 1.5$ a VBB typically begins to weaken and disappear around $R_{e_{ew}} = 2,000$. However, analysis of turbulent kinetic energy () and turbulent intensity (I_T) plots, as well as higher POD modes, revealed that while there were still areas of recirculating flow in the core region beyond $R_{e_{ew}} = 2,000$, the energy contained in those regions was far less than that at $944 \leq R_{e_{ew}} \leq 1,888$.

Notably large reductions in the core flows I_T and were found to occur around $R_{e_{ew}} = 2,076$, as seen in the plots of Figures 3.5. Here it is noted that for $\Gamma_{ew} = 1.5$ the largest area of I_T was generally located in the region of the vortex core. As $R_{e_{ew}}$ increased from $944 - 1,888$ flow intensity in the region around the VBB was also found to increase, ranging from approximately $0.15\% - 32\%$. Further increases in $R_{e_{ew}}$ beyond $1,888$ resulted in a

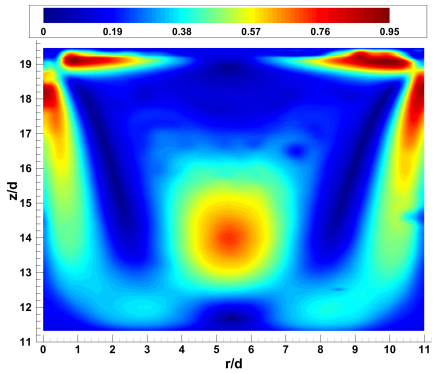

(a) $R_e = 755$

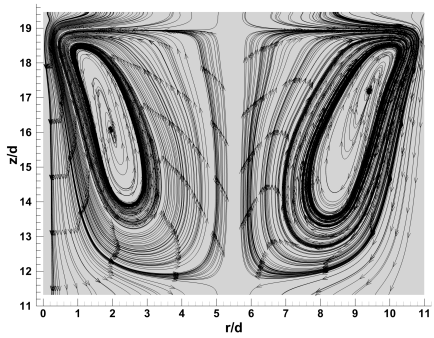

(b) $R_e = 755$

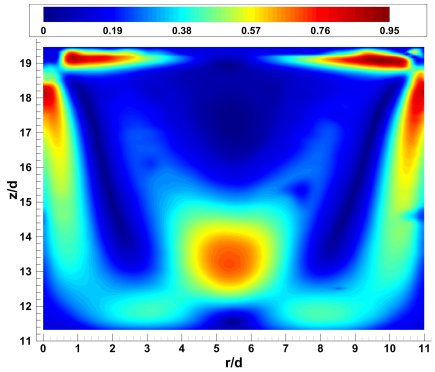

(c) $R_e = 944$

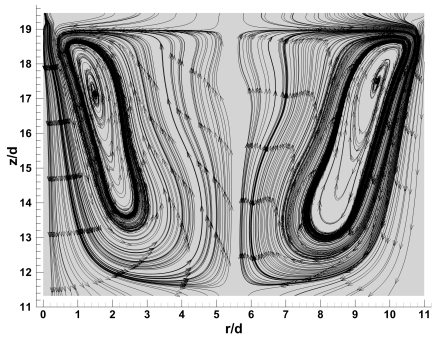

(d) $R_e = 944$

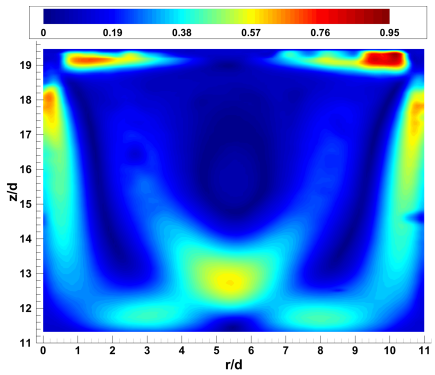

(e) $R_e = 1,133$

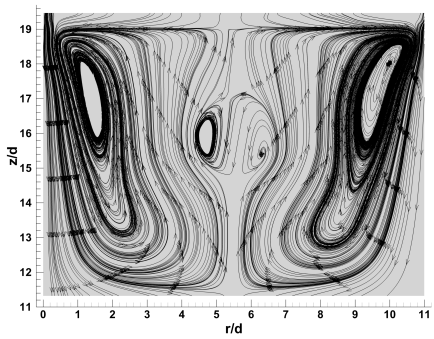

(f) $R_e = 1,133$

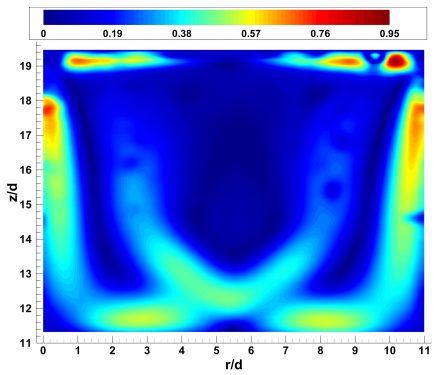

(g) $R_e = 1,510$

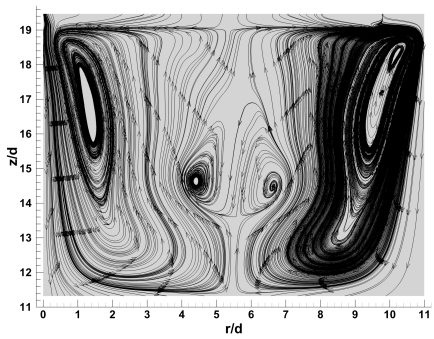

(h) $R_e = 1,510$

Figure 3.3: Vortex breakdown - zone-2 - mean flow (POD mode-0), velocity contours (left) and streamlines (right) at $\Gamma_{ew} = 1.5$

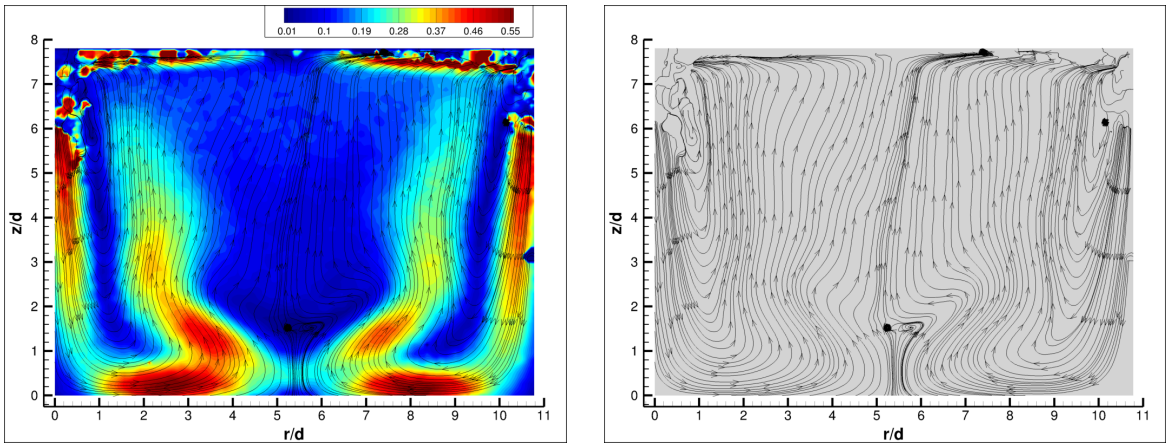

(a) Velocity Contour **(b)** Streamlines

Figure 3.4: Vortex breakdown - zone-2 - (POD mode-0) instantaneous frame for $\Gamma_{ew} = 1.5$ at $R_e = 2,265$, (a): velocity contour with streamlines, (b): streamlines

continuous reduction in I_T, implying that the VBB began to weaken at Reynolds numbers $R_{ew} > 1,888$.

Weakening of the VBB at higher Reynolds numbers was verified through analysis of the raw PIV images and streamline plots of the individual frames. From such analysis the last visible indication of onset of a VBB within the mean flow was noted to occur at $R_{e_{ew}} = 2,265$, as seen in Figure 3.4. While this is a slightly higher $R_{e_{ew}}$ number than that reported by Escudier and Vogel, these results confirm their general findings of the flows behavior at $\Gamma_{ew} = 1.5$ such that a VBB with recirculating regions existed on the vortex core from an approximate $R_{e_{ew}}$ range of $1,000 \ \ to \ \ 2,000$.

For the cases of $\Gamma_{ew} = 1$ and $\Gamma_{ew} = 0.5$ results were more congruent with the findings of other researchers, such that neither the former nor the latter resulted in the onset of a VBB in the mean flow. However, regions of recirculation within the core were found in a few of the streamline plots at modes 1 and 3. For the case of $\Gamma_{ew} = 0.5$ these recirculation zones were few but when present tended to be located very near the rotating end-wall and slightly off set from the axis of rotation, as seen in Figure 3.10 (b) at $z/\hat{d} \approx 2.25, \ \ r/\hat{d} \approx 6$. At $\Gamma_{ew} = 1$ recirculation's were found to be more indicative of a potential VBB and were

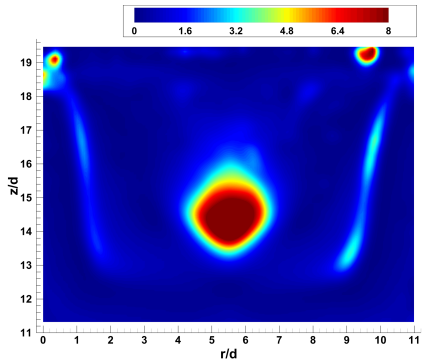

(a) $R_e = 1,510$

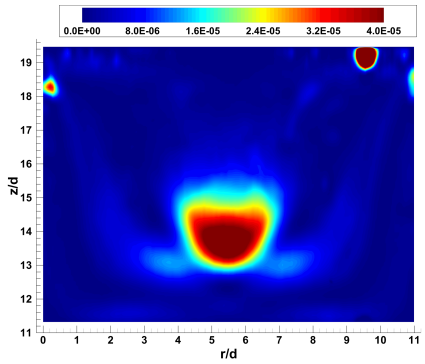

(b) $R_e = 1,510$

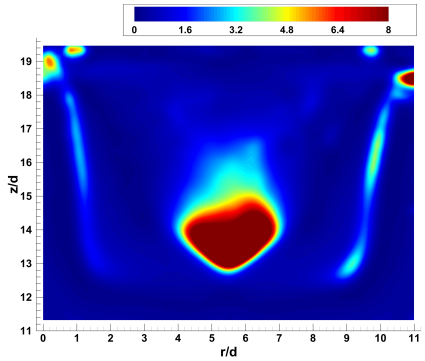

(c) $R_e = 1,888$

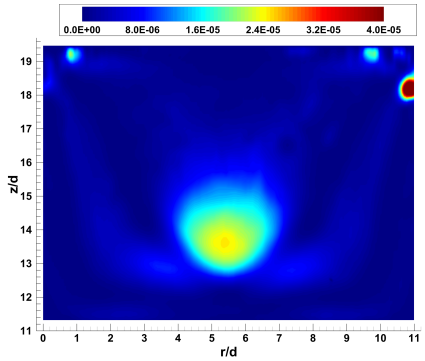

(d) $R_e = 1,888$

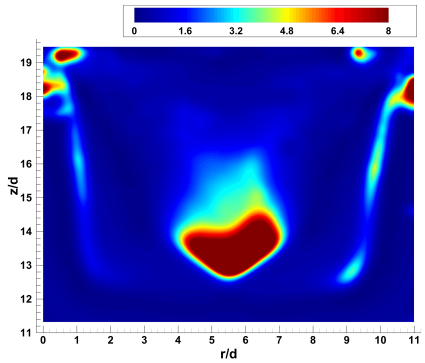

(e) $R_e = 2,076$

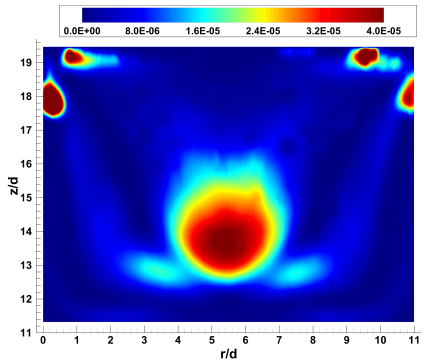

(f) $R_e = 2,076$

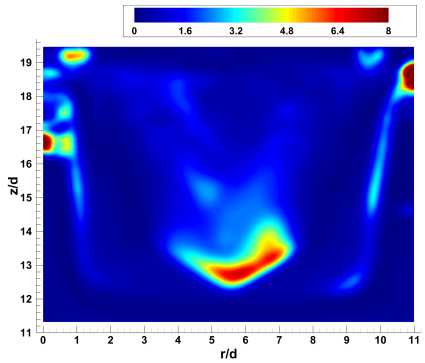

(g) $R_e = 2,643$

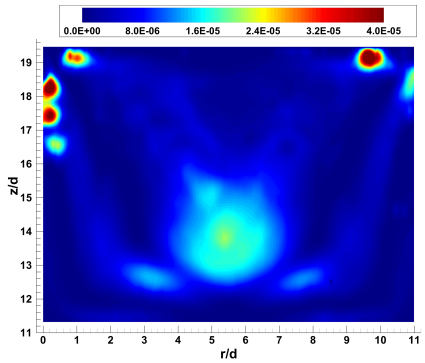

(h) $R_e = 2,643$

Figure 3.5: Vortex breakdown - zone-2 - mean flow (POD mode-0), turbulent intensity (I_T) (left) and turbulent kinetic energy (TKE) (right) at $\Gamma_{ew} = 1.5$

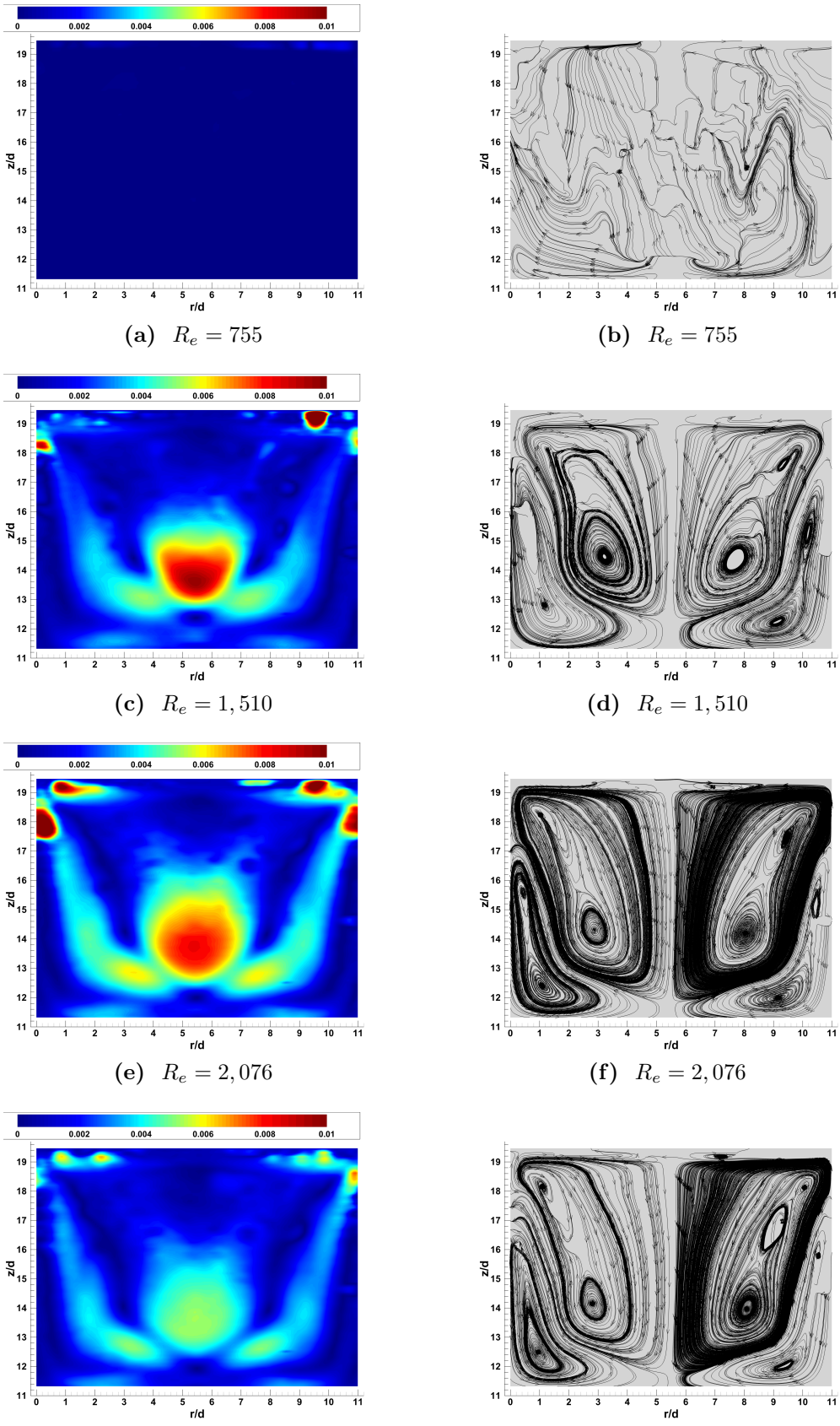

(a) $R_e = 755$ **(b)** $R_e = 755$

(c) $R_e = 1,510$ **(d)** $R_e = 1,510$

(e) $R_e = 2,076$ **(f)** $R_e = 2,076$

(g) $R_e = 2,454$ **(h)** $R_e = 2,454$

Figure 3.6: Vortex breakdown - zone-2 - POD mode-1, velocity contour (left) and streamlines (right) at $\Gamma_{ew} = 1.5$

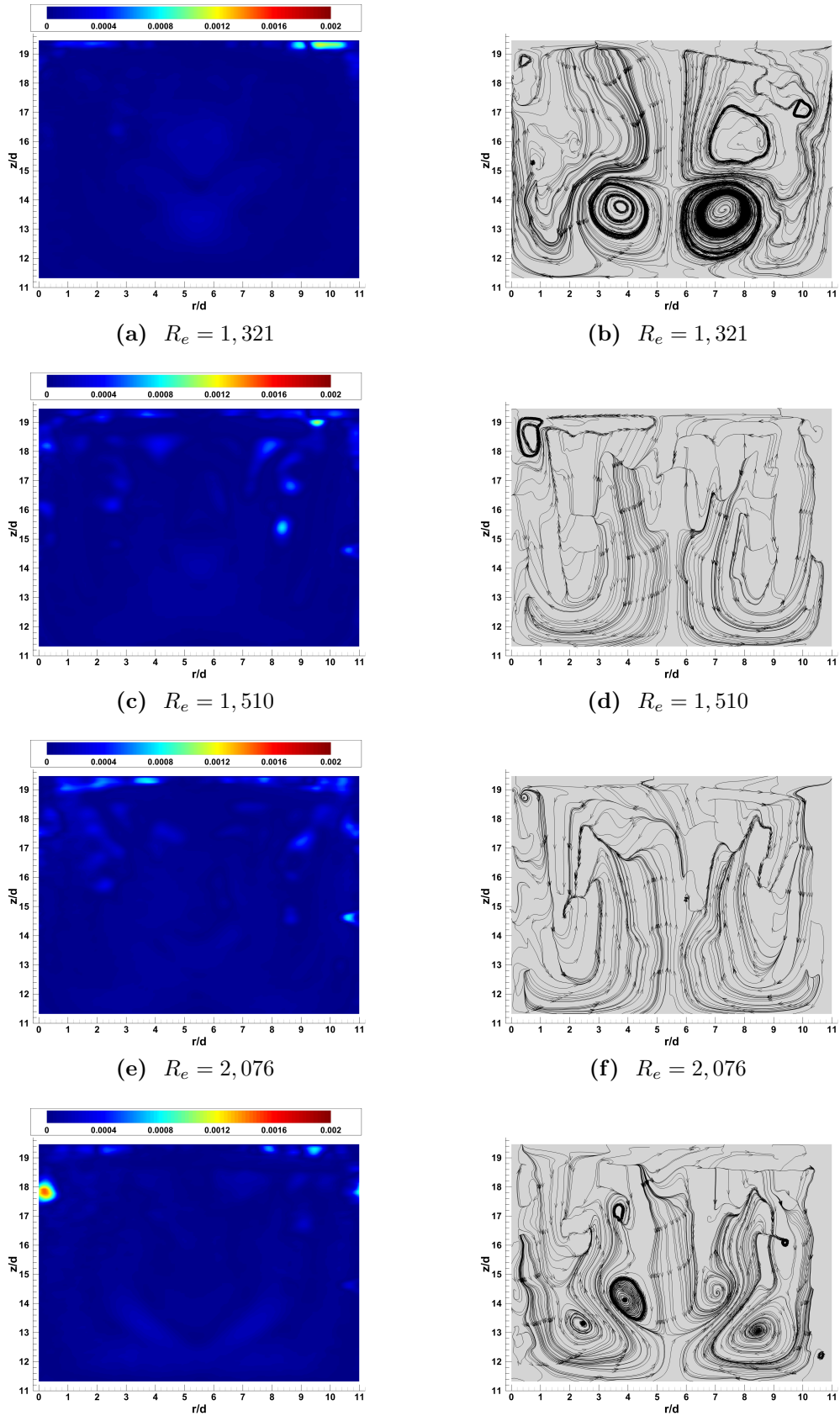

(a) $R_e = 1,321$ **(b)** $R_e = 1,321$

(c) $R_e = 1,510$ **(d)** $R_e = 1,510$

(e) $R_e = 2,076$ **(f)** $R_e = 2,076$

(g) $R_e = 2,454$ **(h)** $R_e = 2,454$

Figure 3.7: Vortex breakdown - zone-2 - POD mode-3, velocity contours (left) and streamlines (right) at $\Gamma_{ew} = 1.5$

seen to occur in the actual core regions of both mode-1 and mode-3 results, (Figures 3.10 (e-h) and 3.11 (e-h)).

From Figures 3.6 - 3.7 and 3.10 - 3.11 two large counter rotating vortices can be seen flanking either side of the rotational axis for $\Gamma_{ew} = 1$ & 1.5. At $\Gamma_{ew} = 1.5$ these vortices occurred directly on either side of the VBB, indicated by the area of increased velocity in the left hand plots of Figure 3.6. $\Gamma_{ew} = 1$ results however showed no significant signs of increases in the core regions for either mode 1 or 3. Additionally, vortices near the $\Gamma_{ew} = 1$ core were noted to have an axially compressed form, compared to those at $\Gamma_{ew} = 1.5$, with a large wedge shaped gap seen to occur between them. The formation and generally circular form of these higher modal vortices seemed to be paramount in the creation of a VBB but became attenuated by either decreases in Γ_{ew} or large increases in $R_{e_{ew}}$. Mode-3 streamlines presented in Figures 3.7 (h) and 3.11 (h) also show small wavy vortex structures along the side walls, indicating the potential onset of oscillatory fluctuation along the axis of rotation. These side wall structures were first noted to occur at Reynolds numbers slightly beyond the point at which the VBB disappeared from the $\Gamma_{ew} = 1.5$ mean flow, at $R_{e_{ew}} = 2,265$. These results seem to suggest that the appearance of axial flow oscillations in the higher modes at $R_{e_{ew}}$ numbers beyond $2,076$ acted to destabilize VBB onset.

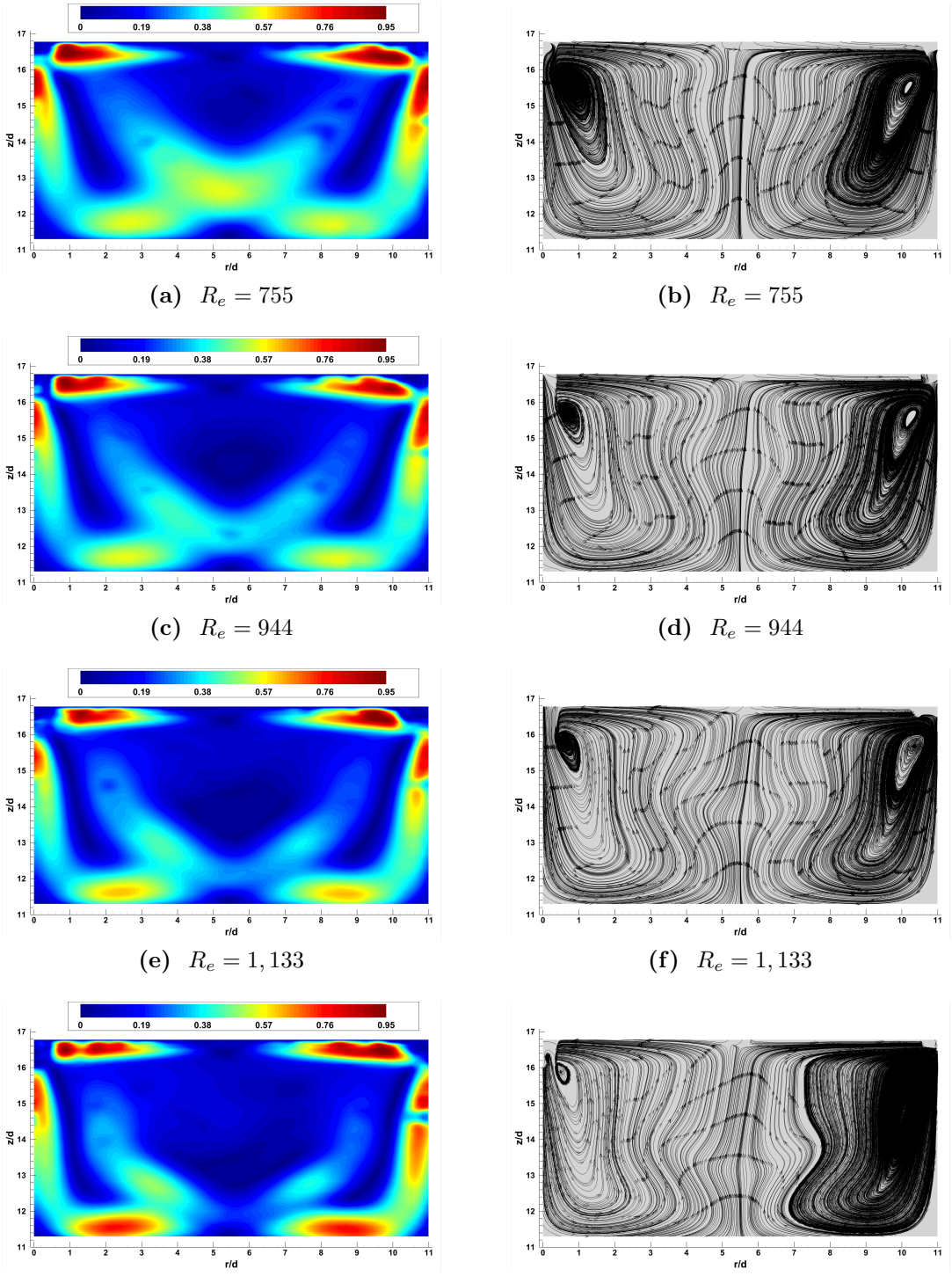

(a) $R_e = 755$ **(b)** $R_e = 755$

(c) $R_e = 944$ **(d)** $R_e = 944$

(e) $R_e = 1,133$ **(f)** $R_e = 1,133$

(g) $R_e = 1,510$ **(h)** $R_e = 1,510$

Figure 3.8: Vortex breakdown - zone-2 - mean flow (POD mode-0), velocity contours (left) and streamlines (right) at $\Gamma_{ew} = 1$

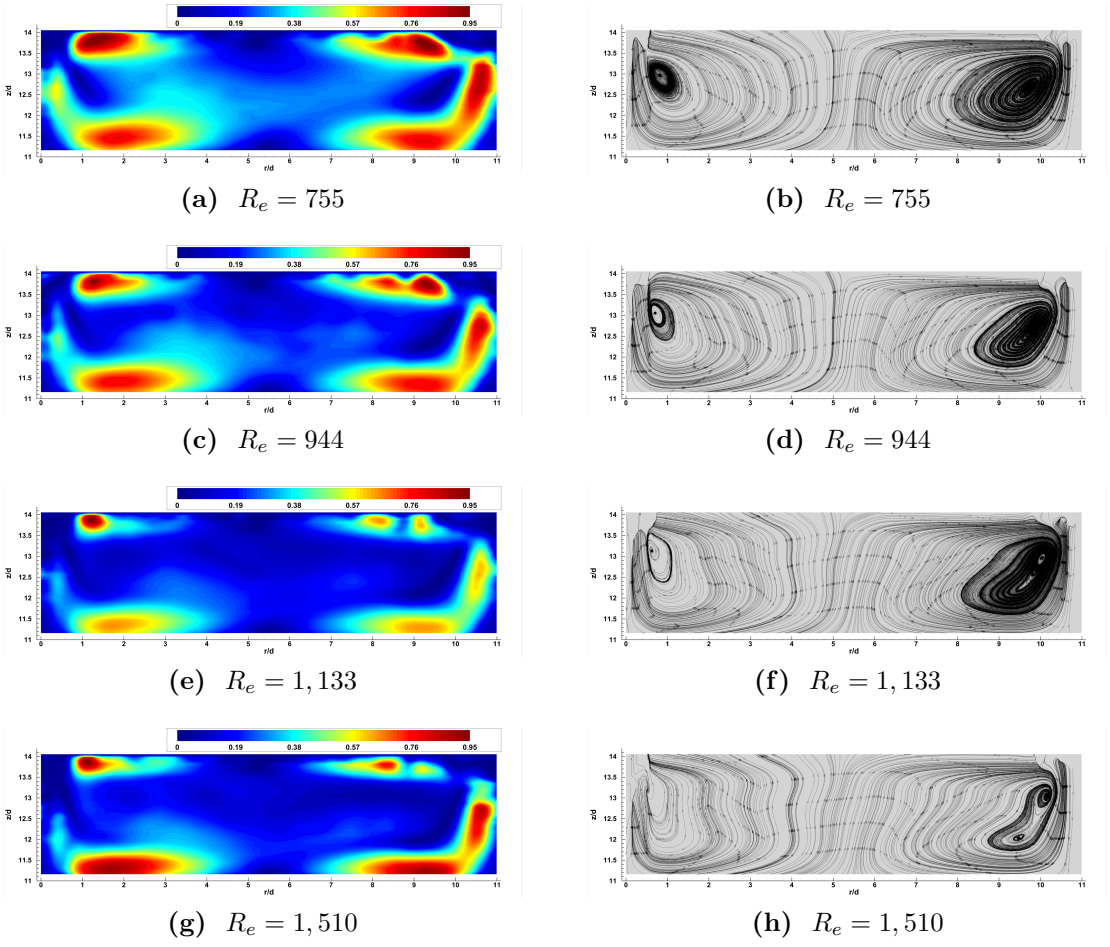

(a) $R_e = 755$ **(b)** $R_e = 755$

(c) $R_e = 944$ **(d)** $R_e = 944$

(e) $R_e = 1,133$ **(f)** $R_e = 1,133$

(g) $R_e = 1,510$ **(h)** $R_e = 1,510$

Figure 3.9: Vortex breakdown - zone-2 - baseline mean flow (POD mode-0), velocity contours (left) and streamlines (right); at $\Gamma_{ew} = 0.5$

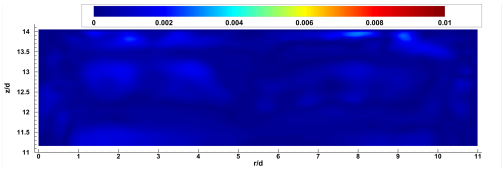

(a) $R_e = 1,510$

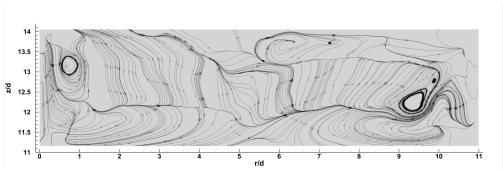

(b) $R_e = 1,510$

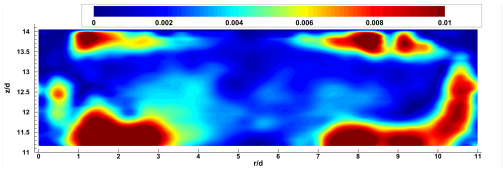

(c) $R_e = 2,454$

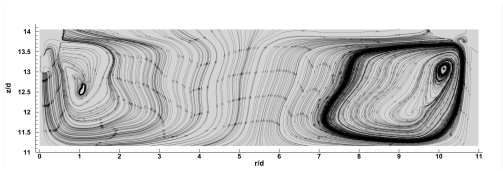

(d) $R_e = 2,454$

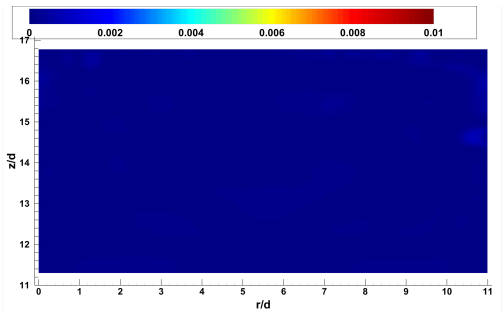

(e) $R_e = 1,510$

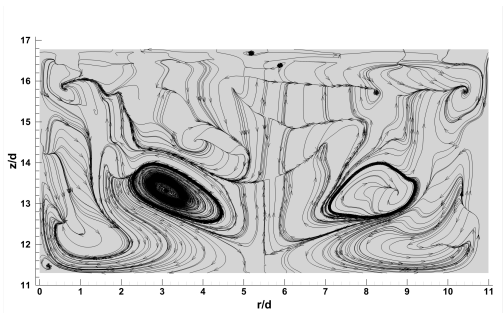

(f) $R_e = 1,510$

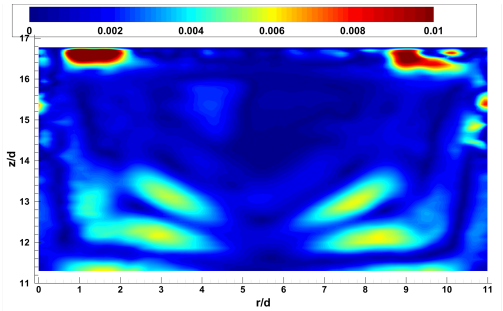

(g) $R_e = 2,454$

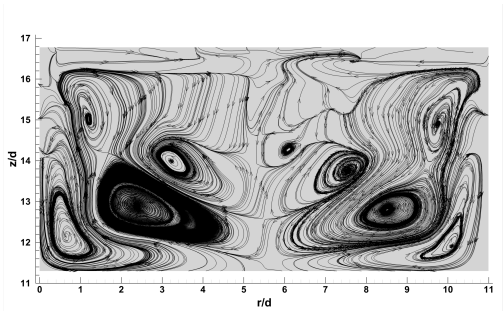

(h) $R_e = 2,454$

Figure 3.10: Vortex breakdown - zone-2 - POD mode-1, velocity contours (left) and Streamlines (right); at $\Gamma_{ew} = 0.5$

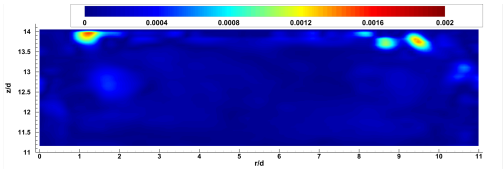

(a) $R_e = 1,510$

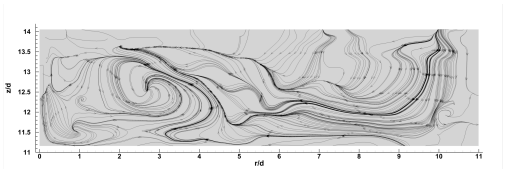

(b) $R_e = 1,510$

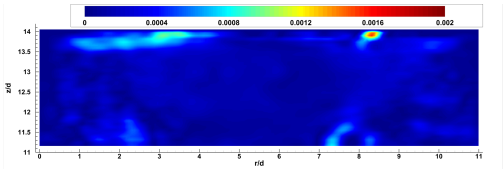

(c) $R_e = 2,454$

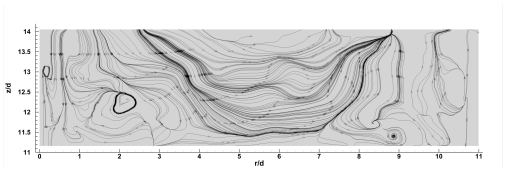

(d) $R_e = 2,454$

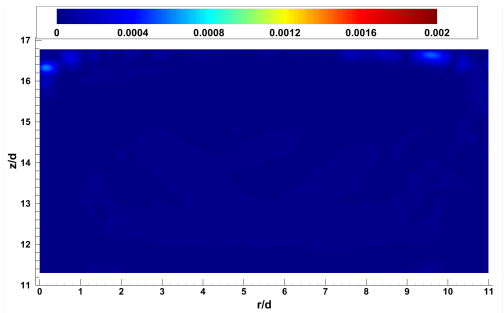

(e) $R_e = 1,510$

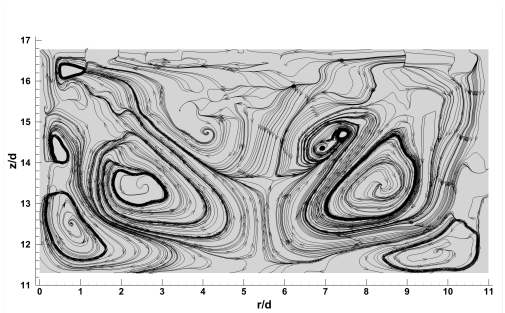

(f) $R_e = 1,510$

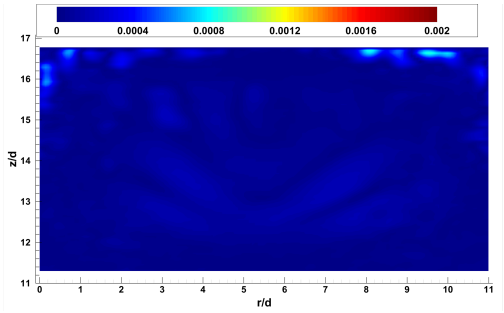

(g) $R_e = 2,454$

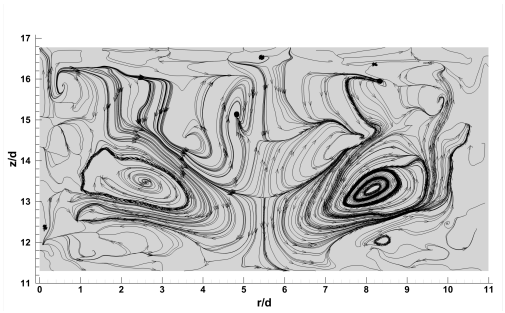

(h) $R_e = 2,454$

Figure 3.11: Vortex breakdown - zone-2 - POD mode-3, velocity contours (left) and Streamlines (right); at $\Gamma_{ew} = 0.5$

3.1.2 Non-Annular Taylor-Couette Flow - Zone-2 - Rotationally Independent Inner Cylinder

Energy plots for zone-2 at TCF conditions are presented in Figure 3.13. Modal energy levels show a rather high degree of variability as they did for the rotationally independent upper end-wall (VB) conditions. Similarly, $\Gamma_{ew} = 0.5$ is still shown to have the most consistently elevated levels of modal energy (Figure 3.13 (b)) however, for $\Gamma_{ew} = 1$ it displays the largest drop in mean-flow energies (Figure 3.13 (a)). $\Gamma_{ew} = 1$ also shows elevated modal energy levels between modes $1 - 4$ relative to those at $\Gamma_{ew} = 1.5$, a result which was found to be contrary to the VB results previously discussed. Some of these differences between the varying aspect ratios energy content were accounted for by the varying percentage of annulus inclusion within zone-2s' field of view and thus energy content results do not necessarily represent a true 1:1 comparison to VB conditions, most notably at the $\Gamma_{ew} = 0.5$ condition. Some of these changes however were the result of transfers in energy from the larger to smaller scale structures and was most likely caused by the reduced surface area of the rotating cylinder end wall and presence of the annular gap.

Plots of the zone-2 Taylor-Couette test cases are presented in Figures 3.14 - 3.20. Comparisons between the streamline and vorticity plots at $\Gamma = 0.5, 1, 1.5$ with those of the VB tests, reveals that flow patterns between like aspect ratios were relatively similar, with a few notable exceptions. In order to facilitate a more complete comparison between the two baselines a Reynolds number for the TCF cases was calculated using the same form as that used for the vortex breakdown Reynolds calculations where:

$$R_{e_{tcvb}} = \frac{\Omega_I R_I^2}{\nu} \tag{3.1}$$

Utilizing Eq. 3.1 a comparable Reynolds number range of $314 \; - \; 1,632$ was established for the Taylor-Couette test cases.

As with the vortex breakdown case flow conditions at the $\Gamma_{ew} = 0.5$ aspect ratio displayed no pockets of mean flow recirculation within region around the central core. One

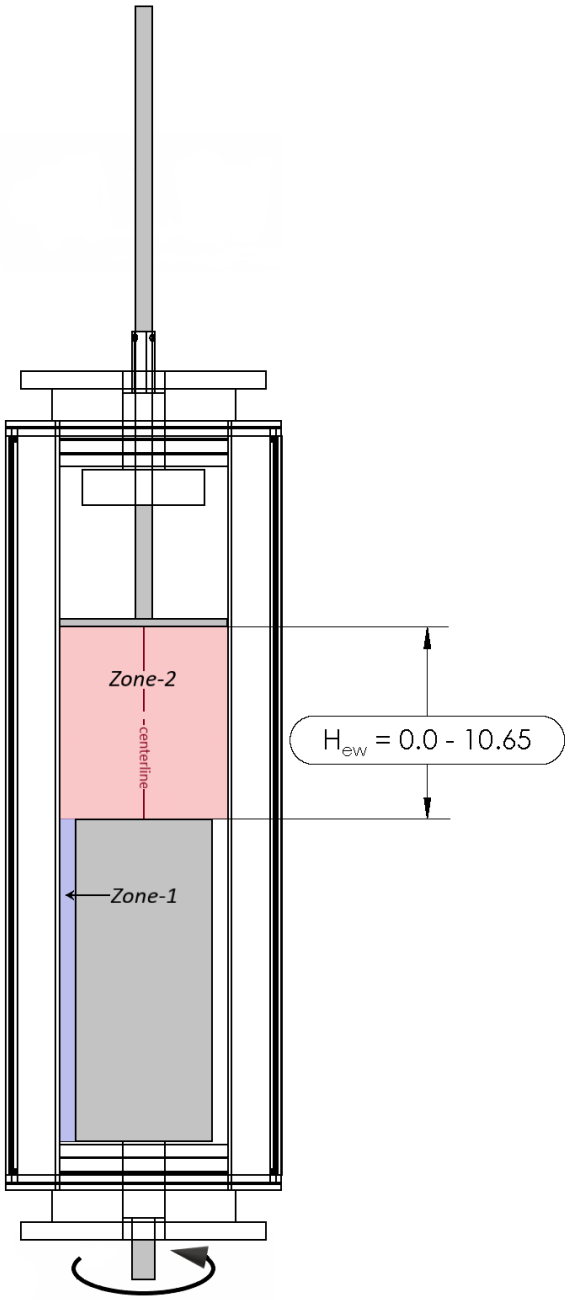

Figure 3.12: Configuration of TCF - rotationally independent inner cylinder test case

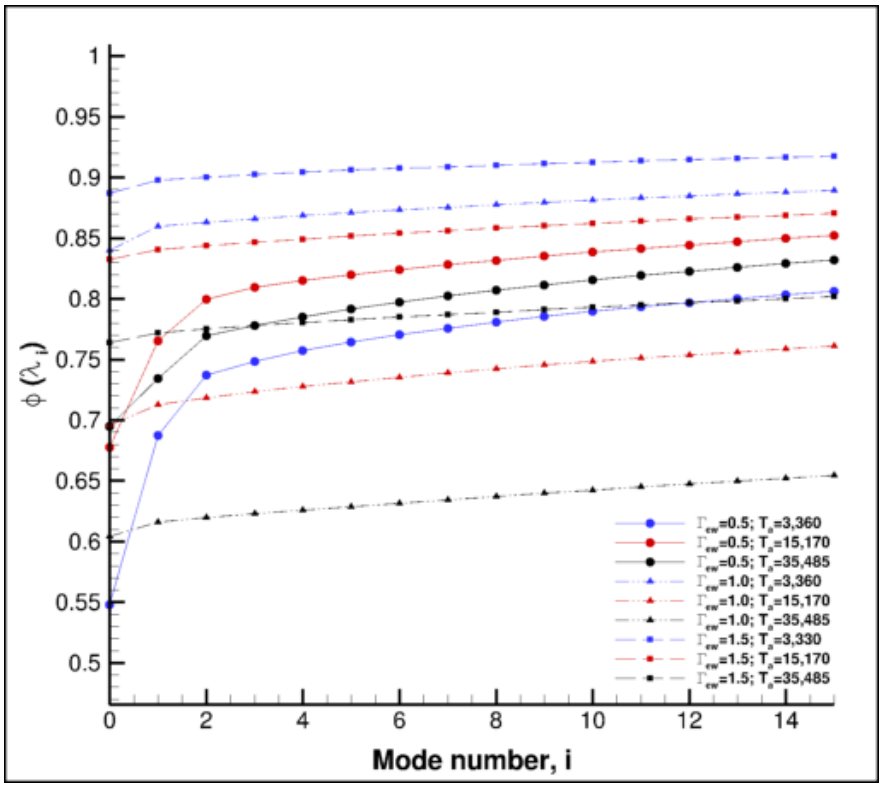

(a) cumulative distribution

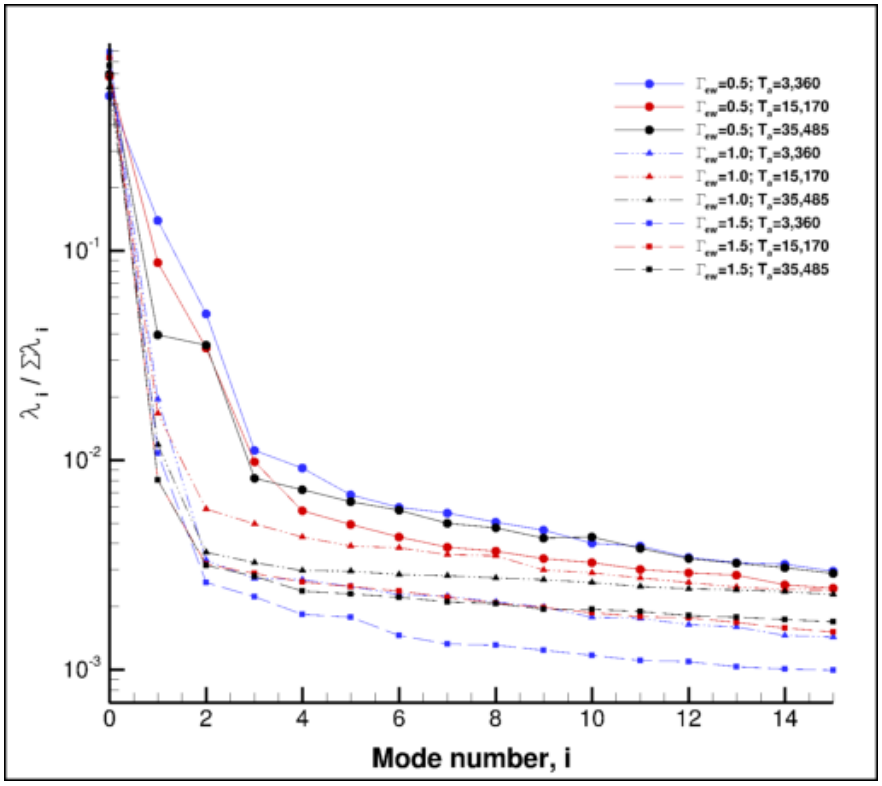

(b) POD spectrum, modes 0-15

Figure 3.13: TCF zone-2 energy distribution - rotationally independent inner cylinder

noticeable difference in the TCF case however was the appearance of a radial cross flow which was found to originate from the right side of the upper stationary end-wall and terminated at the bottom left corner of zone-2 as flow encountered the rotating cylinder. This cross flow was caused by a lack of symmetry in zone-2 vorticity. The right side of zone-2s primary vortex was found to have higher vorticity levels than that of the left and was also seen to have a vortical loci with a negative axial position relative to the left, as evident from the velocity and vorticity plots presented in Figure 3.14. The exact cause of this imbalance was not entirely clear, however the most likely explanation is that it resulted from the interaction between zone-2 vortices and the upper most Taylor vortex at the top of the annular gap. This was found to be the most probable cause due to the fact that this imbalance was not found to occur until after the point at which Taylor vortices first began to appear within the annulus around $T_a = 3,360$, $R_{e_{tcvb}} = 502$. Additionally this imbalance was also found to appear at $\Gamma_{ew} = 1$ and $\Gamma_{ew} = 1.5$ and was similarly first observed to occur at $T_a = 3,360$, $R_{e_{tcvb}} = 502$. The exact reason for why this imbalance resulted in a stronger left side vortex closer to the rotating surface at $\Gamma_{ew} = 0.5$ was unclear and while this relationship between left and right zone-2 vortices was found to be the dominant result within the whole of TCF test cases results at, $\Gamma_{ew} = 1.5$ were found to display a slight inversion of this trend where the zone-2 left side vortex was seen to have greater circulation. However, the relative positions of the vortical loci at $\Gamma_{ew} = 1.5$ were found to remained unchanged.

Modes 1 and 3 for zone-2 at $\Gamma_{ew} = 0.5$ were found to display relatively few identifiable structures. Flow patterns presented in Figures 3.15 and 3.16 are found to be less distinguishable than those of VB results, most notably at the lower $T_a/R_{e_{tcvb}}$ values. The flow structures that are present in zone-2 show almost no significant difference from that of the mean flow results, consisting predominantly of the primary side wall vortices, produced by the flows centerline circulation, and a core region with a significant amount of radial cross flow. Additionally there were no indications of the centerline vortices which were noted to occur near the rotating surface in mode-1 results at the VB condition. In fact all vortical loci

were found to lie slightly further out from the centerline than those seen in the higher modes of the $\Gamma_{ew} = 0.5$ VB cases, indicating that the likelihood of a recirculating VBB appearing along the axial centerline at these conditions is even less than that of the VB conditions.

For the $\Gamma_{ew} = 1.5$ test case the velocity contours presented in Figure 3.17, show patterns similar to those seen in th VB results for the same aspect ratio. Increases in T_a / $R_{e_{tcvb}}$ were similarly found to result in a widening of the central core and a progressive movement of the stagnation point towards the stationary end-wall. However, as previously stated this core flow was axially skewed, moving from the upper right to bottom left in a manner that was not seen to occur in the $\Gamma_{ew} = 1.5$ vortex breakdown cases. At $R_{e_{tcvb}} = 1,067$ recirculating flow structures were noted to appear within zone-2 along the rotational axis as shown in Figure 3.17 (g-i). This appearance of core recirculation at $R_{e_{tcvb}} = 1,067$ was found to be comparable with the $R_{e_{ew}} = 1,133$ condition at which the VBB first appeared in the mean flow results of the VB tests. This indicated that a VBB like structure dose begin to form in a Taylor-Couette cell in the presence of and an axial end wall / cylinder gap at conditions similar to those described by Escudier and Vogel for end wall driven cylindrical flow. However, the recirculating core formation in the present case cannot necessarily be described as a true breakdown bubble due to the skewed nature of the core region, which resulted in a highly asymmetric structure.This skew and the imbalance in vorticity resulted in what appeared to be a single recirculating region at the center of zone-2, (Figure 3.17 (f)). Further investigation of POD modes 1 - 3 reveled that there were in-fact two counter rotating regions in the core which formed along the rotational axis.

POD plots for the $\Gamma_{ew} = 1.5$ TCF conditions at modes 1 and 3 are presented in Figures 3.18 and 3.19 respectively. As with the $\Gamma_{ew} = 0.5$ results, streamlines display a relatively incoherent flow with few distinguishable structures when compared to $\Gamma_{ew} = 0.5$ VB results. There are also no indications of the large counter rotating vortices that were found in mode-1 results at the VB conditions. However, what looks to be a distorted VBB can be seen in the streamlines of Figures 3.18 (f) and (i). This recirculating region appears to show the right

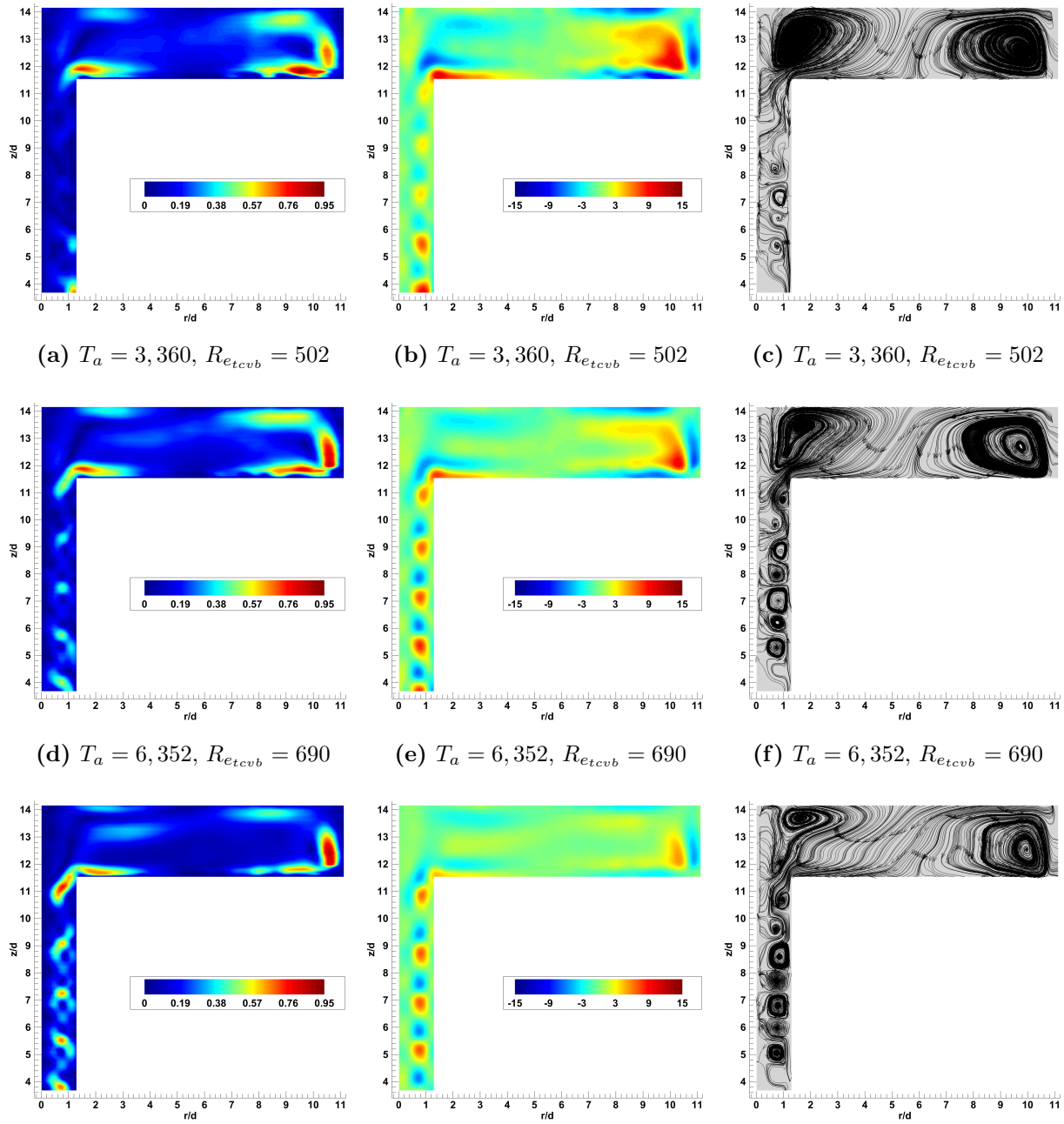

(a) $T_a = 3,360$, $R_{e_{tcvb}} = 502$ **(b)** $T_a = 3,360$, $R_{e_{tcvb}} = 502$ **(c)** $T_a = 3,360$, $R_{e_{tcvb}} = 502$

(d) $T_a = 6,352$, $R_{e_{tcvb}} = 690$ **(e)** $T_a = 6,352$, $R_{e_{tcvb}} = 690$ **(f)** $T_a = 6,352$, $R_{e_{tcvb}} = 690$

(g) $T_a = 15,170$, $R_{e_{tcvb}} = 1,067$ **(h)** $T_a = 15,170$, $R_{e_{tcvb}} = 1,067$ **(i)** $T_a = 15,170$, $R_{e_{tcvb}} = 1,067$

Figure 3.14: Taylor-Couette - zone-2 - mean flow (POD mode-0), velocity contours (left), non-dimensionalized vorticity $[\frac{\omega \hat{\mathbf{d}}}{2\Omega_I R_I}]$ (middle), streamlines (right) at $\Gamma_{ew} = 0.5$

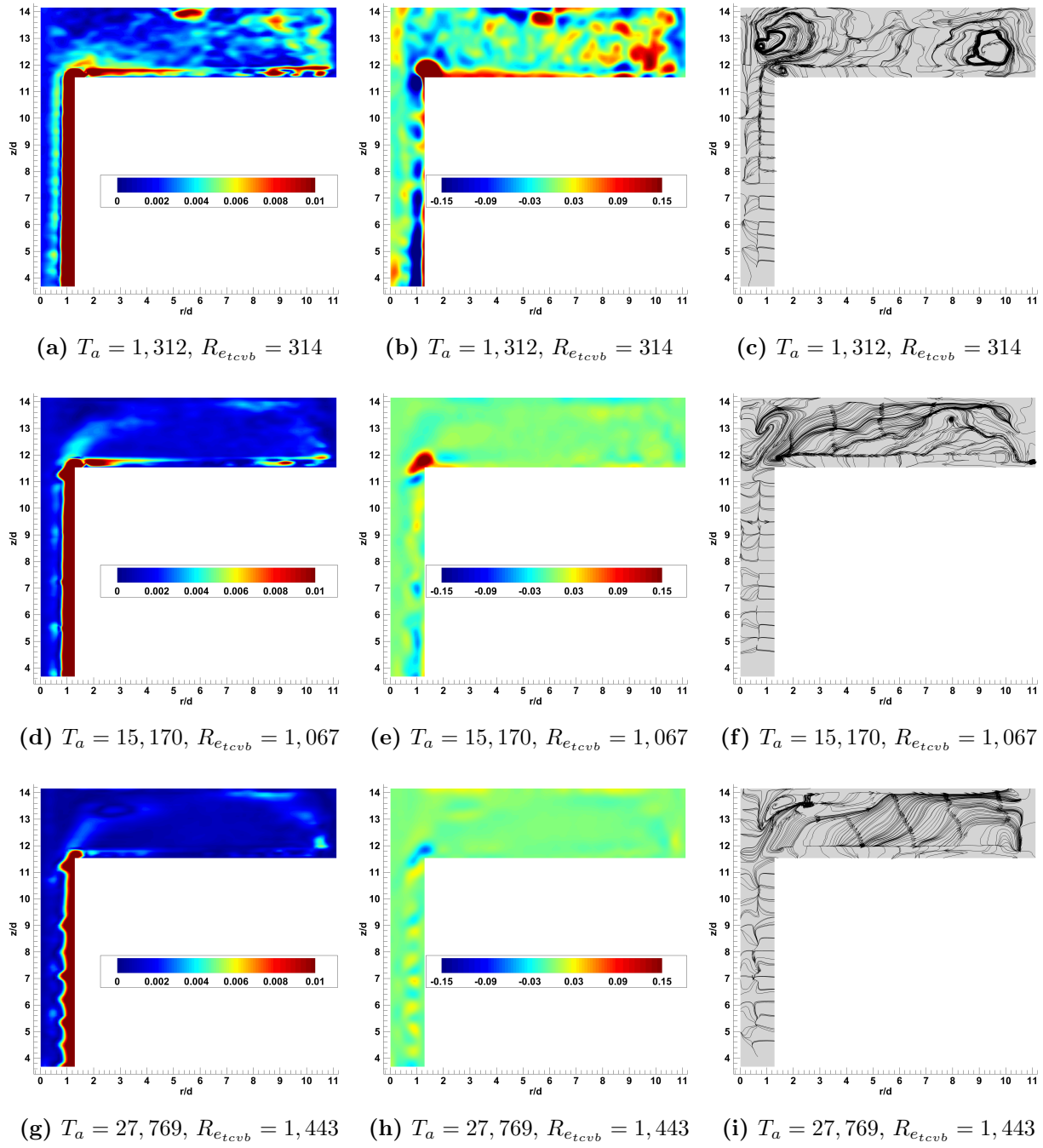

(a) $T_a = 1,312,\ R_{e_{tcvb}} = 314$ **(b)** $T_a = 1,312,\ R_{e_{tcvb}} = 314$ **(c)** $T_a = 1,312,\ R_{e_{tcvb}} = 314$

(d) $T_a = 15,170,\ R_{e_{tcvb}} = 1,067$ **(e)** $T_a = 15,170,\ R_{e_{tcvb}} = 1,067$ **(f)** $T_a = 15,170,\ R_{e_{tcvb}} = 1,067$

(g) $T_a = 27,769,\ R_{e_{tcvb}} = 1,443$ **(h)** $T_a = 27,769,\ R_{e_{tcvb}} = 1,443$ **(i)** $T_a = 27,769,\ R_{e_{tcvb}} = 1,443$

Figure 3.15: Taylor-Couette - zone-2 - POD mode-1, velocity contours (left), non-dimensionalized vorticity $[\frac{\omega \hat{\mathrm{d}}}{2\Omega_I R_I}]$ (middle), streamlines (right) at $\Gamma_{ew} = 0.5$

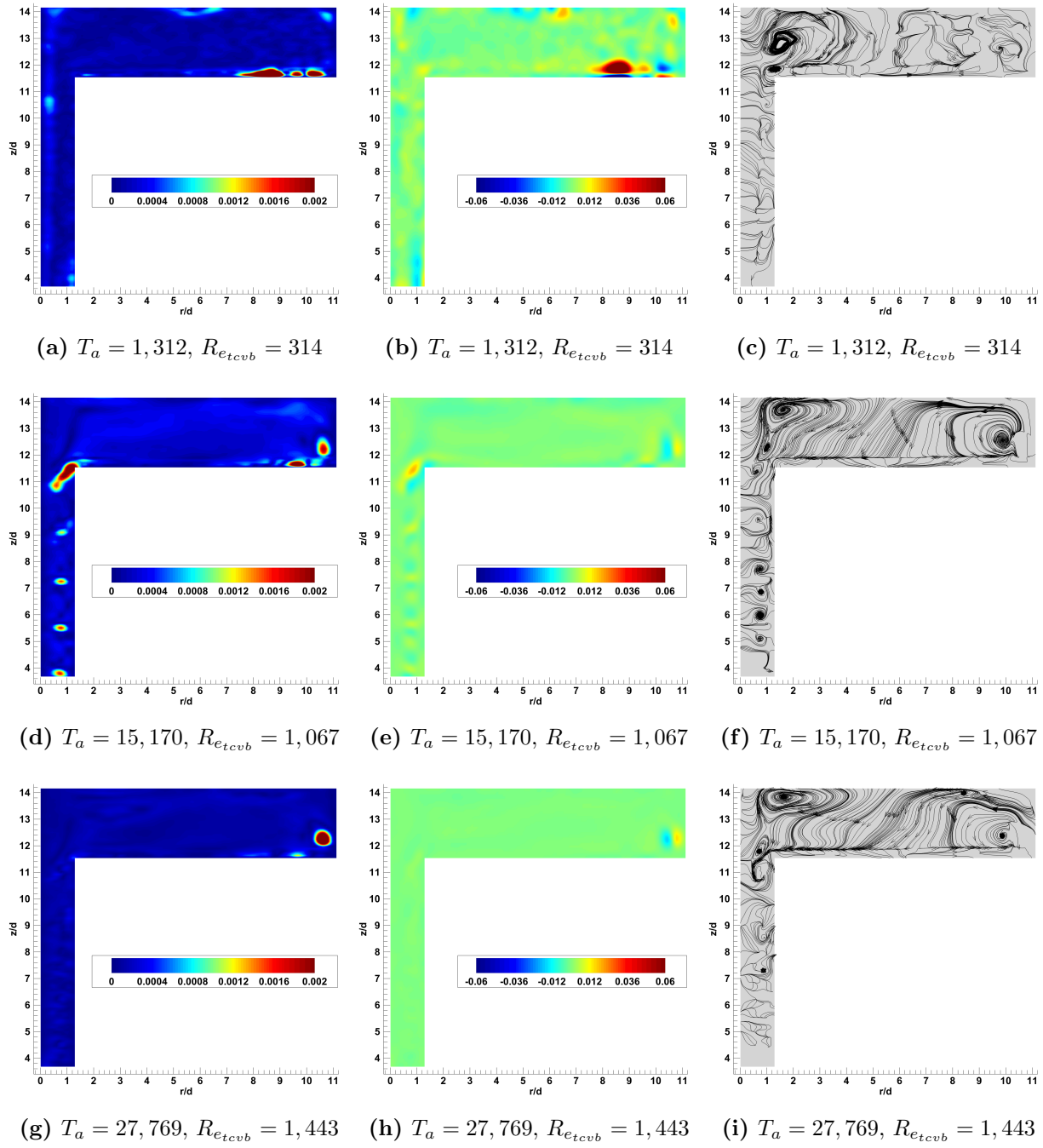

(a) $T_a = 1,312,\ R_{e_{tcvb}} = 314$ **(b)** $T_a = 1,312,\ R_{e_{tcvb}} = 314$ **(c)** $T_a = 1,312,\ R_{e_{tcvb}} = 314$

(d) $T_a = 15,170,\ R_{e_{tcvb}} = 1,067$ **(e)** $T_a = 15,170,\ R_{e_{tcvb}} = 1,067$ **(f)** $T_a = 15,170,\ R_{e_{tcvb}} = 1,067$

(g) $T_a = 27,769,\ R_{e_{tcvb}} = 1,443$ **(h)** $T_a = 27,769,\ R_{e_{tcvb}} = 1,443$ **(i)** $T_a = 27,769,\ R_{e_{tcvb}} = 1,443$

Figure 3.16: Taylor-Couette - zone-2 - POD mode-3, velocity contours (left) non-dimensionalized vorticity $[\frac{\omega \hat{\mathrm{d}}}{2\Omega_I R_I}]$ (middle), streamlines (right) at $\Gamma_{ew} = 0.5$

side of a VBB like structure that is compressed into a crescent shape by a more dominant axial vortex on the left side. Distortion of the axial vortex on the right side is likely due to the radial cross flow and asymmetric vortical nature, which was found to be inherent, of zone-2 at TCF conditions. Velocity and vorticity contours at mode-1 also support these findings of a VBB like structure forming in the Couette cells zone-2 at $\Gamma_{ew} = 1.5$ where, from Figures 3.18 (a), (d), and (g) specifically, a contained region of increased velocity, similar to that seen in VB mode-1 results, can be seen to occur along the axis. Interestingly, this region of increased velocity was found to display the greatest magnitudes at lower $T_a/R_{e_{tcvb}}$ values and was noted to first occur at $R_{e_{tcvb}} = 314$ a Reynolds number that is noted to be well below the critical $R_{e_{ew}}$, which resulted in a similar velocity region, found in the $\Gamma_{ew} = 1.5$ VB tests. The increased velocity and vorticity at $R_{e_{tcvb}} = 314$ is also seen in mode-3 results presented in Figures 3.19 (a) and (b). However, the aforementioned plots were found to be the only instance of such a result and in general, unlike that of the VB cases, mode-3 was found to provide very little insights into zone-2 flow behavior for TCF at $\Gamma_{ew} = 1.5$.

Mean flow results for the TCF test cases at $\Gamma_{ew} = 1$ are presented in the plots of Figure 3.20. From the streamlines of Figure 3.20 (i) a region of recirculating flow similar to that previously described for the $\Gamma_{ew} = 1.5$ TCF condition, can be seen to exist on the rotational axis of the zone-2 appearing as a single vortex along the axial centerline. Unlike the results at $\Gamma_{ew} = 1.5$ the more dominate circulatory region appeared on the right side of the system as opposed to the left. More importantly appearance of this region at $\Gamma_{ew} = 1$ was found to be a significant divergence from expectations due to the fact that unlike the VB results recirculating core structures were not limited to the higher modes. Additionally previous investigations from the likes of Escudier and Vogel give no indications of either a VBB or core recirculation's existing within the mean flow for aspect ratios $\Gamma_{ew} \approx 1.25$. However, investigations by Valentine and Jahnke (1994) as well as those conducted by Mullin et al. (1998) found that the creation of a recirculating zone, different from that of the type-B VBB, does occur within the vortex core at aspect ratios below $\Gamma_{ew} = 1.25$. Such results were found

to occur under conditions where either both end walls were made to rotate symmetrically, as in the case investigated by Valentine and Jahnke, or in the presence of a thin solid cylinder placed along the rotational axis as was studied by Mullin et al. [57], [40]. Taking such results into consideration it was inferred that a VBB like structure did in fact begin to form in the zone-2 at $\Gamma_{ew} = 1$ TCF conditions around a Reynolds numbers of $R_{e_{tcvb}} \approx 1,067$. It is also noted that, similar to the findings of Valentine and Jahnke, the recirculation found to occur in TCF test at $\Gamma_{ew} = 1.0$, as well as $\Gamma_{ew} = 1.5$, was of a different form than that of the VBB described to occur in the VB test cases.

While the results of Valentine and Jahnke, and Mullin et al. give confirmation of the possible existence of core recirculation's at aspect ratios below $\Gamma_{ew} \approx 1.25$ its existence in the present case can not be entirely accounted for by their works. The most likely explanation for the appearance of a "pseudo-vortex bubble breakdown" at the $\Gamma_{ew} = 1.0$ test condition is that it stemmed from either the radial slant of the vortex core or that it was the result of annular gaps presence within the flow field. These two effects either individually or in combination most likely acted to alter the flows effective aspect ratio within zone-2 thus allowing for the formation of a pseudo-vortex breakdown bubble in the central core.

Mode-1 results at $\Gamma_{ew} = 1.0$ shows the recirculating region exhibited the same structural pattern that was observed at $\Gamma_{ew} = 1.5$ with two recirculating regions present in the core and was fount to be best exemplified by the streamlines of Figure 3.21 (i). This formation was noted to be much more indicative of a VBB like structure than those found to occur in mode-1 results of the $\Gamma_{ew} = 1.0$ VB case. Streamline presented in Figures 3.21 (f) and (i) seem to confirm that annular gap presence did in-fact have an effect on the zone-2s effective aspect ratio and shows the flow directly above the annular gap to be predominantly in the axial direction. If this axial flow did in fact act as a kind of stationary side wall within the zone-2 it would have resulted in an effective aspect ratio of $\Gamma_{ew} \approx 1.23$ and thus helps to explain why core recirculation was seen to occur in mean flow results. As with $\Gamma_{ew} = 1.5$, mode-3 was found to be relatively insignificant energy for zone-2, displaying very little additional

formations with the noted exception of Figures 3.22 (a) and (b) which display increased velocity an vorticity levels, respectively, similar to what was found to occur in the core region at $\Gamma_{ew} = 1.5$; increased core velocity and vorticity levels were also seen to occur in $\Gamma_{ew} = 1.0$ mode-1 results.

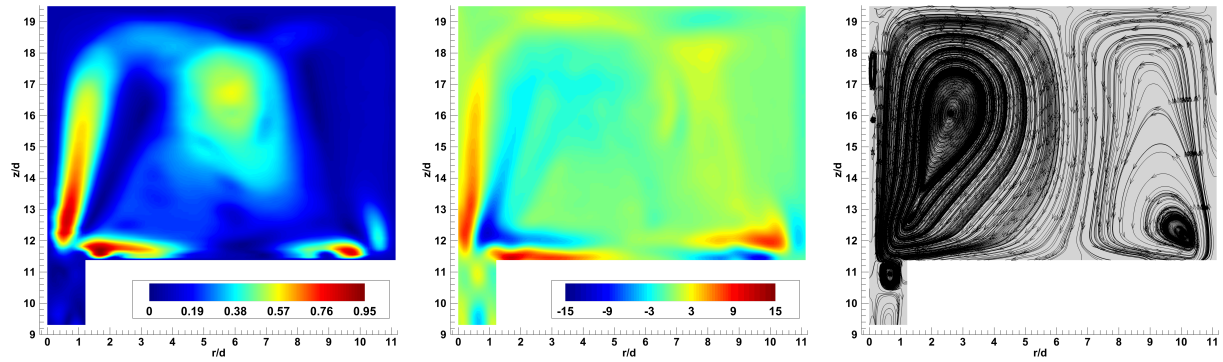

(a) $T_a = 3,360,\ R_{e_{tcvb}} = 502$ **(b)** $T_a = 3,360,\ R_{e_{tcvb}} = 502$ **(c)** $T_a = 3,360,\ R_{e_{tcvb}} = 502$

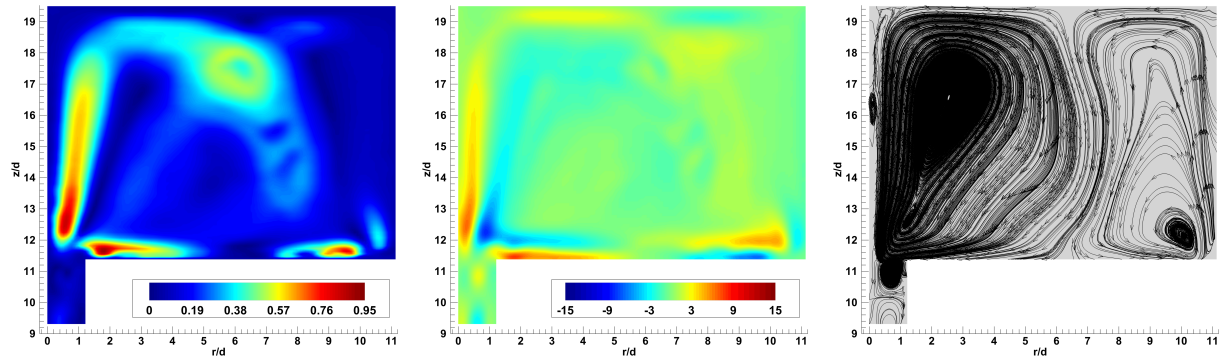

(d) $T_a = 6,352,\ R_{e_{tcvb}} = 690$ **(e)** $T_a = 6,352,\ R_{e_{tcvb}} = 690$ **(f)** $T_a = 6,352,\ R_{e_{tcvb}} = 690$

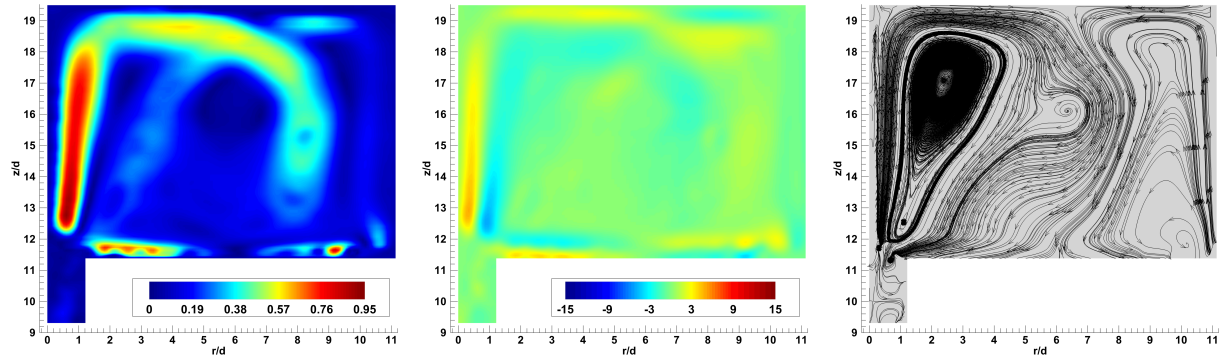

(g) $T_a = 15,170,\ R_{e_{tcvb}} = 1,067$ **(h)** $T_a = 15,170,\ R_{e_{tcvb}} = 1,067$ **(i)** $T_a = 15,170,\ R_{e_{tcvb}} = 1,067$

Figure 3.17: Taylor-Couette - zone-2 - mean flow (POD mode-0), velocity contours (left), non-dimensionalized vorticity $[\frac{\omega \hat{\mathbf{d}}}{2\Omega_I R_I}]$ (middle) Streamlines (right) at $\Gamma_{ew} = 1.5$

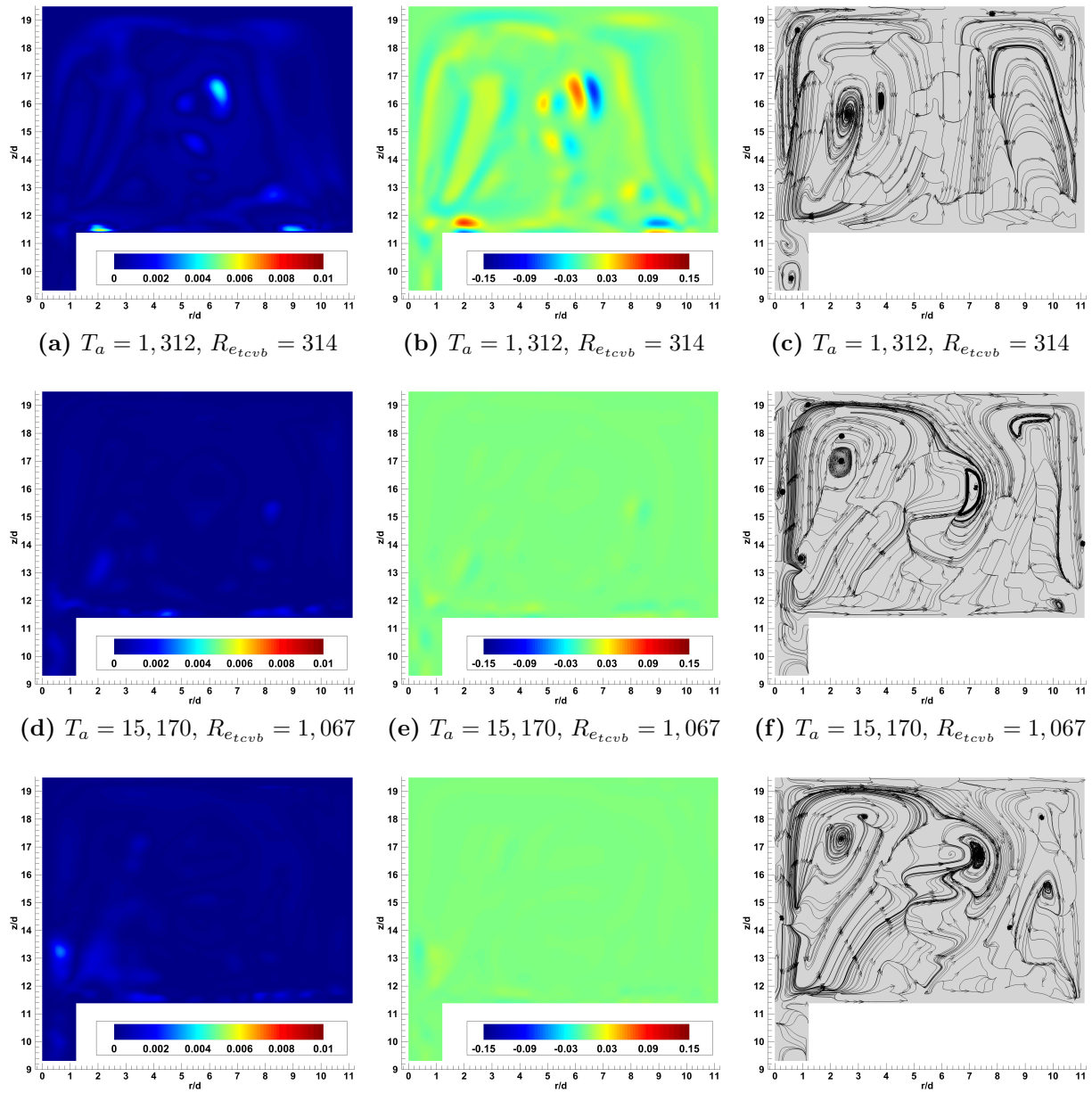

(a) $T_a = 1,312,\ R_{e_{tcvb}} = 314$ **(b)** $T_a = 1,312,\ R_{e_{tcvb}} = 314$ **(c)** $T_a = 1,312,\ R_{e_{tcvb}} = 314$

(d) $T_a = 15,170,\ R_{e_{tcvb}} = 1,067$ **(e)** $T_a = 15,170,\ R_{e_{tcvb}} = 1,067$ **(f)** $T_a = 15,170,\ R_{e_{tcvb}} = 1,067$

(g) $T_a = 27,769,\ R_{e_{tcvb}} = 1,443$ **(h)** $T_a = 27,769,\ R_{e_{tcvb}} = 1,443$ **(i)** $T_a = 27,769,\ R_{e_{tcvb}} = 1,443$

Figure 3.18: Taylor-Couette - zone-2 - POD mode-1, velocity contours (left), non-dimensionalized vorticity $[\frac{\omega \hat{\mathbf{d}}}{2\Omega_I R_I}]$ (middle), Streamlines (right) at $\Gamma_{ew} = 1.5$

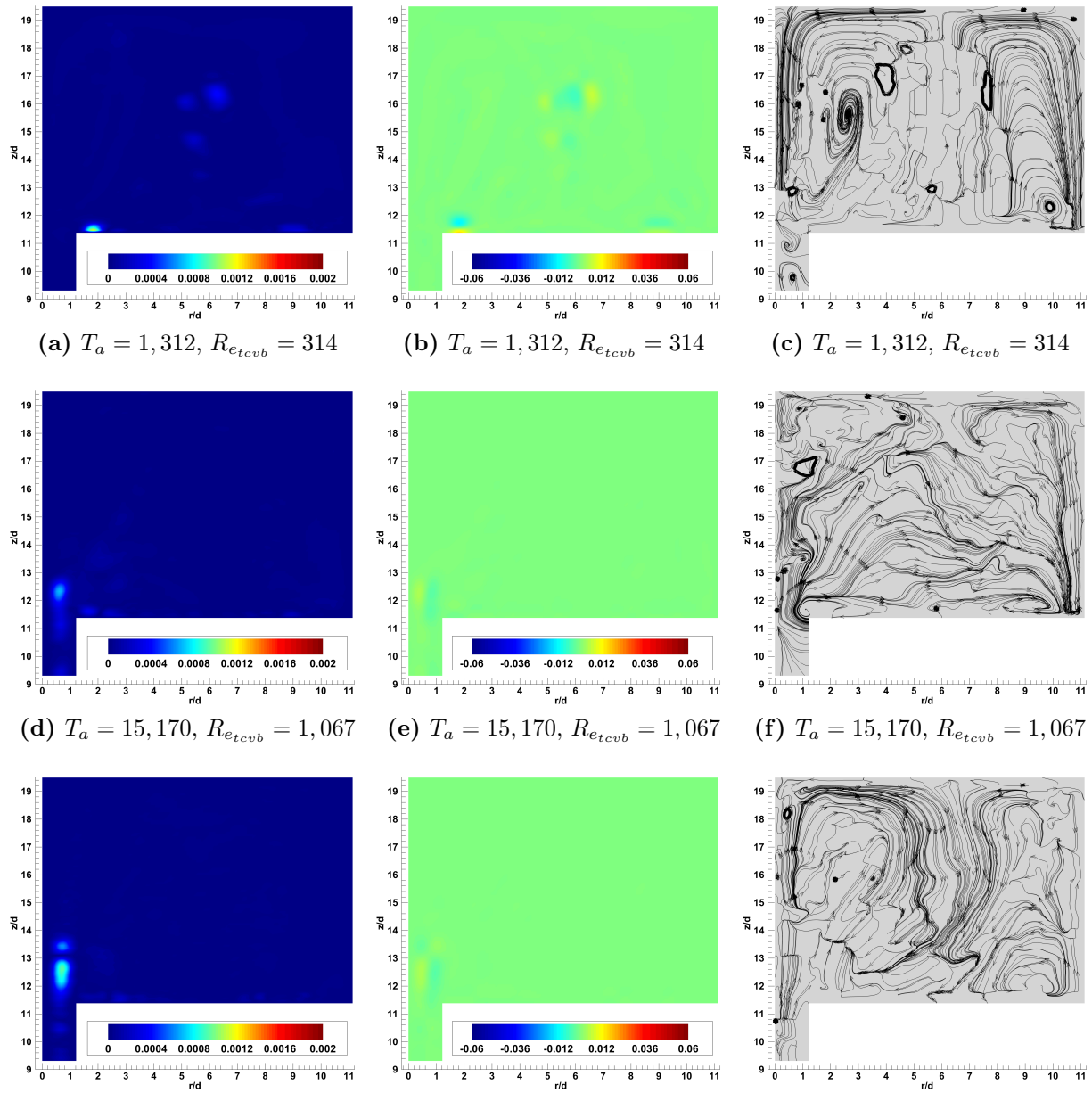

(a) $T_a = 1,312,\ R_{e_{tcvb}} = 314$ **(b)** $T_a = 1,312,\ R_{e_{tcvb}} = 314$ **(c)** $T_a = 1,312,\ R_{e_{tcvb}} = 314$

(d) $T_a = 15,170,\ R_{e_{tcvb}} = 1,067$ **(e)** $T_a = 15,170,\ R_{e_{tcvb}} = 1,067$ **(f)** $T_a = 15,170,\ R_{e_{tcvb}} = 1,067$

(g) $T_a = 27,769,\ R_{e_{tcvb}} = 1,443$ **(h)** $T_a = 27,769,\ R_{e_{tcvb}} = 1,443$ **(i)** $T_a = 27,769,\ R_{e_{tcvb}} = 1,443$

Figure 3.19: Taylor-Couette - zone-2 - POD mode-3, velocity contours (left), non-dimensionalized vorticity $[\frac{\omega \hat{\mathbf{d}}}{2\Omega_I R_I}]$ (middle), Streamlines (right) at $\Gamma_{ew} = 1.5$

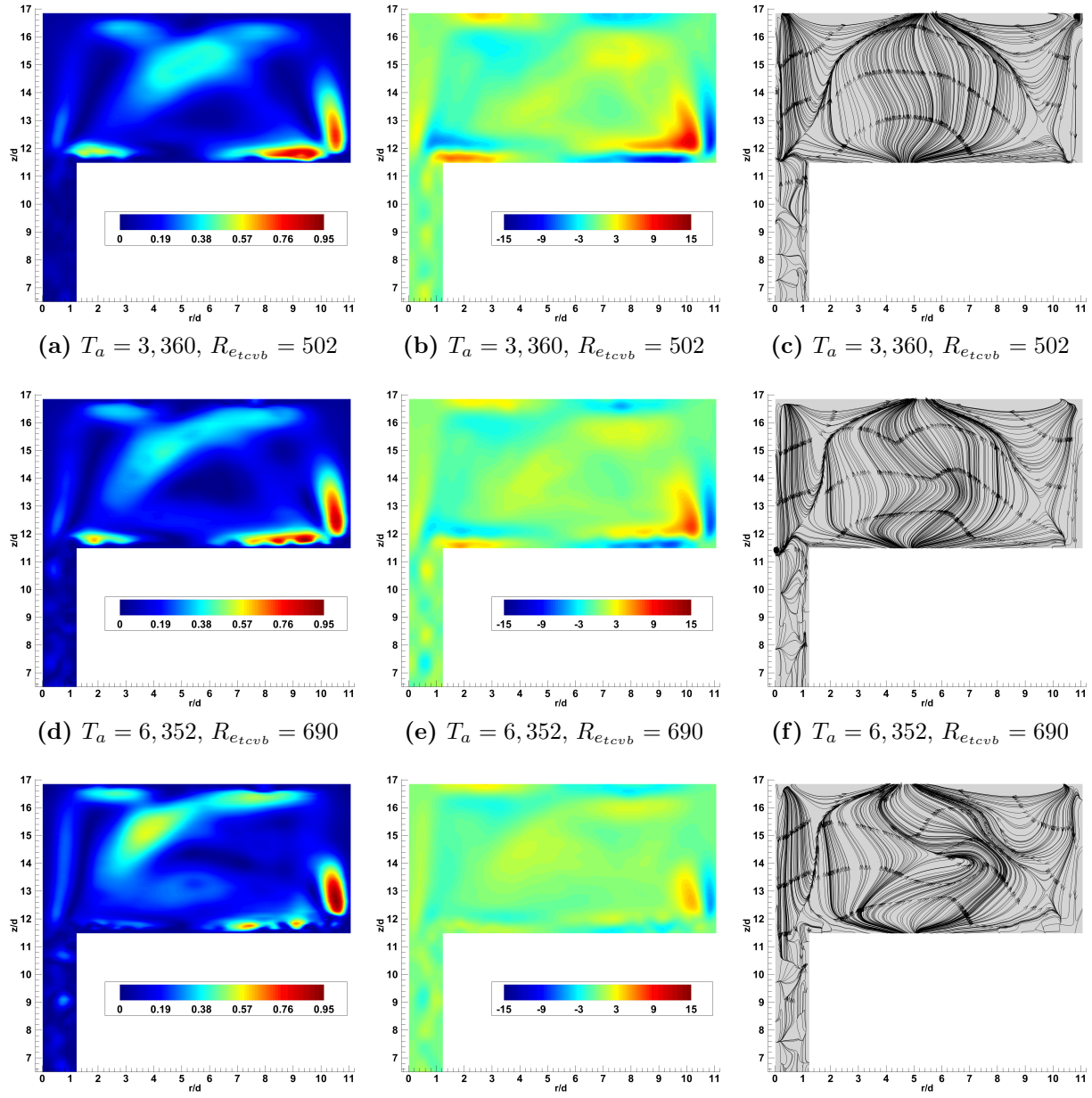

(a) $T_a = 3,360,\ R_{e_{tcvb}} = 502$ **(b)** $T_a = 3,360,\ R_{e_{tcvb}} = 502$ **(c)** $T_a = 3,360,\ R_{e_{tcvb}} = 502$

(d) $T_a = 6,352,\ R_{e_{tcvb}} = 690$ **(e)** $T_a = 6,352,\ R_{e_{tcvb}} = 690$ **(f)** $T_a = 6,352,\ R_{e_{tcvb}} = 690$

(g) $T_a = 15,170,\ R_{e_{tcvb}} = 1,067$ **(h)** $T_a = 15,170,\ R_{e_{tcvb}} = 1,067$ **(i)** $T_a = 15,170,\ R_{e_{tcvb}} = 1,067$

Figure 3.20: Taylor-Couette - zone-2 - mean flow (POD mode-0), velocity contours (left), non-dimensionalized vorticity $[\frac{\omega \hat{\mathbf{d}}}{2\Omega_I R_I}]$ (middle), Streamlines (right) at $\Gamma_{ew} = 1$

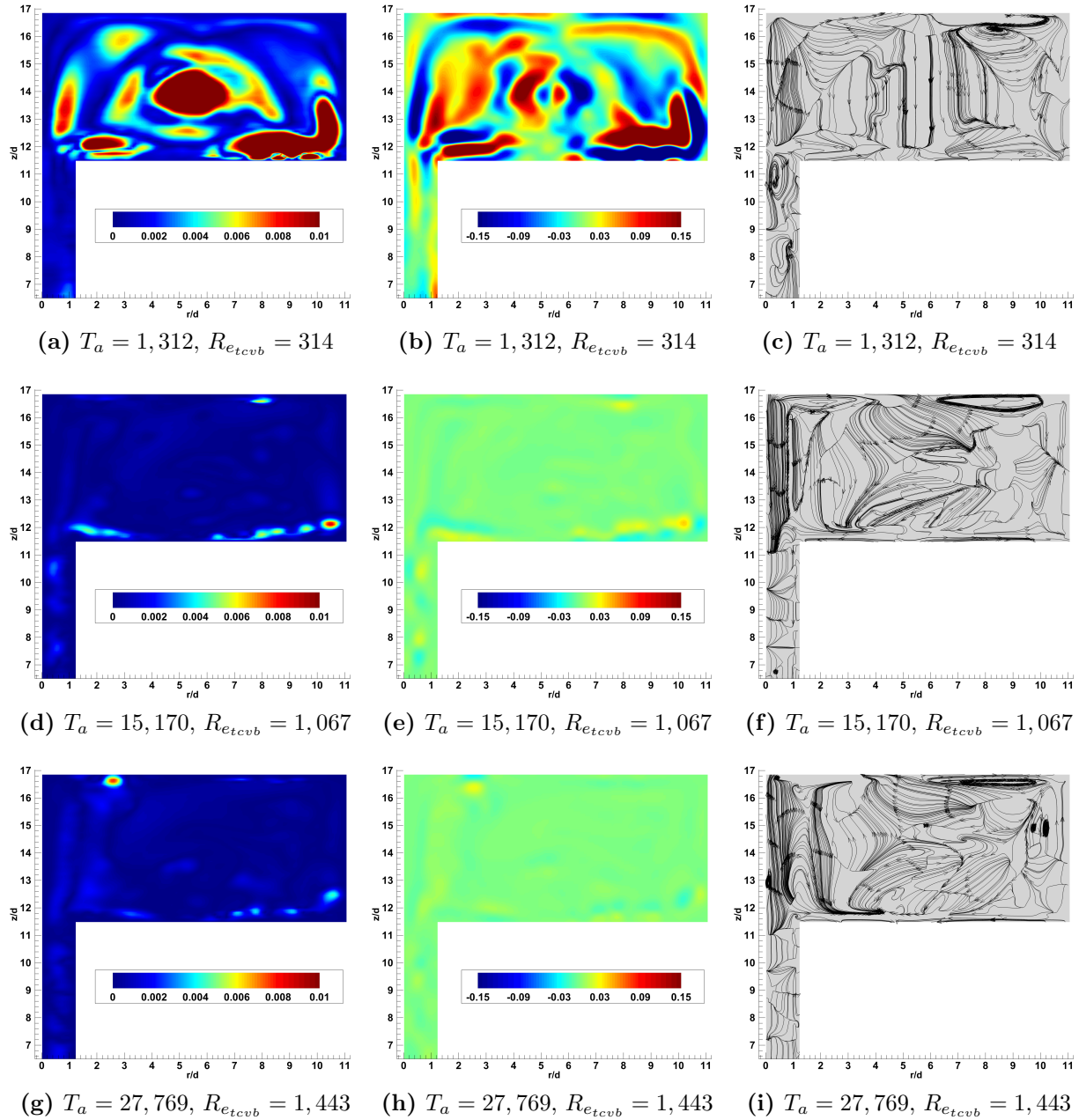

(a) $T_a = 1,312,\ R_{e_{tcvb}} = 314$ **(b)** $T_a = 1,312,\ R_{e_{tcvb}} = 314$ **(c)** $T_a = 1,312,\ R_{e_{tcvb}} = 314$

(d) $T_a = 15,170,\ R_{e_{tcvb}} = 1,067$ **(e)** $T_a = 15,170,\ R_{e_{tcvb}} = 1,067$ **(f)** $T_a = 15,170,\ R_{e_{tcvb}} = 1,067$

(g) $T_a = 27,769,\ R_{e_{tcvb}} = 1,443$ **(h)** $T_a = 27,769,\ R_{e_{tcvb}} = 1,443$ **(i)** $T_a = 27,769,\ R_{e_{tcvb}} = 1,443$

Figure 3.21: Taylor-Couette - zone-2 - mean flow (POD mode-0), velocity contours (left), non-dimensionalized vorticity $[\frac{\omega \hat{\mathbf{d}}}{2\Omega_I R_I}]$ (middle), Streamlines (right) at $\Gamma_{ew} = 1$

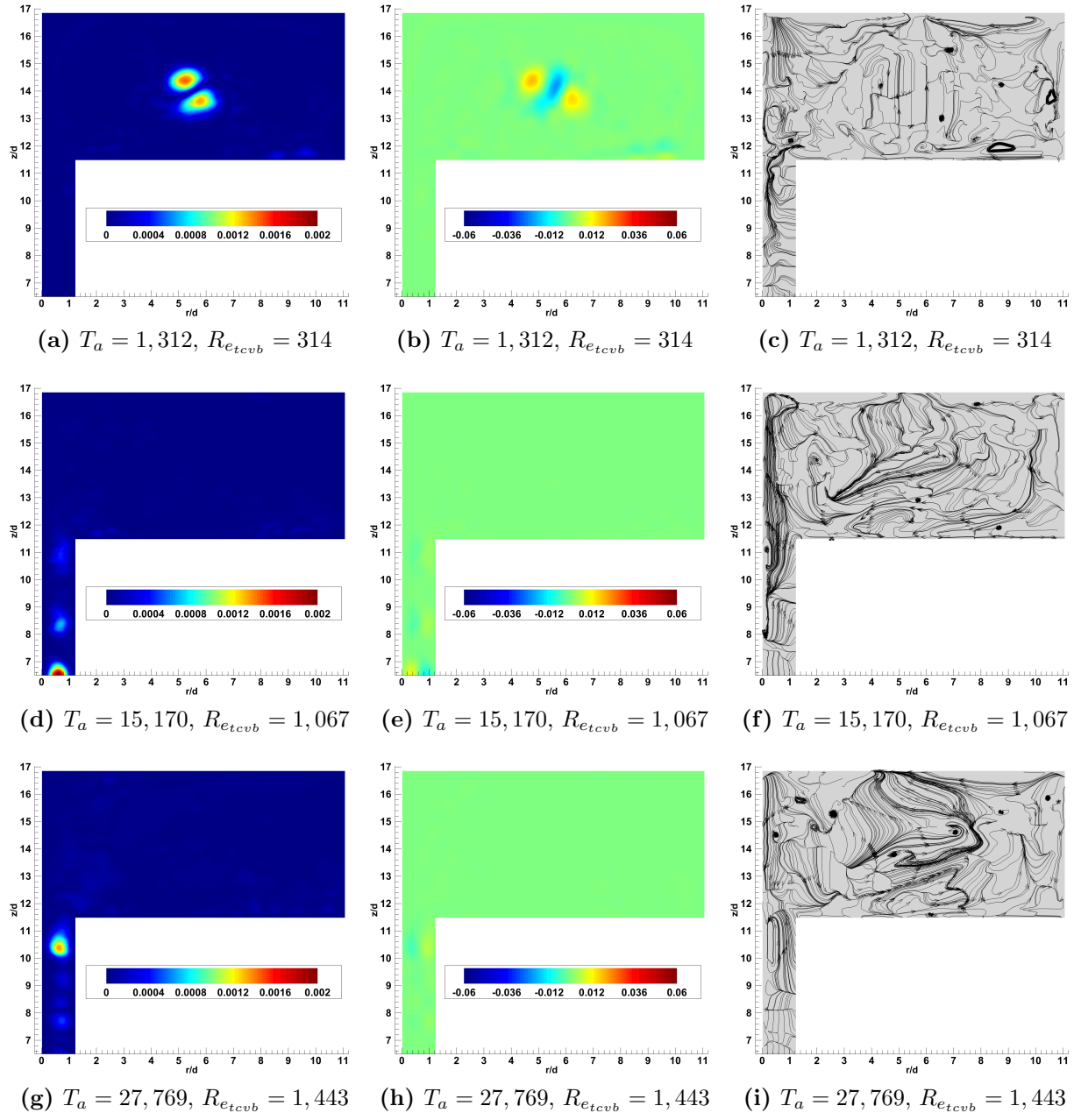

(a) $T_a = 1,312,\ R_{e_{tcvb}} = 314$ **(b)** $T_a = 1,312,\ R_{e_{tcvb}} = 314$ **(c)** $T_a = 1,312,\ R_{e_{tcvb}} = 314$

(d) $T_a = 15,170,\ R_{e_{tcvb}} = 1,067$ **(e)** $T_a = 15,170,\ R_{e_{tcvb}} = 1,067$ **(f)** $T_a = 15,170,\ R_{e_{tcvb}} = 1,067$

(g) $T_a = 27,769,\ R_{e_{tcvb}} = 1,443$ **(h)** $T_a = 27,769,\ R_{e_{tcvb}} = 1,443$ **(i)** $T_a = 27,769,\ R_{e_{tcvb}} = 1,443$

Figure 3.22: Taylor-Couette - zone-2 - mean flow (POD mode-0), velocity contours (left), non-dimensionalized vorticity $[\frac{\omega \hat{\mathbf{d}}}{2\Omega_I R_I}]$ (middle), Streamlines (right) at $\Gamma_{ew} = 1$

3.1.3 Annular Taylor-Couette Flow - Zone-1 - Rotationally Independent Inner Cylinder

PIV measurements of the flow in the annular gap were for $\Gamma_{ew} = 0,\ 0.5,\ 1$ and 1.5. As previously mentioned, testing at the largest two aspect ratios required the position of the CCD camera to be vertically adjusted to capture a large enough area of the flow between the two cylinders. Results of this annular investigation at the TCF condition are presented in Figures 3.23 - 3.35 and discussed in the proceeding text.

Energy plots for TCF annular flows are presented in Figure 3.23. Cumulative energies, seen in Figure 3.23 (a), have a far wider ranger than those of the VB and TCF zone-2 results. This wider range is primarily due to extremely low mean flow energy levels at the $\Gamma_{ew} = 1.5$ aspect ratio. The large drop and the subsequent segregation of $\Gamma_{ew} = 1.5$ modal energies that can be seen to occur beyond mode-3, (Figure 3.23 (b)), signifies a drastic change in annular flow conditions caused by an increase in aspect ratio beyond some critical point which lay between $\Gamma_{ew} = 1.0\ -\ 1.5$ and resulted in a large amount of energy being transferred from the larger to smaller scales. $\Gamma_{ew} = 1.5$ mean flow energy reductions are also noted to be greater at larger T_a values and were found to range from $\approx 38\%$ to as low as $\approx 5\%$. This indicated that changes in flow energy, caused by increases in end-wall aspect ratio, became amplified as the Taylor number increased. However, this reduction in energy was not entirely continuous at ever increasing Taylor numbers as indicated by the comparison of mean flow energy at $\Gamma_{ew} = 1.5\ T_a = 35,485$ and $\Gamma_{ew} = 1.5\ T_a = 15,170$ in Figure 3.23 (a). Through detailed examination, utilizing a more inclusive comparison of all rotational test cases at the $\Gamma_{ew} = 1.5$ aspect ratio, it was found that the two largest reductions in mean flow energy occurred between Taylor numbers $T_a = 3,360$ and $T_a = 6,352$, beyond which mean flow energy levels were found to remain between 5% and 23%.

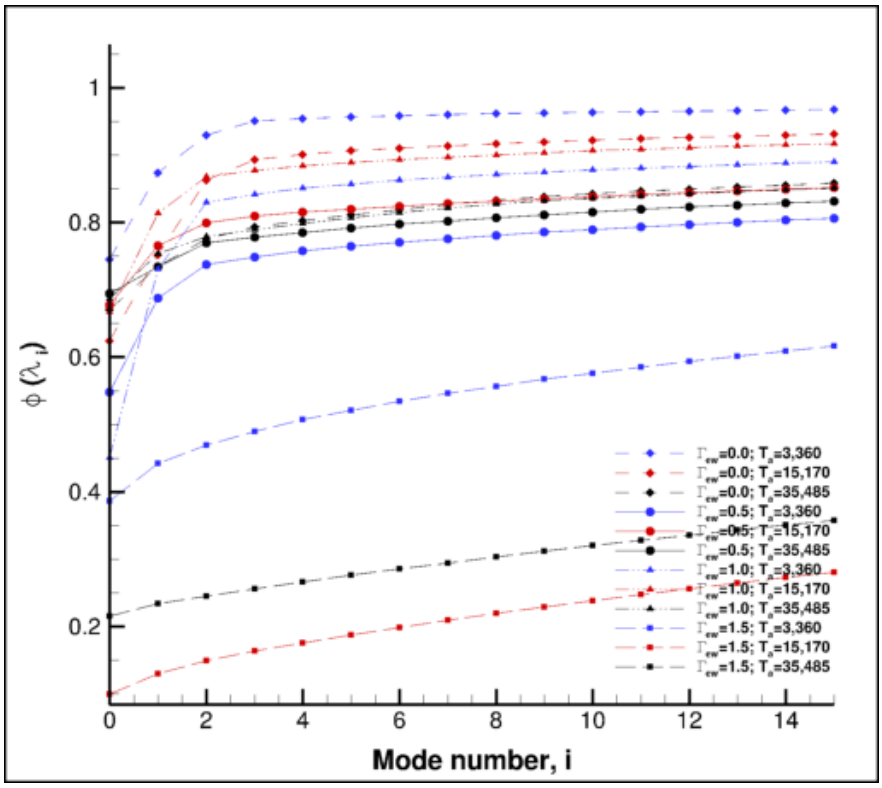

(a) cumulative distribution

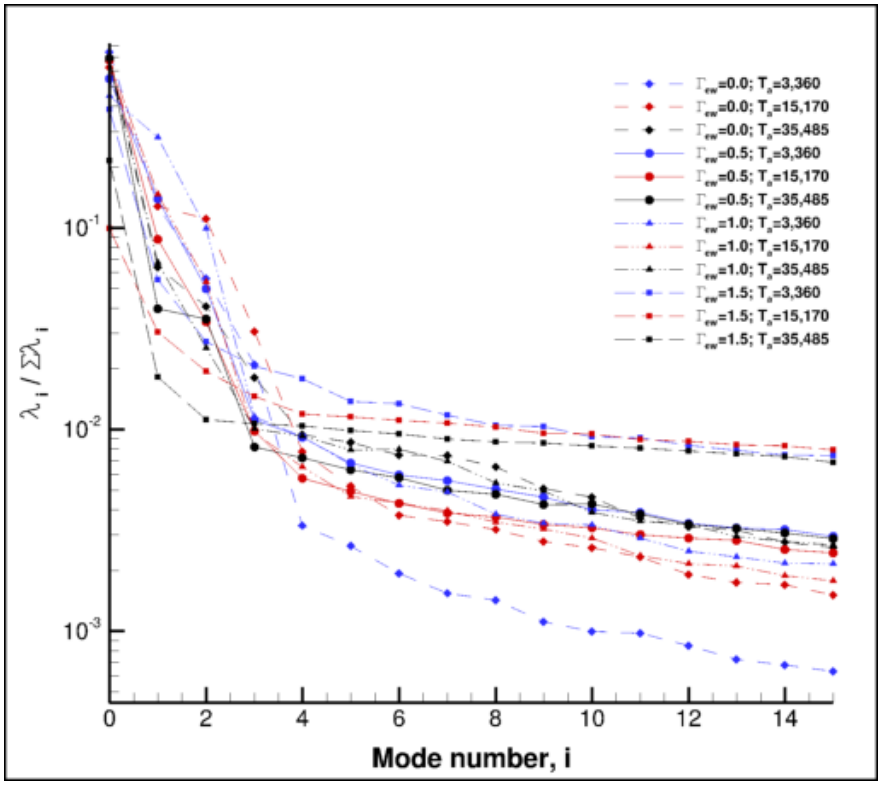

(b) POD spectrum, modes 0-15

Figure 3.23: TCF annular POD energy distribution

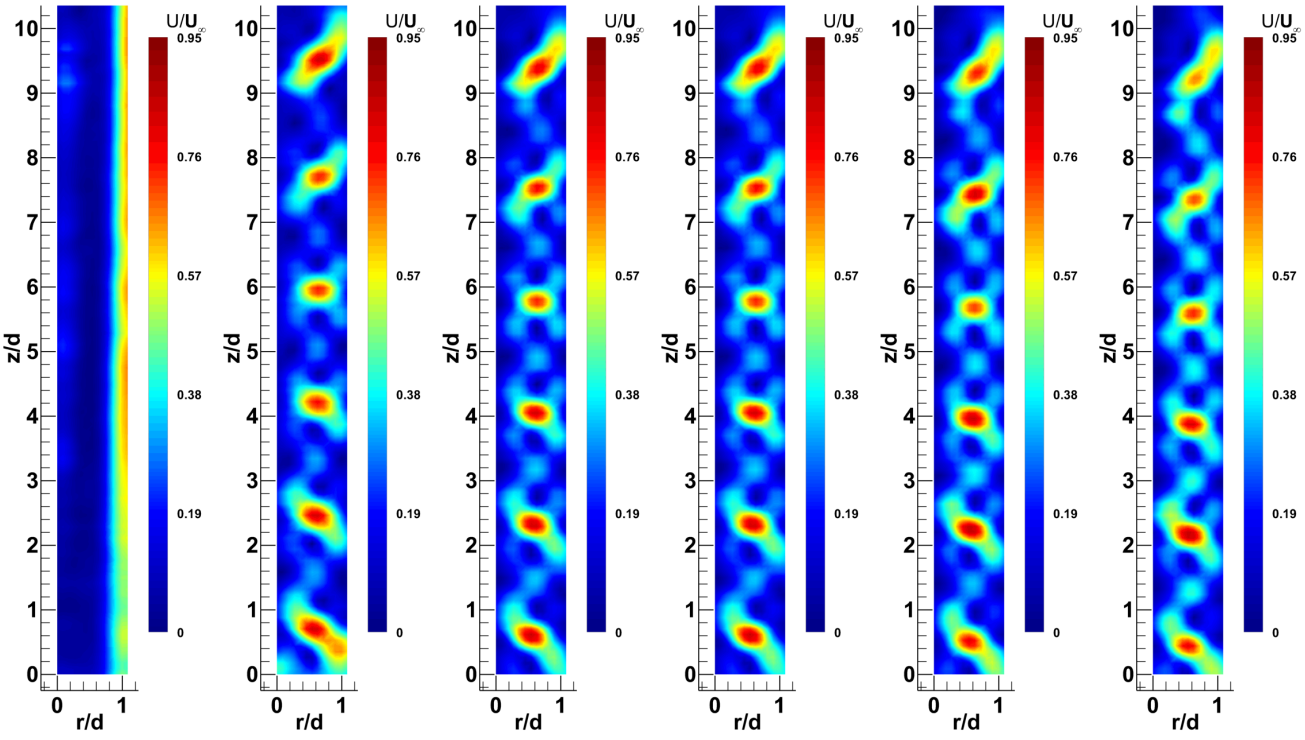

(a) $T_a = 1,312$ **(b)** $T_a = 3,360$ **(c)** $T_a = 6,352$ **(d)** $T_a = 10,289$ **(e)** $T_a = 20,997$ **(f)** $T_a = 35,485$

Figure 3.24: Taylor-Couette annular mean flow (POD mode-0 Zone-1), velocity contours at $\Gamma_{ew} = 0$

Measurements at $\Gamma_{ew} = 0$ were taken in order to establish a true baseline for the Taylor vortices which are known to form within the annular gap between two rotating concentric cylinders. From these measurements the initial onset of Taylor vortices was found to occur at $T_a = 3,360$, however, this was almost certainly not the actual point of bifurcation but was instead the lowest Taylor number tested which lie above T_{a-crit}. True onset of TV's most likely occurred somewhere between $1,320$ *and* $3,360$ as the critical Taylor number predicted by small gap stability theory is $T_{a-crit} \approx 1,708 \Rightarrow R_{e_{tc}-crit} \approx 85$ as previously stated. In fact at $T_a = 3,360 \Rightarrow R_{e_{tc}} = 120$ the onset of WVF would typically be expected for the given gap ratio ($\eta = 0.815$) that was used in the present work. From the experimental data of Cole, Edwards et al. and others, at an aspect ratio of $\Gamma_c = 20$ the onset of WVF is reported to lie between $1.2 \leq \epsilon^{wv}_{crit} \leq 1.35$, where $\epsilon^{wv}_{crit} = \frac{R_{e_{tcvb}}}{R_{e_{tcvb}-crit}}$. Using this criterion the value of ϵ^{wv}_{crit} for a T_a of $3,360$ was found to be ≈ 1.4, a value which is just beyond the upper limit for the expected onset of WVF. It was difficult to discern if the flow was in fact wavy due to

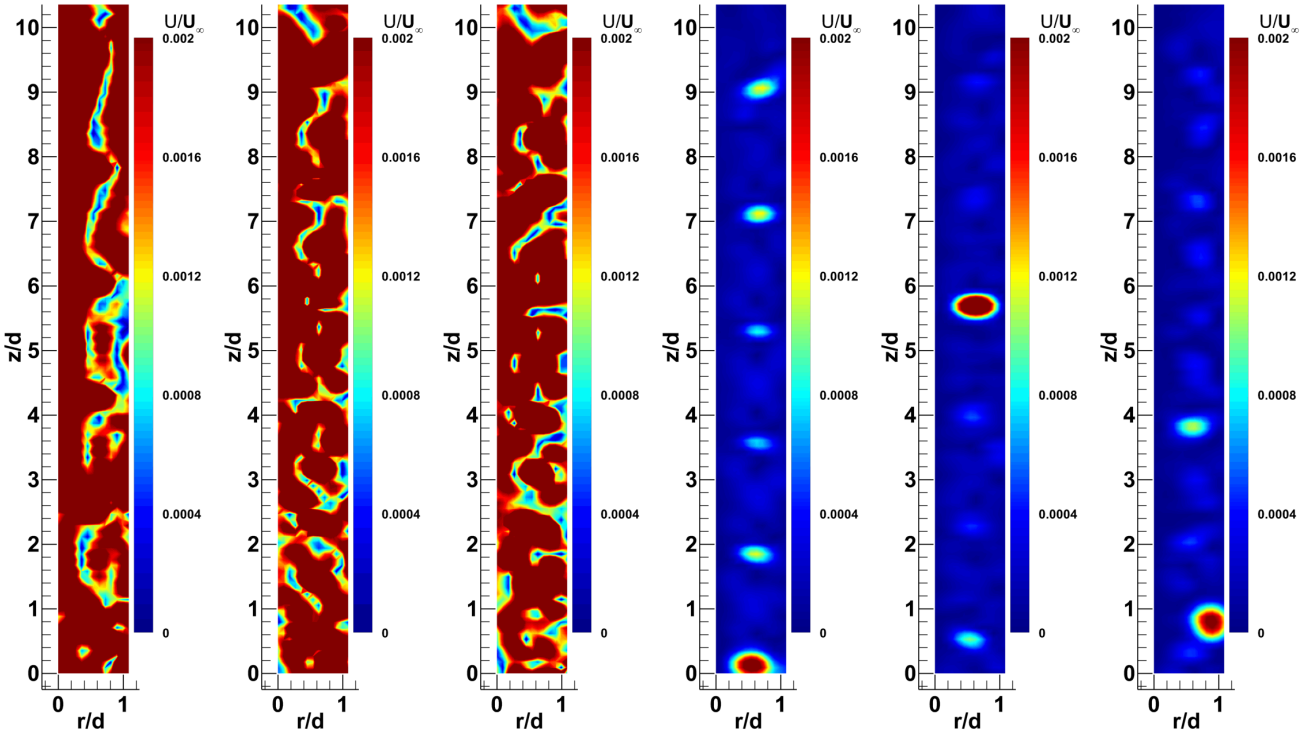

(a) $T_a = 3, 360$ **(b)** $T_a = 15, 1700$ **(c)** $T_a = 35, 485$ **(d)** $T_a = 3, 360$ **(e)** $T_a = 15, 170$ **(f)** $T_a = 35, 485$

Figure 3.25: Taylor-Couette annular flow (Zone-1), velocity contours at $\Gamma_{ew} = 0$, POD mode-1 (a-c), POD mode-3 (d-f)

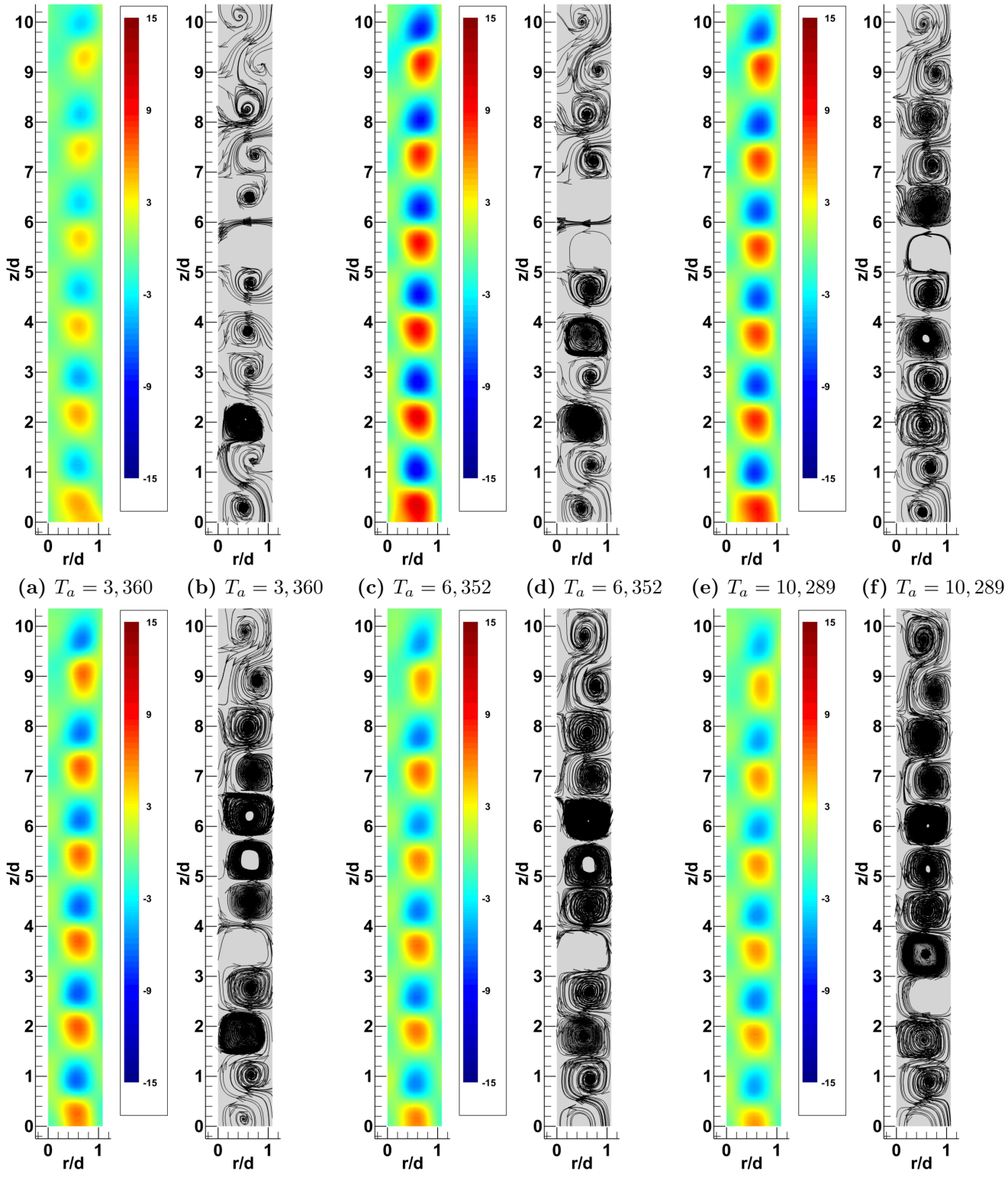

(a) $T_a = 3,360$ (b) $T_a = 3,360$ (c) $T_a = 6,352$ (d) $T_a = 6,352$ (e) $T_a = 10,289$ (f) $T_a = 10,289$

(g) $T_a = 15,170$ (h) $T_a = 15,170$ (i) $T_a = 27,769)$ (j) $T_a = 27,769$ (k) $T_a = 35,485$ (l) $T_a = 35,485$

Figure 3.26: Taylor-Couette annular mean flow (POD mode-0 Zone-1), non-dimensionalized vorticity $[\frac{\omega \hat{\mathbf{d}}}{2\Omega_I R_I}]$ & streamlines $\Gamma_{ew} = 0$

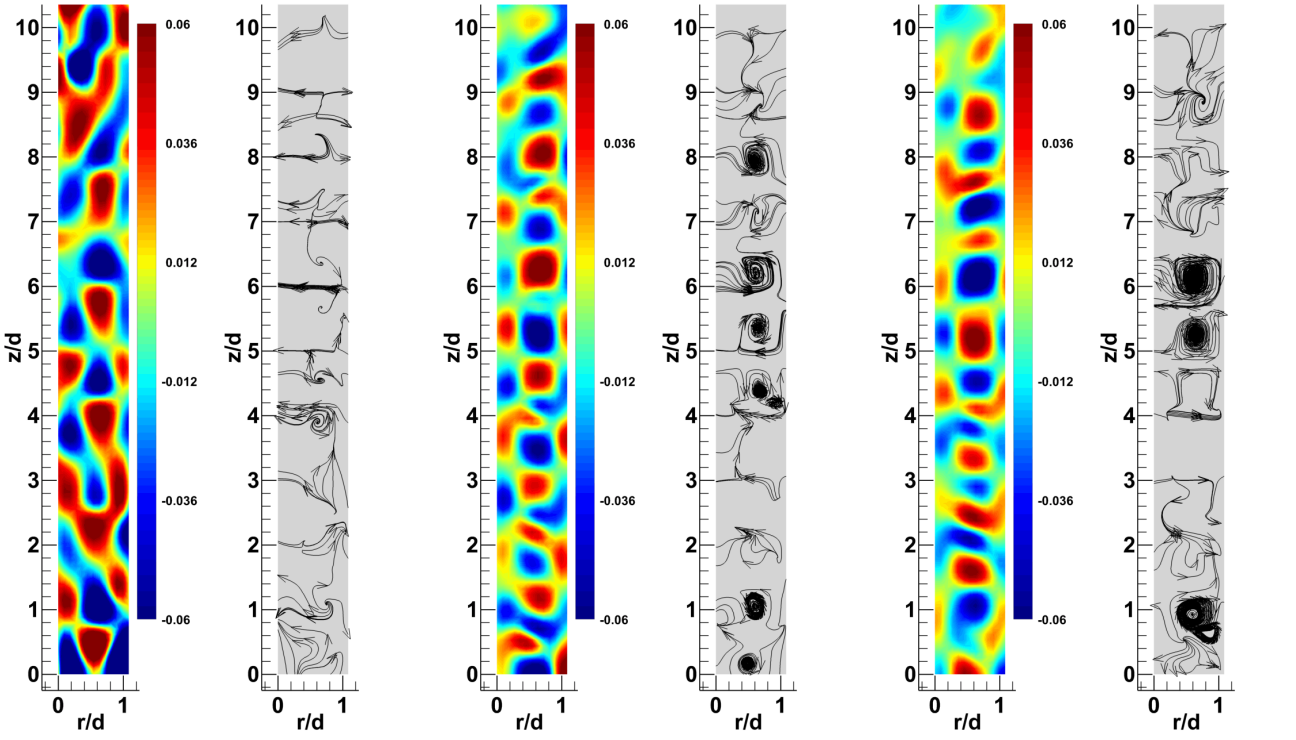

(a) $T_a = 3,360$ (b) $T_a = 3,360$ (c) $T_a = 15,170$ (d) $T_a = 15,170$ (e) $T_a = 35,485$ (f) $T_a = 35,485$

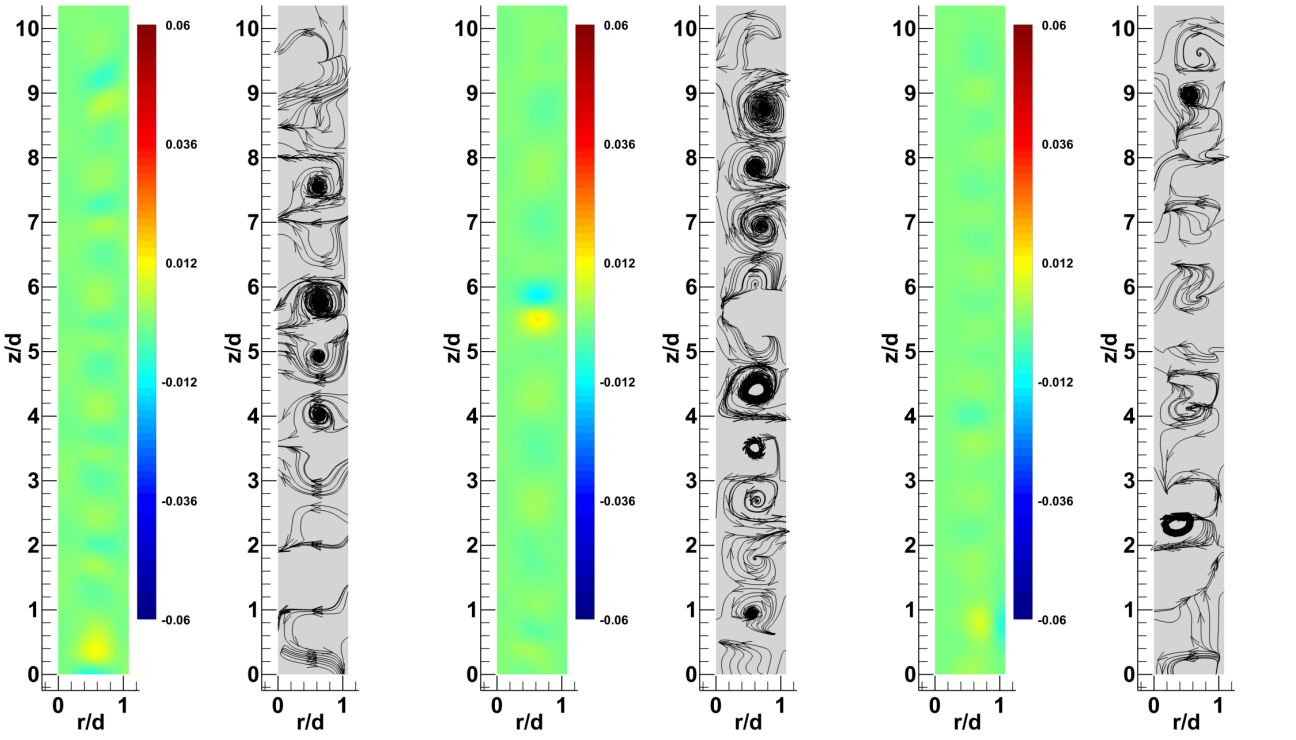

(g) $T_a = 3,360$ (h) $T_a = 3,360$ (i) $T_a = 15,170)$ (j) $T_a = 15,170$ (k) $T_a = 35,485$ (l) $T_a = 35,485$

Figure 3.27: Taylor-Couette annular flow for POD mode-1 (top) & mode-3 (bottom), non-dimensionalized vorticity $[\frac{\omega \hat{\mathbf{d}}}{2\Omega_I R_I}]$ & streamlines $\Gamma_{ew} = 0$

lighting limitations of the laser such that only one side of the annular gap was observable. However, detailed analysis of the vorticity and velocity plots as well as the streamlines of Figures 3.24(b) and 3.26 (a-b) reveals Taylor vortices at $T_a = 3,360$ to have a slight axial slant and display patterns indicative of intra-vortex fluid exchange. Flow features such as those previously describe indicated that the TV's were of a wavy form when they were first noted to appear at $T_a = 3,360$. This basic flow pattern was maintained even as T_a was increased to the highest value of $T_a = 35,485 \Rightarrow R_{e_{tc}} = 387$. The only significant changes that were found to occur in the mean flow at $\Gamma_{ew} = 0$ as Taylor number was increased beyond $3,360$ was a small continuous reduction in relative vorticity and a general progression of the Taylor vortices taking on a more square like form; these results are displayed in Figures 3.24 and 3.26.

For $\Gamma_{ew} = 0$ results of higher POD modes are presented in Figures 3.25 and 3.27, while these results were not found to display the same level of divergence from mean flow trends as some of the larger aspect ratio results, they reveal some of the more subtle nuances contained within the base flow structure. Mode-1 vorticity results, presented in Figures 3.27 (a-f), display an enhanced view of the intra vortex fluid exchange that was noted to occur in the mean flow results presented in Figure 3.26 were right angle like structures can be seen in the regions between vortex pairs. A left to right progression of the mode-1 plots shows these areas of vortical exchange becoming more pronounced as T_a increased. Additionally Taylor vortex structures are seen to have become increasingly more defined at ever increasing Taylor numbers similar to what was seen in $\Gamma_{ew} = 0$ mean flow results. Mode-1 results also display what appear to be small counter rotating vortices positioned between the cylinder walls and the Taylor vortices. These side wall vortices appear on either side of the TVs in velocity plots of Figures **??** (b-c) while appearing almost exclusively on the left hand side of the annulus, between the outer cylinder wall and the TVs, in the vorticity plots of Figures **??** (a, c & e). Extremely weak indications of these side wall vortices were also noted to appear in mean flow vorticity plots of Figure 3.26. Mode-1 results however show that these additional formations

caused the Taylor vortices to be displaced in the positive radial direction, an effect which became increasingly mitigated at higher Taylor numbers as indicated by the streamlines of Figures 3.27 (b, d, & f).

Mode-3 results were similarly found to display enhanced views of the minute features of the flow, specifically the inflow (positive radial flow) and outflow (negative radial flow) boundaries that occur between the Taylor vortices. Velocity magnitude presented in Figure 3.25 (d) most clearly show these regions where outflows especially, are noted to display the largest relative velocities. Similarly, Figure 3.27 (h) shows the outflow boundaries at $T_a = 3,360$ mode-3 to be dominant constituting nearly every region of radial flow within the streamlines. Inflow boundaries at $T_a = 3,360$ were found to only be visible in the mode-3 vorticity plot of Figure 3.27 (g) and are seen to be directly below the more dominant outflow regions taking on what appears to be a weaker form of the right angle flow formations noted to occur in $\Gamma_{ew} = 0$ mode-1 results. Imbalances between the inflow and outflow regions of mode-3 were found to become mitigated as T_a was increased such that at $T_a = 15,170$ Figures 3.25 (e) and 3.27 (i-j) display almost no noticeable disproportionality. One noted exception however can be seen at $z/\hat{d} \approx 5.5$ in Figures 3.25 (e) and 3.27 (i) where the outflow bound is seen to have higher relative vorticity and velocity values and appears to act as a barrier segregating the flow into an upper and lower region. Further increase in the Taylor number resulted in mode-3 results taking on a slightly more chaotic appearance, where from Figure 3.27 (k) inflow and outflow bounds and the individual Taylor vortices are relatively indistinguishable from one another. This lack of differentiation between flow features and the tangled appearance of the streamlines in Figure 3.27 (l) indicates increasing flow perturbations within the annulus and suggests that further increases in T_a would have lead to an additional flow bifurcation, most likely modulated wave flow (MWF) [2].

Adjustment of the upper end wall to an aspect ratio of $\Gamma_{ew} = 0.5$ was found to result in Taylor vortex structures that were noticeably altered from those of $\Gamma_{ew} = 0$. While the initial formation of the TV's within mean flow results was still seen to occur at $T_a = 3,360$,

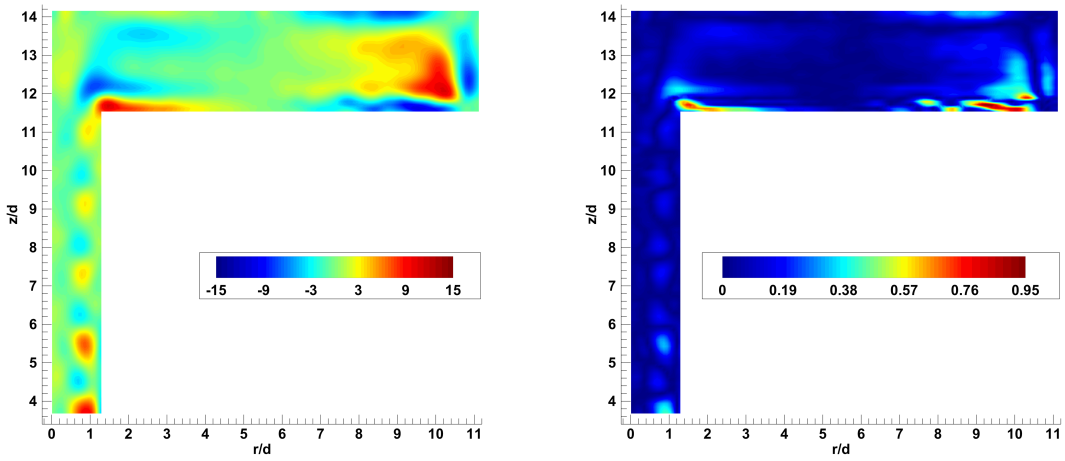

(a) $T_a = 3,360$, $R_{e_{tc-vb}} = 502$ **(b)** $T_a = 3,360$, $R_{e_{tcvb}} = 502$

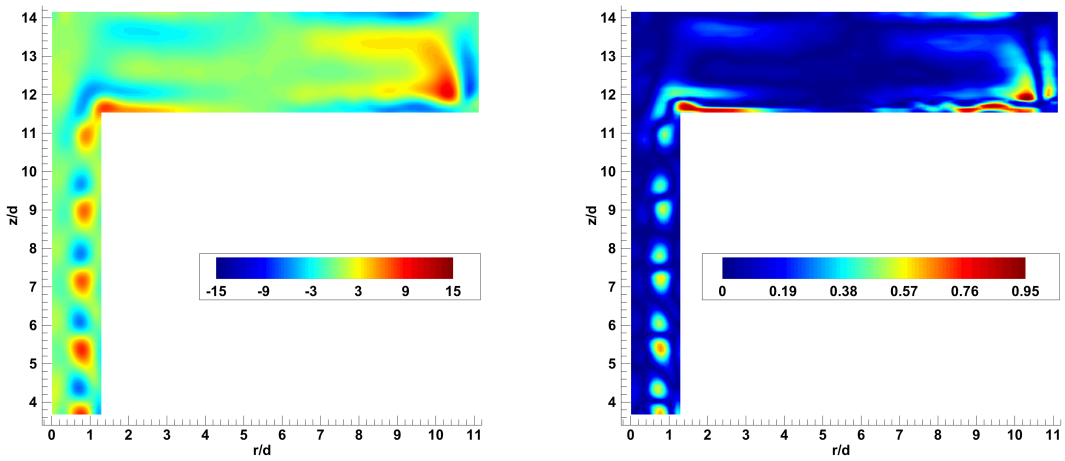

(c) $T_a = 6,352$, $R_{e_{tcvb}} = 690.2$ **(d)** $T_a = 6,352$, $R_{e_{tcvb}} = 690.2$

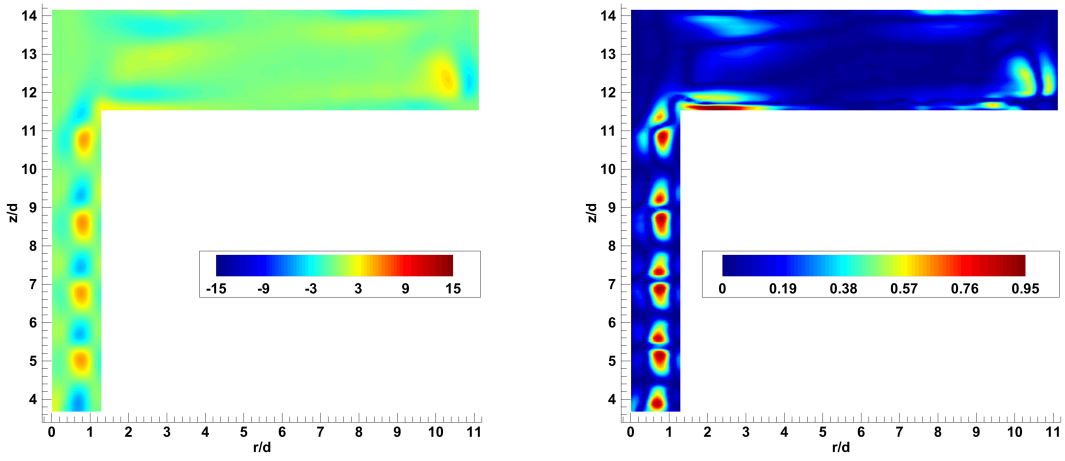

(e) $T_a = 27,769$, $R_{e_{tcvb}} = 1,443.2$ **(f)** $T_a = 27,769$, $R_{e_{tcvb}} = 1,443.2$

Figure 3.28: Taylor-Couette mean flow (POD mode-0), non-dimensionalized vorticity $[\frac{\omega \hat{\mathbf{d}}}{2\Omega_I R_I}]$ (left) and vorticity magnitude (right) at $\Gamma_{ew} = 0.5$

their form was much less coherent than those observed at $\Gamma_{ew} = 0$. This altered structure can be seen in Figures 3.14 (b) and 3.28 (a) where vortices take on a roughly triangular shape in the latter with a significant amount of axial flow at $z/\hat{d} \approx 11.5 - 8$ displayed in the former. Figure 3.28 also displays a large reduction in the Taylor vortices relative vorticity when compared to the $\Gamma_{ew} = 0$ case of Figure 3.26. This reduction in vortex circulation was noted to be greatest near the top of the annulus and was caused by a negative axial encroachment of fluid from zone-2.

Annular encroachment from zone-2 was caused, in part by, the close proximity of the boundary layer, which formed along the upper surface of the rotating cylinder, to the zone-1/2 interface. As fluid was ejected radially outward from the upper surface of the inner cylinder towards the stationary side-wall the boundary layer became larger, causing an ever increasing radial velocity gradient. As this gradient encountered the stationary side-wall it was forced to turn in the axial direction. Thus, due to the presence of the annular gap, a portion of this diverted flow was forced to curl downward into the annulus, where increases in either radial velocity or boundary layer thickness resulted in increased negative axial mass flow. This diverted flow caused the upper most TV to become radially strained inward by $\approx 0.35d$ such that it became pinned near the wall of the inner cylinder. This displacement in the position of the upper TV coupled with an increase in regional T_{a-crit}, due to the presence of negative axial flow, was found to be the primary source of the drastic reduction in $\Gamma_{ew} = 0.5$ TV vorticity. These effects, as previously mentioned, were strongest near the domain interface and cascaded down into the annulus resulting in the axial gradient differences between the Taylor vortices at $\Gamma_{ew} = 0$ and $\Gamma_{ew} = 0.5$.

As the Taylor number was increased beyond $T_a = 3,360$ negative axial mass flow from zone-2 to zone-1 also increased. Surprisingly, this actually resulted in a stabilizing effect on TVs and resulted in a more uniform annular flow in regards to both Taylor vortex structure and vorticity values. This increased stability was found to result from a combination of decreased interactions between the zones and an increase in Taylor vortex circulation,

specifically in the lower portions of the annulus (zone-1). As the mass of fluid rushing into the gap increased, it began to encounter an increased resistance acting in the positive axial direction caused by the increased circulation of the lower TV's. This resistance to linear axial motion grew as T_a was increased and began to force the encroaching fluid to turn back in the positive axial direction resulting in the formation of a barrier which progressively segmented the annulus (zone-1)from zone-2 influences. Nondimensional vorticity values of this encroaching flow were found to increase as T_a increased, and eventually resulted in the formation of an elongated counter rotating vortex pair directly above the upper most Taylor vortice as seen in Figure 3.28 at $z/\hat{d} \approx 10.5$. This elongated vortex acted as a "pseudo Ekman cell" which stabilized the Taylor cells in the upper half of the annulus and resulted in the noted decrease in the $\Gamma_{ew} = 0.5$ mean flow axial vorticity gradient. It was also found that as T_a increased and more fluid began to flow into the annulus, Taylor vortices were progressively forced further down into the annulus. This occurred over the entire range for which TV's were observed, $T_a = 3,360 - 35,485$, and resulted in an overall displacement of $\approx 0.3d$ in the negative axial direction.

Results from modes 1 and 3 at $\Gamma_{ew} = 0.5$ were found to display inappreciable amounts of additional detail for the flow contained within the annulus (zone-1). Streamlines presented in Figures 3.15 and 3.16 show a trend that is vaguely similar to that seen in the higher modal results at $\Gamma_{ew} = 0$ and display either a weaker form of the mean flow Taylor vortices (Figure 3.16 (f)) or no discernible TV pattern at all. However, unlike POD results at $\Gamma_{ew} = 0$ the vast majority of $\Gamma_{ew} = 0.5$ POD streamlines were found to display no indications of Taylor vortex circulations but were instead noted to predominantly display the axial motion of fluid exchange between zone-2 and annulus, at $z/\hat{d} \approx 8 - 11.5$, that was first noted to occur in $\Gamma_{ew} = 0.5$ mean flow streamline results. Non-dimensional velocity and vorticity plots were similarly found to contain few instances of discernible detail and were instead seen to merely highlight the smaller mean flow structures and predominately consisted of the inflow / outflow boundaries as was seen to occur in $\Gamma_{ew} = 0$ POD results. Mode-1 and mode-3

each display one such instance in Figures 3.15 (g-h) and 3.15 (d-e) showing the radial offset indicative of WVF in the former and pronounced outflow boundaries between vortex pairs in the latter. As with the streamlines, velocity and vorticity plots at the higher modes were found to be primarily dominated by patterns indicative of the axial fluid exchange between the domains rather than TV circulations. Additionally none of the higher modal $\Gamma_{ew} = 0.5$ results investigated were found to give such indications of TV circulation for Taylor numbers lower than $T_a = 15,170$ which is the same point at which the pseudo Ekman cell was first noted to be fully formed in the mean flow results indicating that the formation of such a cell at the top of the annular gap is a key factor in Taylor vortex stability.

Mean flow results for the $\Gamma_{ew} = 1$ aspect ratio were found to displayed trends generally similar to those described for the mean flow at $\Gamma_{ew} = 0.5$ with weaker Taylor vortex formations at the lower Taylor numbers tested that became progressively more structured and uniform as T_a was increased. Initial formation of Taylor vortices was again first noted to appear in the mean flow results at a test condition of $T_a = 3,360$, as seen in Figures 3.29 and 3.31. These initial vortices are seen to be slightly less structured and display vorticity values nearly 1/3 that of the Taylor vortices at similar $\Gamma_{ew} = 0$ conditions. Additionally vorticity of the cells within the annulus can be seen to form an axial gradient similar to what was seen at $T_a = 3,360$ $\Gamma_{ew} = 0.5$ where circulation of the individual cells was weakest at the top of the annulus but became progressively stronger as axial distance from the domain interface increased. As with $\Gamma_{ew} = 0.5$ results this gradient was attributed to a negative axial encroachment of fluid from the zone-2 which acted to reduce T_{a-crit} in the upper half of the annulus. However, this negative axial flow was found to penetrate slightly further down into the annular domain at this higher aspect ratio. At $\Gamma_{ew} = 0.5$ flow penetration was found to reach a depth of approximately $3.5\hat{d}$, (between $z/\hat{d} \approx 11.5 - 8$), where as the streamlines of Figure 3.31 (b) show the same conditions resulting in an annulus penetration depth of $\approx 4.5\hat{d}$ at $\Gamma_{ew} = 1.0$. This increased penetration was found to be $\approx 29\%$ greater than that at $\Gamma_{ew} = 0.5$ and was the most likely cause of the slight reduction in $\Gamma_{ew} = 1.0$

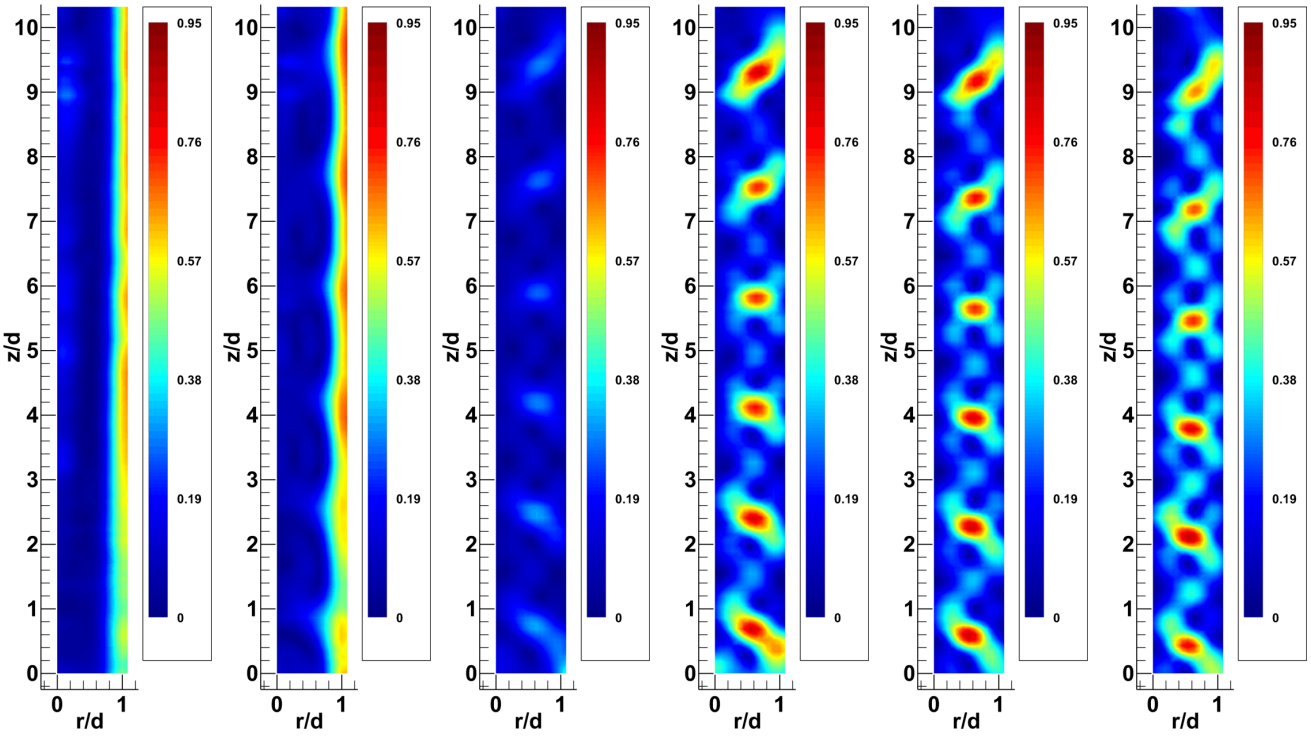

(a) $T_a = 1,312$ **(b)** $T_a = 3,360$ **(c)** $T_a = 6,352$ **(d)** $T_a = 10,289$ **(e)** $T_a = 20,997$ **(f)** $T_a = 35,485$

Figure 3.29: Taylor-Couette mean flow (POD mode-0 Zone-1), velocity contours at $\Gamma_{ew} = 1$

vorticity from the levels seen to occur in Figure 3.28 (b) at $\Gamma_{ew} = 0.5$ where similar axially positioned cells in the $\Gamma_{ew} = 1$ results were found to display a $\approx 31\%$ reduction in vorticity. Increases in Taylor number beyond $T_a = 3,360$ resulted in a progressive reduction of the axial TV vorticity gradient as well as the formation of more square like and uniformly shaped Taylor vortices, which were progressively displaced in the negative axial direction in a similar manner as that noted to occur for increasing T_a numbers at $\Gamma_{ew} = 0.5$. However, these annular results for increases in T_a were noted to have a slight discrepancy with the visible annular (zone-1) results of the $\Gamma_{ew} = 1.0$ zone-2 test.

Initial observations of Figure 3.20, which include the upper flow domain, seemed to indicate that Taylor vortex formations became increasingly unstructured as T_a increased. However, investigations into higher POD modes, specifically mode-1 (Figure 3.21), showed that Taylor cells were actually fairly structured in the zone-2 cases for the vast majority of the Taylor number range with only a slight destabilization of the upper most pair occurring

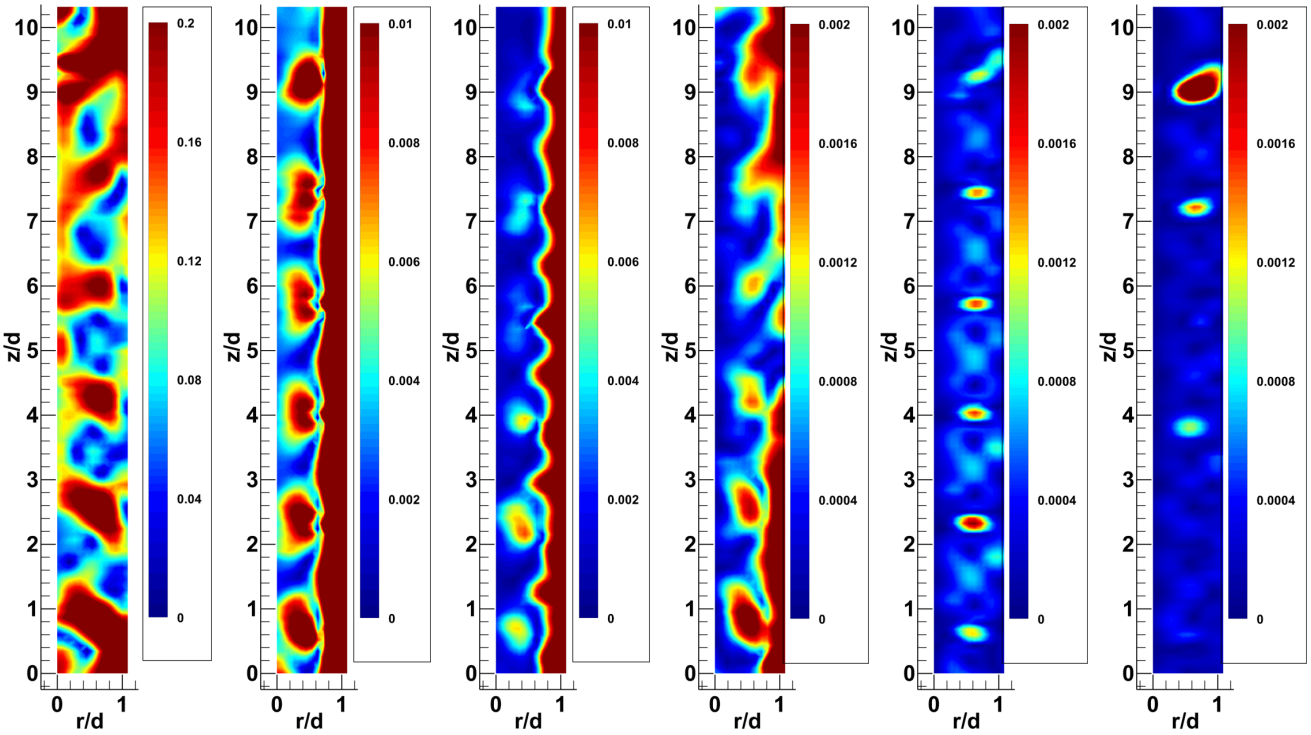

(a) $T_a = 3,360$ **(b)** $T_a = 15,170$ **(c)** $T_a = 35,485$ **(d)** $T_a = 3,360$ **(e)** $T_a = 15,170$ **(f)** $T_a = 35,485$

Figure 3.30: Taylor-Couette Zone-1 POD mode-1 (a-c) & mode-3 (d-f), velocity contours at $\Gamma_{ew} = 1$

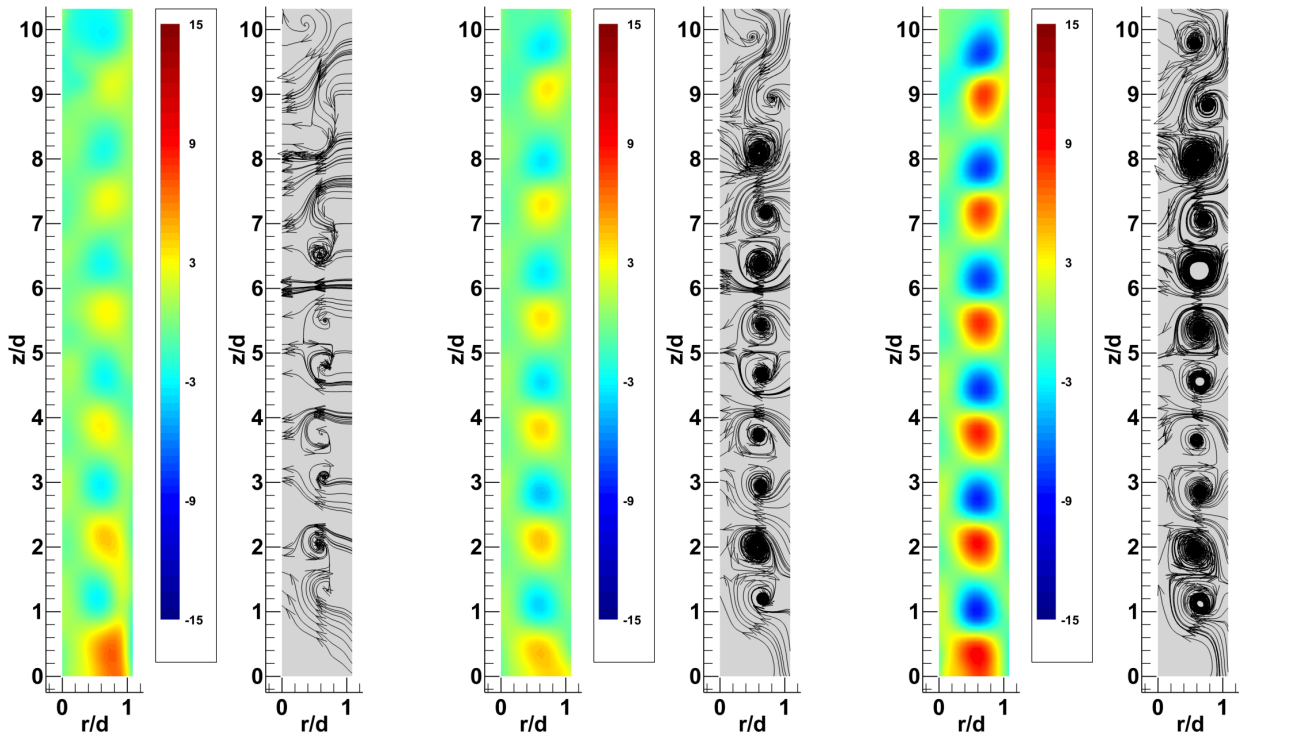

(a) $T_a = 3,360$ (b) $T_a = 3,360$ (c) $T_a = 6,352$ (d) $T_a = 6,352$ (e) $T_a = 10,289$ (f) $T_a = 10,289$

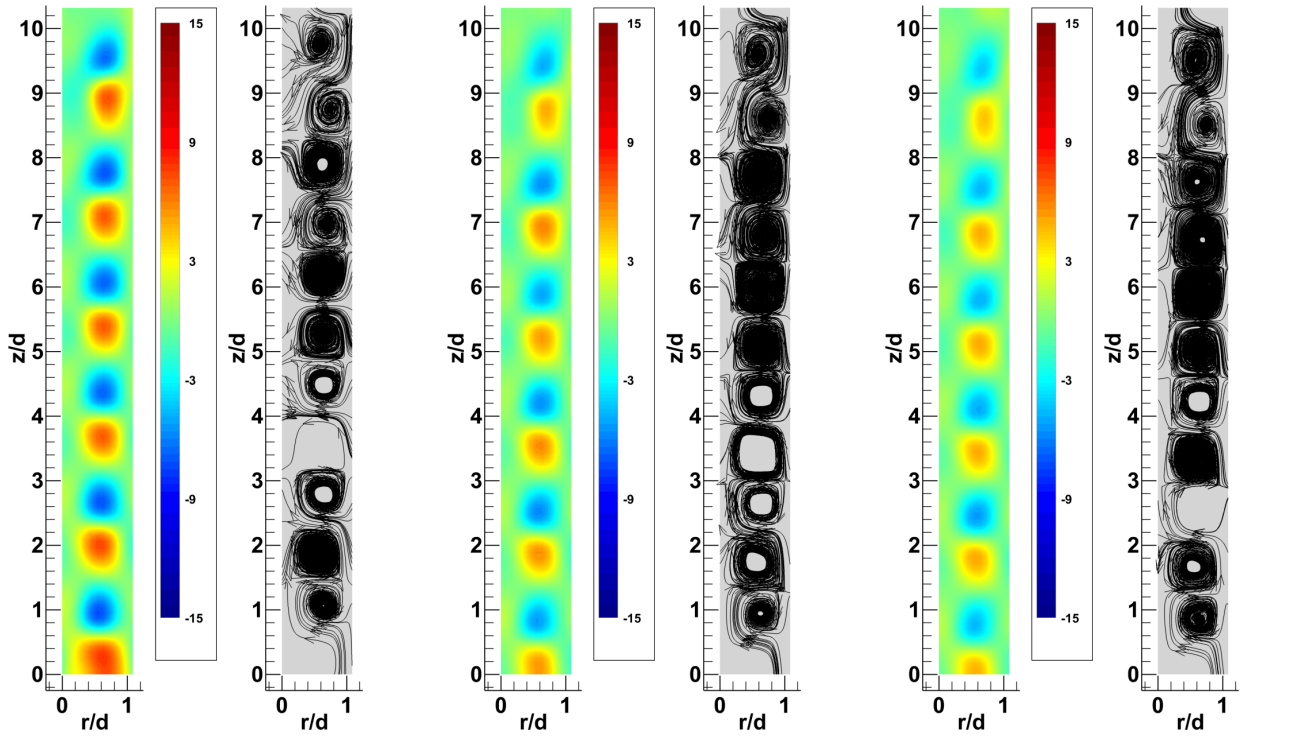

(g) $T_a = 15,170$ (h) $T_a = 15,170$ (i) $T_a = 27,769$ (j) $T_a = 27,769$ (k) $T_a = 35,485$ (l) $T_a = 35,485$

Figure 3.31: Taylor-Couette mean flow (POD mode-0 Zone-1), non-dimensionalized vorticity $[\frac{\omega \hat{\mathrm{d}}}{2\Omega_I R_I}]$ & streamlines at $\Gamma_{ew} = 1$

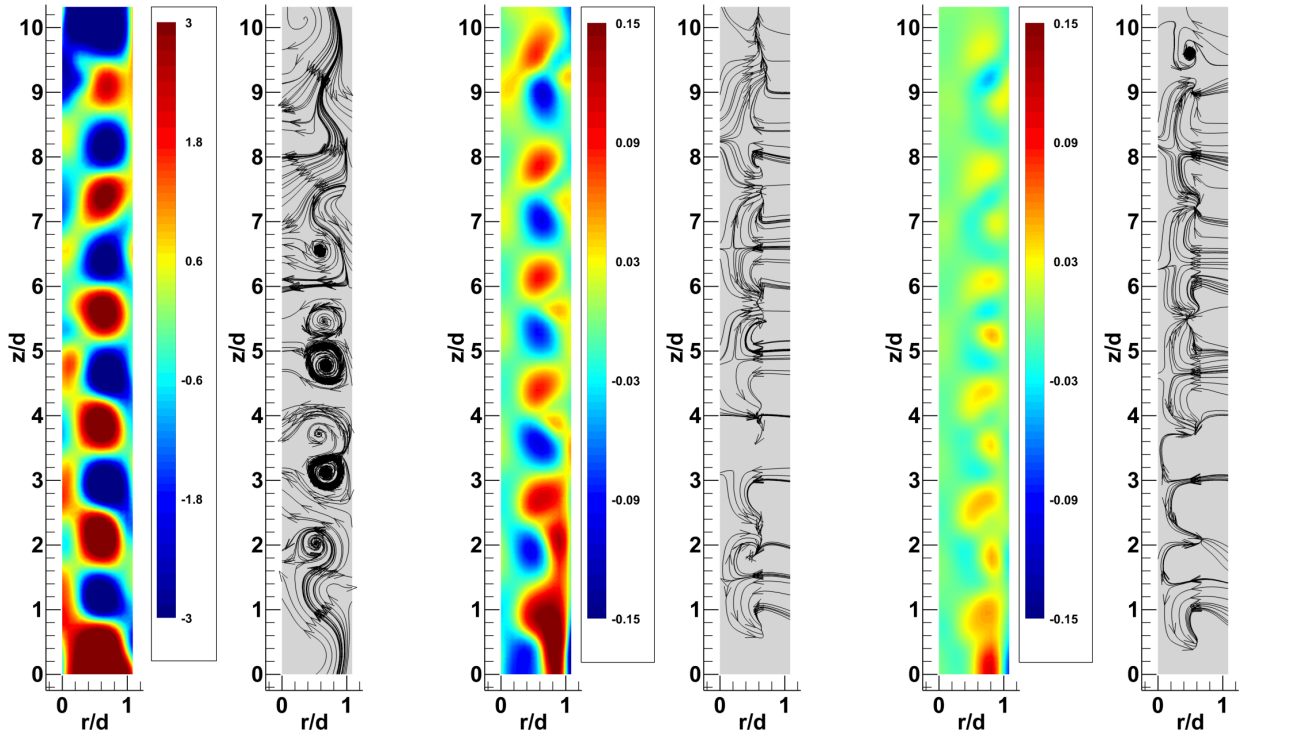

(a) $T_a = 3,360$ (b) $T_a = 3,360$ (c) $T_a = 15,170$ (d) $T_a = 15,170$ (e) $T_a = 35,485$ (f) $T_a = 35,485$

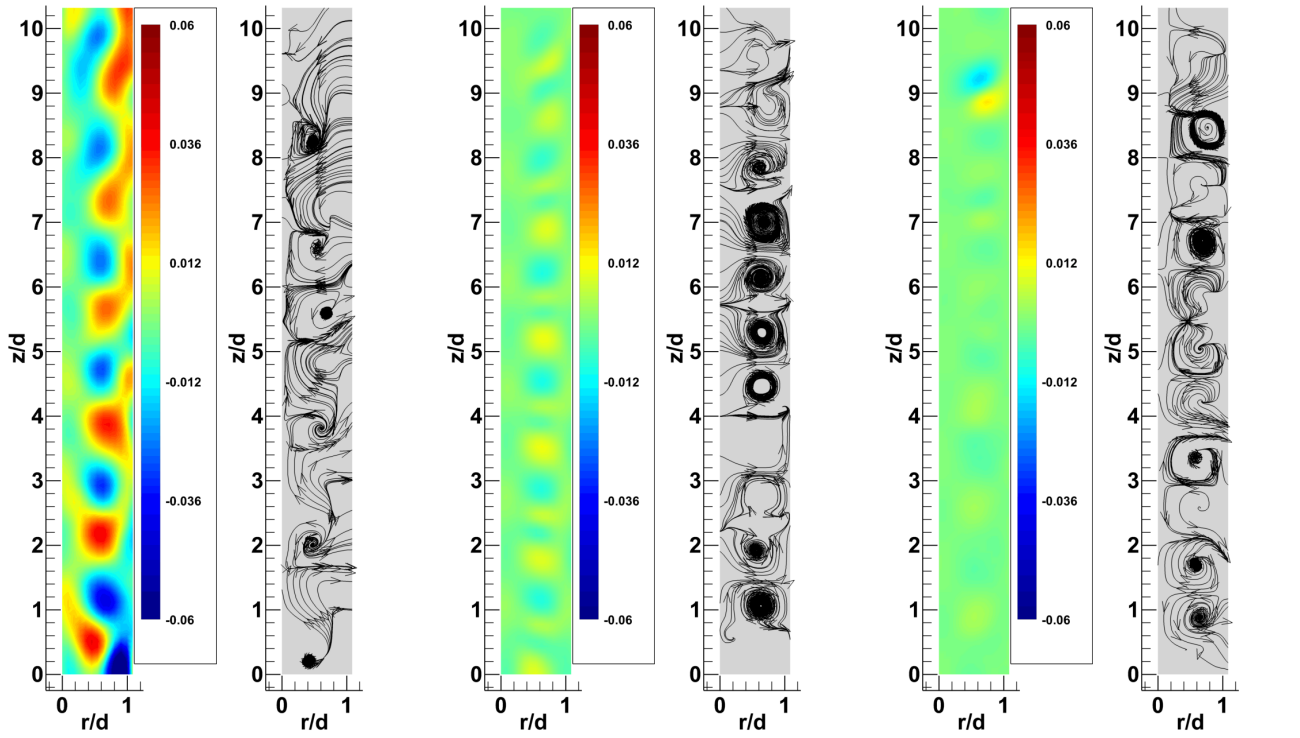

(g) $T_a = 3,360$ (h) $T_a = 3,360$ (i) $T_a = 15,170$ (j) $T_a = 15,170$ (k) $T_a = 35,485$ (l) $T_a = 35,485$

Figure 3.32: Taylor-Couette Zone-1 POD mode-1 (a-f) & mode-3 (g-l), non-dimensionalized vorticity $[\frac{\omega \hat{\mathrm{d}}}{2\Omega_I R_I}]$ & streamlines at $\Gamma_{ew} = 1$

around $T_a = 15,170$, which is noted to be the same point at which the weakly recirculating region in the central core was first seen to appear in the zone-2s mean flow. Results from the lower portion of the annular flow, Figures 3.29 and 3.31, however do not display this loss of TV structure at increasing Taylor numbers as previously sated. The most likely reason for this discrepancy was attribute to the higher momentum of fluid particles within the zone-2, which was noted to be orders of magnitude greater than that of the particles contained within the annular gap. This resulted in annular structures, specifically the Taylor vortices, being averaged out of the mean flow during POD calculations due to their lower energy content which in turn caused such structures to appear relatively negligible when compared to those contained within the zone-2.

POD results for the lower portion of the $\Gamma_{ew} = 1$ annulus at modes 1 and 3 are presented in Figures 3.30 and 3.32 were a general continuation of the mean flow patterns can be seen at lower Taylor numbers while more unique formations not seen to occur at either $\Gamma_{ew} = 0$ or $\Gamma_{ew} = 0.5$ are noted to appear at the higher end of the Taylor number test range. Figures 3.32 (a) and (b) clearly display the radial skew of WVF pairs and the increased flow encroachment from the zone-2 which caused the reduced vorticity seen in the vortex pairs between $z/\hat{d} = 11.25 - 7/6$. The non-dimensional vorticity at $T_a = 3,360$ is also notably higher in mode-1 than it was in the mean flow results, indicating that the increased aspect ratio resulted in a significant increase in energy transfer to the higher modes than that observed to occur at $\Gamma_{ew} = 0$ and 0.5. However, this energy transfer diminished as T_a increased as indicated by the greatly reduced vorticity values in Figures 3.32 (c) and (e). These plots also display an increases in both vortex skew and elongation predominantly between $z/\hat{d} = 0 - 4$ which occurred as T_a was increased. Figure 3.32 (e) also displays what appears to be the formation of additional Taylor cells between the preexisting cell were positive vortices, specifically in the range between $z/\hat{d} = 10.5 - 5$, are seen to be compressed with arcs of negatively circulating flow enveloping their left side. Additionally streamlines in both Figure 3.32 (d) and (f) show an axial flow reversal in the upper half of the annulus were

fluid appears to be have been drawn out of the annular gap as opposed to purely negative axial flow seen to occur in all $\Gamma_{ew} = 1.0$ mean flow results.

Results at mode-3 were also found to highlight the effects of the increased flow penetration noted to occur at $\Gamma_{ew} = 1.0$ where an elongation and a slight radial displacement all vortex pairs, especially in the area between $z/\hat{d} = 10.5 - 7$ where negative axial flow was noted to occur in the mean flow, can been seen in Figures 3.36 (g) and (h). Comparisons of the vorticity values in Figures 3.36 (g, i and k) show levels at $T_a = 3,360$ to be an order of magnitude greater than those at higher Taylor numbers similar to the trend previously described to occur in mode-1 results. However, unlike the results at mode-1 mode-3 plots showed a slight convergence towards $\Gamma_{ew} = 0$ higher modal results as T_a was increased. This is best exemplified by a comparison of Figures 3.27 (g-h) and 3.36 (i-j) where both aspect ratios resulted in a relatively uniform TV structure at mode-3 with an enhanced view of the inflow and outflow boundaries at $T_a = 35,485$.

At the largest aspect ratio of $\Gamma_{ew} = 1.5$ mean flow structural patterns began to diverge from the trends found to occur at $\Gamma_{ew} = 0.5$ & 1.0. Although, initial onset of Taylor vortices was still observed at $T_a = 3,360$ overall structure of the individual Taylor cells was found to be less coherent than those seen at lower aspect ratios. From Figures 3.35 (a-f) vortices can be seen to have a pronounced "S" shape and are noted to display a slight increase in the radial offset between vortex pairs. Interestingly flow interactions and fluid exchange between zone-2 and the annulus (zone-1) was found to be relatively reduced in the Taylor range between $1,312 - 10,289$ when compared to $\Gamma_{ew} = 0.5$ and 1.0 results. Additionally the interactions that were present within the mean flow were found to result in an axial reversal of fluid in the upper half of the annulus between $z/\hat{d} = 11.25 - 7.5$ where flow from zone-2 was seen to draw fluid out of the annular gap. This positive axial flow was a stark contrast to the purely negative axial encroachment that was seen to occur in the mean flow at $\Gamma_{ew} = 1$ and $\Gamma_{ew} = 0.5$. Reversal was attributed to the increased axial distance in zone-2s central core which resulted in reduced fluid momentum of the axially returning flow as it was drawn back

towards the rotating horizontal surface of the inner cylinder. Concurrently, this decrease in core momentum caused a reduction in the fluids radial momentum near the horizontal surface of the cylinder end wall. These reductions in momentum allowed for a smoother and more continuous circulation of zone-2s fluid mass and resulted in a sharper turning angle as radial flow encountered the outer cylinder near the zone-1/2 interface. This sharper turning angle at the interface resulted in less fluid diversion from zone-2 down into the annulus which caused annular circulations near the zone-1/2 interface to become dominant and ultimately resulted in the positive axial reversal in the region between $z/\hat{d} = 11.25 - 7.5$ as previously described. Additionally this increased linear length of radial flow at the domain interface acted as a pseudo end wall and allowed the upper most TV to behave in a manner similar to that of an end wall Ekman cell. From a comparison of Figures 3.28, 3.31 and 3.35 the smaller aspect ratios can be seen to have mean flow vorticity values approximately 55% less than those at $\Gamma_{ew} = 1.5$ for Taylor numbers between $T_a = 3,360 - 6,352$ however values at $\Gamma_{ew} = 0$ for the same T_a range are seen to be quite similar indicating that the sharper turning angle at the domain interface acted to stabilize the Taylor vortices along the entire annular length such that initial vortex formations were at $\Gamma_{ew} = 1.5$ were relatively close to those of the baseline.

Increases in T_a beyond $6,352$ resulted in a destabilization of the mean flow Taylor vortex structure as vortices began to take on a much more slanted appearance and had increases in both axial travel and vortical fluid exchange which in turn was found to ultimately result in a drastic reduction of TV vorticity. Increases beyond $T_a = 10,289$ were found to cause a continuation of this structural breakdown as well as ever increasing axial flow along the annular length. Unlike results at $\Gamma_{ew} = 1$ where plots showed Taylor vortices begin forced into the higher POD modes, particularly in Figures 3.20 - 3.21, this destabilization resulted in structured Taylor vortices disappearing form nearly all investigated modes. From Figure 3.35 (g) TVs are first seen to become chaotic at $T_a = 15,170$, and eventually disappear from the mean flow entirely at $T_a = 35,485$ (Figures 3.35 (k) and (l)). In fact at $35,485$ the flow

with in the annulus vaguely resembles the flow initially seen at $T_a = 1,312$, before the onset of Taylor vortices occurred.

POD results for $\Gamma_{ew} = 1.5$ were found to confirm the breakdown of Taylor vortices seen to occur in mean flow results. In the plots for both modes-1 and 3 presented in Figures 3.34 and 3.36 Taylor vortices are noted to be almost entirely absent; with one exception at $T_a = 3,360$ (Figures 3.36 (a), (b), (g) and (h)) where extremely weak vortex pairs can be seen. Figures 3.36 (b) and (g) also show what appear to be extremely small ($\approx 0.3\hat{d}$ in diameter) vortical sinks which formed along the wall of the stationary outer cylinder. The exact cause of these sinks was unclear, but from the rotational direction of their streamlines they were most likely the positive competent of a Taylor vortex pair which became compressed and displaced radially outward. At $T_a = 15,170$ and $35,485$ mode-1 plots displays a purely negative axial flow along the inner cylinder boundary between $z/\hat{d} = 0 - 5.5$ as seen in Figures 3.34 (b-c) and 3.36 (c-f). Mode-3 similarly shows large amounts of axial flow but was found to be more localized than the mode-1 results and appeared as elongated horizontally aligned vortex pairs (Figures 3.36 (i) and (k)). Increase in T_a showed these localized regions moving progressively in the positive axial direction, indicating that mass flow from the annulus (zone-1) into zone-2 became increased with increasing T_a and was most likely one of the main causes in the destabilization of Taylor vortices.

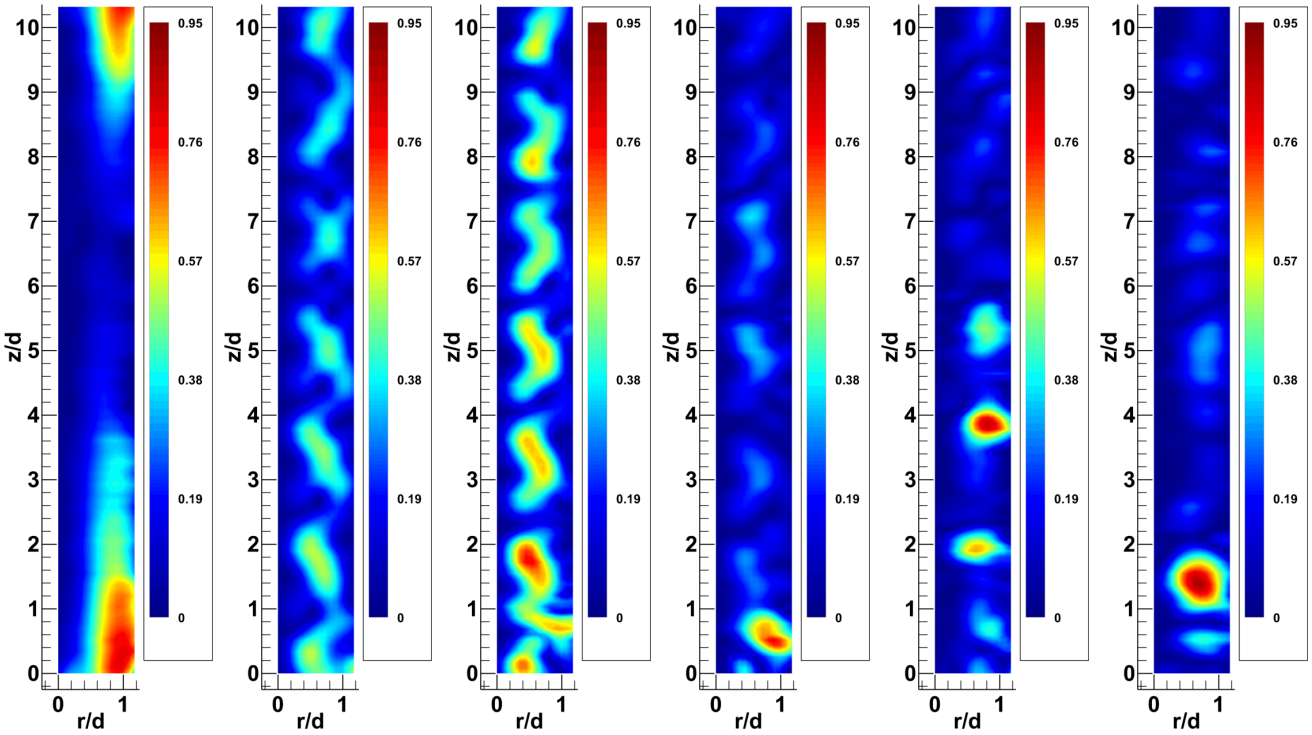

(a) $T_a = 1,312$ **(b)** $T_a = 3,360$ **(c)** $T_a = 6,352$ **(d)** $T_a = 10,289$ **(e)** $T_a = 20,997$ **(f)** $T_a = 35,485$

Figure 3.33: Taylor-Couette mean flow (POD mode-0 Zone-1), velocity contours at $\Gamma_{ew} = 1.5$

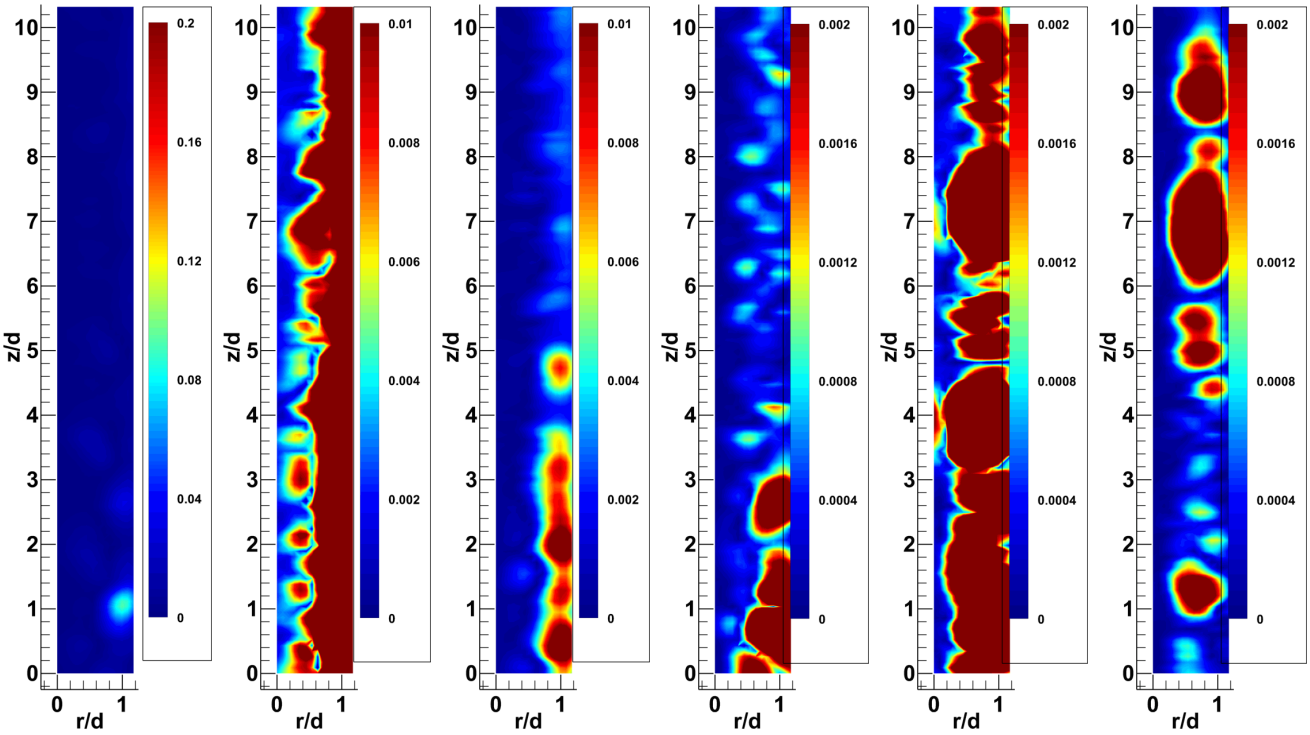

(a) $T_a = 3,360$ **(b)** $T_a = 15,170$ **(c)** $T_a = 35,485$ **(d)** $T_a = 3,360$ **(e)** $T_a = 15,170$ **(f)** $T_a = 35,485$

Figure 3.34: Taylor-Couette Zone-1 POD mode-1 (a-c) & mode-3 (d-f), velocity contours at $\Gamma_{ew} = 1.5$

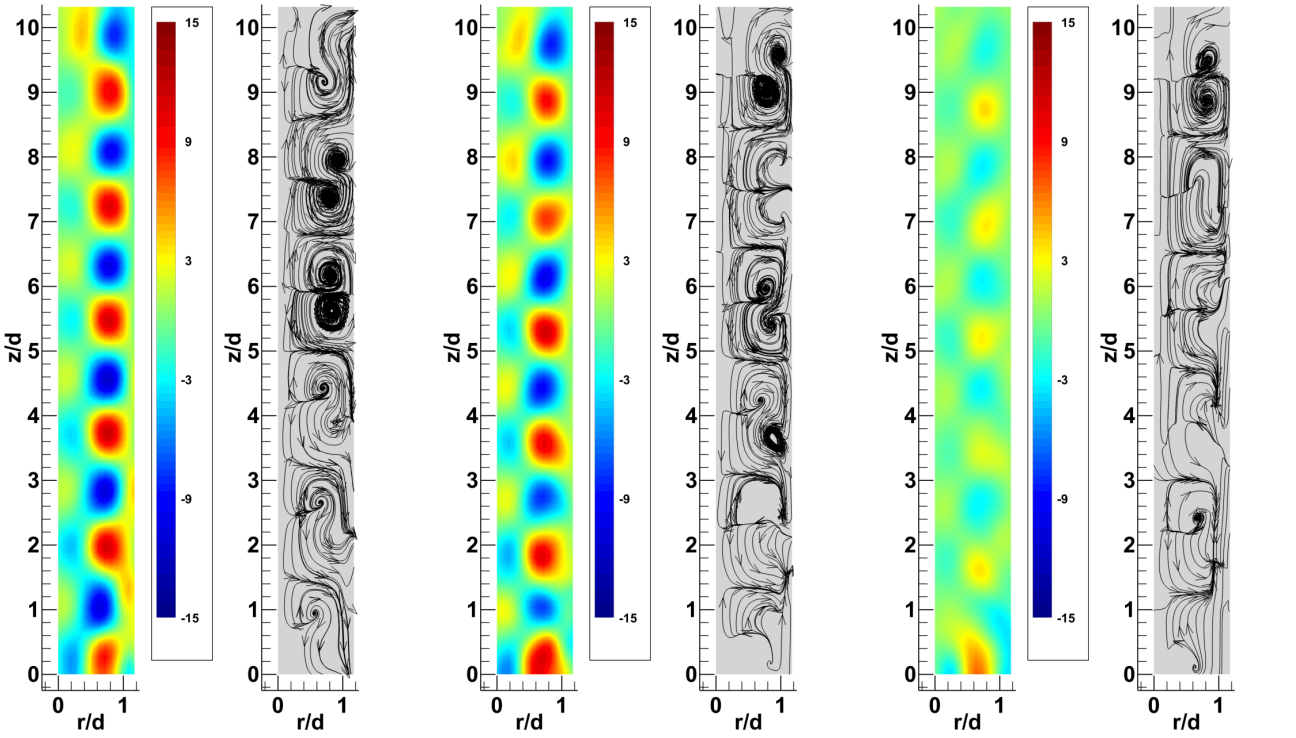

(a) $T_a = 3,360$ (b) $T_a = 3,360$ (c) $T_a = 6,352$ (d) $T_a = 6,352$ (e) $T_a = 10,289$ (f) $T_a = 10,289$

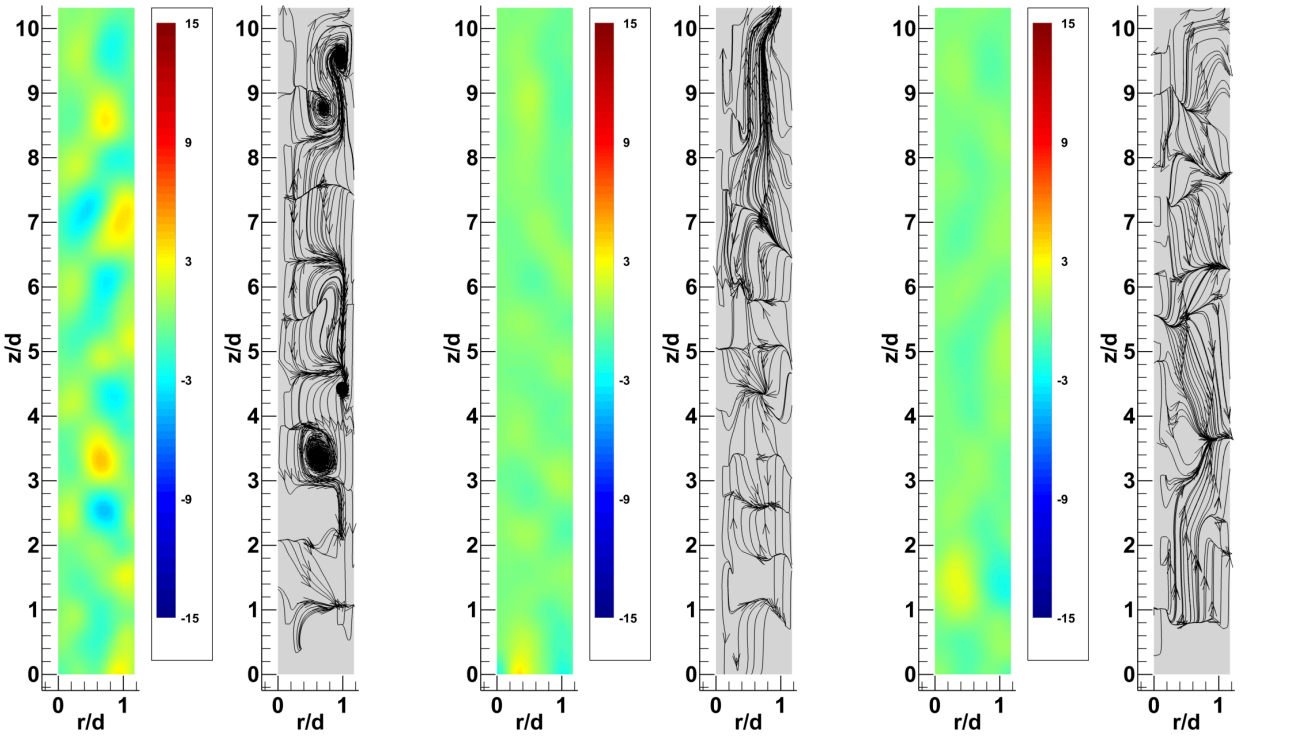

(g) $T_a = 15,170$ (h) $T_a = 15,170$ (i) $T_a = 27,769$ (j) $T_a = 27,769$ (k) $T_a = 35,485$ (l) $T_a = 35,485$

Figure 3.35: Taylor-Couette annular mean flow (POD mode-0 Zone-1), non-dimensionalized vorticity $[\frac{\omega \hat{\mathrm{d}}}{2\Omega_I R_I}]$ & streamlines at $\Gamma_{ew} = 1.5$

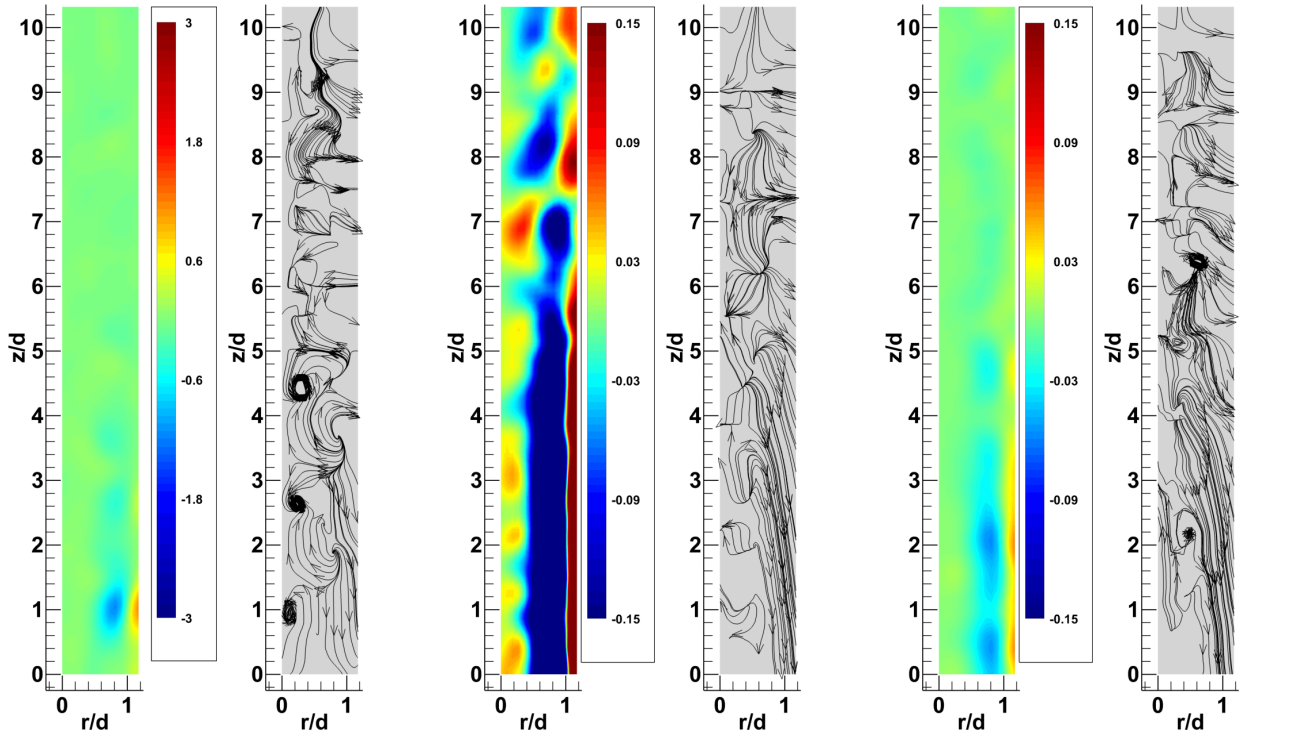

(a) $T_a = 3,360$ (b) $T_a = 3,360$ (c) $T_a = 15,170$ (d) $T_a = 15,170$ (e) $T_a = 35,485$ (f) $T_a = 35,485$

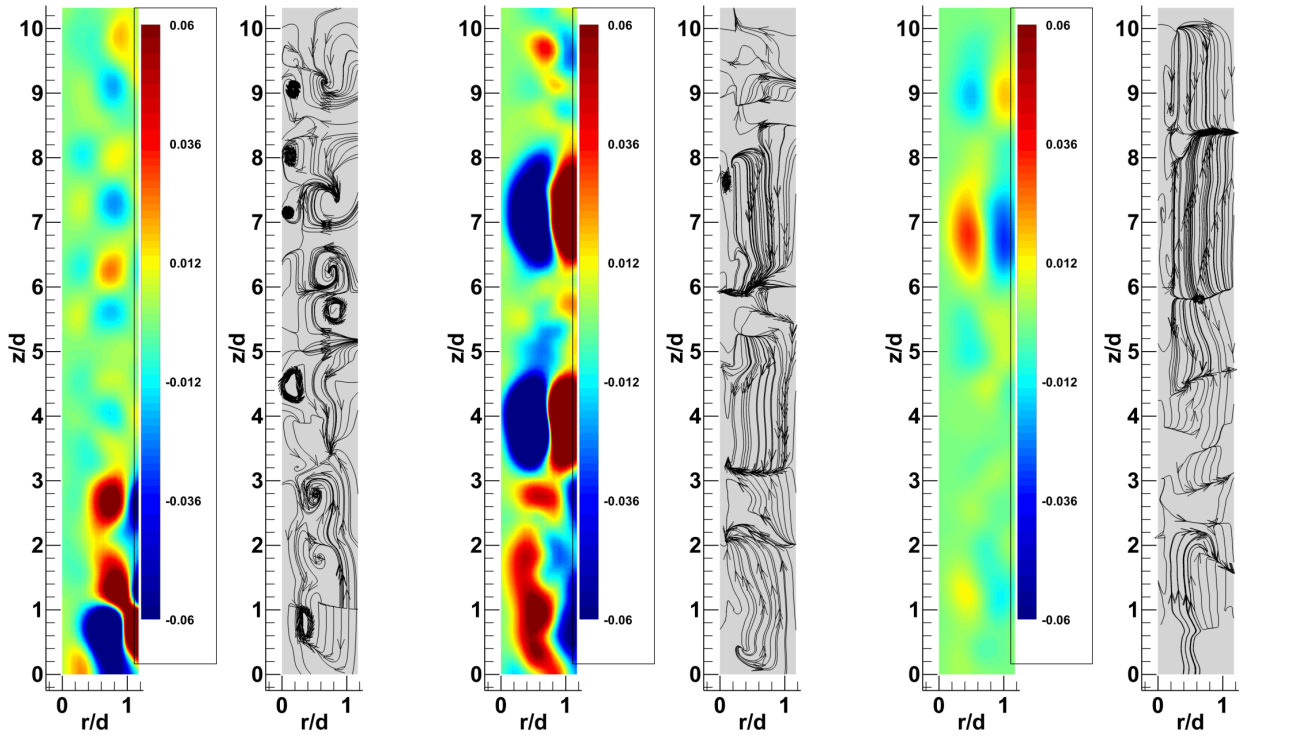

(g) $T_a = 3,360$ (h) $T_a = 3,360$ (i) $T_a = 15,170$ (j) $T_a = 15,170$ (k) $T_a = 35,485$ (l) $T_a = 35,485$

Figure 3.36: Taylor-Couette Zone-1 POD mode-1 (a-c) & mode-3 (d-f), non-dimensionalized vorticity $[\frac{\omega \hat{\mathrm{d}}}{2\Omega_I R_I}]$ & streamlines at $\Gamma_{ew} = 1.5$

3.2 Combined Flow Field

Investigations into the coupling of the two flow fields were conducted by taking PIV measurements of co-rotation and counter-rotation of the upper end-wall and inner cylinder. Aspect ratios of $0.5, 1, \&1.5$ were tested for both rotational cases. As with the TCF and VB test cases, a POD snapshot method was applied to the data in order to extract various modes from the fluctuating velocity components, enabling the identification of coherent structures contained within the more complex flow fields. Similarly modes-1 and 3 were reconstructed in order to obtain a more complete picture of the complex flow structures contained within the system. However due to the large number of additional figures required for this expand investigation plot for POD modes 1 and 3 are omitted from the body of the following sections and have instead been placed in appendices A-D to allow for better visualization and comparison.

3.2.1 Co-Rotation

Co-Rotational modal and cumulative energies are presented in Figures 3.38 - 3.41 Conditions in the zone-2 (Figures 3.38 and 3.39) were found to result in dramatic differences in modal energy compared to similar TCF and VB conditions; most notably at $\Gamma_{ew} = 1.5$. Cumulative distribution plots of Figures 3.38 (a) and 3.41 (a) show mean flow energy at $\Gamma_{ew} = 1.5$ varying from $\approx 0.66 - 0.44$ in the former and $\approx 0.77 - 0.24$ in the latter. This was found to result in an energy fluctuations 1.83 to 4.42 times greater than those of the TCF case and 2.25 to 6.65 times greater than the VB case; indicating a large increase in the amount of energy transferred to the smaller scales caused by co-rotation. These results also show that changes in end-wall rotation rate had greater influence on the energy transfer rate than cylinder changes. Spectral energies in Figures 3.38 (b) and 3.41 (b) also show that these effect were not confined to a few individual modes, as the entire modal curve is noted to be at elevated levels compared to TCF and VB conditions. $\Gamma_{ew} = 1$ was also found to have lower levels of mean flow energy than the TCF and VB cases by $\approx \frac{1}{2}$ and $\frac{2}{3}$ respectively.

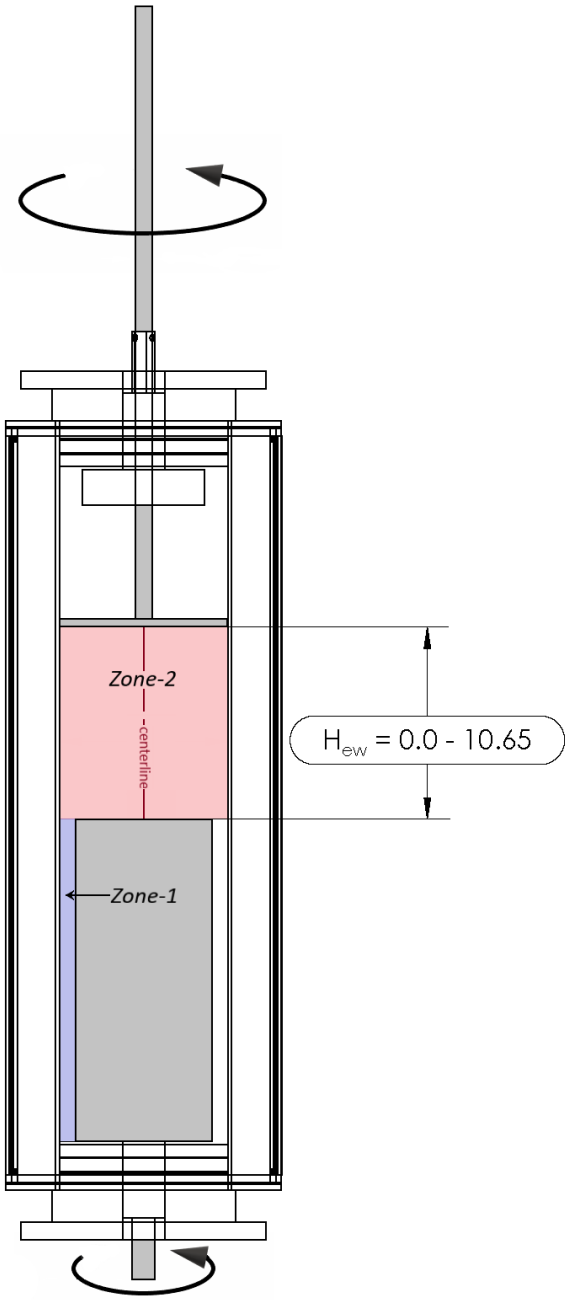

Figure 3.37: Configuration of Co-Rotational test case

However unlike $\Gamma_{ew} = 1.5$, the variability in this energy range was found to be effected more by changes in cylinder rotation rather than end-wall rotation. Individual modal energies for Γ_{ew} display increased levels between modes 2 and 3 especially at lower $T_a/R_{e_{ew}}$ values (Figures 3.38 (b) and 3.41 (b)). Similar increases can be seen for $\Gamma_{ew} = 0.5$ where mode-3 specifically is seen to show a spike in energy. Conversely mean flow energies were found to be relatively similar to TCF results and like wise had higher values and lower variability than the VB case.

Energy plots for co-rotational annular flow were found to be more congruent with TCF results than those of the zone-2. Cumulative energy distributions presented in Figures 3.40 (a) and 3.41 (a) show a similar drop in mean flow energy at $\Gamma_{ew} = 1.5$ that was seen in the TCF energy results. As with zone-2 results this reduction in mean flow energy was noted to be greater than the baseline results where for increasing T_a values co-rotation mean flow energies had reductions of 26% at $T_a = 3,360$ and 76% at $T_a = 35,485$, while at $T_a = 15,170$ mode-0 energy was found to be almost identical to TCF results. Modal spectrum plots presented in Figures 3.40 (b) and 3.41 (b) also show $\Gamma_{ew} = 1.5$ modes 1-14 with energy levels significantly elevated relative to $\Gamma_{ew} = 0.5$ and $\Gamma_{ew} = 1.0$ modes. Additional these individual modal energies for all aspect ratios were found to be slightly elevate when compared to TCF results in the range between mode-1 and mode-4. Modes beyond mode-4 energy levels for $\Gamma_{ew} = 0.5$ and $\Gamma_{ew} = 0.5$ were found to have a rapid decay, while $\Gamma_{ew} = 1.5$ modal energies remained elevated. At TCF conditions beyond mode-9 all modal energies were found to be less than 1% of the total flow, co-rotational $\Gamma_{ew} = 1.5$ energies however were not found to fall below 1% until $\approx\ mode - 11/12$; for both changes in T_a and $R_{e_{ew}}$. Comparisons of Figures 3.40 and 3.41 show the expected result of energy fluctuations within the annulus being driven predominantly y changes in T_a rather than $R_{e_{ew}}$. However Figure 3.41 (a) does show indications of increases in $R_{e_{ew}}$ actually resulting in increased energy transfer from smaller scales back to larger ones, where for Γ_{ew} $T_a = 15,170$ $R_{e_{ew}} = 2,929$ mean flow energy is seen to be higher than $T_a = 15,170$ at lower $R)e_{ew}$ values. This result indicated that at certain

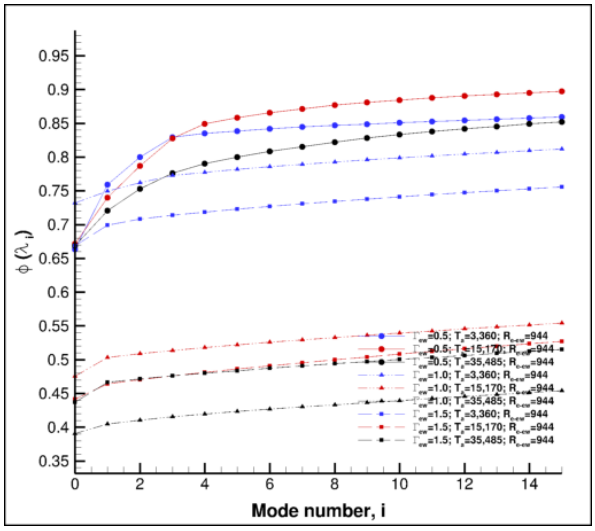

(a) cumulative distribution

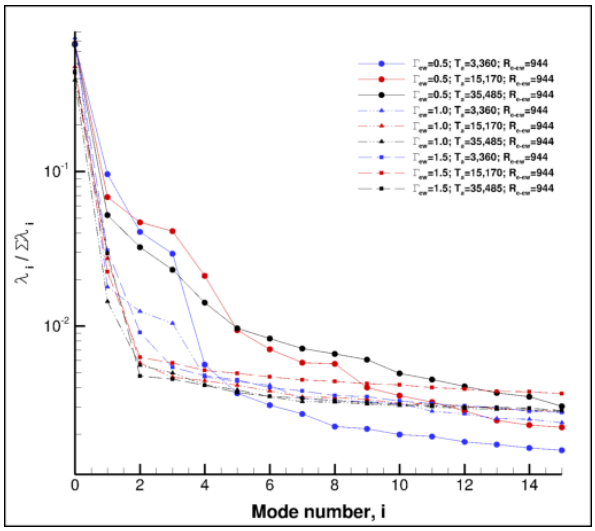

(b) POD spectrum, modes 0-15

Figure 3.38: Co-rotational zone-2 energy distribution for increasing T_a

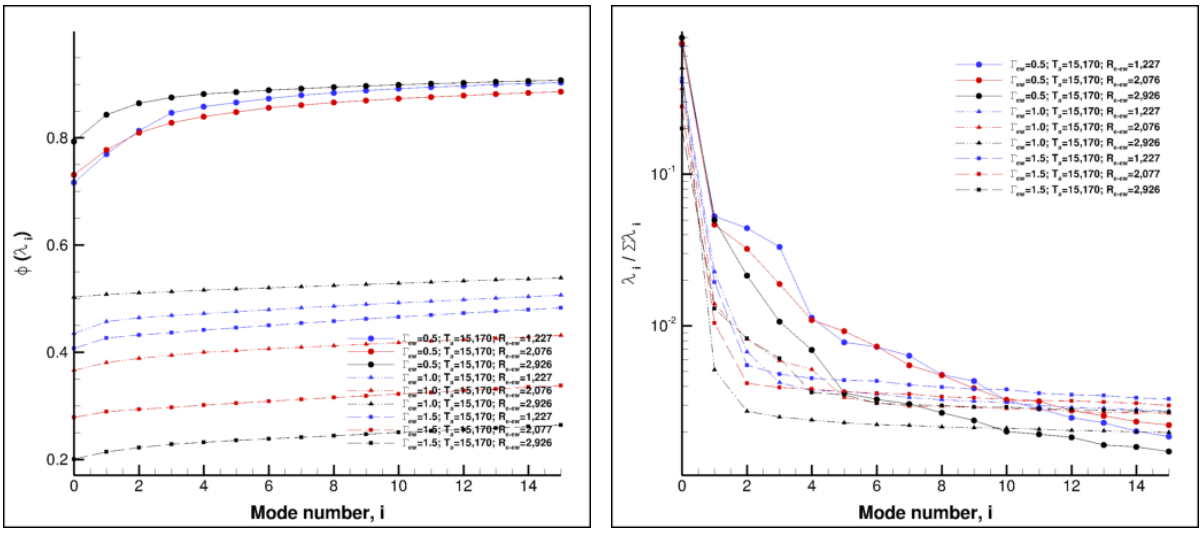

(a) cumulative distribution **(b)** POD spectrum, modes 0-15

Figure 3.39: Co-rotational zone-2 energy distribution for increasing $R_{e_{ew}}$

T_a / $R_{e_{ew}}$ combinations small scale perturbations may have become dampened resulting in slightly more stable flow at the larger scales.

Mean flow contour plots, and streamlines for the co-rotation case at $\Gamma_{ew} = 0.5$ are presented in Figures 3.42 - 3.44. These results show quite a significant change in flow characteristics compared to the TCF results previously discussed. Two of the most significant differences were the flow reversals which occurred with in the central core of the zone-2 and the annulus. Near the domain interface at the top of the annulus flow was drawn out of the annular gap by zone-2 circulation. Unlike the positive axial flow which was only seen to occur in the upper half of the annulus as an vortical fluid exchange at TCF,$\Gamma_{ew} = 1.5$, the positive axial flow in the present case was seen to merge into the returning flow of the zone-2s central core. It was also noted that this effect was only present in the upper most portion of the annulus, in the area between $z/\hat{d} \approx 8 - 11.25$. Reversal to a positive axial flow in the zone-2s central core was not entirely unexpected, due to the initially higher Reynolds number of the upper end-wall at the lower end of the T_a test range. However unlike the VB case flow in this region was not seen to be parallel to the axis of rotation as it is in Figure 3.9; but was in-fact skewed in a similar manner as that seen in the TCF case. As $R_{e_{ew}}$ was increased and

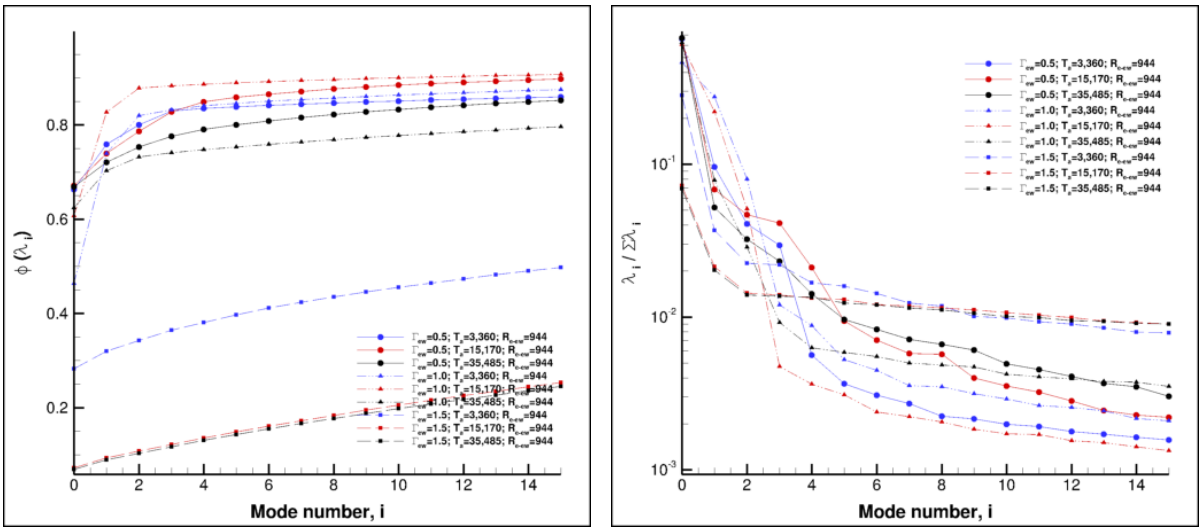

(a) cumulative distribution **(b)** POD spectrum, modes 0-15

Figure 3.40: Co-rotational annular POD energy distribution for increasing T_a

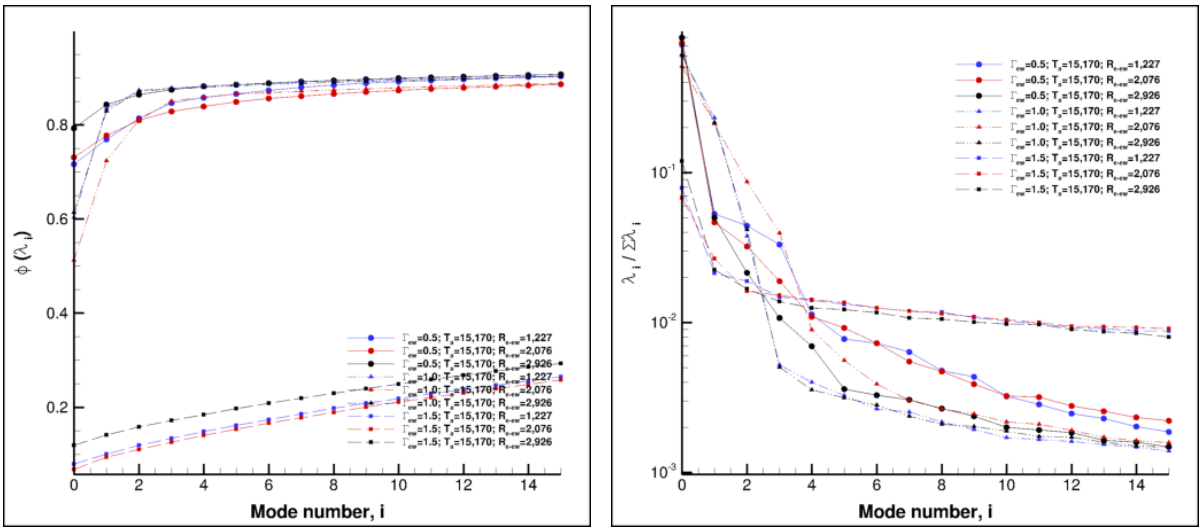

(a) cumulative distribution **(b)** POD spectrum, modes 0-15

Figure 3.41: Co-rotational annular POD energy distribution for increasing $R_{e_{ew}}$

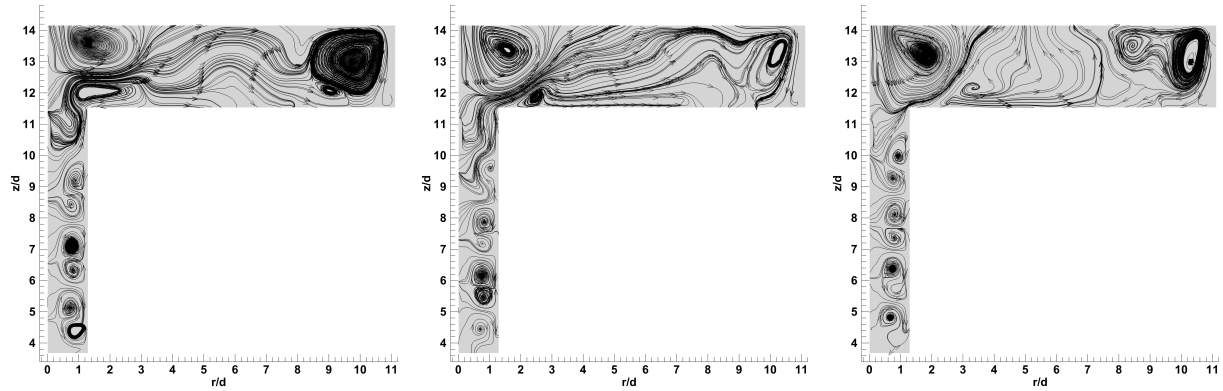

(a) $T_a = 6,352$ $R_{e_{ew}} = 944$ **(b)** $T_a = 6,352$ $R_{e_{ew}} = 2,076$ **(c)** $T_a = 6,352$ $R_{e_{ew}} = 2,926$

Figure 3.42: Co-rotational mean flow streamlines, for varying T_a at $\Gamma_{ew} = 0.5$

T_a held constant, the severity of this radial asymmetry was reduced. Eventually this resulted in core flow traveling parallel to the rotational axis, as the positive axial pull of the end-wall began to dominate. While this effect is seen in the streamline plots of Figure 3.42, it was not seen to occur at the higher T_a numbers of Figure 3.52. Indicating that above $T_a = 6,352$ effect produced by the rotation of the inner cylinder began to dominate, preventing the flow within the central core from becoming parallel to the Z axis.

Taylor vortex formation was also seen to be effected by the co-rotation of the upper end-wall. Initial formation occurred around $T_a = 3,360$ as it did for the TCF case. However there was a slight reduction in the number of observable vortex pairs; where ≈ 3.75 are seen in Figure 3.28(a) while only 3 are visible in Figure 3.43(a). TVs in Figure 3.43 also display a slightly elongated shape, and are not seen to exhibit the same slanted triangular shape nor the unbalance size between pairs that occurred at TCF, $\Gamma_{ew} = 0.5$. Vorticity plots also show that co-rotation resulted in Taylor vortices with slightly reduced vorticity values; differences between the co-rotation and baseline TV vorticity were seen to increase as axial distance from the top of the annulus also increased. As $R_{e_{ew}}$ was increased and T_a held constant, the vorticity of the Taylor vortices further decreased. At the two lowest Taylor numbers of $1,312$ and $3,360$ there was a point where flow from the zone-2 was observed flowing down into the annulus as opposed to flow begin drawn out. This occurred at $R_{e_{ew}} = 2,360$ and

$R_{e_{ew}} = 2,926$ respectively. For $T_a = 3,360$ this resulted in a drastic deformation of TVs along eh entire annular length, such that they were seen to all but disappear from the mean flow plots of Figures 3.43 and 3.44. As Taylor number was increased beyond $3,360$ this negative axial reversal of flow from the upper field was not seen to occur due to the increased vorticity of TVs within the annulus, and the increased strength of the flow produced in the zone-2.

At the lowest $R_{e_{ew}}$ number of 944 for the T_a range of $3,360 - 35,485$, the vortex at the very top of the annulus was seen to be displaced in the positive axial direction such that a gap formed between the upper most vortex pair. It was also noted that this upper TV had a negative slant, and a large amount of fluid exchange with the zone-2s lower corner vortex; taking on the appearance of an unbalanced vortex pair in some cases. As $R_{e_{ew}}$ was further increased end-wall driven flow began to slowly dominate the circulation produced by the cylinder in the zone-2. Once end-wall circulation became large enough it began to compress the lower corner vortices such that they were no longer circular, but were instead of the radially elongated form seen in Figure 3.44 (f). It was at this point that Taylor vortex position was found to shift in the positive axial direction, becoming slightly more elongated and causing a reduction in the number of visible vortex pairs by $\approx 0.5 - 1$. Further increases in $R_{e_{ew}}$ eventually resulted in the upper end-wall completely dominating these cylinder driven vortices to such an extent that they no longer presented any kind of barrier into the annulus. This resulted in an increased amount of fluid being drawn out of the annulus effectively destroying the upper most TV in the range of $z/\hat{d} \approx 8.25 - 11.25$ and greatly reducing the vorticity of the vortices further down within the annulus. This occurred at $3,360 \leq T_a \leq 20,997$. For $T_a \geq 27,769$ however flow produced by rotation of the inner cylinder became strong enough to oppose the forces produced by the rotating end-wall, resulting in continuously stable Taylor vortices within the entire annular length of the mean flow.

POD plots for mode-1 and mode-3, presented in Figures A.1 - A.4 of appendix A, were found to greatly highlight some of the mean flow trends described above. Unlike TCF

POD modal plots for $\Gamma_{ew} = 0.5$, co-rotational results displayed an overwhelming amount of structured flow formations; a few of which will be discussed in the flow text. Most notably the formation of recirculation zones within the core of the zone-2 and the effect of axial flow reversal in the annulus on TV structure. From Figure A.2 (f) streamlines display a large pocket of recirculating flow in the zone-2s core. Unlike the higher modal results at VB conditions this recirculation was not constrained to a small region near the rotating surface but instead occupied the entire axial distance between cylinder and end-wall surfaces. While Figure A.1 (f) A is the best example of this co-rotation induced core circulation it was not the only one, Figures A.2 (e-f) and (h-i) show indications of it as well. Vorticity results at varying $R_{e_{ew}}$ values of the aforementioned plots show that circulation was much higher and of an opposing direction to that of the varying T_a results, indicating that circulation was influenced more by changes in end-wall rotation than changes in the cylinder. Mode-1 streamlines also show complex interactions between end-wall and cylinder driven side wall vortices appearing to compress and displace one another resulting in similarly rotating vortice appearing side by side in the zone-2. Mode-3 (Figures A.3 and A.4) displayed similar interactions between end-wall and cylinder driven corner vortices but was found to lack any overt signs of the core recirculation seen at mode-1.

Annular results at modes-1 3 clearly show the effects of the positive axial flow seen in the mean flow plots and unlike the higher modal result of the TCF tests TV formation was clearly visible for the vast majority of contours and streamlines. In many cases mode-1 displayed annular flow that was nearly identical to mean flow results (Figure A.2), others such as Figure A.1 (h) however give indications that Taylor vortex formation may have been less stable than mean flow results suggest. Vorticity and streamline plots at mod-3 can be seen to confirm this instability, Figures A.3 (h/i) and A.3 (e/f) clearly show that the axial flow between the annulus and the zone-2 resulted in axial stretching of the Taylor vortices. Interestingly though this elongation occurred on one vortex in a pair at a time resulting in dash dot dash like pattern within the annulus. Additional this was found to not only occur

at higher values of $R_{e_{ew}}$ but also at the higher T_a values, even when $R_{e_{ew}}$. This suggest that axial flow effects were not as end-wall depended as initially believed.

For the $\Gamma_{ew} = 1$ test case, results showed quite a large divergence form those of its respective baseline, especially in the zone-2. One of the most notable differences was the increased diameter of the central vortex which was found to be approximately $2d$ wider at the cylinder surface for $T_a = 1,312$ specifically; a trend that was observed at all T_a *and* $R_{e_{ew}}$ combinations. Figure 3.45 (c) shows the initial formation of the combined circulation of both the end-wall and cylinder, where an unbalanced four roll mill like structure with counter rotating vortices in the four corners of the zone-2 can be seen. This formation was more prevalent, and more coherent at this larger aspect ratio, than that observed at $\Gamma_{ew} = 0.5$. As with the lower aspect ratio case, increases in $R_{e_{ew}}$ resulted in end-wall driven circulation progressively dominating and compressing that of the cylinder. In the zone-2 maximum vorticity was also noted to be larger than either the TCF or VB cases at $\Gamma_{ew} = 1$. Most likely this was due to the wider central core which acted to radially compress the zone-2s corner vortices against the outer cylinder; effectively constricting the volume without any reduction in mass transport. This effect was compounded by the manner in which the two flows interacted at the stationary wall of the outer cylinder. At this interface the two flows meet at a glancing angle, resulting in very little momentum loss for either. When combined Reynolds numbers reached $R_{eew} + R_{e_{tc-vb}} \approx 2,500$ cylinder and end-wall driven circulations began to merge in the area between the central core and side wall. Eventually this resulted in an extremely unstructured and turbulent flow in the zone-2 that became increasingly more chaotic as either T_a or $R_{e_{ew}}$ increased.

In Figure 3.46(c) a large negative vortex can be seen in the central core near the upper end-wall. This vortex was observed at all Taylor numbers above $1,312$. Observations also showed that it had a negative axial movement, accompanied by a positive radial displacement in many instances, as $R_{e_{ew}}$ increased. At higher T_a numbers a companion vortex was seen to form directly below this large central vortex. Figures 3.46(h) and (i) display the first initial

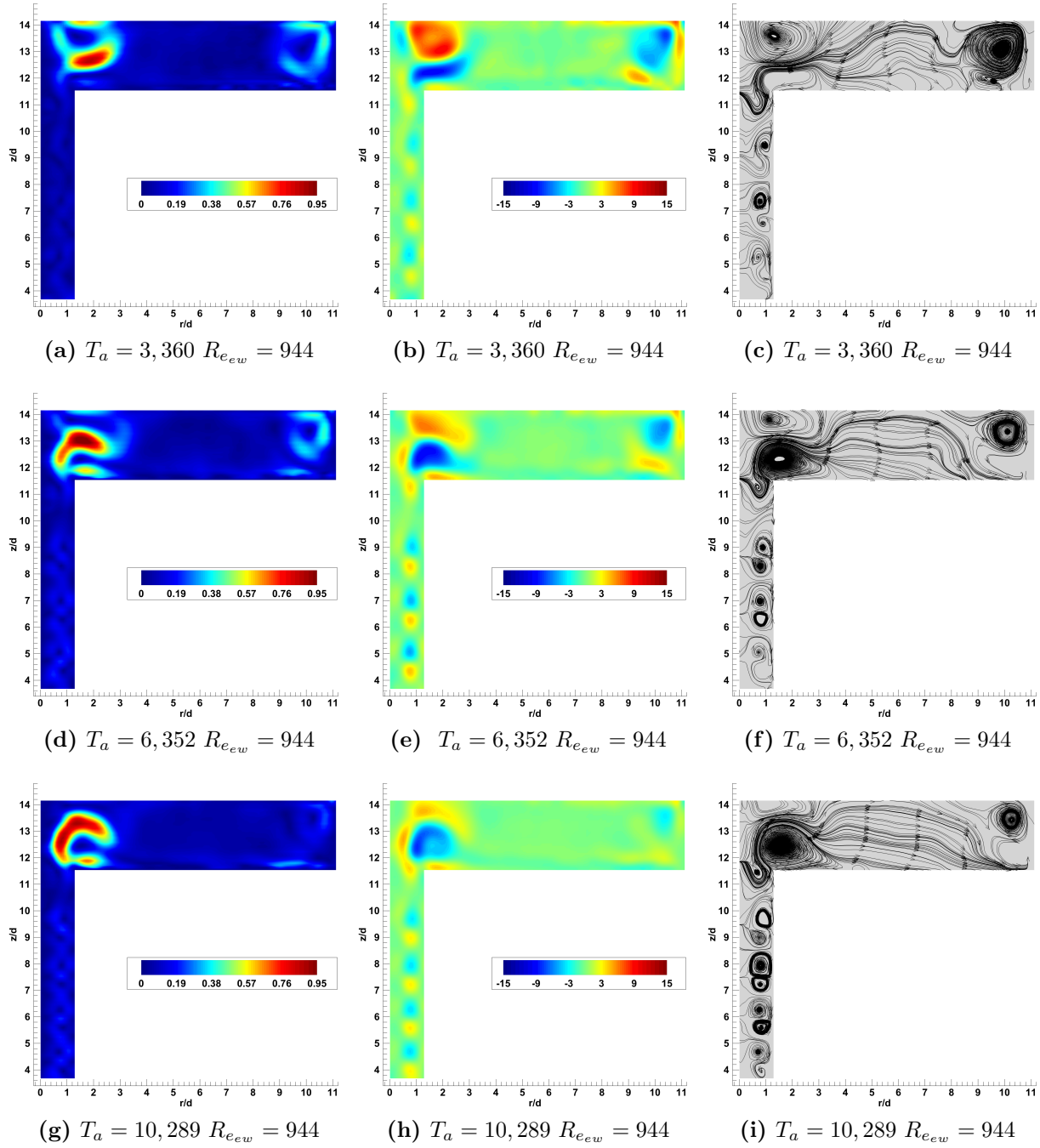

(a) $T_a = 3,360$ $R_{e_{ew}} = 944$ **(b)** $T_a = 3,360$ $R_{e_{ew}} = 944$ **(c)** $T_a = 3,360$ $R_{e_{ew}} = 944$

(d) $T_a = 6,352$ $R_{e_{ew}} = 944$ **(e)** $T_a = 6,352$ $R_{e_{ew}} = 944$ **(f)** $T_a = 6,352$ $R_{e_{ew}} = 944$

(g) $T_a = 10,289$ $R_{e_{ew}} = 944$ **(h)** $T_a = 10,289$ $R_{e_{ew}} = 944$ **(i)** $T_a = 10,289$ $R_{e_{ew}} = 944$

Figure 3.43: Co-rotational mean flow, velocity profile (left), non-dimensionalized vorticity $[\frac{\omega \hat{\mathbf{d}}}{2\Omega_I R_I}]$ (middle), streamlines (right), for varying T_a at $\Gamma_{ew} = 0.5$

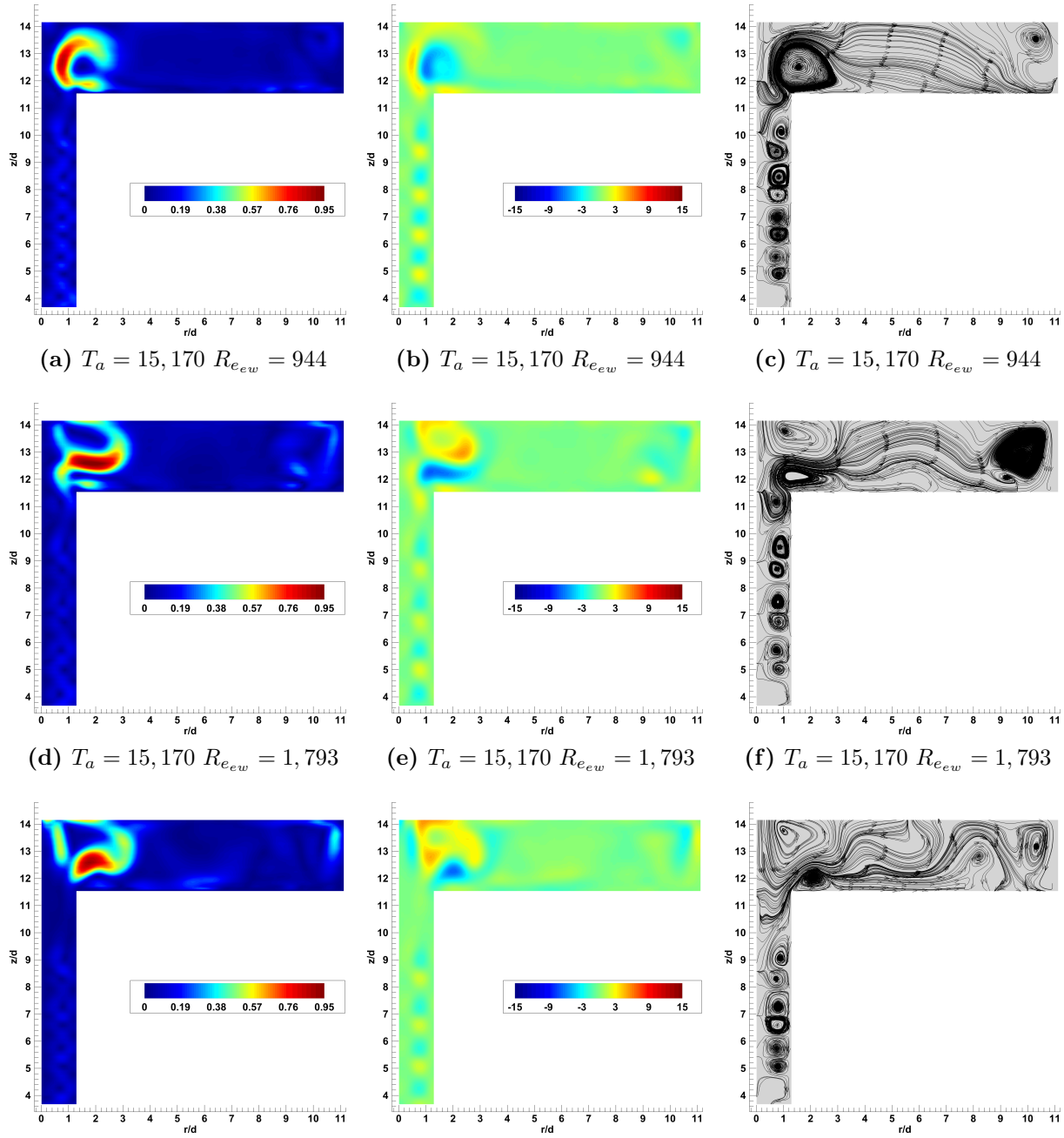

(a) $T_a = 15,170$ $R_{e_{ew}} = 944$ **(b)** $T_a = 15,170$ $R_{e_{ew}} = 944$ **(c)** $T_a = 15,170$ $R_{e_{ew}} = 944$

(d) $T_a = 15,170$ $R_{e_{ew}} = 1,793$ **(e)** $T_a = 15,170$ $R_{e_{ew}} = 1,793$ **(f)** $T_a = 15,170$ $R_{e_{ew}} = 1,793$

(g) $T_a = 15,170$ $R_{e_{ew}} = 2,926$ **(h)** Vorticity $T_a = 15170$ $R_{e_{ew}} = 2,926$ **(i)** $T_a = 15,170$ $R_{e_{ew}} = 2,926$

Figure 3.44: Co-rotational mean flow, velocity profile (left), non-dimensionalized vorticity $[\frac{\omega \hat{\mathbf{d}}}{2\Omega_I R_I}]$ (middle), streamlines (right), for varying $R_{e_{ew}}$ at $\Gamma_{ew} = 0.5$

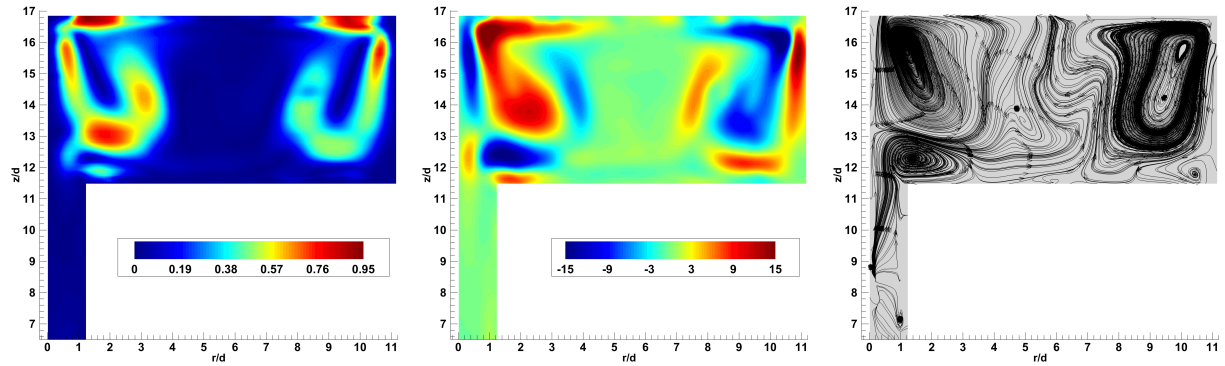

(a) $T_a = 1,312,\ R_{e_{ew}} = 944$ **(b)** $T_a = 1,312,\ R_{e_{ew}} = 944$ **(c)** $T_a = 1,312,\ R_{e_{ew}} = 944$

Figure 3.45: Co-rotational mean flow, velocity profile (left), non-dimensionalized vorticity $[\frac{\omega \hat{\mathbf{d}}}{2\Omega_I R_I}]$ (middle), streamlines (left), at $\Gamma_{ew} = 1$

formation of this lower central vortex at $T_a = 10,289$, which is seen to be less structured and of a much lower vorticity than the one above. As $R_{e_{ew}}$ was increased this lower vortex was quickly over powered disappearing from the mean flow in both streamline and vorticity plots. There were instances, such as that displayed in Figure 3.47(i), where a positive vortex was seen to reform in the upper half of the core. In fact through out the test range a multitude of various recirculating regions were observed in the central core. Generally these regions were found to be unstable, randomly appearing and disappearing from the mean flow. As with the $\Gamma_{ew} = 1$ TCF case these recirculating zones seemed to indicate that some form of weak VBB like structure does forms in the central core. However due to the turbulent interaction of cylinder and end-wall driven circulation near the stationary side walls and the adversarial nature of the axial flow it was extremely unstable.

Investigations into the annular flow at $\Gamma_{ew} = 1$ showed that the initial onset of TVs was significantly affected by the additional co-rotation of the upper end-wall. While counter rotating vortices did form in the annulus at $T_a = 3,360$ their vortical strength was found to be approximately half of that seen in the $\Gamma_{ew} = 1$ TCF case. Structural formation of the vortices was also affected, taking on highly elongated shapes that were approximately 30% larger than those of the baseline. This elongation, as well as a radial offset between positively and negatively rotating vortices, became more pronounced as axial distance decreased. In

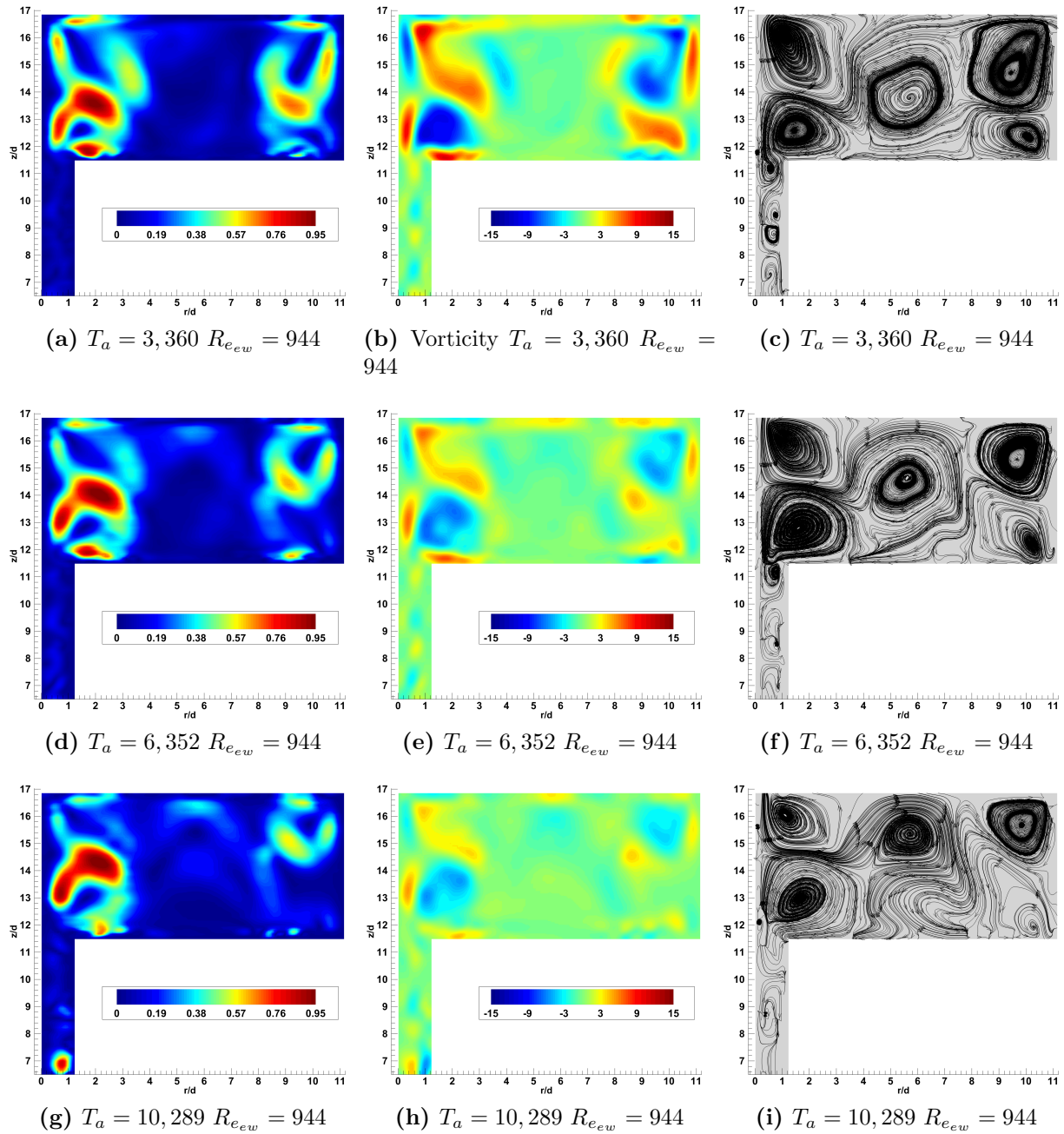

(a) $T_a = 3,360$ $R_{e_{ew}} = 944$ **(b)** Vorticity $T_a = 3,360$ $R_{e_{ew}} = 944$ **(c)** $T_a = 3,360$ $R_{e_{ew}} = 944$

(d) $T_a = 6,352$ $R_{e_{ew}} = 944$ **(e)** $T_a = 6,352$ $R_{e_{ew}} = 944$ **(f)** $T_a = 6,352$ $R_{e_{ew}} = 944$

(g) $T_a = 10,289$ $R_{e_{ew}} = 944$ **(h)** $T_a = 10,289$ $R_{e_{ew}} = 944$ **(i)** $T_a = 10,289$ $R_{e_{ew}} = 944$

Figure 3.46: Co-rotational mean flow, velocity profile (left), non-dimensionalized vorticity $[\frac{\omega \hat{\mathbf{d}}}{2\Omega_I R_I}]$ (middle), streamlines (right), for varying T_a at $\Gamma_{ew} = 1$

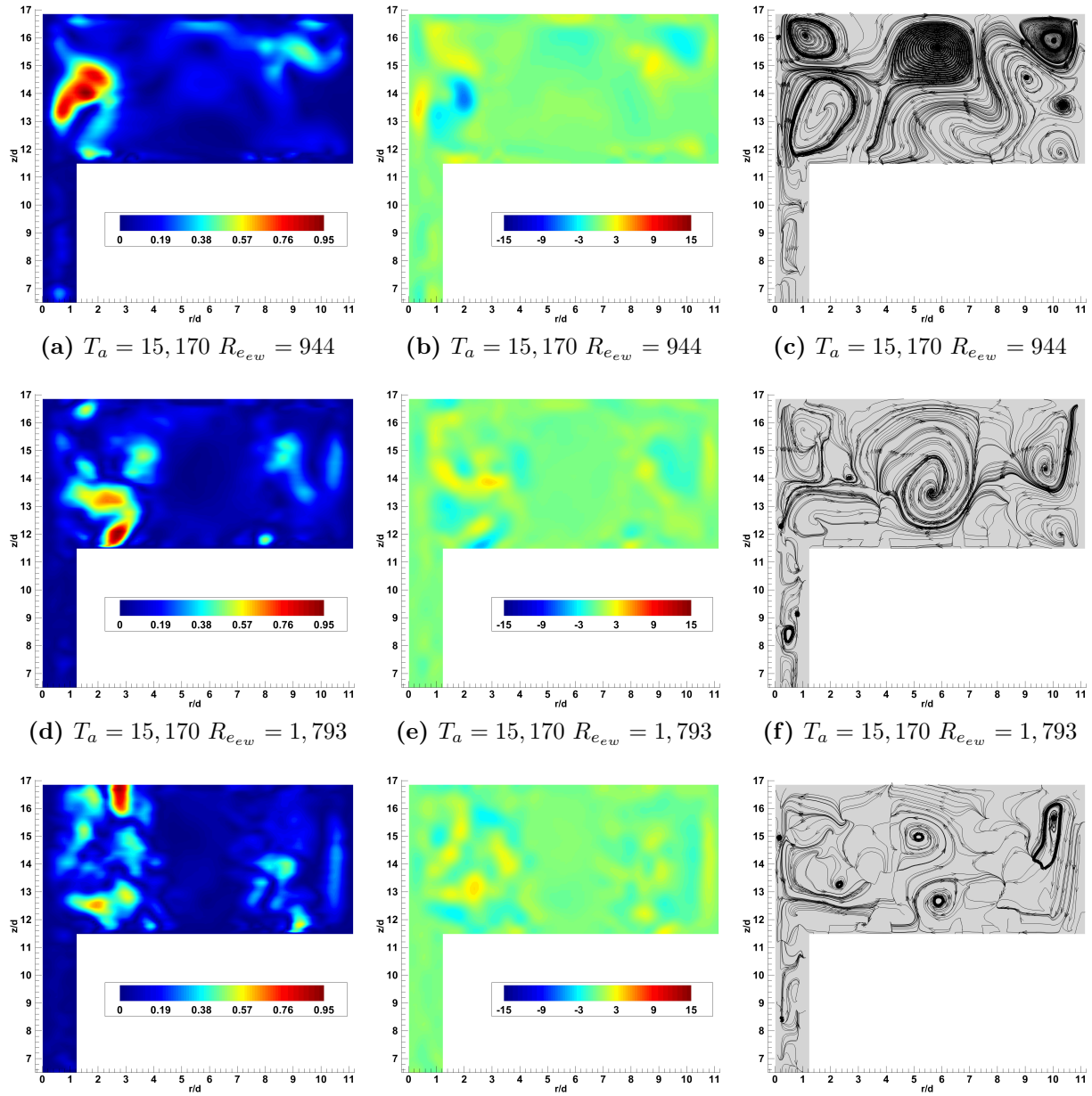

(a) $T_a = 15,170$ $R_{e_{ew}} = 944$ **(b)** $T_a = 15,170$ $R_{e_{ew}} = 944$ **(c)** $T_a = 15,170$ $R_{e_{ew}} = 944$

(d) $T_a = 15,170$ $R_{e_{ew}} = 1,793$ **(e)** $T_a = 15,170$ $R_{e_{ew}} = 1,793$ **(f)** $T_a = 15,170$ $R_{e_{ew}} = 1,793$

(g) $T_a = 15,170$ $R_{e_{ew}} = 2,926$ **(h)** $T_a = 15,170$ $R_{e_{ew}} = 2,926$ **(i)** $T_a = 15,170$ $R_{e_{ew}} = 2,926$

Figure 3.47: Co-rotational mean flow, velocity profile (left), non-dimensionalized vorticity $[\frac{\omega \hat{\mathbf{d}}}{2\Omega_I R_I}]$ (middle), streamlines (right), for varying $R_{e_{ew}}$ at $\Gamma_{ew} = 1$

Figures 3.49 (a) & (b), between $z/\hat{d} \approx 0-4$, this radial offset is seen to be the most sever; producing Taylor vortices with a sinusoidal shape. As $R_{e_{ew}}$ was increased for $T_a = 3,360$ the radial offset of TVs remained in the lower half of the annulus, while TV from $z/\hat{d} = 6-10.25$ were seen to become slightly compressed as they moved in the negative axial direction.

Beyond $T_a = 3,360$ Taylor vortex formation took on a more familiar form. Figures 3.49 $(c)-(l)$ show six observable vortex pairs within the annulus. This number was found to remain constant for all T_a numbers tested between $6,352-35,485$, and at all coupled $R_{e_{ew}}$ numbers. These results were congruent with those at TCF $\Gamma_{ew} = 1$. Unlike the baseline case however the TVs were not only observed moving in the negative axial direction as cylinder rotation rates were increased, but were also seen to exhibit a slight positive axial displacement at $R_{e_{ew}}/R_{e_{tc-vb}} \approx 2$. This displacement resulted in a sudden drop in vortex strength, and seemed to be caused by the decay of cylinder driven vorticity in the zone-2. Although flow in the upper part of the annulus was drawn out by the circulation of the zone-2, as it was for the $\Gamma_{ew} = 1.5$ TCF case, mean flow TVs remained stable through out the entire test range due to the sharp turning angle the flow encountered as it merged with the zone-2. This turning angle resulted from the opposite rotational direction of the end-wall and cylinder driven cores, which acted to segregate flow interaction and effectively negated much of the zone-2s influence on the annulus. This effect can be seen in the streamline plots of Figure 3.46, where for all rotational rates flow at the intersection of end-wall and cylinder circulation is seen to remain relatively parallel to the rotational surfaces.

POD modes 1 and 3 for the zone-2 at $\Gamma_{ew} = 1$ were found to display the same basic flow patterns observed within the mean flow. In particularly mode-1 results presented in Figures A.5 - A.6 are seen to have nearly identical core flow structures to those seen in the mean flow. Vorticity plots were found to highlight these recirculating regions, Figures A.5 (h) and A.6 (h) demonstrate this clearly showing vertically stacked counter rotating vortices in the very center of the zone-2. Mean flow indications of the instability of these vortices was further enhanced by the results presented in Figures A.5 (e) and A.6 (e) where circulation

of the central region is noted to be in an opposing direction to that of mean flow results indicating the potential for circulation breakdowns and reversals caused by the opposing forces of the end-wall and cylinder driven cores. Mode-3 results for the zone-2 were less informative and generally found to display the same flow structure found at higher modes. However the streamlines of Figures A.7 (c) and (i) do show reversals in circulation to that of mode-1, further indicating circulatory instability in the core of the zone-2 as end-wall and cylinder driven circulations alternated between dominant / dominated; even when no changes in rotational were made.

Annular results for modes 1 and 3 were found to display an increased variability from the mean flow than those of the zone-2. Mode-1 vorticity plots presented in Figures B.5 and B.3 display increased values at $T_a = 3,360$ similar to those seen at TCF conditions and are noted to be ≈ 2.7 times greater than that of the mean flow with a more TV structure (Figure B.5 (a) & (b)). Results for increases in T_a displayed increased Taylor vortex elongation to that seen in mode-1 results at TCF $\Gamma_{ew} = 1$. Figures B.3 (a-f) however shows almost no discernible change in annular flow formation for increases in $R_{e_{ew}}$. Only Figure B.3 (e) at $T_a = 15,170$, $R_{e_{ew}} = 2,926$ show any noteworthy variation were vorticity values are seen to be reversed indicating that zone-2 fluctuations may have had a significant effect on Taylor vortices. Mode-3 results of Figures B.2 (k-l) and B.3 (i-j) also display the effects caused by co-rotation induced fluctuations with two different types of TV distortion. Plots (k) and (l) of the aforementioned Figures show an extremely coherent formation were vortex pairs are seen to unbalanced with negative vortics elongated and positive vortices compressed, in a similar dash dot dash like pattern seen in mode-3 results for co-rotation, $\Gamma_{ew} = 0.5$. Figures B.3 (i) and (j) show what appear to be the formation of small 2 additional vortices on either side of each Taylor vortex rotating in the opposite direction, the cause of which was not clear but was generally found to occur a the lower $R_{e_{ew}}$ values preceding T_a and R_{eew} combinations that resulted in the dash dot dash pattern previously described.

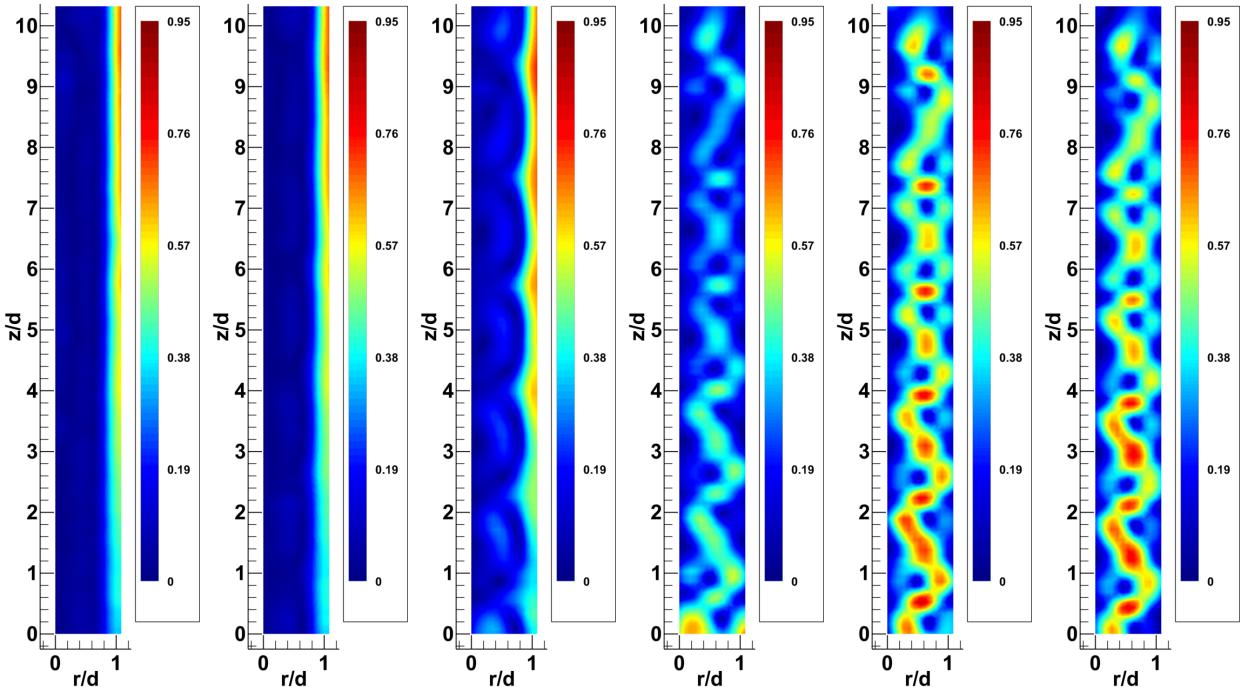

(a) $T_a = 1,312$ $R_{e_{ew}} = 944$ **(b)** $T_a = 3,360$ $R_{e_{ew}} = 944$ **(c)** $T_a = 6,352$ $R_{e_{ew}} = 944$ **(d)** $T_a = 10,289$ $R_{e_{ew}} = 944$ **(e)** $T_a = 20,997$ $R_{e_{ew}} = 944$ **(f)** $T_a = 35,485$ $R_{e_{ew}} = 944$

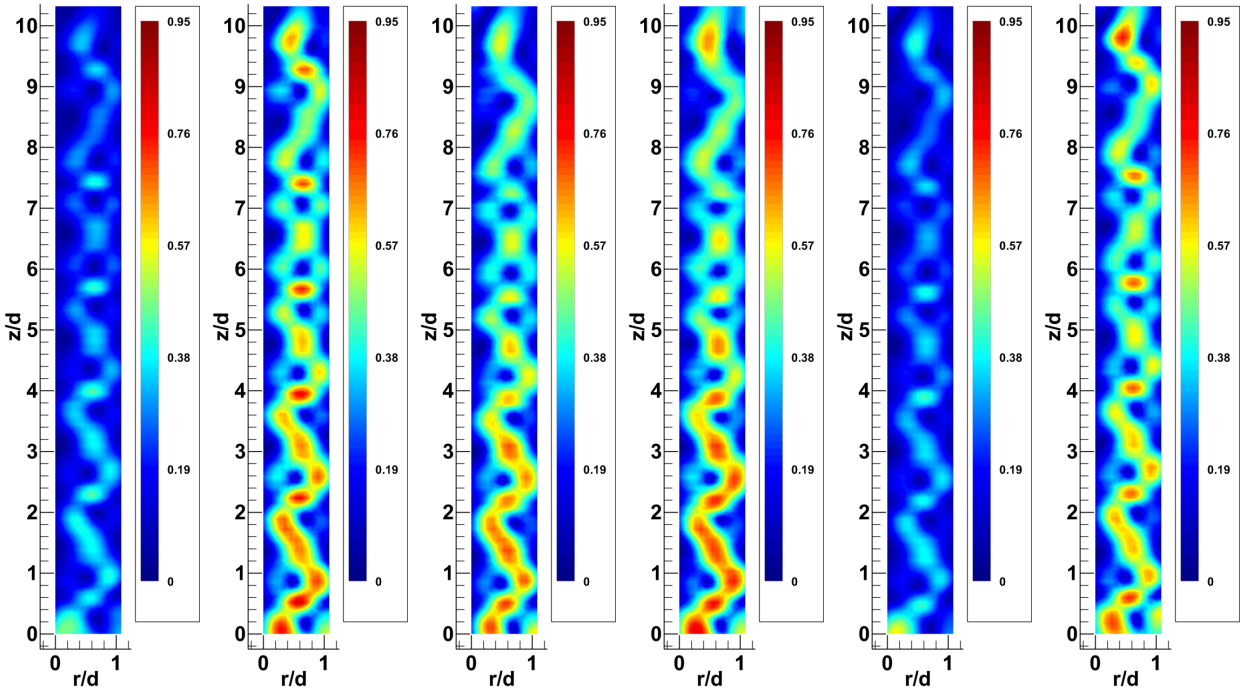

(g) $T_a = 15,170$ $R_{e_{ew}} = 944$ **(h)** $T_a = 15,170$ $R_{e_{ew}} = 1,227$ **(i)** $T_a = 15,170$ $R_{e_{ew}} = 1,793$ **(j)** $T_a = 15,170$ $R_{e_{ew}} = 2,076$ **(k)** $T_a = 15,170$ $R_{e_{ew}} = 2,360$ **(l)** $T_a = 15,170$ $R_{e_{ew}} = 2,926$

Figure 3.48: Co-rotational annular mean flow, velocity profile $(a)-(f)$: for varying T_a, $(g)-(l)$: for varying $R_{e_{ew}}$ at $\Gamma_{ew} = 1$

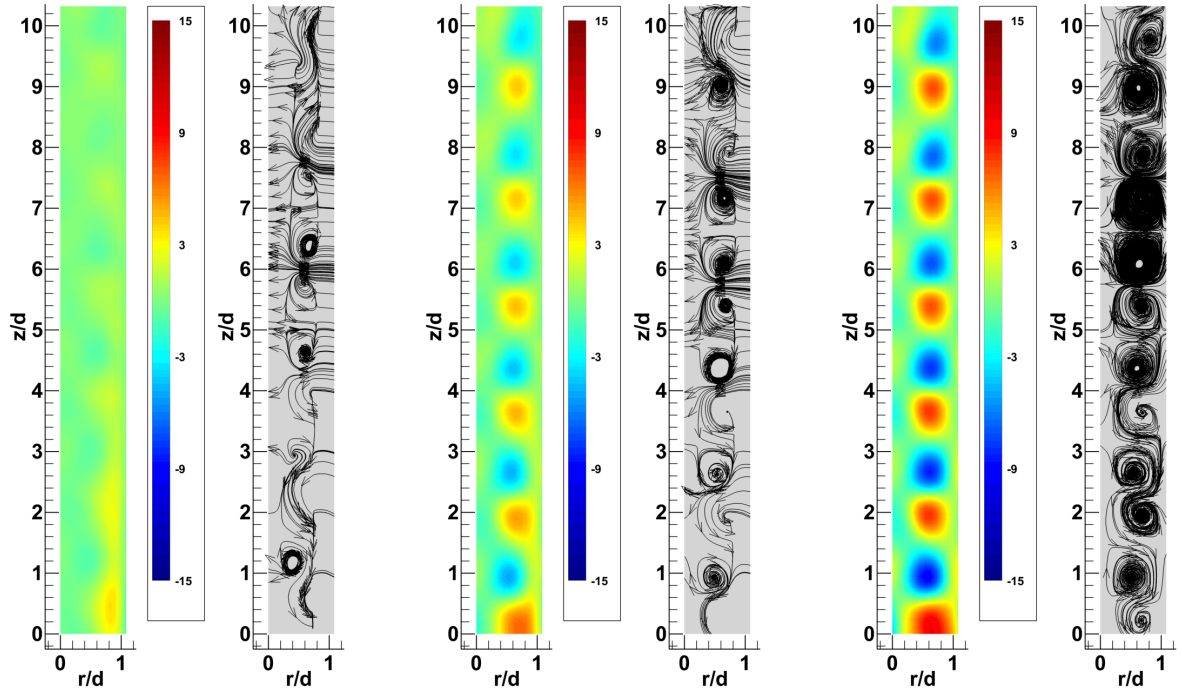

(a) $T_a = 3,360$ $R_{e_{ew}} = 944$ (b) $T_a = 3,360$ $R_{e_{ew}} = 944$ (c) $T_a = 6,352$ $R_{e_{ew}} = 944$ (d) $T_a = 6,352$ $R_{e_{ew}} = 944$ (e) $T_a = 10,289$ $R_{e_{ew}} = 944$ (f) $T_a = 10,289$ $R_{e_{ew}} = 944$

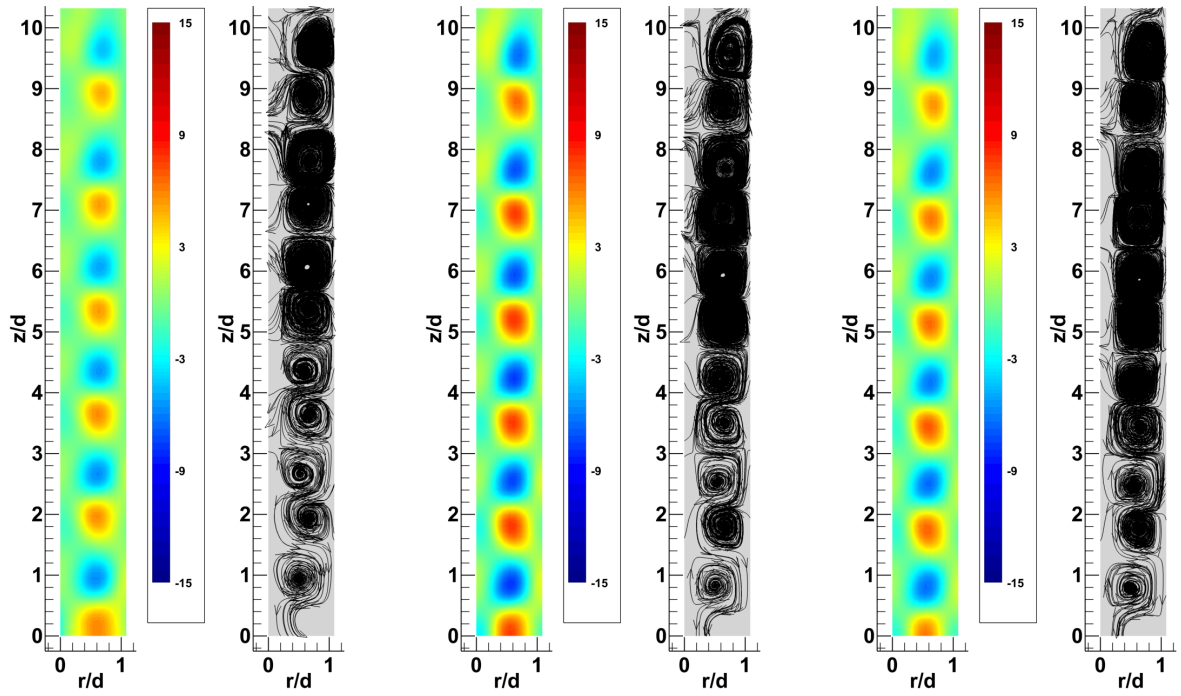

(g) $T_a = 15,170$ $R_{e_{ew}} = 944$ (h) $T_a = 15,170$ $R_{e_{ew}} = 944$ (i) $T_a = 27,769$ $R_{e_{ew}} = 944$ (j) $T_a = 27,769$ $R_{e_{ew}} = 944$ (k) $T_a = 35,485$ $R_{e_{ew}} = 944$ (l) $T_a = 35,485$ $R_{e_{ew}} = 944$

Figure 3.49: Co-rotational annular mean flow, non-dimensionalized vorticity $[\frac{\omega \hat{\mathrm{d}}}{2\Omega_I R_I}]$ & streamlines, for varying T_a at $\Gamma_{ew} = 1$

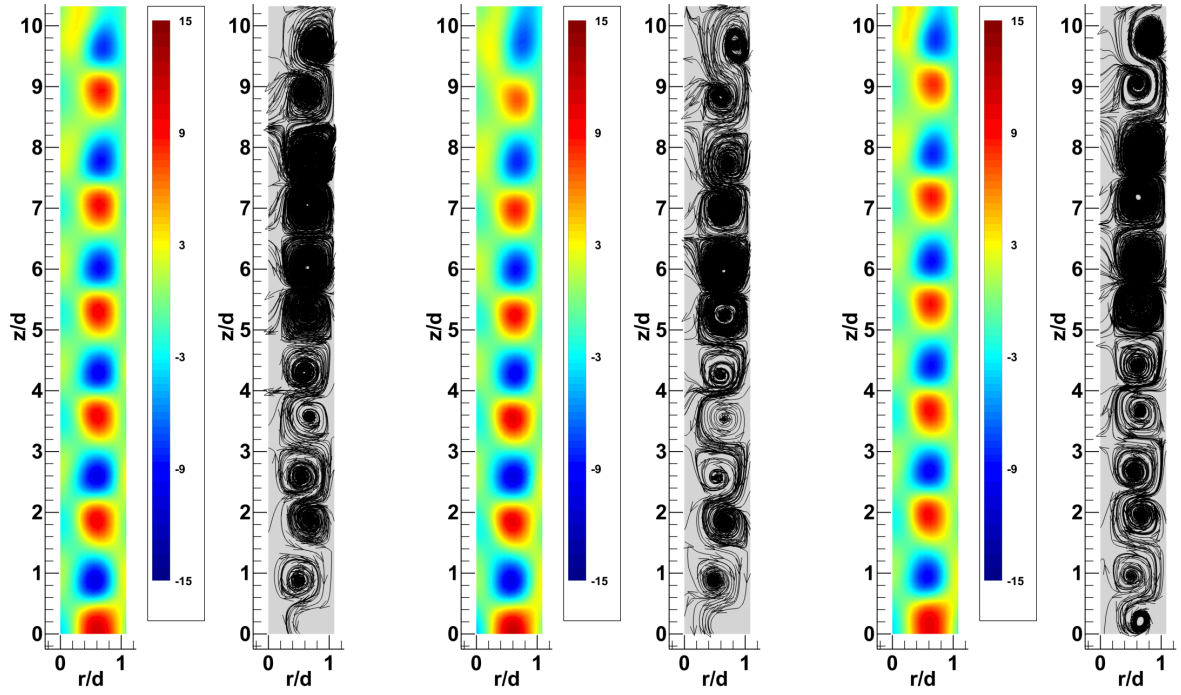

(a) $T_a = 15,170$ $R_{e_{ew}} = 1,227$ **(b)** $T_a = 15,170$ $R_{e_{ew}} = 1,227$ **(c)** $T_a = 15,170$ $R_{e_{ew}} = 2,076$ **(d)** $T_a = 15,170$ $R_{e_{ew}} = 2,076$ **(e)** $T_a = 15,170$ $R_{e_{ew}} = 2,926$ **(f)** $T_a = 15,170$ $R_{e_{ew}} = 2,926$

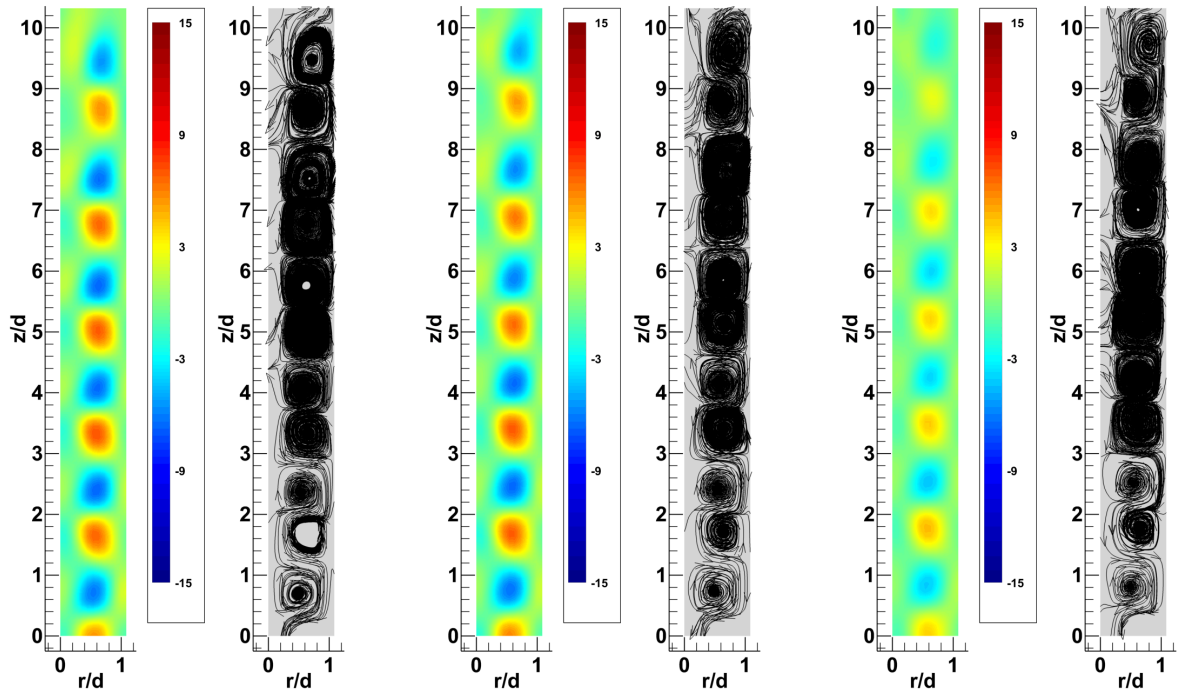

(g) $T_a = 35,485$ $R_{e_{ew}} = 1,227$ **(h)** $T_a = 35,485$ $R_{e_{ew}} = 1,227$ **(i)** $T_a = 35,485$ $R_{e_{ew}} = 2,076$ **(j)** $T_a = 35,485$ $R_{e_{ew}} = 2,076$ **(k)** $T_a = 35,485$ $R_{e_{ew}} = 2,926$ **(l)** $T_a = 35,485$ $R_{e_{ew}} = 2,926$

Figure 3.50: Co-rotational annular mean flow, non-dimensionalized vorticity $[\frac{\omega \hat{\mathrm{d}}}{2\Omega_I R_I}]$ & streamlines, for varying $R_{e_{ew}}$ at $\Gamma_{ew} = 1$

Many of the same flow features observed at $\Gamma_{ew} = 1$ were also seen to form when the aspect ratio was increased to $\Gamma_{ew} = 1.5$. Central core diameter at the cylinder surface was approximately $2d$ wider than that of its respective TCF case. A negatively rotating vortex was also seen to appear in the mean flow of the central core at $T_a = 3,360$, which for both $\Gamma_{ew} = 1$ and $\Gamma_{ew} = 1.5$ was much sooner than either TCF cases. However, unlike the formation seen at $\Gamma_{ew} = 1$, this vortex was also accompanied by a positively rotating vortex directly below it; something that was not seen to form at $\Gamma_{ew} = 1$ until $T_a = 10,289$. Another notable difference was that flow in the zone-2 remained relatively structured as $R_{e_{ew}}$ was increased. This trend was noted to occur at all Taylor numbers tested, and can be seen in the streamline and velocity plots of Figures 3.51 and 3.52. Since the magnitude of vorticity for all three aspect ratios was relatively similar, the most likely explanation for why turbulent, unstructured flow in the zone-2 was only seen to occur at $\Gamma_{ew} = 1$, is that it was a combination of the two flows in close proximity and the presence of recirculating regions within the core. Where for $\Gamma_{ew} = 0.5$, although the cylinder and end-wall had a closer proximity the absence of recirculating zones in the core allowed cylinder driven vortices to move radially inward as they became increasingly compressed by the end-wall driven vortices at increased $R_{e_{ew}}$ numbers. The opposite was true in the case of $\Gamma_{ew} = 1.5$ where, although recirculation was seen to be present in the central core, the distance between the two surfaces was sufficiently large for the two flows to co-exist without overt interference.

As T_a number was increased for $\Gamma_{ew} = 1.5$ the relative strength of the vortices found in the central core were seen to also increase. In all instances the two stacked counter rotating vortices, which formed in the central core, had a negative axial movement as end-wall rotation rate increased for a constant T_a number. In a few instances at the lower Taylor numbers these vortices where seen to completely disappear from the mean flow. It is likely that these vortices where predominantly the result of cylinder driven rotation, as seen in the TCF case, and not the result of a true VBB caused by the upper end-wall. This was also found to be applicable to the $\Gamma_{ew} = 1$ aspect ratio. These results were found to be in general agreement

with those of Mununga et. al. who found that co-rotation of the end-walls precipitates the onset of a VBB and causes the bubble to shift in the upstream direction [41]. This also helps to explain why core recirculation was seen to occur sooner in the co-rotation case than in the TCF cases.

Initial onset of Taylor vortices at $\Gamma_{ew} = 1.5$ was found to be the most uniform of the three co-rotating aspect ratios tested. As with all other previous test, initial formation was observed at $T_a = 3,360$. From both the vorticity and streamline plots of Figure 3.55 these initial Taylor vortices are seen to be more uniform in terms of shape, size and vorticity than that of the two lower co-rotational aspect ratios. It is also noted that these TVs take on the same S like shape that was seen to occur at the TCF case, with a significant amount of vortical fluid exchange. For the lower portion of the Taylor number range $(3,360 - 6,352)$, no significant change in either vortex formation or circulation were noted to occur as $R_{e_{ew}}$ was increased. The only observable changes were a slight negative axial displacement, and a progressively more pronounce square like shape; resembling the more stable TVs observed at $\Gamma_{ew} = 0$.

As Taylor number increased to $T_a = 10289$ radial fluctuations were observed in the lower half of the annular gap. In Figure 3.53, at $z/\hat{d} \approx 1$ & 3.4 respectively, vortex size for the two negatively rotating vortices is seen to fluctuate between -25% and $+50\%$ for increasing $R_{e_{ew}}$. These fluctuations in the lower half of the annulus became more pronounced as T_a increased and eventually resulted in a flow structure very similar to that seen at the $\Gamma_{ew} = 1.5$ TCF case. However for the case of co-rotation the magnitude of Taylor vortex deformation was noted to be much less than that of the TCF case. In-fact in the upper half of the annulus between $z/\hat{d} \approx 5 - 11.25$ Taylor vortices remained relatively coherent in the mean flow up to $T_a = 27769$; after which flow with in the annulus became highly elongated and tended towards an increasingly chaotic structure. Comparison of the zone-2s at the point of TV deformation reveled that in both the TCF and co-rotational cases there is a large amount fluid encroachment form the zone-2 down into the annulus. From Figures 3.55

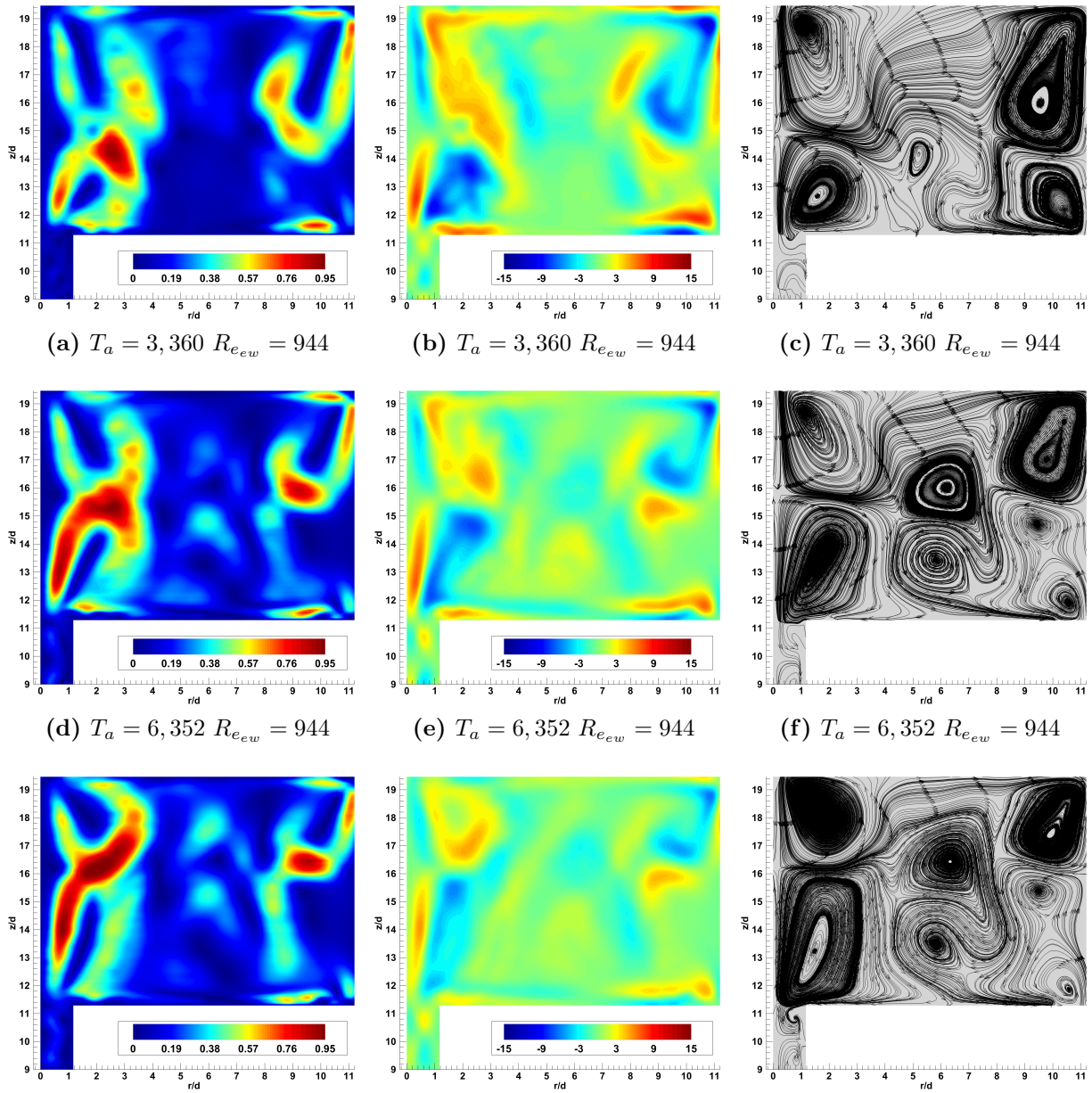

(a) $T_a = 3,360$ $R_{e_{ew}} = 944$ **(b)** $T_a = 3,360$ $R_{e_{ew}} = 944$ **(c)** $T_a = 3,360$ $R_{e_{ew}} = 944$

(d) $T_a = 6,352$ $R_{e_{ew}} = 944$ **(e)** $T_a = 6,352$ $R_{e_{ew}} = 944$ **(f)** $T_a = 6,352$ $R_{e_{ew}} = 944$

(g) $T_a = 10,289$ $R_{e_{ew}} = 944$ **(h)** $T_a = 10,289$ $R_{e_{ew}} = 944$ **(i)** $T_a = 10,289$ $R_{e_{ew}} = 944$

Figure 3.51: Co-rotational mean flow, velocity profile (left), non-dimensionalized vorticity $[\frac{\omega \hat{\mathbf{d}}}{2\Omega_I R_I}]$ (middle), streamlines (left), for varying T_a at $\Gamma_{ew} = 1.5$

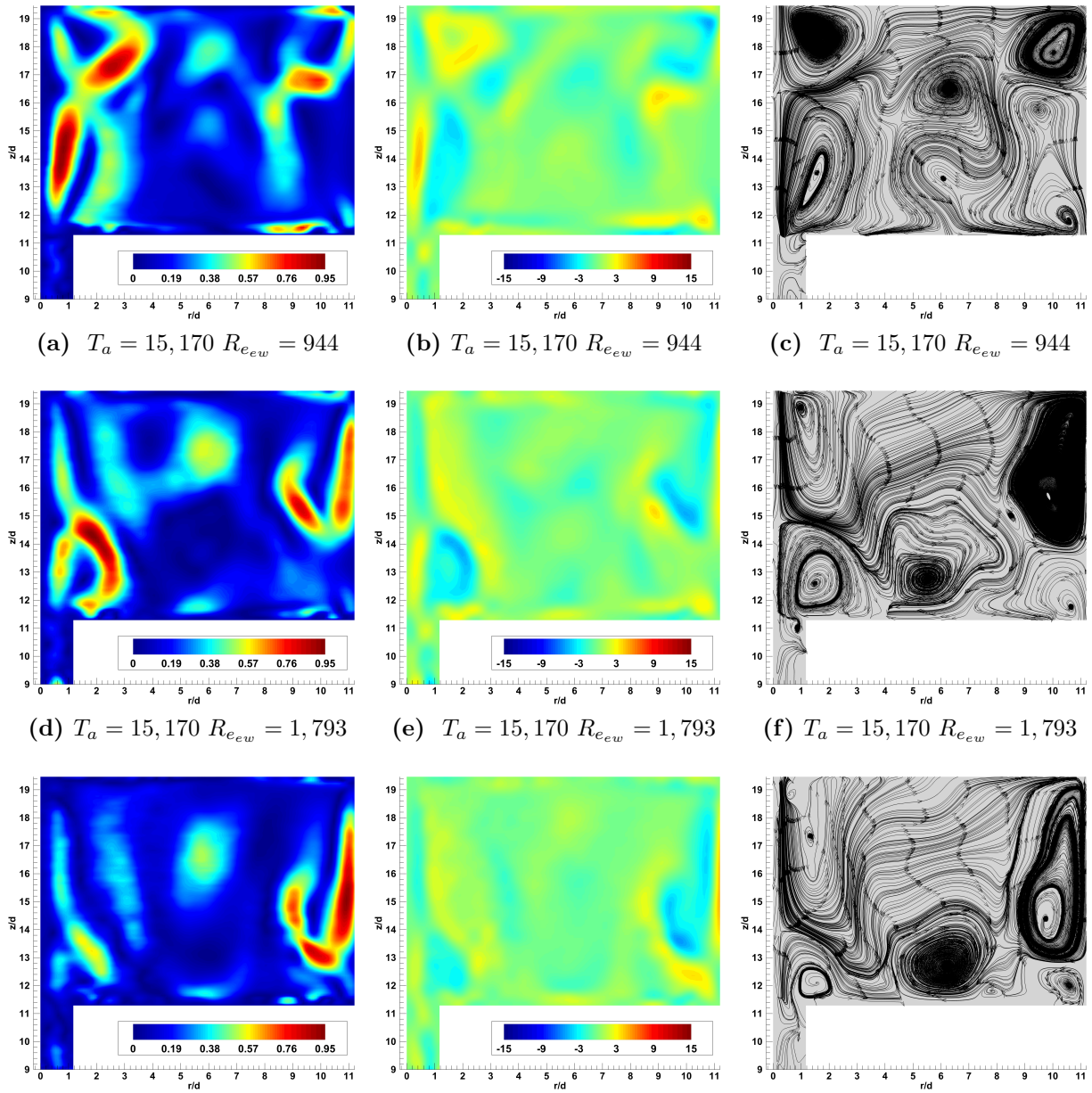

(a) $T_a = 15,170$ $R_{e_{ew}} = 944$ **(b)** $T_a = 15,170$ $R_{e_{ew}} = 944$ **(c)** $T_a = 15,170$ $R_{e_{ew}} = 944$

(d) $T_a = 15,170$ $R_{e_{ew}} = 1,793$ **(e)** $T_a = 15,170$ $R_{e_{ew}} = 1,793$ **(f)** $T_a = 15,170$ $R_{e_{ew}} = 1,793$

(g) $T_a = 15,170$ $R_{e_{ew}} = 2,926$ **(h)** $T_a = 15,170$ $R_{e_{ew}} = 2,926$ **(i)** $T_a = 15,170$ $R_{e_{ew}} = 2,926$

Figure 3.52: Co-rotational mean flow, velocity profile (left), non-dimensionalized vorticity $[\frac{\omega \hat{\mathbf{d}}}{2\Omega_I R_I}]$ (middle), streamlines (right), for varying $R_{e_{ew}}$ at $\Gamma_{ew} = 1.5$

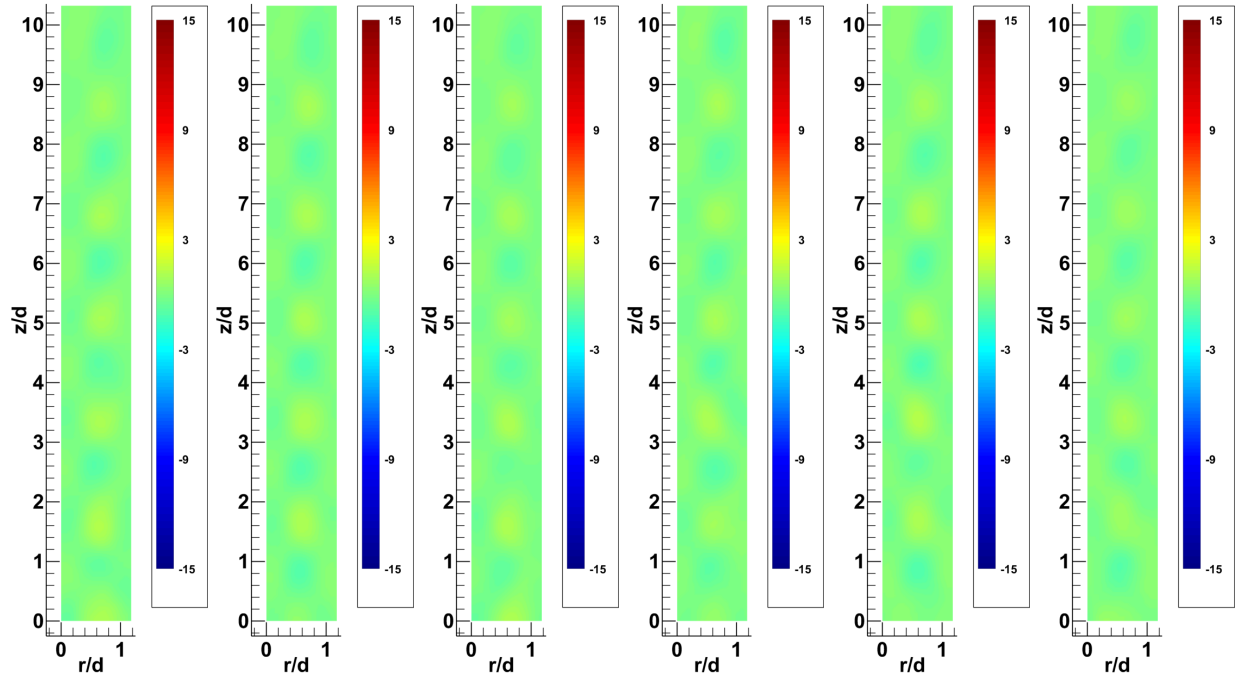

(a) $T_a = 10,289$ $R_{e_{ew}} = 1,227$ **(b)** $T_a = 10,289$ $R_{e_{ew}} = 1,510$ **(c)** $T_a = 10,289$ $R_{e_{ew}} = 1,793$ **(d)** $T_a = 10,289$ $R_{e_{ew}} = 2,076$ **(e)** $T_a = 10,289$ $R_{e_{ew}} = 2,360$ **(f)** $T_a = 10,289$ $R_{e_{ew}} = 2,926$

Figure 3.53: Co-rotational annular mean flow, non-dimensionalized vorticity $[\frac{\omega \hat{\mathbf{d}}}{2\Omega_I R_I}]$ for varying $R_{e_{ew}}$ at $T_a = 10289$ at $\Gamma_{ew} = 1.5$

and 3.35 it was found that this increased fluid exchange between the two domains resulted from the left side of the cylinder driven central vortex moving in a positive radial and axial direction. This had the effect of removing any flow barrier into the annular gap, destroying the pseudo-Ekman cell at the domain interface ($z/\hat{d} \approx 11.25$). While it is not entirely clear whether the presence of recirculation zones within the central core had any direct influence in these regards, one interesting observation was that in both the TCF and co-rotational cases the central point of mean flow recirculation in the zone-2 occurred at $z/\hat{d} \approx 16$.

Higher modal POD results for the co-rotating zone-2 at $\Gamma_{ew} = 1.5$ were found to be much more chaotic than mean flow results indicated. Mode-1 plots presented in Figures A.9 and A.10 present a flow more reminiscent of the chaotic structure seen at $\Gamma_{ew} = 1$ with a multitude of vortical formations appearing throughout the domain at various locations; exemplified by the streamlines at $z/\hat{d} \approx 7.5 - 10.5$ of Figure A.10 (i). However the large recirculating core regions observed in mean flow plots were generally found in mode-1 results at the same location. Figures A.9 (b) & (c) as well as A.10 (h) & (i), ($T_a = 3,360 R_{e_{ew}} = 944$ and $T_a = 15,170 R_{e_{ew}} = 2,926$), show the same core recirculation seen in the mean flow but as with the higher modal results at $\Gamma_{ew} = 1$ circulatory direction of these structures is inverted to that of the mean flow. Mode-3 results (Figures A.11 and A.12) further highlight flow field complexities not seen at mode-0 (mean flow); specifically in the streamlines of Figure A.12 (i) were 3 pairs of horizontally aligned counter rotating vortices can be seen vertically stacked on top of one another in the central core. Additionally velocity and vorticity plots presented in Figure A.11 more definitively show the positive radial and axial displacement of vorticity near the top of the annular gap which become more pronounced as T_a increased. The plots also show how this displacement increased axial flow interactions between the two domains, resulting in Taylor vortex destabilization.

Annular flow results at POD modes 1 and 3 displayed large axial flow patterns similar to those seen at the higher modes of the TCF test cases. Figures B.5 (a-f) show mode-1 results for increasing T_a values, from which vorticity plots can be seen to have the same negative

axial flow pattern between $z/\hat{d} \approx 0 - 5$ that was found in TCF results at mode-1. However the axial elongations are noted to be somewhat subdued with coherent vortices still seen to occur (Figures B.5 (c) (d) and (f)). Mode-3 result for increasing T_a values were also found to resemble a more restrained version of the TCF results displaying horizontally aligned vortex pairs in Figures B.5 (g-l). Although these vortex pairs were found to display a positive axial movement as T_a increased the total displacement of the largest horizontal pair was found to be $\frac{1}{2}$ that of the TCF case. Additionally there was a noted lack of the vortical sinks that were seen to form along the outer cylinder wall at TCF conditions.

Mode-1 results for increasing $R_{e_{ew}}$ values at a constant T_a were generally found to display the same patterns as those seen in Figures B.5 (a-f). However instances of Taylor vortex reappearance similar to that of Figure B.6 (e) were found to occur. The conditions at which this reappearance occurred was typically found to be at rotational combinations were cylinder rate was $\approx \frac{1}{2}$ or equal to that of the end-walls.

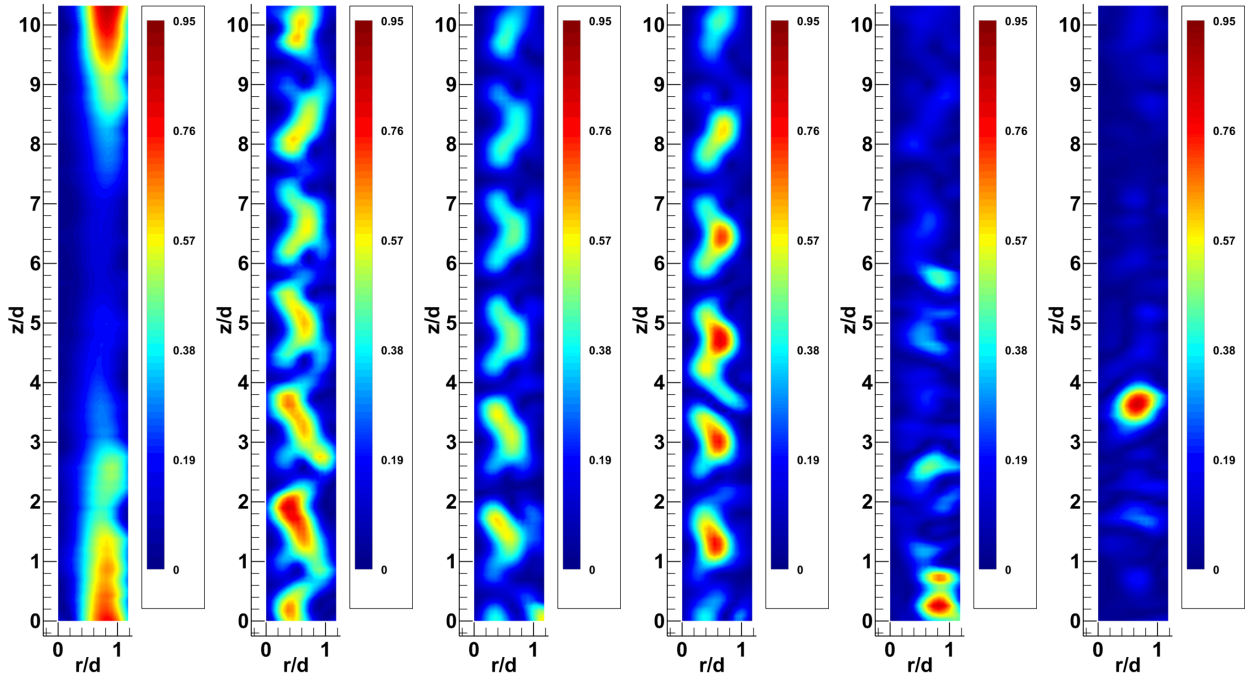

(a) $T_a = 1,312$ $R_{e_{ew}} = 944$ **(b)** $T_a = 3,360$ $R_{e_{ew}} = 944$ **(c)** $T_a = 6,352$ $R_{e_{ew}} = 944$ **(d)** $T_a = 10,289$ $R_{e_{ew}} = 944$ **(e)** $T_a = 20,997$ $R_{e_{ew}} = 944$ **(f)** $T_a = 35,485$ $R_{e_{ew}} = 944$

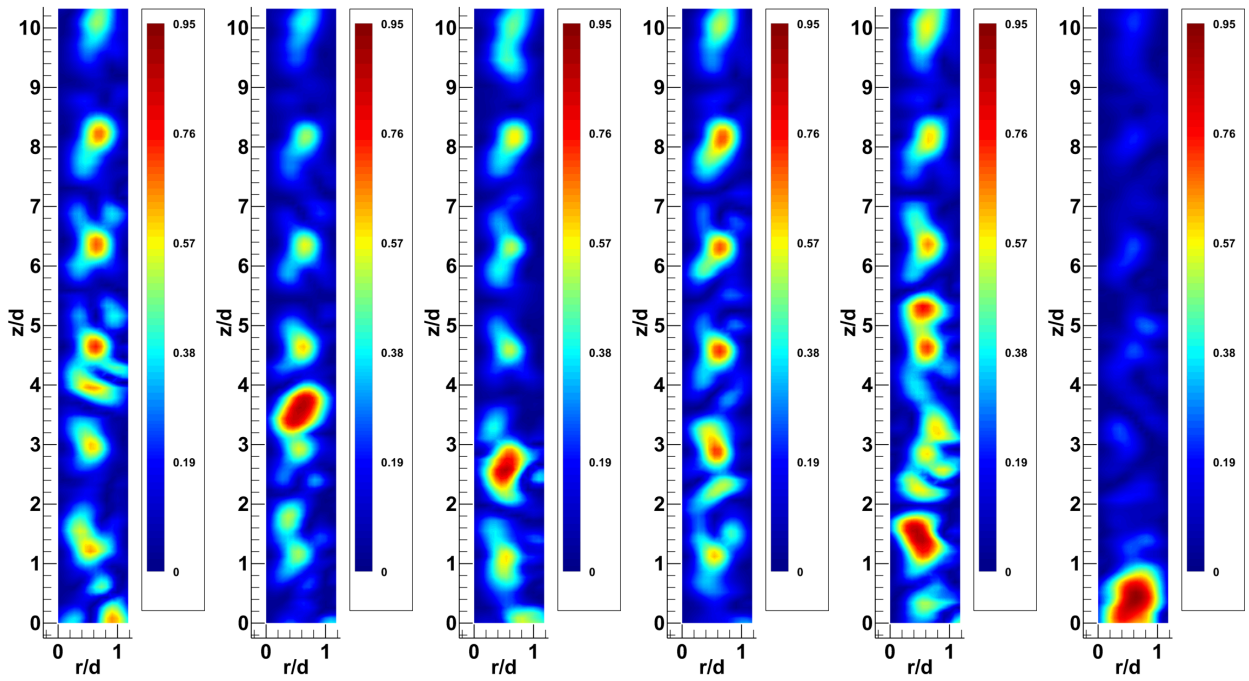

(g) $T_a = 15,170$ $R_{e_{ew}} = 944$ **(h)** $T_a = 15,170$ $R_{e_{ew}} = 12,27$ **(i)** $T_a = 15,170$ $R_{e_{ew}} = 1,793$ **(j)** $T_a = 15,170$ $R_{e_{ew}} = 2,076$ **(k)** $T_a = 15,170$ $R_{e_{ew}} = 2,360$ **(l)** $T_a = 15,170$ $R_{e_{ew}} = 2,926$

Figure 3.54: Co-rotational annular mean flow, velocity profile $(a)-(f)$ for varying T_a, $(g)-(l)$ for varying $R_{e_{ew}}$; 1^{st} at $\Gamma_{ew} = 1.5$

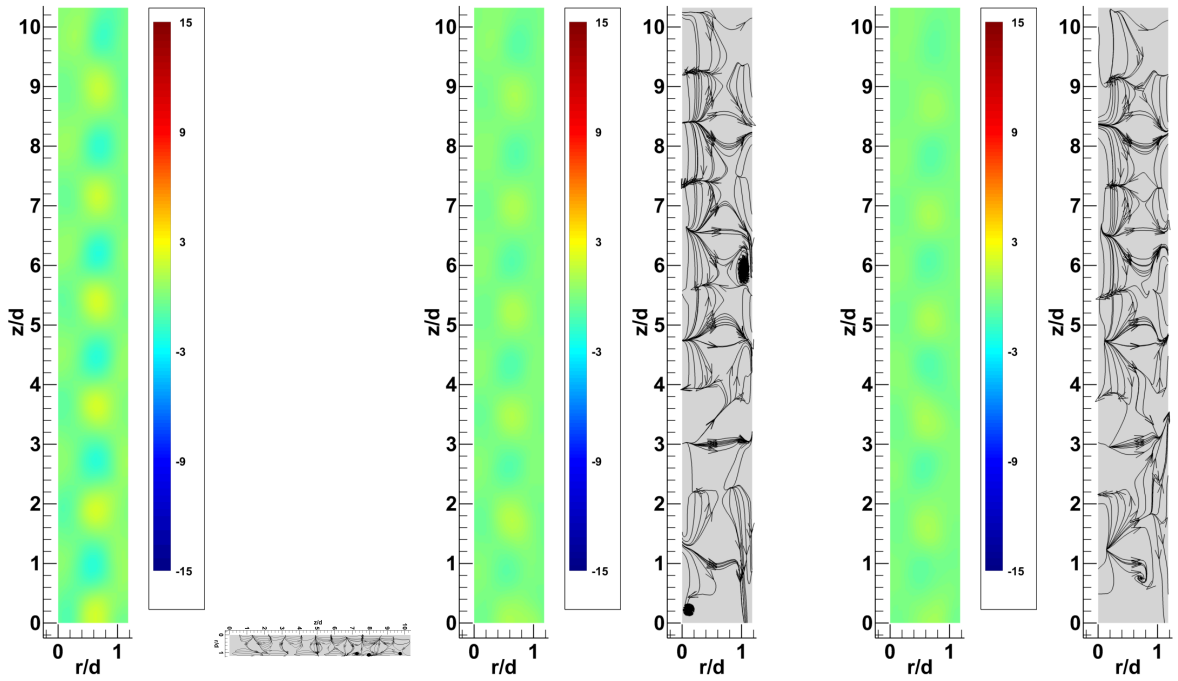

(a) $T_a = 3,360$ $R_{e_{ew}} = 944$ **(b)** $T_a = 3,360$ $R_{e_{ew}} = 944$ **(c)** $T_a = 6,352$ $R_{e_{ew}} = 944$ **(d)** $T_a = 6,352$ $R_{e_{ew}} = 944$ **(e)** $T_a = 10,289$ $R_{e_{ew}} = 944$ **(f)** $T_a = 10,289$ $R_{e_{ew}} = 944$

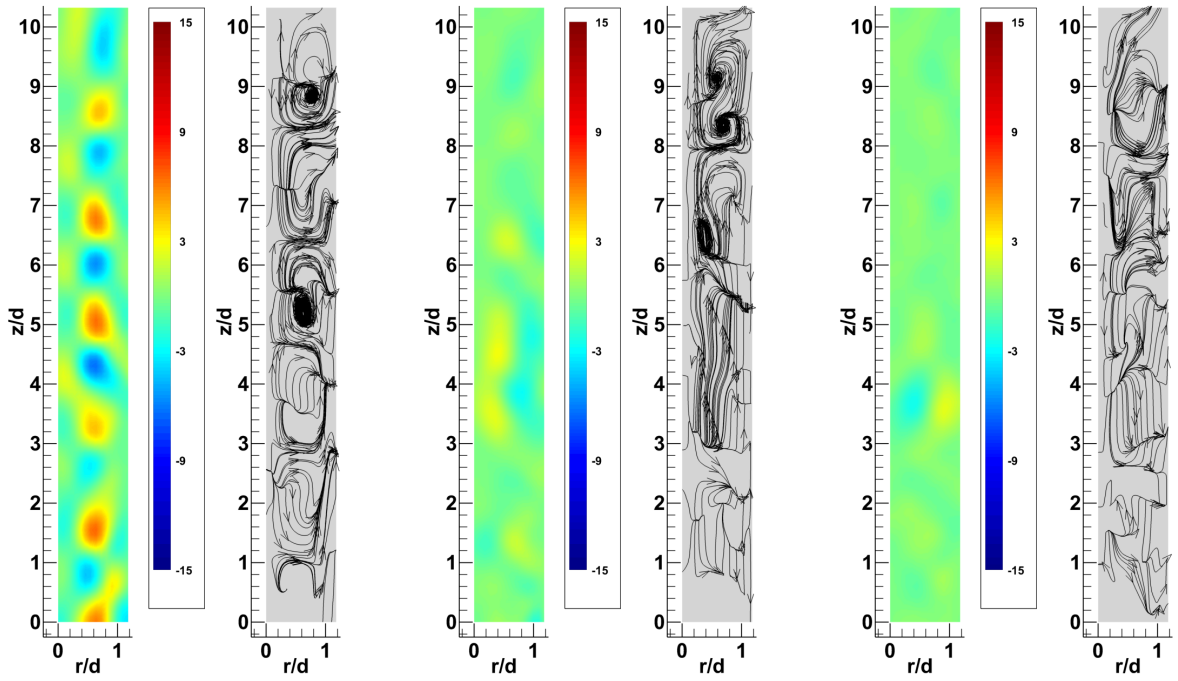

(g) $T_a = 15,170$ $R_{e_{ew}} = 944$ **(h)** $T_a = 15,170$ $R_{e_{ew}} = 944$ **(i)** $T_a = 27,769$ $R_{e_{ew}} = 944$ **(j)** $T_a = 27,769$ $R_{e_{ew}} = 944$ **(k)** $T_a = 35,485$ $R_{e_{ew}} = 944$ **(l)** $T_a = 35,485$ $R_{e_{ew}} = 944$

Figure 3.55: Co-rotational annular mean flow, non-dimensionalized vorticity $[\frac{\omega \hat{\mathrm{d}}}{2\Omega_I R_I}]$ & streamlines for varying T_a at $\Gamma_{ew} = 1.5$

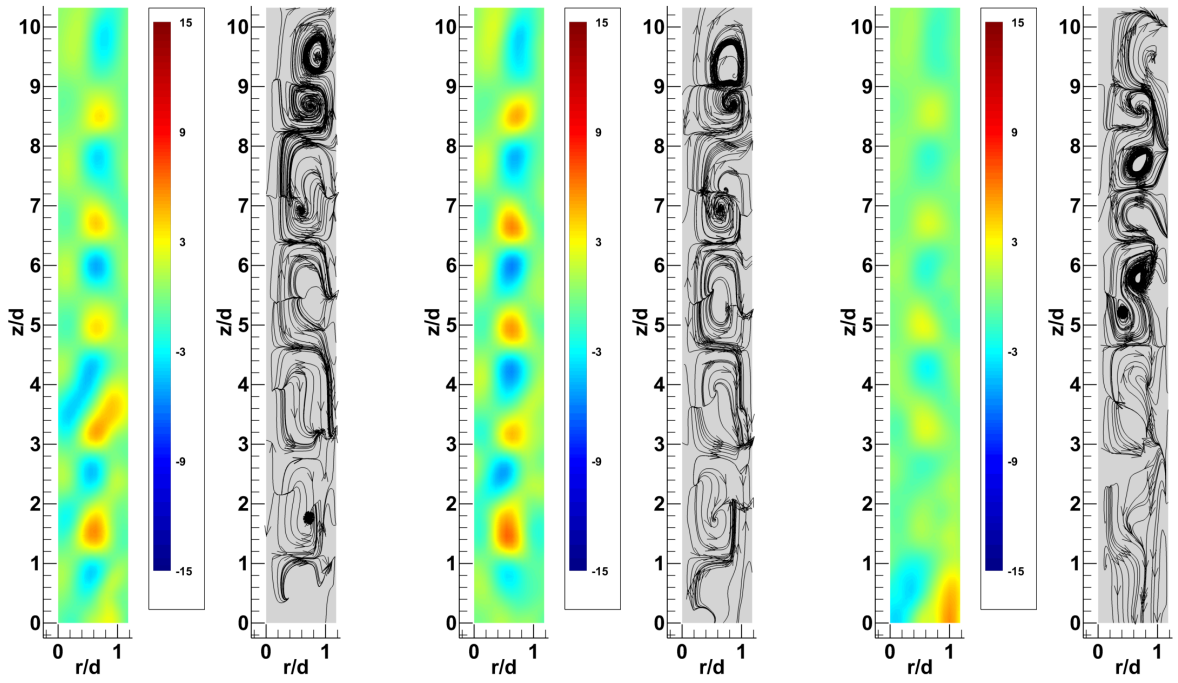

(a) $T_a = 15,170$ $R_{e_{ew}} = 1,227$ **(b)** $T_a = 15,170$ $R_{e_{ew}} = 1,227$ **(c)** $T_a = 15,170$ $R_{e_{ew}} = 2,076$ **(d)** $T_a = 15,170$ $R_{e_{ew}} = 2,076$ **(e)** $T_a = 15,170$ $R_{e_{ew}} = 2,926$ **(f)** $T_a = 15,170$ $R_{e_{ew}} = 2,926$

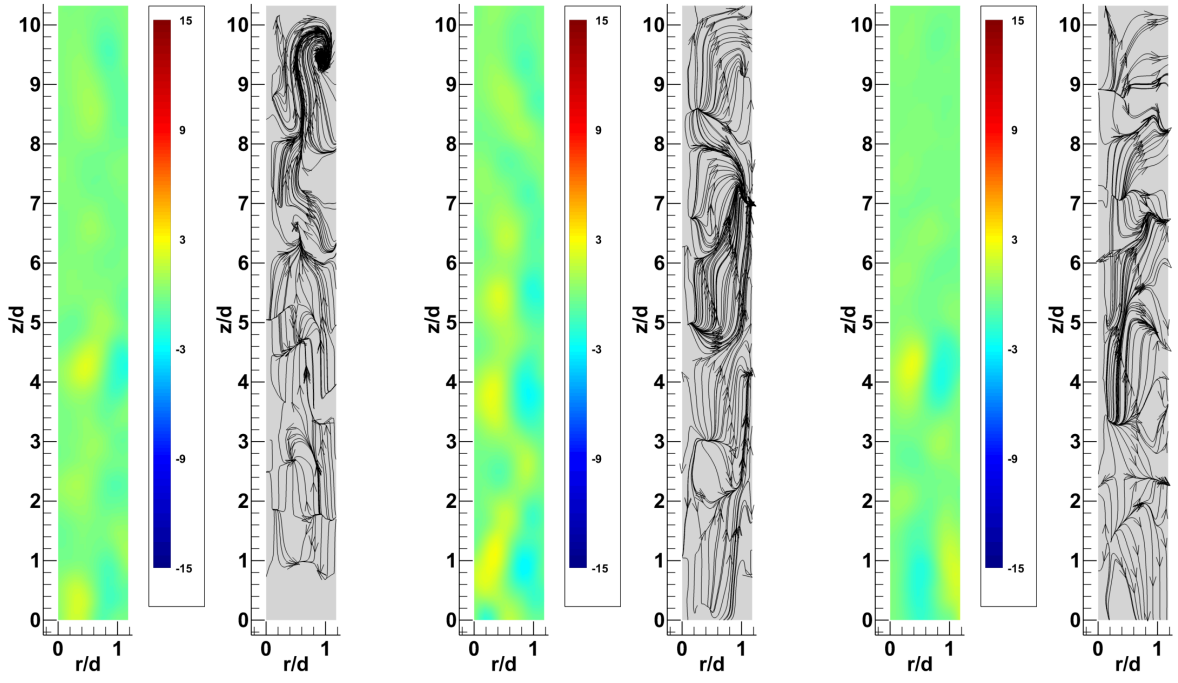

(g) $T_a = 35,485$ $R_{e_{ew}} = 1,227$ **(h)** $T_a = 35,485$ $R_{e_{ew}} = 1,227$ **(i)** $T_a = 35,485$ $R_{e_{ew}} = 2,076$ **(j)** $T_a = 35,485$ $R_{e_{ew}} = 2,076$ **(k)** $T_a = 35,485$ $R_{e_{ew}} = 2,926$ **(l)** $T_a = 35,485$ $R_{e_{ew}} = 2,926$

Figure 3.56: Co-rotational annular mean flow, non-dimensionalized vorticity $[\frac{\omega \hat{\mathrm{d}}}{2\Omega_I R_I}]$ & streamlines for varying $R_{e_{ew}}$ at $\Gamma_{ew} = 1.5$

3.2.2 Counter Rotation

Investigations into flow characteristics for counter rotation of the end-wall and cylinder were conducted. Aspect ratios of $\Gamma_{ew} = 0.5, 1,$ & 1.5 were tested in-order to facilitate a direct comparison between the co-rotation and TCF baseline results previously discussed.

Energy distributions for counter-rotational results are presented in Figures 3.58 - 3.59 for the zone-2 and Figures 3.60 - 3.61 for annular flow. Cumulative distributions for the zone-2 (Figures 3.58 (a) and 3.59 (a)) display significantly reduced mean flow energies compared to TCF and VB results similar to what was seen at co-rotational conditions. However the reduction in mode-0 energies of $\Gamma_{ew} = 1$ and $\Gamma_{ew} = 1.5$ was found to be less severs than co-rotational mode-0 reductions at the same aspect ratios. This was especially true for variations in T_a at constant $R_{e_{ew}}$ values, were from Figure 3.58 (a) most notably at $\Gamma_{ew} = 1.5$ $T_a = 3,360$ $R_{e_{ew}} = 944$ mean flow energy is seen to be 4.6% higher than similar TCF conditions. However the previous example was found to be an outlier as mean flow energies were typically found to be in the range of $\approx 3\% - 17.5\%$ lower than TCF results at varying T_a values. Additionally individual modal energies were found to show elevated levels relative to TCF and VB energies, where the bulk of the modal energies at the conditions presented Figure 3.58 (b) are not seen to drop below 1% until $\approx mode - 5$. This decay of energies below 1% was found to occur at mode-2 for the VB case and $approxmode - 4$ at TCF conditions. Surprisingly for Γ_{ew} and $\Gamma_{ew} = 1.5$ counter-rotational modes 1-10 actually displayed elevated modal energies compared to co-rotational results even though mean flow energies were typically higher. This steeper reduction in modal energy contend between progressive modes indicated that any small scale structures in the zone-2 at counter-rotational conditions were more likely to be contained in higher modal results.

Energy levels for varying $R_{e_{ew}}$ values at constant $T_a = 15,170$ were found to result in further reductions of mean flow energy. From Figures 3.59 (a) mean flow is shown to have and average reduction of 41%, 29%, and 47% for $\Gamma_{ew} = 0.5$, $\Gamma_{ew} = 1$, and $\Gamma_{ew} = 1.5$ respectively. From the mean flow energy values of $T_a = 15,170$ $R_{e_{ew}}$ (Figure 3.58 (a)). Counter-rotational

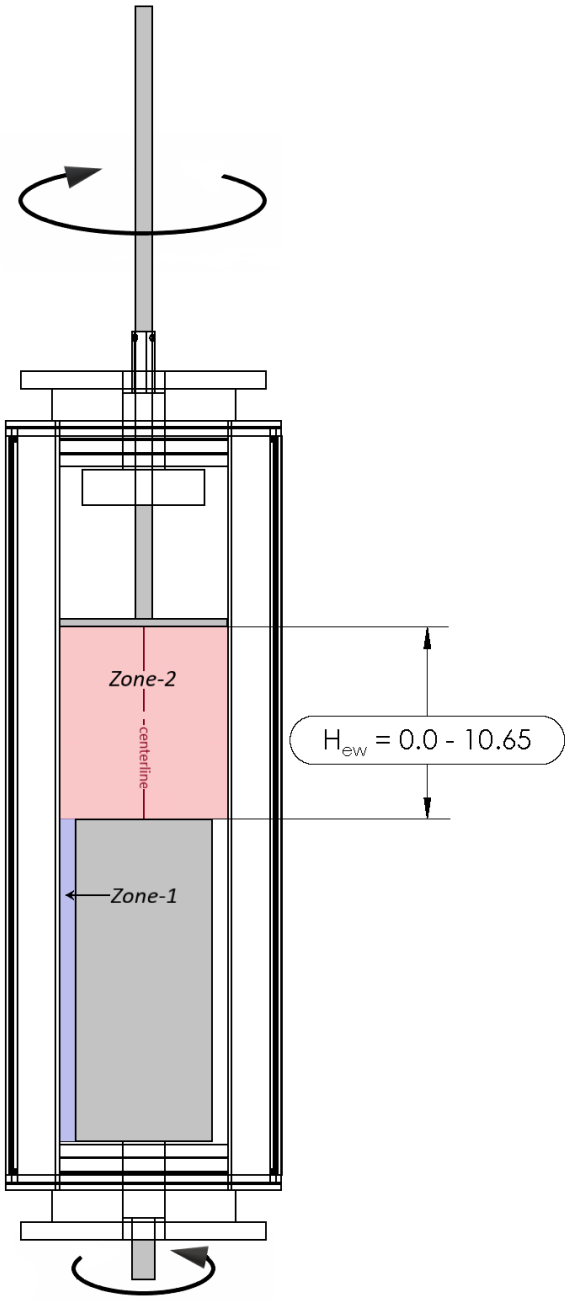

Figure 3.57: Configuration of Counter Rotational test case

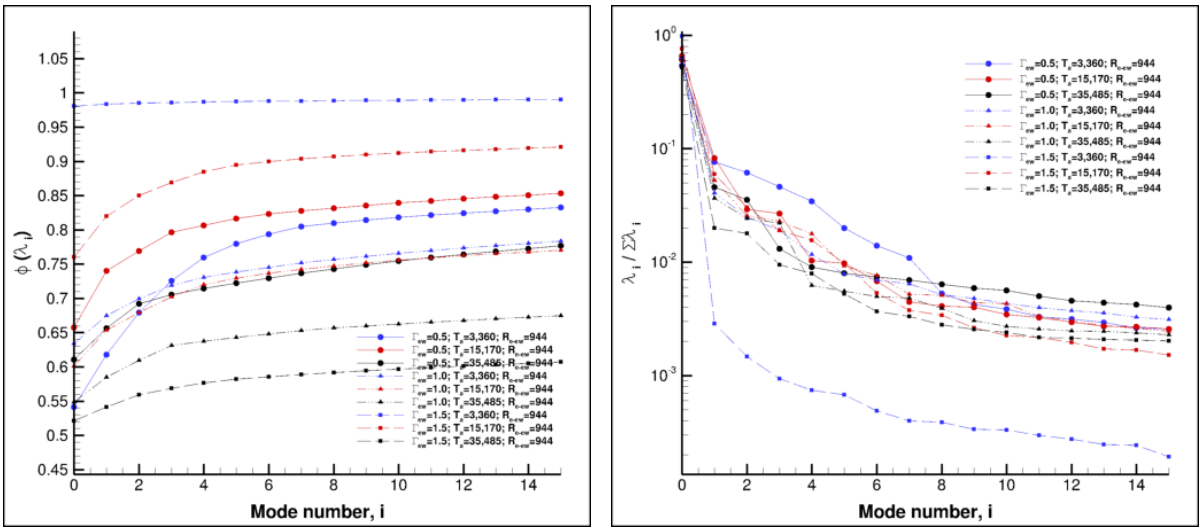

(a) cumulative distribution **(b)** POD spectrum, modes 0-15

Figure 3.58: Counter-rotational zone-2 energy distribution for increasing T_a

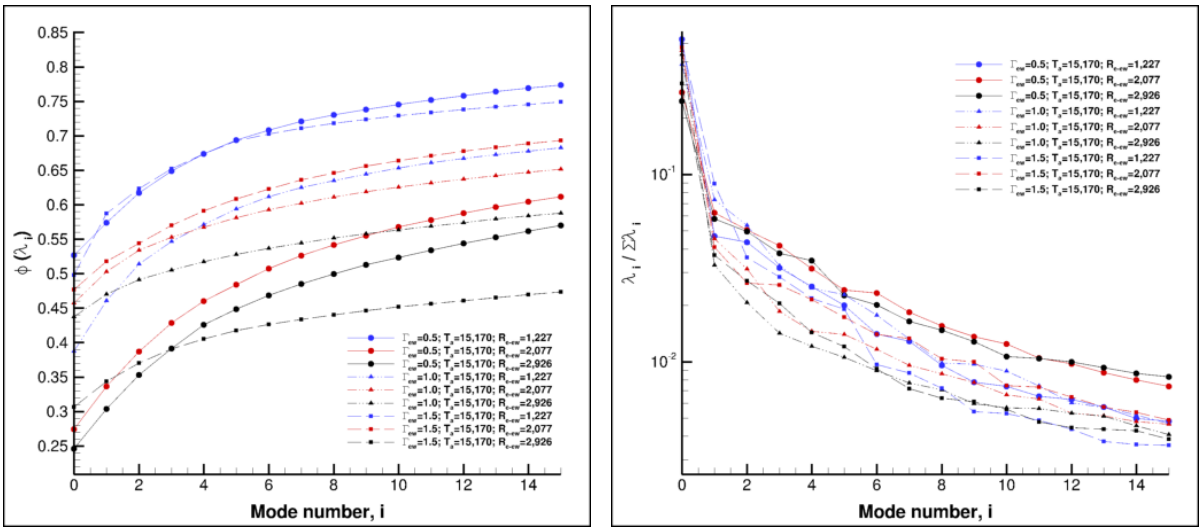

(a) cumulative distribution **(b)** POD spectrum, modes 0-15

Figure 3.59: Counter-rotational zone-2 energy distribution for increasing $R_{e_{ew}}$

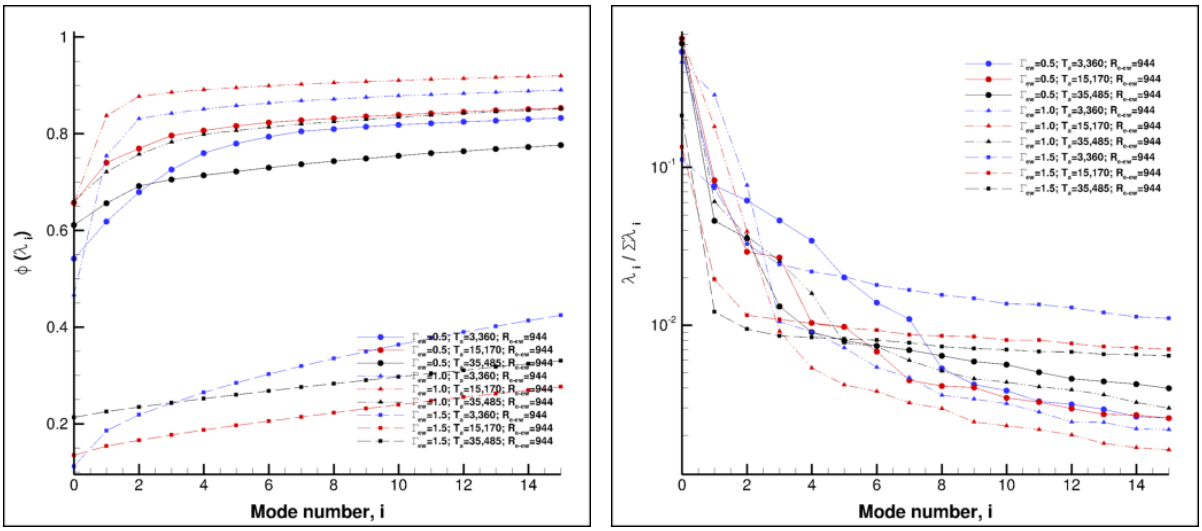

(a) cumulative distribution **(b)** POD spectrum, modes 0-15

Figure 3.60: Counter-rotational annular POD energy distribution for increasing T_a

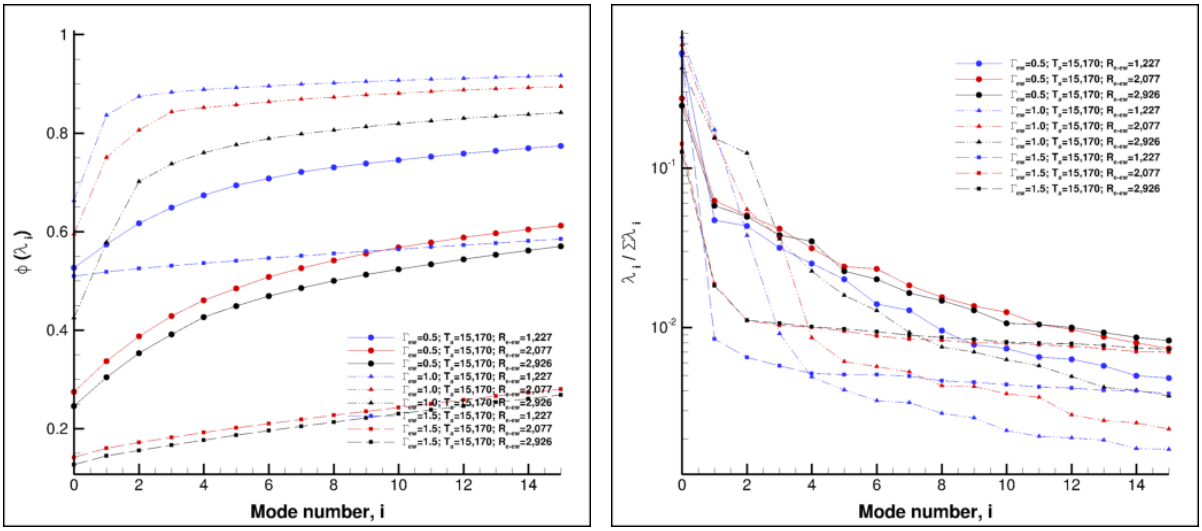

(a) cumulative distribution **(b)** POD spectrum, modes 0-15

Figure 3.61: Counter-rotational annular POD energy distribution for increasing $R_{e_{ew}}$

increases in $R_{e_{ew}}$ were found to result in larger changes in modal energy than co-rotational increases. Comparison of Figures 3.39 (b) and 3.59 (b) show counter-rotational modes $1-14$ to be elevated, were for co-rotation all modes are seen to be less than 1% beyond mode-4 while for counter-rotation the vast majority of modal energies are not seen to fall below 1% until mode-6; $\Gamma_{ew} = 0.5$ is even noted to display energies above 1% up to mode-12. The largest shift in energy between co and counter rotational cases was seen in the mean flow of $\Gamma_{ew} = 0.5$ where for co-rotation mean flow energies were never found to fall below 55% at the varying T_a values and stay above 72% for varying $R_{e_{ew}}$ at a constant $T_a = 15,170$. Counter-rotation however resulted in minimum values of 54% and 25% respectively. Comparison of all test cases showed that counter-rotation was influenced by end-wall rotational changes more than any other case and that energy transfer from the mean flow was more constrained within the higher modes between $1-12$ and not as distributed as the co-rotational results.

Annular flow energy was found to display the same reduction in the mean flow at $\Gamma_{ew} = 1.5$ that was seen to occur in TCF and co-rotational results. However unlike the aforementioned cases $\Gamma_{ew} = 1.5$ lowest values of mean flow energy were found at T_a values between $1,312-10,289$ $R_{e_{ew}} = 944$ opposed to $T_a = 15,170$ $R_{e_{ew}} = 944$. From figure 3.60 (a) mean flow energy at $T_a = 3,360$ $R_{e_{ew}} = 944$ is seen to be $\approx 5\%$ while $T_a = 15,170$ $R_{e_{ew}} = 944$ and $T_a = 35,485$ $R_{e_{ew}} = 944$ mean flow energy is noted to be 9% and 21% respectively; for the later two conditions this was found to be an increase compared to co-rotational results and nearly equal to TCF results. This large transfer of energy out of the mean flow at $\Gamma_{ew} = 1.5,\ T_a = 3,360,\ R_{e_{ew}} = 944$ is noted in Figure 3.60 (b) where no modal energy between $1-14$ is seen to fall below 1%. However for the two larger $\Gamma_{ew} = 1.5$ Taylor numbers presented modal spectrum shows slightly lower energy content than either TCF or co-rotation results, were both $T_a = 15,170$ & $35,485$ are seen to have modal energies below 1% beyond mode-5 something that didn't occur until mode-9 at TCF conditions and mode-11 at co-rotational conditions. The revers was found to be true for $\Gamma_{ew} = 0.5$ and $\Gamma_{ew} = 1$ results were although mean flow energies were found to be relatively similar to

those found at other rotational conditions, modes $1-3$ (Figure 3.60 (b)) display slightly decreased energies while beyond mode-3 levels were noted to be slightly elevated. $R_{e_{ew}}$ variations at a constant $T_a = 15,170$ were also found to display significant energy variations form co-rotational results most interestingly the shift in energy back to the higher modes that occurred at $\Gamma_{ew} = 1.5$ $T_a = 15,170$ $R_{e_{ew}} = 1,227$ (Figure 3.61 (a) and (b)). In fact the increased variability of the conditions presented in Figure 3.61 (a) indicate that as with zone-2 results counter-rotational annular flow was significantly effected by changes in end-wall rotation; and to a much greater extent than co-rotational changes.

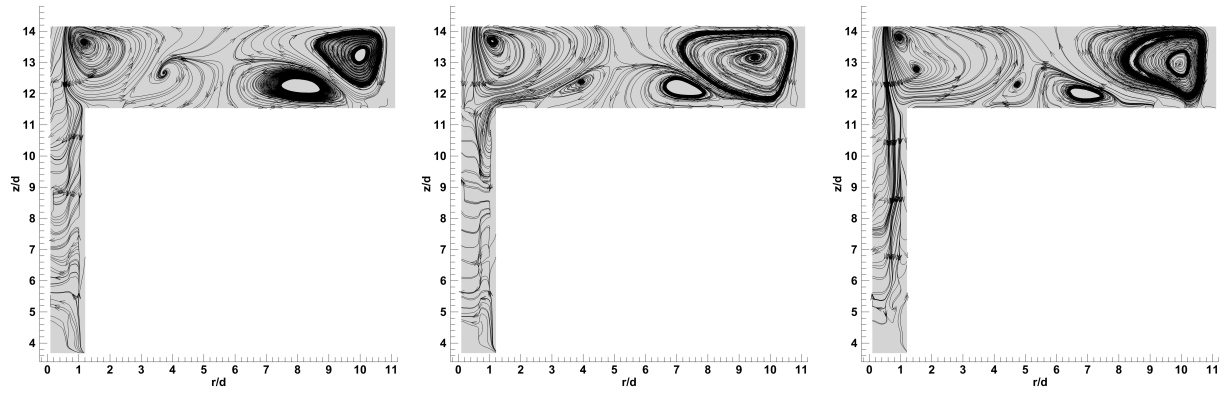

(a) $T_a = 1,312$ $R_{e_{ew}} = 1,227$ **(b)** $T_a = 1,312$ $R_{e_{ew}} = 1,793$ **(c)** $T_a = 1,312$ $R_{e_{ew}} = 2,643$

Figure 3.62: Counter-rotational mean flow streamlines for varying $R_{e_{ew}}$ at $\Gamma_{ew} = 0.5$

Figures 3.62 , 3.62 and 3.64 contain the mean flow plots for the $\Gamma_{ew} = 0.5$ counter-rotational test case. From the streamline plots one of the most notable differences that was found to occur at the counter-rotational condition was the increased amount of negative axial fluid encroachment into the annulus. At $T_a = 1,312$ this initial encroachment was seen to penetrate to a depth of $z/\hat{d} \approx 7.5$. This was similar to the penetration depth that was observed at the TCF case; but was noted to be slightly less by a measure of approximately $0.4d$. A positive correlation between the depth of flow penetration and Reynolds number of the end-wall was seen to occur, with a maximum penetration depth of $z/\hat{d} \approx 5$ at $R_{e_{ew}} = 2,926$ These depths corresponded with an axial encroachment range of $26\% - 44\%$, as a percentage of total annulus length. Increased flow penetration was due to the complementary

rotational nature of the zone-2s central core. Unlike flow produced in the co-rotational case counter rotation resulted in the central cores of both the cylinder and end-wall driven flows circulating in the same direction. This resulted in a relatively constricted central core when compared to the other rotational cases. It also resulted in the weaker of the two vortices being drawn into the central core of the more dominate; at $T_a = 1,312$ this was found to be the vortex produced by the inner cylinder for all Reynolds numbers. Displacement of the cylinders upper vortices radially inward resulted in an unimpeded path for the end-wall driven negative axial flow along the stationary side wall. This helps to explain why the counter-rotation resulted in a deeper maximum annular penetration than the $\Gamma_{ew} = 0.5$ TCF case, where the flow encountered a 90° turning angle at the top of the cylinder.

Higher levels of flow encroachment, relative to TCF and co-rotational cases, from the zone-2 were observed at all T_a number. This had a profound effect on Taylor vortex stability and formation. While the trend of initial TV formation at $T_a = 3,360$ was still seen to occur, the number of vortices and their relative strength was found to be less than either of the other two rotational conditions previously discussed. From Figure 3.63 average vorticity of the TVs can be seen to be approximately 40% lower than that of the other two cases. While the same number of vortices are seen in the vorticity plots of the co and counter rotation cases the much lower vorticity of the counter-rotational case resulted in the upper most vortex pair not being visible in the mean flow of Figure 3.63 (c). Increases in $R_{e_{ew}}$ resulted in a negative axial movement of the TVs and a further reduction of vortex strength as fluid encroachment from the zone-2 increased; with the greatest of these effects occurring in the upper half of the annulus between $z/\hat{d} \approx 7.5 - 11.5$.

As T_a increased beyond $3,360$ Taylor vortices began to more closely resemble those see at the $\Gamma_{ew} = 0.5$ TCF case. This was due to an increased domination of cylinder driven flow in the zone-2. Comparison of Figures 3.63(f) and 3.14(b) shows that the mean flow in the upper field more closely resembles that of the TCF case with flow contouring around the upper edge of the cylinder before entering into the annulus, thus reducing the momentum of

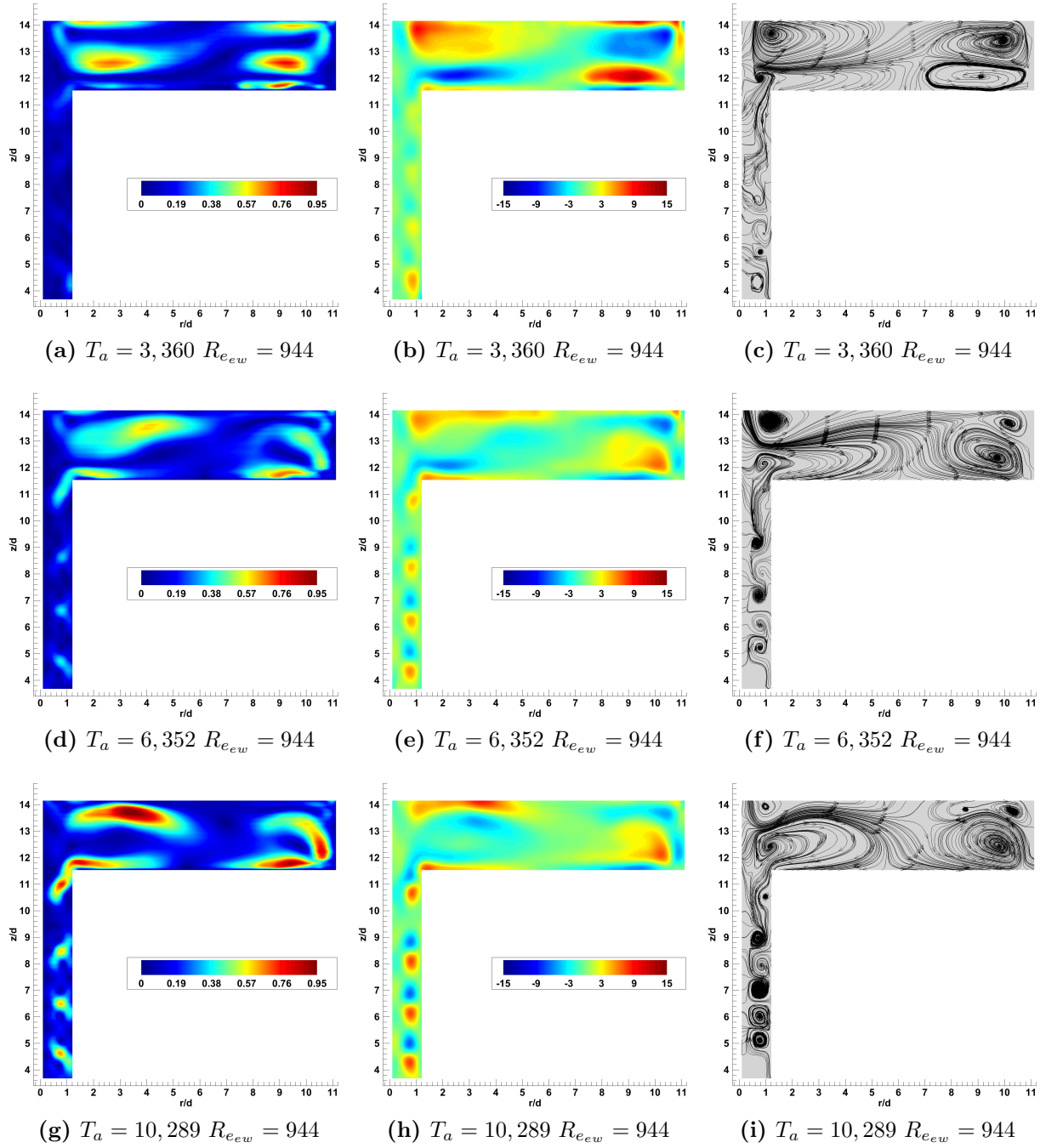

(a) $T_a = 3,360$ $R_{e_{ew}} = 944$ **(b)** $T_a = 3,360$ $R_{e_{ew}} = 944$ **(c)** $T_a = 3,360$ $R_{e_{ew}} = 944$

(d) $T_a = 6,352$ $R_{e_{ew}} = 944$ **(e)** $T_a = 6,352$ $R_{e_{ew}} = 944$ **(f)** $T_a = 6,352$ $R_{e_{ew}} = 944$

(g) $T_a = 10,289$ $R_{e_{ew}} = 944$ **(h)** $T_a = 10,289$ $R_{e_{ew}} = 944$ **(i)** $T_a = 10,289$ $R_{e_{ew}} = 944$

Figure 3.63: Counter-rotational mean flow, velocity contours (left), non-dimensionalized vorticity $[\frac{\omega \hat{\mathbf{d}}}{2\Omega_I R_I}]$ (middle), streamlines (right), at $\Gamma_{ew} = 0.5$

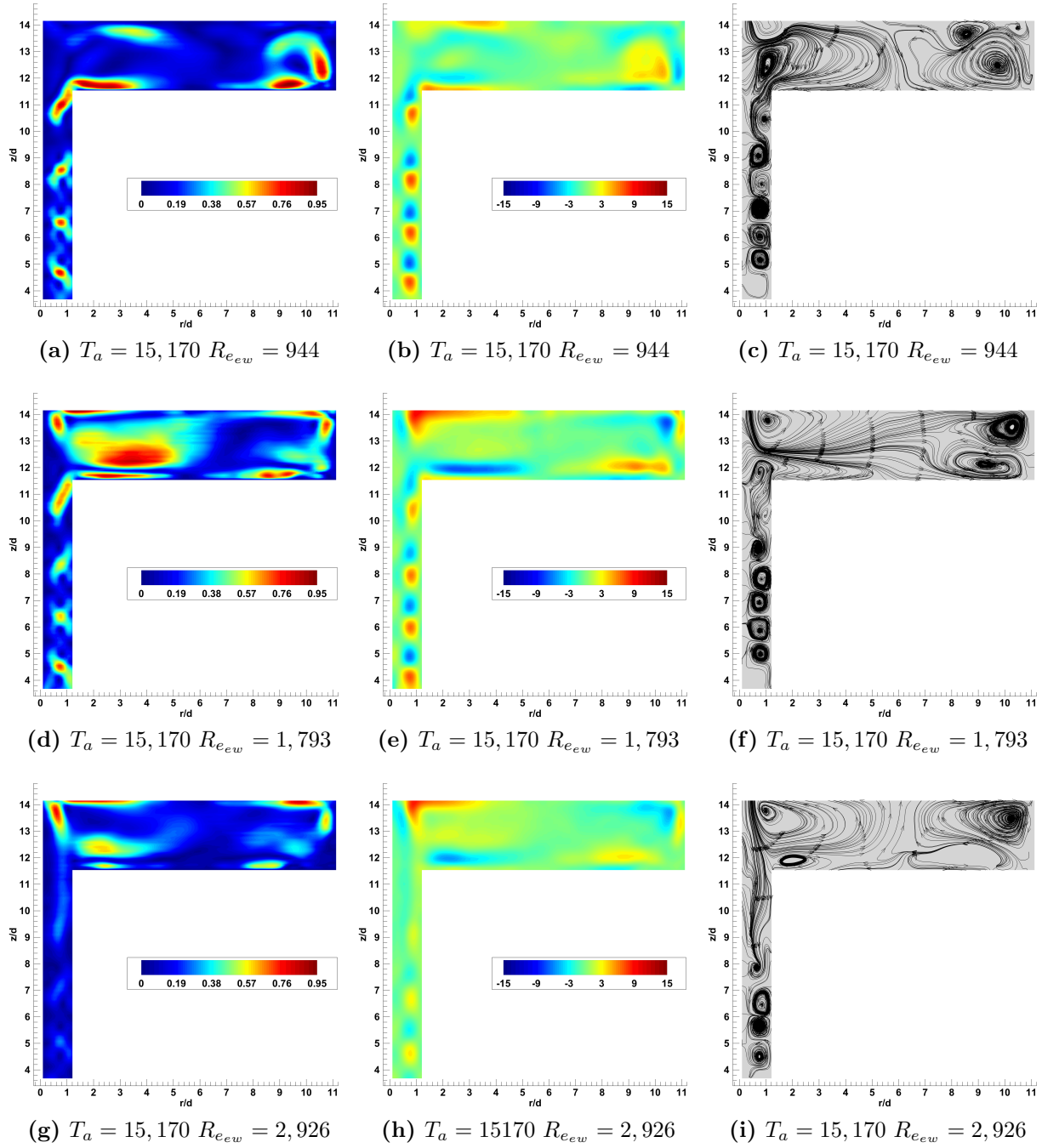

(a) $T_a = 15,170$ $R_{e_{ew}} = 944$ **(b)** $T_a = 15,170$ $R_{e_{ew}} = 944$ **(c)** $T_a = 15,170$ $R_{e_{ew}} = 944$

(d) $T_a = 15,170$ $R_{e_{ew}} = 1,793$ **(e)** $T_a = 15,170$ $R_{e_{ew}} = 1,793$ **(f)** $T_a = 15,170$ $R_{e_{ew}} = 1,793$

(g) $T_a = 15,170$ $R_{e_{ew}} = 2,926$ **(h)** $T_a = 15170$ $R_{e_{ew}} = 2,926$ **(i)** $T_a = 15,170$ $R_{e_{ew}} = 2,926$

Figure 3.64: Counter-rotational mean flow, velocity contours (left), non-dimensionalized vorticity $[\frac{\omega \hat{\mathbf{d}}}{2\Omega_I R_I}]$ (middle), streamlines (right), at $\Gamma_{ew} = 0.5$

encroaching fluid. Although TV stability and vorticity increased as T_a increased, the number of observable vortex pairs was always seen to be less than that of the other two rotational cases. At $\Gamma_{ew} = 0.5$, $T_a \geq 10,289$ four vortex pairs were seen to form in the annulus at both TCF and co-rotational conditions. Mean flow plots of the counter-rotational case however display only three visible vortex pairs. In many instances the vortices that were seen to form in the counter-rotation case were highly elongated, and found to be $\approx 40\%$ larger than those of the TCF case.

POD counter-rotational modes 1 and 3 results for $\Gamma_{ew} = 0.5$ are presented in Figures C.1 - C.4, mode-1 plots show a significant increase in fluid exchange between end-wall and cylinder driven flows in the zone-2. Comparison of Figures A.1, C.1, and 3.15 show zone-2 vortices in the counter-rotational case to be greatly elongated in the radial direction. Elongation is most apparent in Figures C.1 (a-c) and is seen to be accompanied by an inward radial displacement due to the reduced diameter of the central core; which in turn allowed for greatly increased axial flow into the annulus seen in the streamline plot. Mode-1 results were also noted to display relatively few areas of recirculation within the zone-2 core when compared to co-rotational results. In fact results were found to more closely resemble VB mode-1 results in the zone-2 than any other test case; displaying small regions of recirculation near the core positions next to one of the rotating surfaces (Figures C.2 (c) and (i)). However unlike VB results recirculating regions near the core were predominantly found to be the result of either cylinder or end-wall driven corner vortices being displaced radially inward as was noted in counter-rotational mean flow results and not necessarily a VBB like structure. POD mode-3 Figures C.3 and C.4 were found to display additional areas of core recirculation and in some instances (Figure C.3 (i)) show the same horizontally aligned core vortices that were found in the higher modal results of $\Gamma_{ew} = 0.5$ co-rotation.

Annular flow at modes 1 and 3 more clearly showed the effects that increased axial flow, noted to occur in mean flow results, had on Taylor vortex structure. A progression form $T_a = 3,360$ $R_{e_{ew}} = 944$ to $T_a = 35,485$ $R_{e_{ew}} = 944$ in the plots of Figure C.1 clearly shows

increased domain segregation at increasing T_a values, specifically in the streamlines of Figure C.1 (f) where the presence of increased TV circulation is seen to impede axial flow from the zone-2 resulting in a nearly straight flow barrier at $z/\hat{d} \approx 11$. These results helped to further explain the mechanics behind the increased stability of TV structures at increasing T_a values that was seen in mean flow results, as being a combination of increased TV circulation as well as a progressive outward radial movement of zone-2 vortices. From Figure C.3 mode-3 annular results are seen to display a much more complex flow than either modes 0 or 1. Figures C.3 (e), (h), and (i) show indications of potential flow oscillation displaying TV structures similar to those seen in mode-3 results at $\Gamma_{ew} = 1$ co-rotational conditions (Figure A.8 (i)) in the former, and elongated negative vortices as well as a positive axial flow reversal at $z/\hat{d} \approx 7.5 - 11.5$ in the later 2 plots respectively. Additionally the streamlines of Figure C.3 (i) show TVs between $z/\hat{d} \approx 6.5 - 4.5$ to have an alternating $\pm$ radial displacement between vortex pairs, resembling a subdued version of the streamlines seen in mode 1 and 3 results at TCF $\Gamma_{ew} = 1.5$; (Figures 3.36 (b) and (h)). Increases in $R_{e_{ew}}$ for both modes 1 and 3 at constant $T_a = 15,170$ were found to highlight the destabilizing effects of increased axial flow encroachment as a result of greater end-wall rotation rates. Comparison of Figures C.1 (d-f) and C.2 show a progressive increase in axial fluid penetration from the zone-2, ranging form $\approx 0.5d$ at $R_{e_{ew}} = 944$ to as much as $\approx 6.5d$ at $R_{e_{ew}} = 2,926$, as a percentage of annulus length theses depths correspond to $\approx$ 4.35% and $\approx$ 56.52% respectively. While mode-3 showed slightly less penetration, ranging form $\approx 0.5d - 5.3d$, as with mean flow results this increased encroachment was found to reduce TV circulation in both of the higher modes presented. Additionally mode-1 results were found to display a progressive elongation in Taylor vortex structure between $z/\hat{d} \approx 11.5 - 7$ eventually resulting in a complete absence in the streamlines of Figure C.2 (i) at $R_{e_{ew}} = 2,92$.

$\Gamma_{ew} = 1$ mean flow plots show similar trends as those found at $\Gamma_{ew} = 0.5$. At $T_a = 1,312$ a large amount of flow encroachment from the zone-2 into the annulus was observed. From Figure 3.65 (a) this encroachment is noted to extend down to $z/\hat{d} \approx 7$; which was only

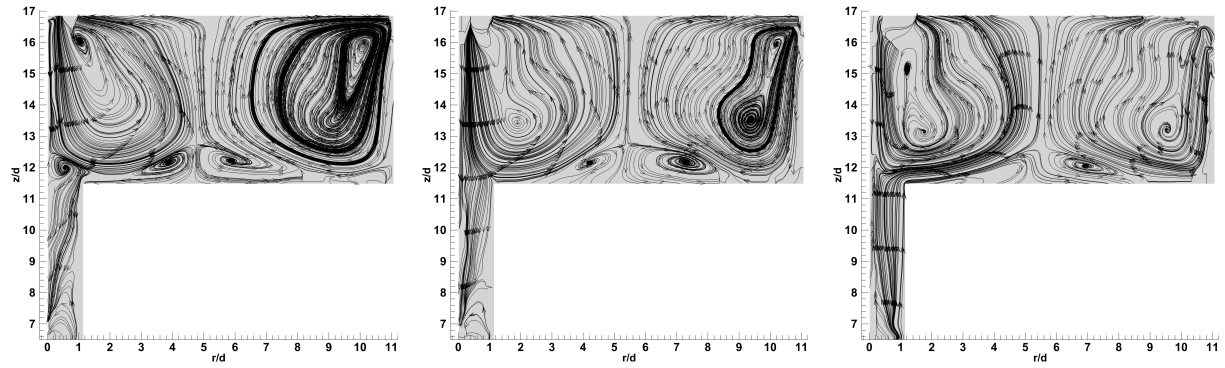

(a) $T_a = 1,312$ $R_{e_{ew}} = 1,227$ **(b)** $T_a = 1,312$ $R_{e_{ew}} = 1,793$ **(c)** $T_a = 1,312$ $R_{e_{ew}} = 2,643$

Figure 3.65: Counter-rotational mean flow, streamlines for varying $R_{e_{ew}}$ at $\Gamma_{ew} = 1$

slightly further than that seen at TCF conditions. Similar to $\Gamma_{ew} = 0.5$ counter-rotation results penetration depth was found to increase as end-wall rotation increased and at $R_{e_{ew}}$ values of $2,643$ & $2,926$ maximum flow penetration was found to occur at $z/\hat{d} = 6$, (Figure 3.66(c)). This resulted in a penetration range of $30\% - 37\%$, as a percentage of total annulus length. Comparison of this penetration range with that of $\Gamma_{ew} = 0.5$ showed that the increase in aspect ratio reduced the momentum of end-wall driven flow as it moved towards the domain interface, additionally reducing the effects of end-wall rotational changes in regards to annular encroachment. This was most likely due to the increased distance for which the flow had to travel resulting in a larger boundary layer on the side walls of the outer cylinder. There was one notable discrepancy that was observed at higher $R_{e_{ew}}$ numbers. In Figure 3.65 (c) streamlines display a positive axial flow moving from the annulus into the zone-2, a reversal that was first noted to occur at $R_{e_{ew}} = 2,077$ for $T_a = 1,312$. Streamlines from Figure 3.66 however only show negative axial flow, a result that was found at all T_a $R_{e_{ew}}$ combinations. This discrepancy was most likely a result of the averaging scheme used in the POD calculations. Further invention at higher modes indicated that there was in fact a combination of both positive and negative axial flow between the two domains. However since the positive axial flow was more prevalent in the upper half of the annulus it only appears in the mean flow of Figure 3.65 (c) while only small positive axial movements of the Taylor vortices was noted to occur within the annular mean flow.

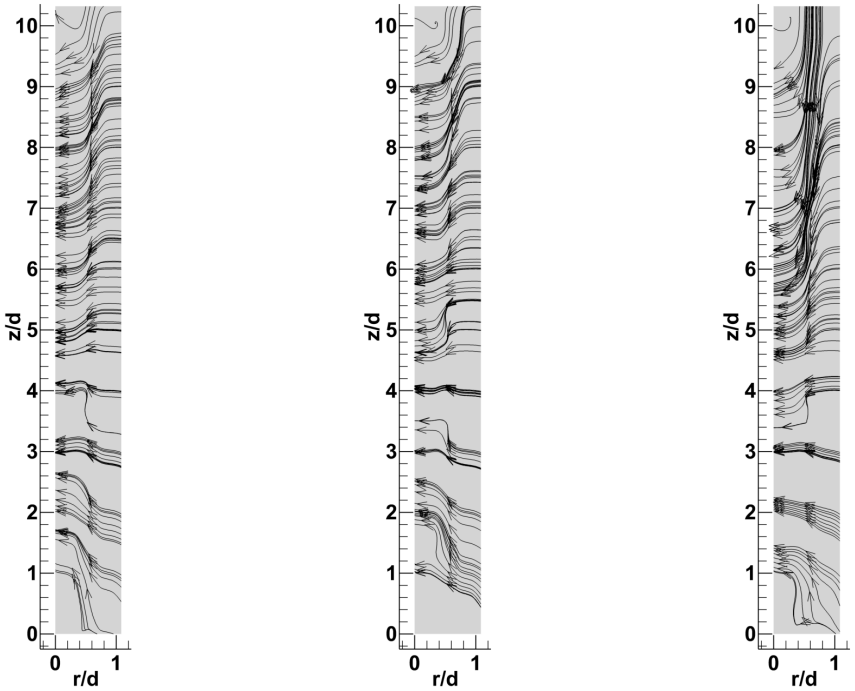

(a) $T_a = 1,312$ $R_{e_{ew}} = 1,227$ **(b)** $T_a = 1,312$ $R_{e_{ew}} = 1,793$ **(c)** $T_a = 1,312$ $R_{e_{ew}} = 2,643$

Figure 3.66: Counter-rotational mean flow, streamlines for varying $R_{e_{ew}}$ at $\Gamma_{ew} = 1$

Circulation within the central core was found to be similar to that seen at $\Gamma_{ew} = 0.5$, with the more dominate circulation of either end-wall or cylinder driven flow drew the weaker flow radially inward towards the centerline; resulting in a relatively narrow high velocity central core when compared to $\Gamma_{ew} = 1$ TCF results. However unlike the flow seen at $\Gamma_{ew} = 0.5$ not all of the zone-2s cylinder driven flow was drawn into the central core at lower T_a numbers. Instead it was found to be bisected by end-wall driven circulation such that four vortical loci were created; two near the centerline and two near the side walls directly above the annulus. This resulted in two saddle like formations on either side of the central axis, as seen in Figure 3.65 (a). Increasing T_a to $15,170$ caused these saddle formations to begin forming near the upper end-wall, as Reynolds number ratios became of the form $R_{e_{tcvb}}/R_{e_{ew}} > 1$.

One of the more notable differences found between $\Gamma_{ew} = 1$ counter-rotational results and the other two rotational conditions was the absence of any recirculating regions in the central core. It was also noted that counter-rotation did not result in any significant level

of flow destabilization in the upper field. This increased stability in the upper field, when compared to co-rotation, most likely stemmed form the fact that central core circulation produced by both the end-wall and cylinder was in a complementary direction.

Taylor vortices were found to more closely resemble the $\Gamma_{ew} = 1$ TCF case, at initial onset, than that of co-rotation. Onset occurred at $T_a = 3,360$ with six visible vortex pairs, as seen in Figure 3.71 (a) & (b). These initial vortices were found to have the same level of vorticity and generally slanted shape as those found at TCF conditions. As with all other test cases increases in $R_{e_{ew}}$ resulted in a negative axial travel of the TVs, however at $R_{e_{ew}} = 1,793$, (Figure 3.67), a large positive axial shift occurred. This positive shift was much larger than that of any other rotational conditions previously described and resulted in a significant structural change to the Taylor vortices. Vortex formation began to resembled that of the co-rotation case at $\Gamma_{ew} = 1$, $T_a = 3,360$ (Figure 3.49(a) & (b)) with a notable reduction in the number of vortex pairs from 6 to 5. Increases in $R_{e_{ew}}$ beyond $1,793$ resulted in further positive axial movement and reductions in vortex pairs; with only 3.5 pairs visible in Figure 3.67 (f).

Taylor numbers beyond $3,360$ resulted in more stable Taylor vortices and increased vorticity. However unlike the co-rotation and TCF cases, as $R_{e_{ew}}$ was increased a critical point was reached where TV stability and vorticity dramatically decreased as it did at the $T_a = 3,360,\ R_{e_{ew}} = 1,793$ condition. In all instances these decreases in vortex stability and vorticity were accompanied by a sudden positive axial shift in TV location. After such a point was reached further increases in $R_{e_{ew}}$ resulted in increased positive axial travel and progressive reductions in vorticity, leading to the eventual destruction of one or more vortex pairs, predominantly occurring in the range between $z/\hat{d} = 6 - 11$. The $R_{e_{ew}}$ number at which these sudden shift occurred was found to increase as T_a increased. The cause of these axial shifts was likely due to the inward radial shift of cylinder driven flow in the zone-2 as end-wall driven circulation became more dominant. This lead to an unobstructed flow path between the zone-2 and the annulus allowing for increased axial flow similar to the results

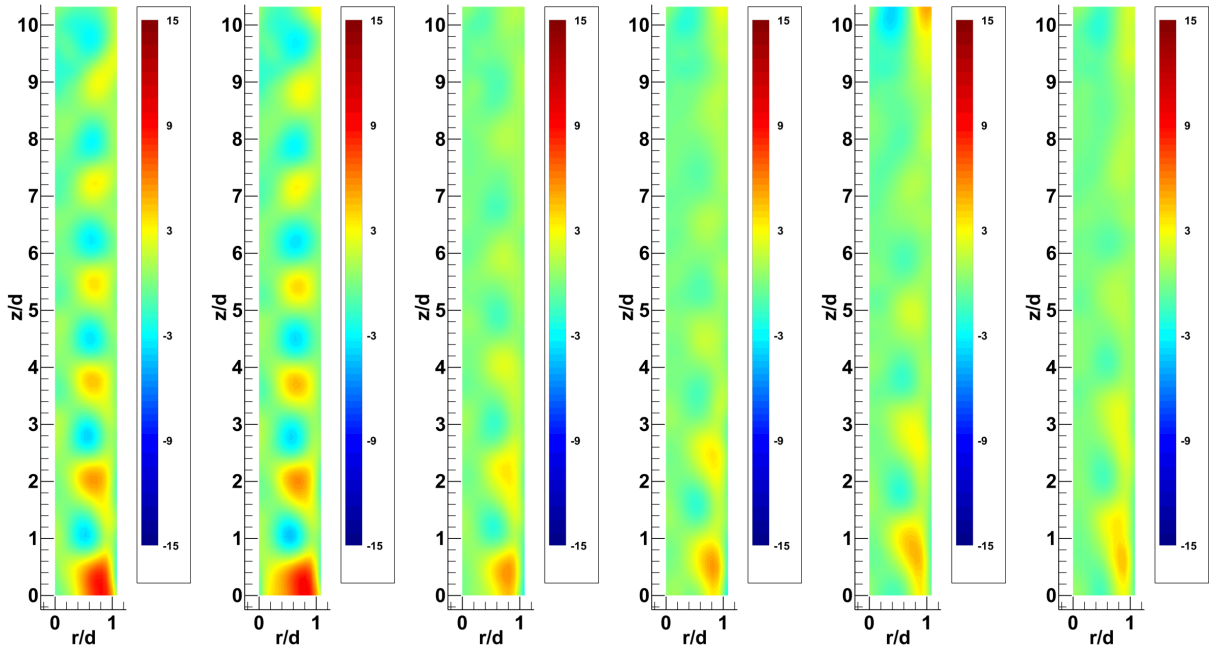

(a) $R_{e_{ew}} = 1,227$ **(b)** $R_{e_{ew}} = 1,510$ **(c)** $R_{e_{ew}} = 1,793$ **(d)** $R_{e_{ew}} = 2,076$ **(e)** $R_{e_{ew}} = 2,360$ **(f)** $R_{e_{ew}} = 2,643$

Figure 3.67: Counter-rotational mean flow, non-dimensionalized vorticity $[\frac{\omega \hat{\mathbf{d}}}{2\Omega_I R_I}]$ for varying $R_{e_{ew}}$ at $T_a = 3,360$ at $\Gamma_{ew} = 1$

found at $\Gamma_{ew} = 0.5$ for modes 1 and 3. The direction of this axial flow is seen to vary in the streamline plots of Figures 3.65, 3.66, 3.68 and 3.69; however, as previously stated, actual flow direction was most likely a combination of both positive and negative axial flow.

For Taylor numbers above $6,352$ the number of visible vortex pairs, and their respective size, was noted to decrease and increase, respectively. Figures 3.71(e)-(l) displays a progressive reduction in the number of vortex pairs from $5-4$ as T_a increased. This occurred even at the lowest $R_{e_{ew}}$ number of 944, and thus was not due to any increase in end-wall driven axial flow. Analysis of the zone-2 at these conditions showed a decrease in vorticity near the top of the annulus as cylinder driven circulations began to move in the positive axial direction towards the upper wall. This most likely resulted in a momentum loss to cylinder driven circulations as fluid began to be drawn upward towards the rotating end-wall. Ultimately this transfer of momentum and vorticity resulted in an extremely weak pseudo-Eckman cell near the top of the annular gap. Eventually this resulted in an imbalance between the top

(pseudo) and bottom Eckman cells causing vortices further down within the annulus to become dominant; merging with those above until TV vorticity was relatively balanced and ultimately elongated.

Modes 1 & 3 results for counter-rotation at $\Gamma_{ew} = 1$ showed a significantly more complex flow structure than mean flow results indicated; most notably in the zone-2. Figures C.5-C.8 display areas of recirculation in the zone-2 core, while these core structures are not as consistent in their radial position as those at co-rotational conditions their relative vorticity is noted to be larger in both modes 1 & 3 results. As with $\Gamma_{ew} = 0.5$ counter-rotation results radial position of zone-2 vortices was found to be a major factor in the strength and depth of fluid encroachment into the annulus. Streamline and vorticity plots in Figures C.6 and C.8 at increasing $R_{e_{ew}}$ values show a generally progressive increase in flow penetration. However this penetration in modes 1 & 3 was noted to be significantly less than $\Gamma_{ew} = 0.5$ results, especially at lower $R_{e_{ew}}$ values and increasing T_a values of Figures C.5 and C.7 indicating that the presence of recirculation within the core of the zone-2 most likely prevented end-wall and cylinder driven vortices from moving radially inward to the same extend as $\Gamma_{ew} = 0.5$ counter-rotation.

Flow results further down within the annulus for $\Gamma_{ew} = 1$ counter-rotation were found to closely resemble flow structures found at TCF conditions for modes 1 & 3 and Taylor numbers between $3,360 - 15,170$. Comparisons of Figures 3.32, B.2 and D.2 show that both vorticity and streamlines for counter-rotational conditions more closely resemble the $\Gamma_{ew} = 1$ baseline than co-rotational results. At $T_a = 3,360$ mode-1 streamlines in Figure D.5 (b) show a nearly identical flow penetration depth as TCF streamlines at similar conditions; reaching $z/\hat{d} \approx 7$ approximately 80% greater than co-rotational results. Additionally mode-1 vorticity displayed in Figure D.2 (a) is noted to be only 3.3% greater than TCF results while co-rotation was found to be 13.3% less; however it was noted that in all 3 $\Gamma_{ew} = 1$ rotational cases vorticity at $T_A = 3,360$ mode-1 was found to be greater than mean flow values. Similarly mode-3 results presented in Figures D.2 (g-l) show flow structures very

similar to those seen in TCF results with only a slight increase in TV axial elongation. Beyond $T_a = 15,170$ however TV structure at higher modes become more distorted and in many instances, such as that presented in Figures D.5 (k-l), vortices began to resemble an enhanced form of alternating elongated TVs found in co-rotational results (Figure B.2 (k-l)). Comparison of the aforementioned figures shows counter-rotational TVS to be $\approx 30\%$ larger in the axial direction, with a notable absence of positive Taylor vortices as well as a vast amount of vortical fluid exchange; which was not found in co-rotational results.

POD results for increasing $R_{e_{ew}}$ values at $T_a = 15,170$ for counter-rotation $\Gamma_{ew} = 1$ are presented in Figure D.3. From mode-1 results in plots (a-e) TVs are seen to be surprisingly structured relative to $\Gamma_{ew} = 1$ co-rotational mod-1 results, showing minimal axial flow effects and small radial displacements. Mode-3 results however (Figure D.3 (g-l)) showed a flow structure relatively similar to $\Gamma_{ew} = 1$ co-rotation mode-3 results. Flow structures seen in Figure D.3 (i) are of particular interest, displaying a less homogeneous form of the 3 horizontally aligned counter rotating vortices first noted in co-rotation results of Figure B.3. The presence of this formation in addition to the axial elongations of Figure D.5 (k) indicated that axial oscillation similar to those postulated to exist at co-rotational conditions also occurred for counter rotation. However due to the increased axial flow from the zone-2 counter-rotation resulted in much greater distortion of Taylor vortex structures.

Results for the $\Gamma_{ew} = 1.5$ test case are presented in Figures 3.73 - 3.78. At the initial conditions of $T_a = 1,312$, $R_{e_{ew}} = 944$ flow in the zone-2 resembled that of the $\Gamma_{ew} = 1$ test case previously discussed, with a much smaller vortex core in the area directly above the cylinder compared to the other rotational conditions at $\Gamma_{ew} = 1.5$. Additionally similar saddle shaped vortex structures for cylinder driven circulation are seen in Figure 3.73 (c). This flow also resulted in a central core with much higher velocities than the $\Gamma_{ew} = 1.5$ TCF case (Figure 3.73 (a)).

For Taylor numbers above $1,312$ flow in the zone-2 began to resemble a four rolls mill with a more typical flow structure than that seen to occur in the co-rotational case due

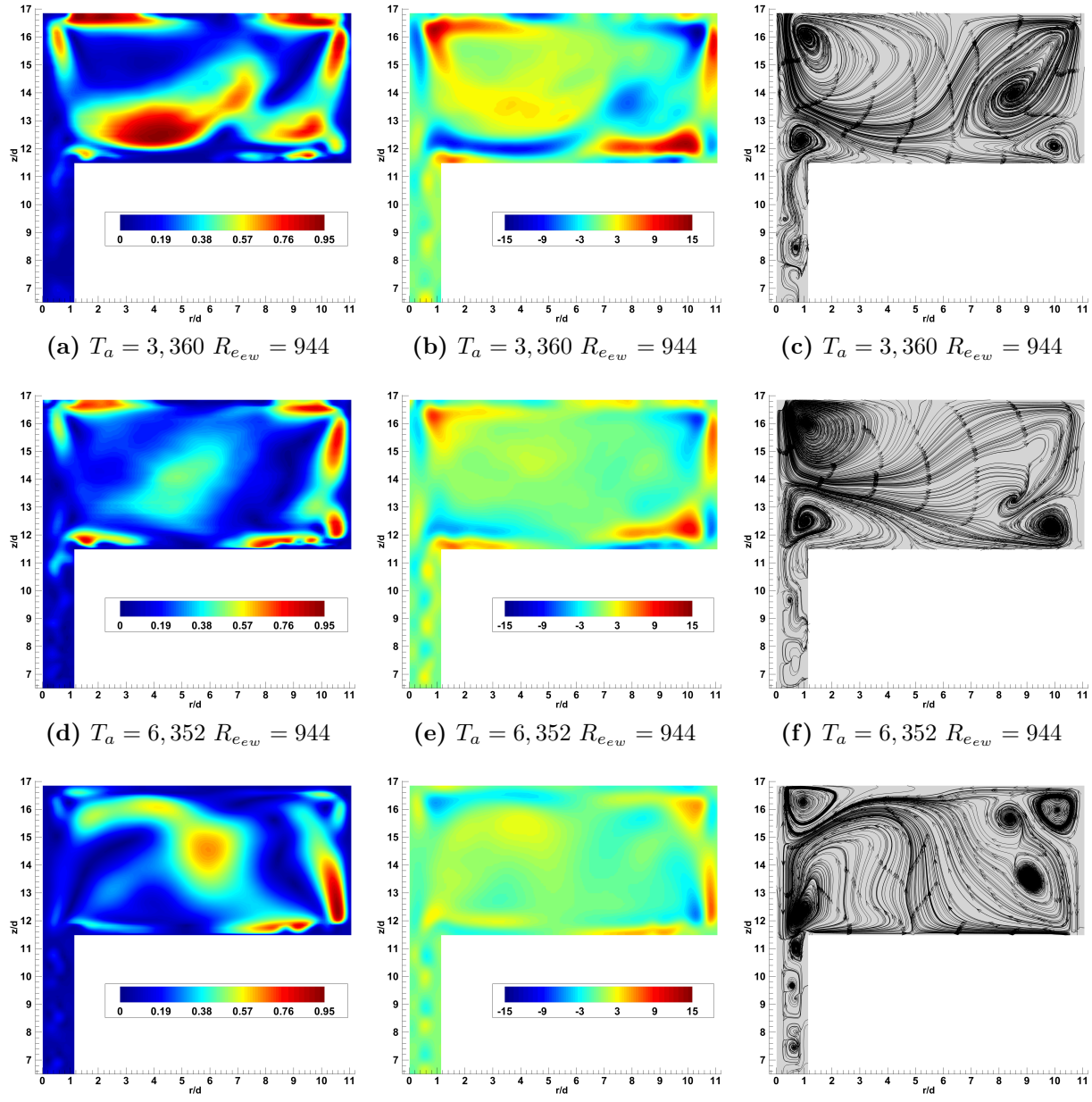

(a) $T_a = 3,360$ $R_{e_{ew}} = 944$ **(b)** $T_a = 3,360$ $R_{e_{ew}} = 944$ **(c)** $T_a = 3,360$ $R_{e_{ew}} = 944$

(d) $T_a = 6,352$ $R_{e_{ew}} = 944$ **(e)** $T_a = 6,352$ $R_{e_{ew}} = 944$ **(f)** $T_a = 6,352$ $R_{e_{ew}} = 944$

(g) $T_a = 10,289$ $R_{e_{ew}} = 944$ **(h)** $T_a = 10,289$ $R_{e_{ew}} = 944$ **(i)** $T_a = 10,289$ $R_{e_{ew}} = 944$

Figure 3.68: Counter-rotational mean flow, velocity contours (left), non-dimensionalized vorticity $[\frac{\omega \hat{\mathbf{d}}}{2\Omega_I R_I}]$ (middle), streamlines (right), for varying T_a at $\Gamma_{ew} = 1$

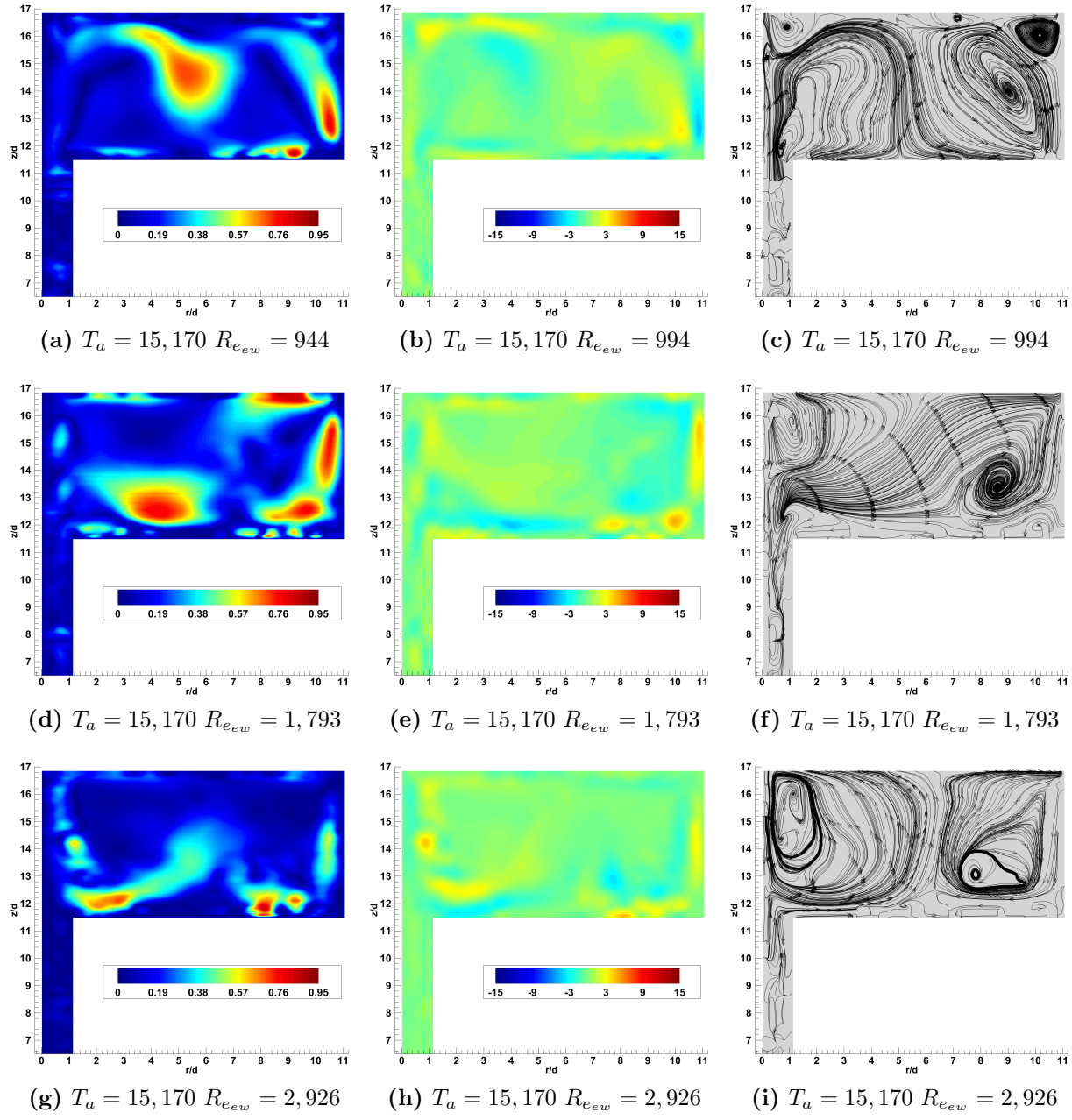

(a) $T_a = 15,170\ R_{e_{ew}} = 944$ **(b)** $T_a = 15,170\ R_{e_{ew}} = 994$ **(c)** $T_a = 15,170\ R_{e_{ew}} = 994$

(d) $T_a = 15,170\ R_{e_{ew}} = 1,793$ **(e)** $T_a = 15,170\ R_{e_{ew}} = 1,793$ **(f)** $T_a = 15,170\ R_{e_{ew}} = 1,793$

(g) $T_a = 15,170\ R_{e_{ew}} = 2,926$ **(h)** $T_a = 15,170\ R_{e_{ew}} = 2,926$ **(i)** $T_a = 15,170\ R_{e_{ew}} = 2,926$

Figure 3.69: Counter-rotational mean flow , velocity contours (left), non-dimensionalized vorticity $[\frac{\omega \hat{\mathbf{d}}}{2\Omega_I R_I}]$ (middle), streamlines (right), for varying $R_{e_{ew}}$ at $\Gamma_{ew} = 1$

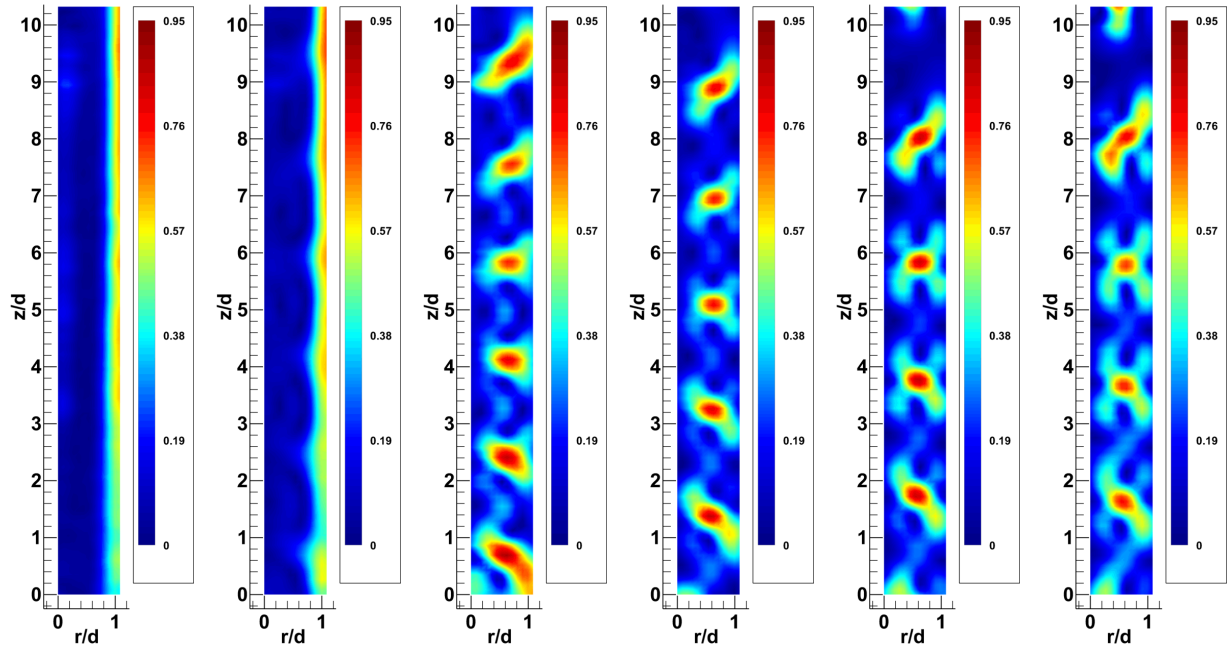

(a) $T_a = 1,312$, $R_{e_{ew}} = 944$ (b) $T_a = 3,360$, $R_{e_{ew}} = 944$ (c) $T_a = 6,352$, $R_{e_{ew}} = 944$ (d) $T_a = 10,289$, $R_{e_{ew}} = 944$ (e) $T_a = 2,0997$, $R_{e_{ew}} = 944$ (f) $T_a = 35,485$, $R_{e_{ew}} = 944$

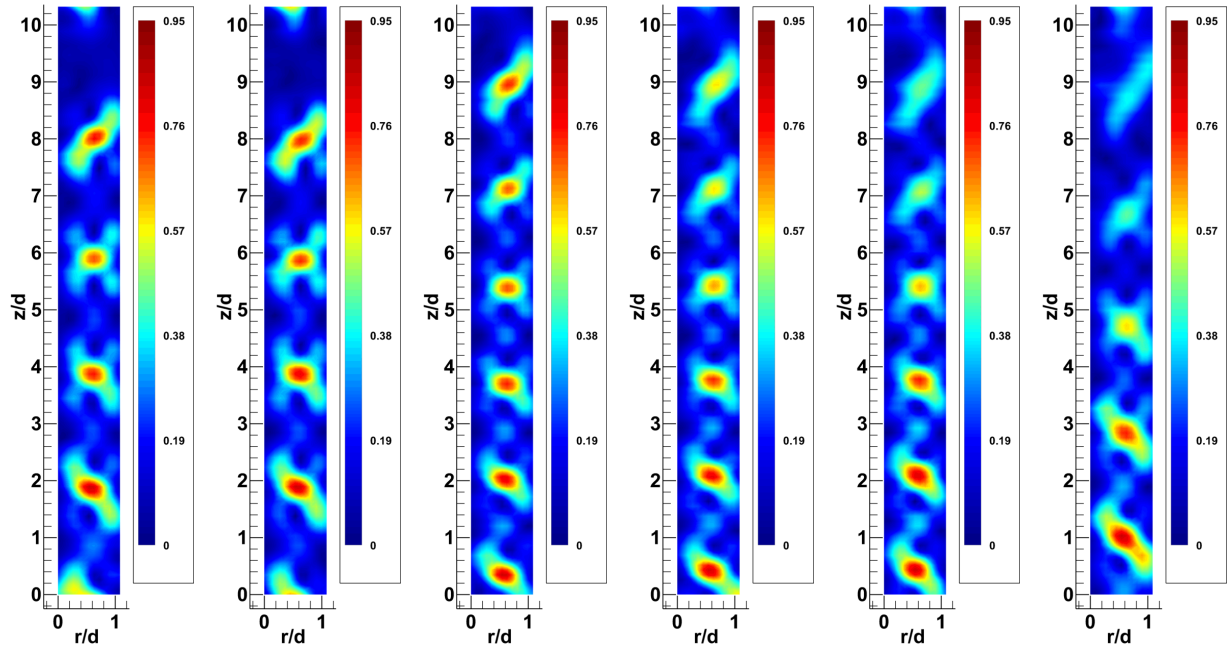

(g) $T_a = 15,170$, $R_{e_{ew}} = 944$ (h) $T_a = 15,170$, $R_{e_{ew}} = 1,227$ (i) $T_a = 15,170$, $R_{e_{ew}} = 1,793$ (j) $T_a = 15,170$, $R_{e_{ew}} = 2,076$ (k) $T_a = 15,170$, $R_{e_{ew}} = 2,360$ (l) $T_a = 15,170$, $R_{e_{ew}} = 2,926$

Figure 3.70: Counter-rotational mean flow, velocity contours, $(a)-(f)$ for varying T_a, $(g)-(l)$ for varying $R_{e_{ew}}$ at $\Gamma_{ew} = 1$

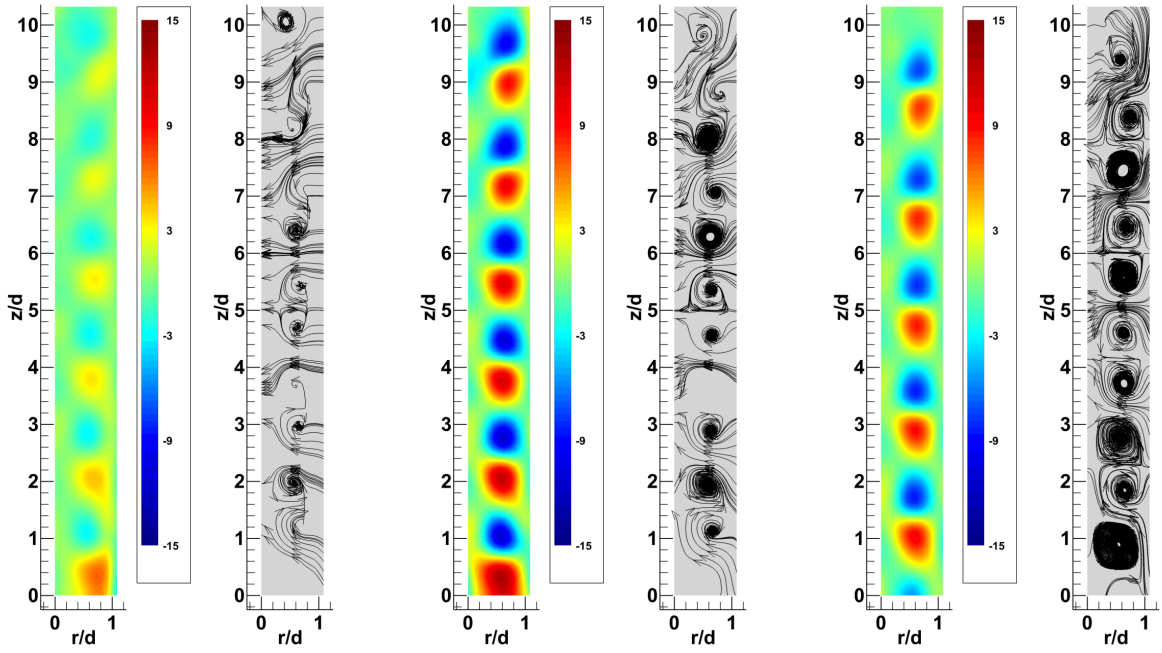

(a) $T_a = 3,360$ $R_{e_{ew}} = 944$ (b) $T_a = 3,360$ $R_{e_{ew}} = 944$ (c) $T_a = 6,352$ $R_{e_{ew}} = 944$ (d) $T_a = 6,352$ $R_{e_{ew}} = 944$ (e) $T_a = 10,289$ $R_{e_{ew}} = 944$ (f) $T_a = 10,289$ $R_{e_{ew}} = 944$

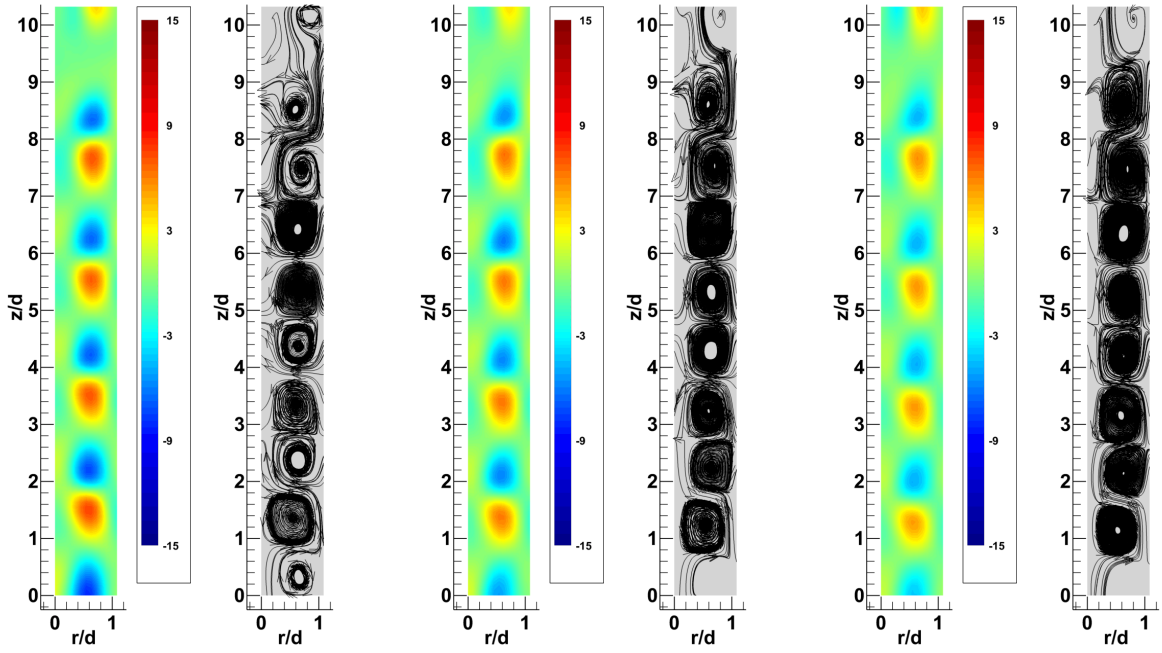

(g) $T_a = 15,170$, $R_{e_{ew}} = 944$ (h) $T_a = 15,170$, $R_{e_{ew}} = 944$ (i) $T_a = 27,769$, $R_{e_{ew}} = 944$ (j) $T_a = 27,769$, $R_{e_{ew}} = 944$ (k) $T_a = 35,485$, $R_{e_{ew}} = 944$ (l) $T_a = 35,485$, $R_{e_{ew}} = 944$

Figure 3.71: Counter-rotational annular mean flow, non-dimensionalized vorticity $[\frac{\omega \hat{\mathrm{d}}}{2\Omega_I R_I}]$ & streamlines, for varying T_a at $\Gamma_{ew} = 1$

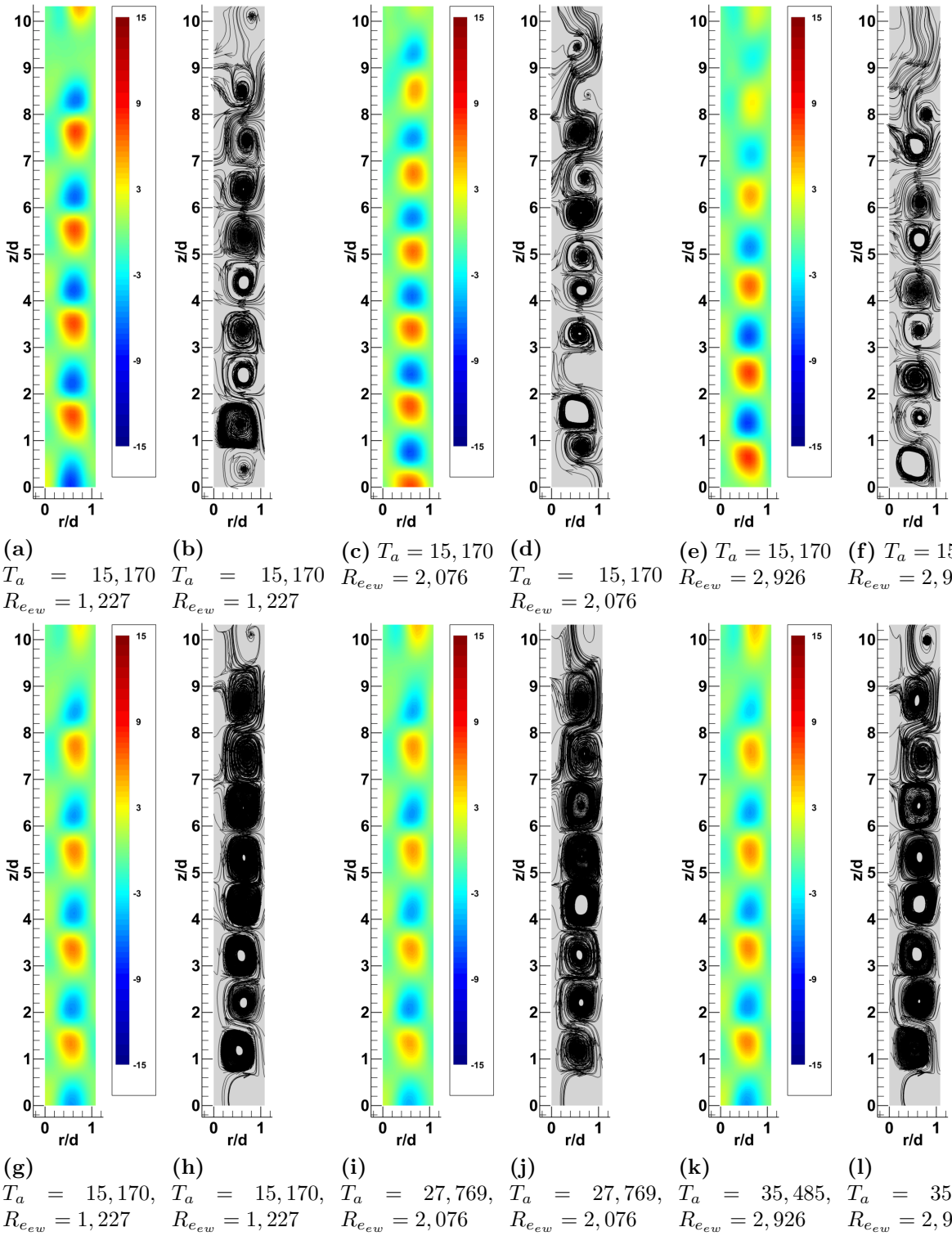

(a) $T_a = 15,170$ $R_{e_{ew}} = 1,227$ (b) $T_a = 15,170$ $R_{e_{ew}} = 1,227$ (c) $T_a = 15,170$ $R_{e_{ew}} = 2,076$ (d) $T_a = 15,170$ $R_{e_{ew}} = 2,076$ (e) $T_a = 15,170$ $R_{e_{ew}} = 2,926$ (f) $T_a = 15,170$ $R_{e_{ew}} = 2,926$

(g) $T_a = 15,170,$ $R_{e_{ew}} = 1,227$ (h) $T_a = 15,170,$ $R_{e_{ew}} = 1,227$ (i) $T_a = 27,769,$ $R_{e_{ew}} = 2,076$ (j) $T_a = 27,769,$ $R_{e_{ew}} = 2,076$ (k) $T_a = 35,485,$ $R_{e_{ew}} = 2,926$ (l) $T_a = 35,485,$ $R_{e_{ew}} = 2,926$

Figure 3.72: Counter-rotational annular mean flow, non-dimensionalized vorticity $[\frac{\omega \hat{\mathrm{d}}}{2\Omega_I R_I}]$ & streamlines, for varying $R_{e_{ew}}$ at $\Gamma_{ew} = 1$

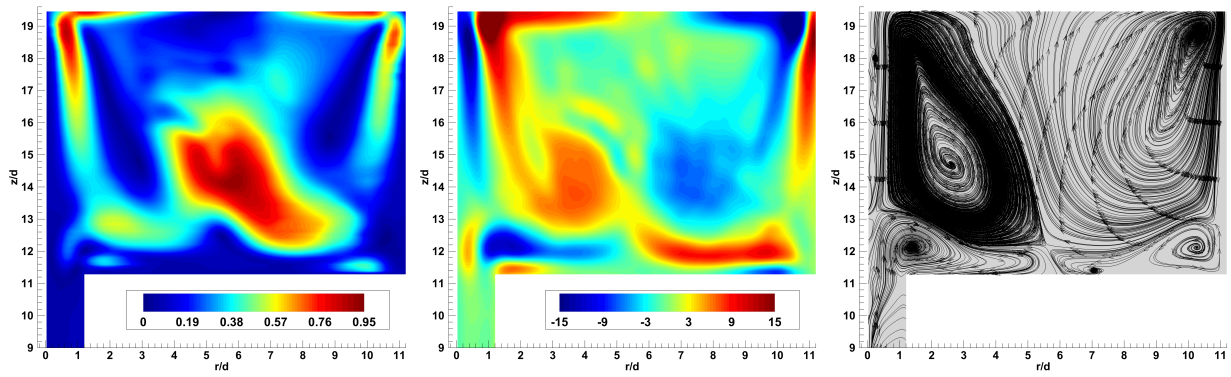

(a) $T_a = 1,312$, $R_{e_{ew}} = 944$ **(b)** $T_a = 1,312$, $R_{e_{ew}} = 944$ **(c)** $T_a = 1,312$, $R_{e_{ew}} = 944$

Figure 3.73: Counter-rotational mean flow streamlines, at $\Gamma_{ew} = 1.5$

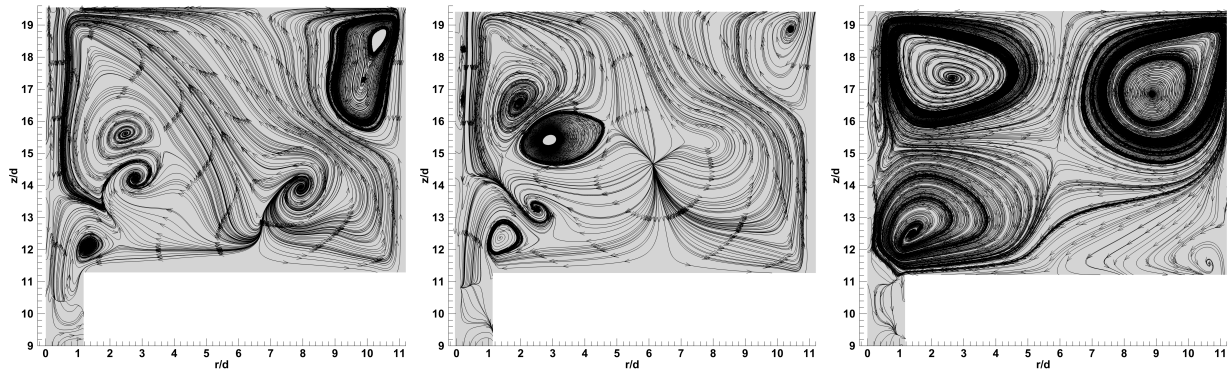

(a) $T_a = 6,352$, $R_{e_{ew}} = 1,510$ **(b)** $T_a = 10,289$, $R_{e_{ew}} = 1,510$ **(c)** $T_a = 15,170$, $R_{e_{ew}} = 1,510$

Figure 3.74: Counter-rotational mean flow streamlines, at $\Gamma_{ew} = 1.5$

to the coalescence of end-wall and cylinder driven cores. The most ideal example of this flow occurred at $T_a = 15,170$, $R_{e_{ew}} = 1,510$, and is presented in Figure 3.74 (c). This type of structure however, was only seen to occur at certain rotational combinations with no explicit Reynolds ratio found to cause its onset, but did tend towards conditions where rotational rates of the end-wall and cylinder were relatively similar. As with the $\Gamma_{ew} = 1$ case the recirculating regions seen in the central core at $\Gamma_{ew} = 1.5$ co-rotational conditions were not seen to occur in the mean flow of the present case. As such, vorticity in the zone-2 was found to generally consist of four vortical loci near the corners of the domain. Two notable exceptions were found to occur at $Ta = 6,352$ & $10,289$ for varying $R_{e_{ew}}$ numbers; were addition vortex loci where found to appear on either side of the rotational

axis, approximately $1.2d$ radially out. Most interestingly it was also at these Taylor numbers that Taylor vortices first began to show signs of instability and deformation. Figures 3.74 (a) & (b) display these additional zone-2 loci where the counter rotation of these vortices and the positive axial direction of flow from the annulus, gives the impression of TVs being drawn out of the annular gap and into the zone-2. However such flow movement could not be verified due to the time averaged nature of the data used in the present work. These fluctuations, as well as those seen in the test cases previously discussed, indicate that the flow with in the system was not entirely steady, but was instead extremely dynamic and may have in-fact been oscillatory in nature.

Mean flow within the annulus at $\Gamma_{ew} = 1.5$ for the counter-rotating case was found to be extremely dynamic and the most chaotic of all the configurations tested. Initial formation stilled occurred at $T_a = 3,360$, however as with counter-rotational conditions at $\Gamma_{ew} = 0.5$ & 1 vortex size was seen to be slightly larger than either the TCF or co-rotation cases. Number of visible vortex pairs was also found to be less, where form Figures 3.78, 3.47 and 3.35 only 5 pairs are visible in the former, while 6 pairs were seen to form in the latter two plots at the same conditions. Streamline plots in Figure 3.78 show that Taylor vortices formed with the same S like structure that was observed for the other two $\Gamma_{ew} = 1.5$ rotational conditions. Vortex pairs at $z/\hat{d} = 0 - 2$ and $z/\hat{d} = 8 - 10$ were also notably distorted and stretched in the axial direction. As $R_{e_{ew}}$ was increase the predominately negative axial movement of TV that was seen to occur for all configurations previously discussed, was also see to occur for the present configuration. However unlike other rotational conditions vortex structure did not remain entirely static. Vortices in the lower half of the annulus, between $z/\hat{d} = 0-5$, were seen to both increase and decrease in size and occasionally became displaced radially outward; doing so in an alternating fashion between pairs. These effect gave further credence to the assumption of flow osculations produced by conditions in the zone-2. At $R_{e_{ew}} = 2,926$ a drastic reduction in vorticity of approximately 70% was noted to occur. Most likely this was caused by an increased inward radial displacement of cylinder

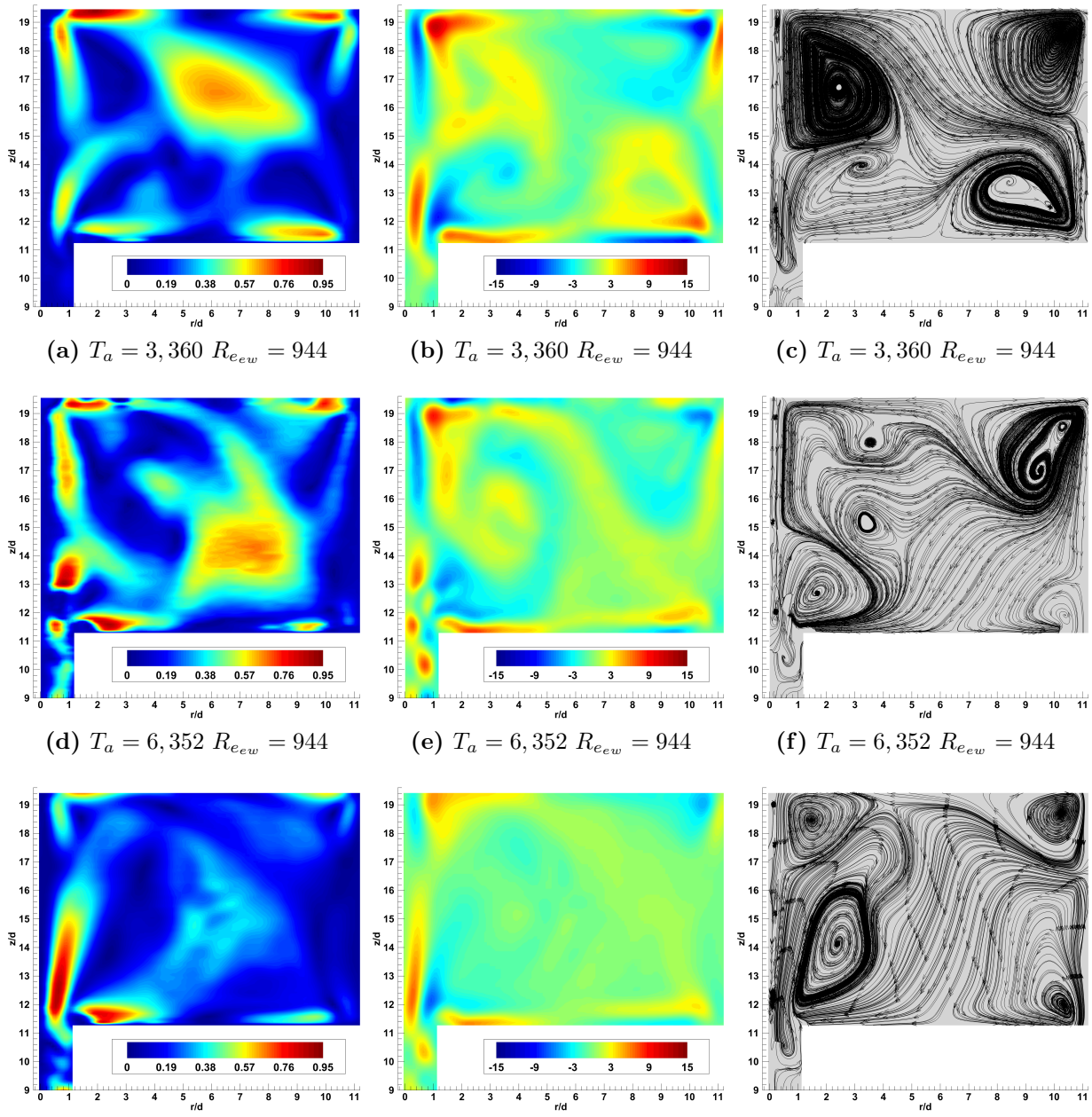

(a) $T_a = 3,360\ R_{e_{ew}} = 944$ **(b)** $T_a = 3,360\ R_{e_{ew}} = 944$ **(c)** $T_a = 3,360\ R_{e_{ew}} = 944$

(d) $T_a = 6,352\ R_{e_{ew}} = 944$ **(e)** $T_a = 6,352\ R_{e_{ew}} = 944$ **(f)** $T_a = 6,352\ R_{e_{ew}} = 944$

(g) $T_a = 10,289\ R_{e_{ew}} = 944$ **(h)** $T_a = 10,289\ R_{e_{ew}} = 944$ **(i)** $T_a = 10,289\ R_{e_{ew}} = 944$

Figure 3.75: Counter-rotational mean flow, velocity contours (left), non-dimensionalized vorticity $[\frac{\omega \hat{\mathbf{d}}}{2\Omega_I R_I}]$ (middle), streamlines (right), at $\Gamma_{ew} = 1.5$

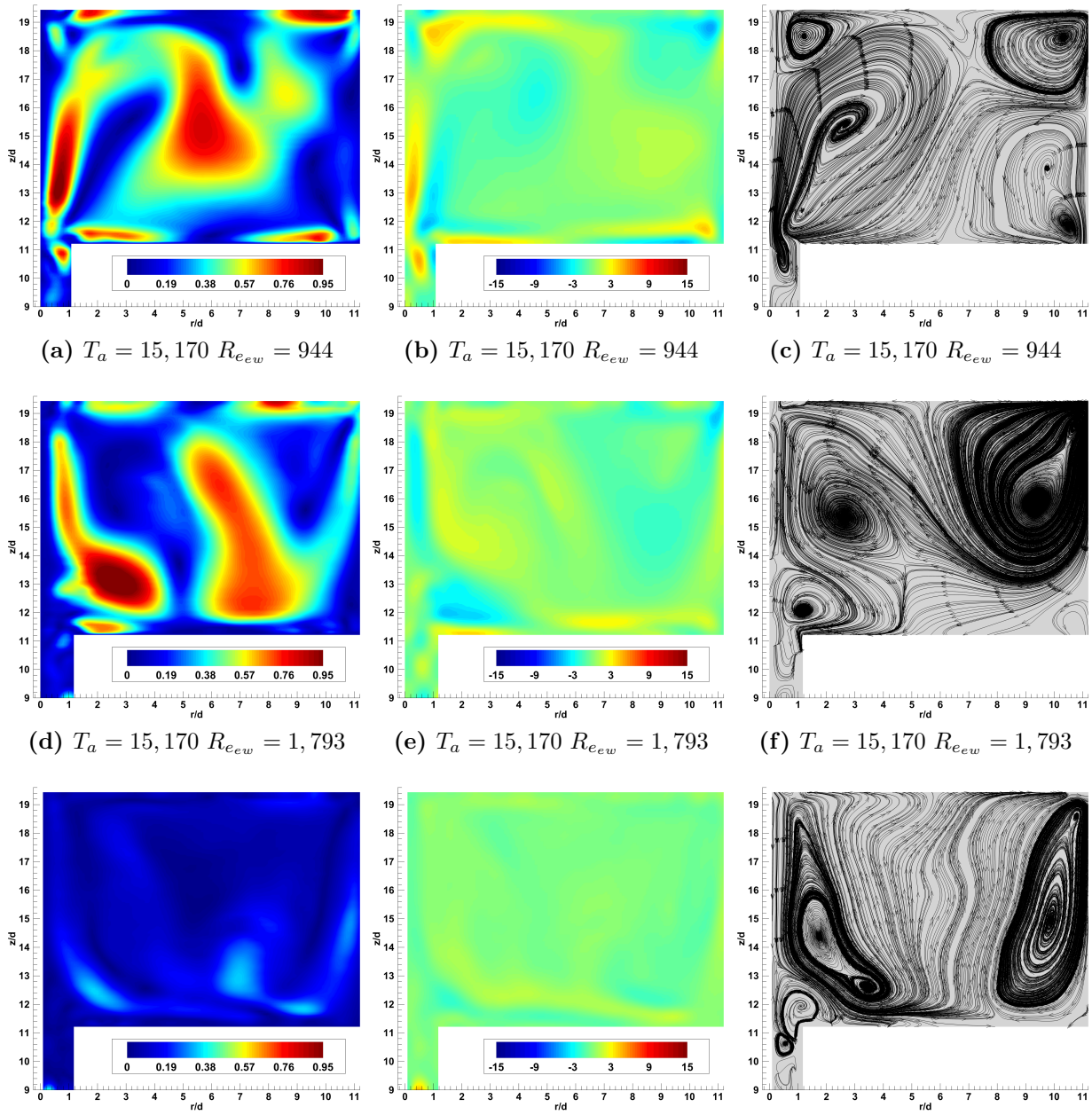

(a) $T_a = 15,170$ $R_{e_{ew}} = 944$ **(b)** $T_a = 15,170$ $R_{e_{ew}} = 944$ **(c)** $T_a = 15,170$ $R_{e_{ew}} = 944$

(d) $T_a = 15,170$ $R_{e_{ew}} = 1,793$ **(e)** $T_a = 15,170$ $R_{e_{ew}} = 1,793$ **(f)** $T_a = 15,170$ $R_{e_{ew}} = 1,793$

(g) $T_a = 15,170$ $R_{e_{ew}} = 2,926$ **(h)** $T_a = 15,170$ $R_{e_{ew}} = 2,926$ **(i)** $T_a = 15,170$ $R_{e_{ew}} = 2,926$

Figure 3.76: Counter-rotational mean flow, velocity contours (left), non-dimensionalized vorticity $[\frac{\omega \hat{\mathbf{d}}}{2\Omega_I R_I}]$ (middle), streamlines (right), at $\Gamma_{ew} = 1.5$

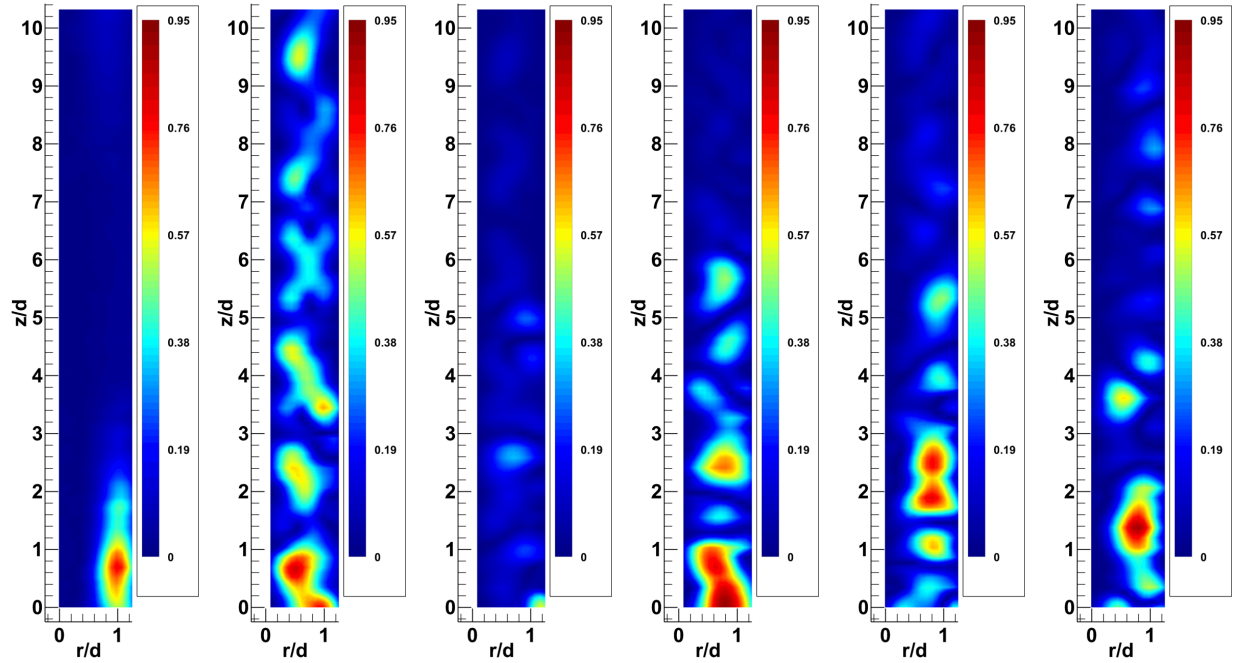

(a) $T_a = 1,312$, $R_{e_{ew}} = 944$ (b) $T_a = 3,360$, $R_{e_{ew}} = 944$ (c) $T_a = 6,352$, $R_{e_{ew}} = 944$ (d) $T_a = 10,289$, $R_{e_{ew}} = 944$ (e) $T_a = 20,997$, $R_{e_{ew}} = 944$ (f) $T_a = 35,485$, $R_{e_{ew}} = 944$

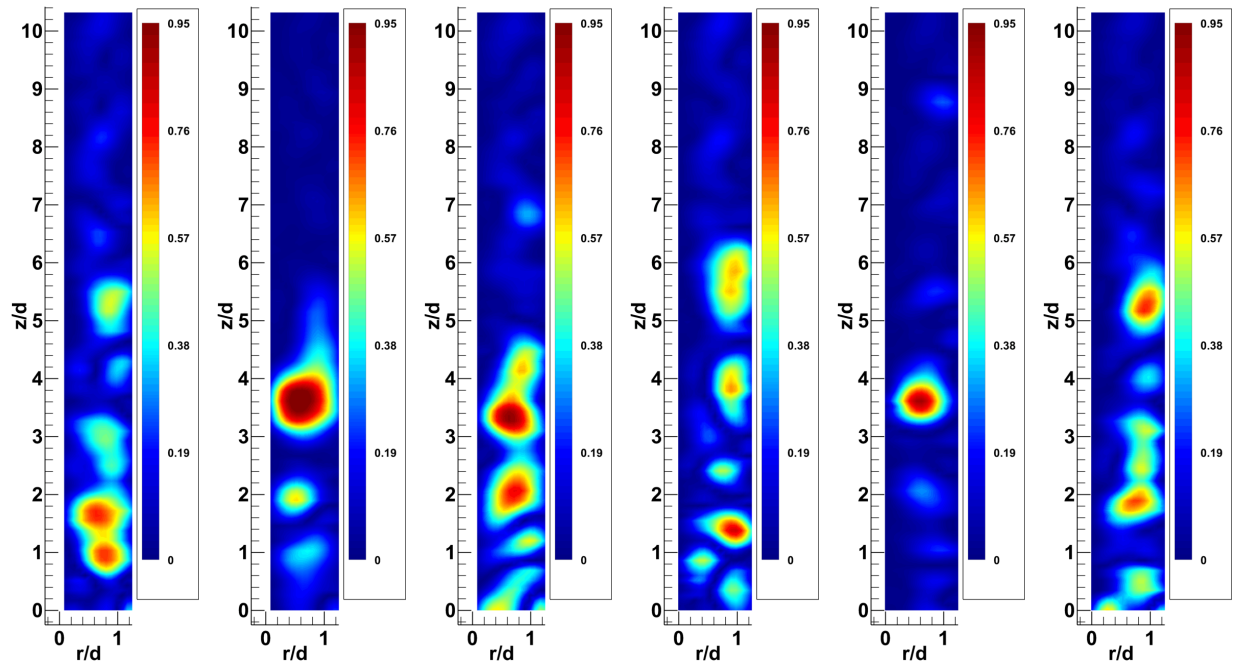

(g) $T_a = 15,170$, $R_{e_{ew}} = 944$ (h) $T_a = 15,170$, $R_{e_{ew}} = 1,227$ (i) $T_a = 15,170$, $R_{e_{ew}} = 1,793$ (j) $T_a = 15,170$, $R_{e_{ew}} = 2,076$ (k) $T_a = 15,170$, $R_{e_{ew}} = 2,360$ (l) $T_a = 15,170$, $R_{e_{ew}} = 2,926$

Figure 3.77: Counter-rotational annular mean flow, velocity contours, $(a) - (f)$ for varying T_a, $(g) - (l)$ for varying $R_{e_{ew}}$ at $\Gamma_{ew} = 1.5$

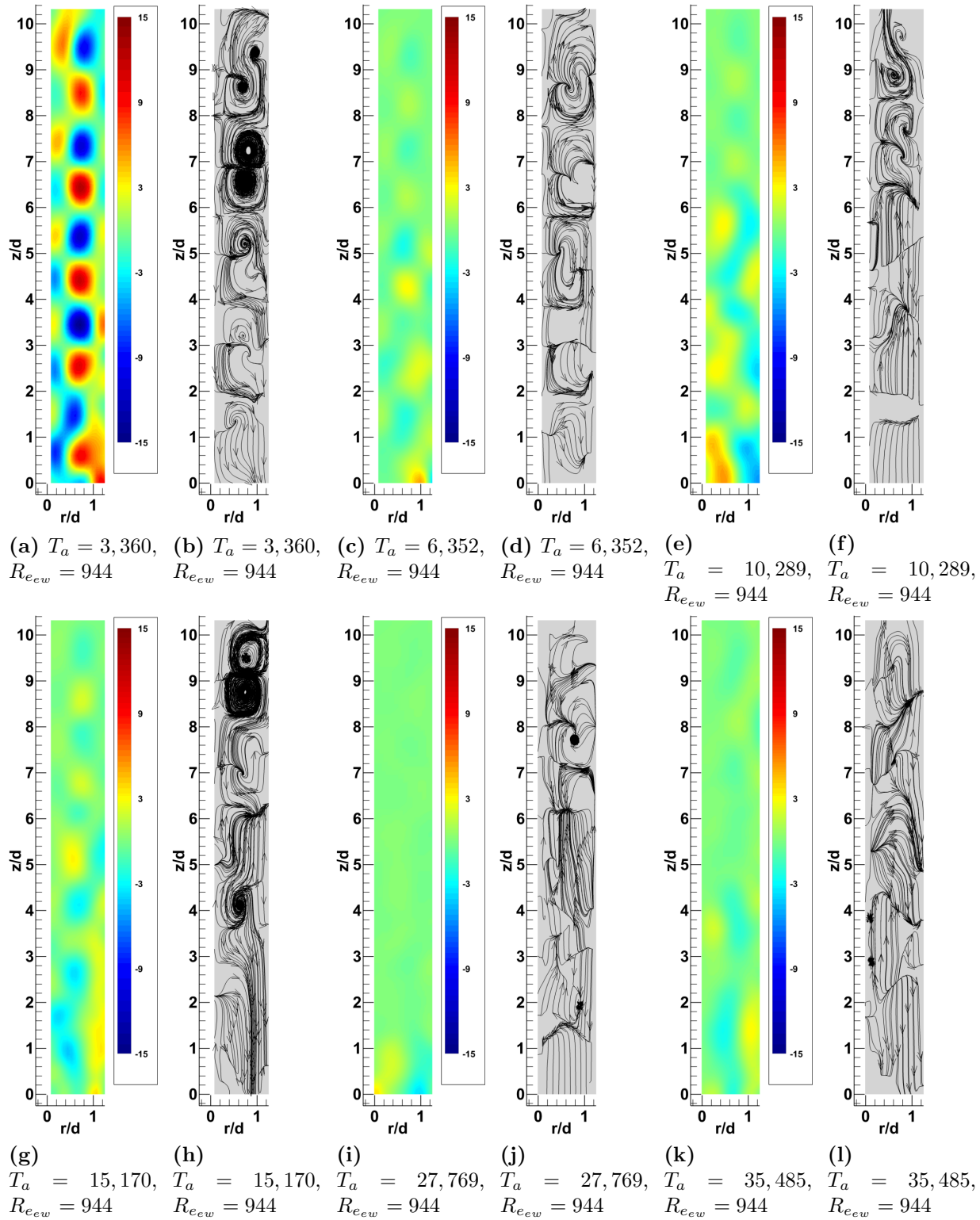

(a) $T_a = 3,360$, $R_{e_{ew}} = 944$ **(b)** $T_a = 3,360$, $R_{e_{ew}} = 944$ **(c)** $T_a = 6,352$, $R_{e_{ew}} = 944$ **(d)** $T_a = 6,352$, $R_{e_{ew}} = 944$ **(e)** $T_a = 10,289$, $R_{e_{ew}} = 944$ **(f)** $T_a = 10,289$, $R_{e_{ew}} = 944$

(g) $T_a = 15,170$, $R_{e_{ew}} = 944$ **(h)** $T_a = 15,170$, $R_{e_{ew}} = 944$ **(i)** $T_a = 27,769$, $R_{e_{ew}} = 944$ **(j)** $T_a = 27,769$, $R_{e_{ew}} = 944$ **(k)** $T_a = 35,485$, $R_{e_{ew}} = 944$ **(l)** $T_a = 35,485$, $R_{e_{ew}} = 944$

Figure 3.78: Counter-rotational annular mean flow, non-dimensionalized vorticity $[\frac{\omega \hat{\mathbf{d}}}{2\Omega_I R_I}]$ & streamlines, for varying T_a at $\Gamma_{ew} = 1.5$

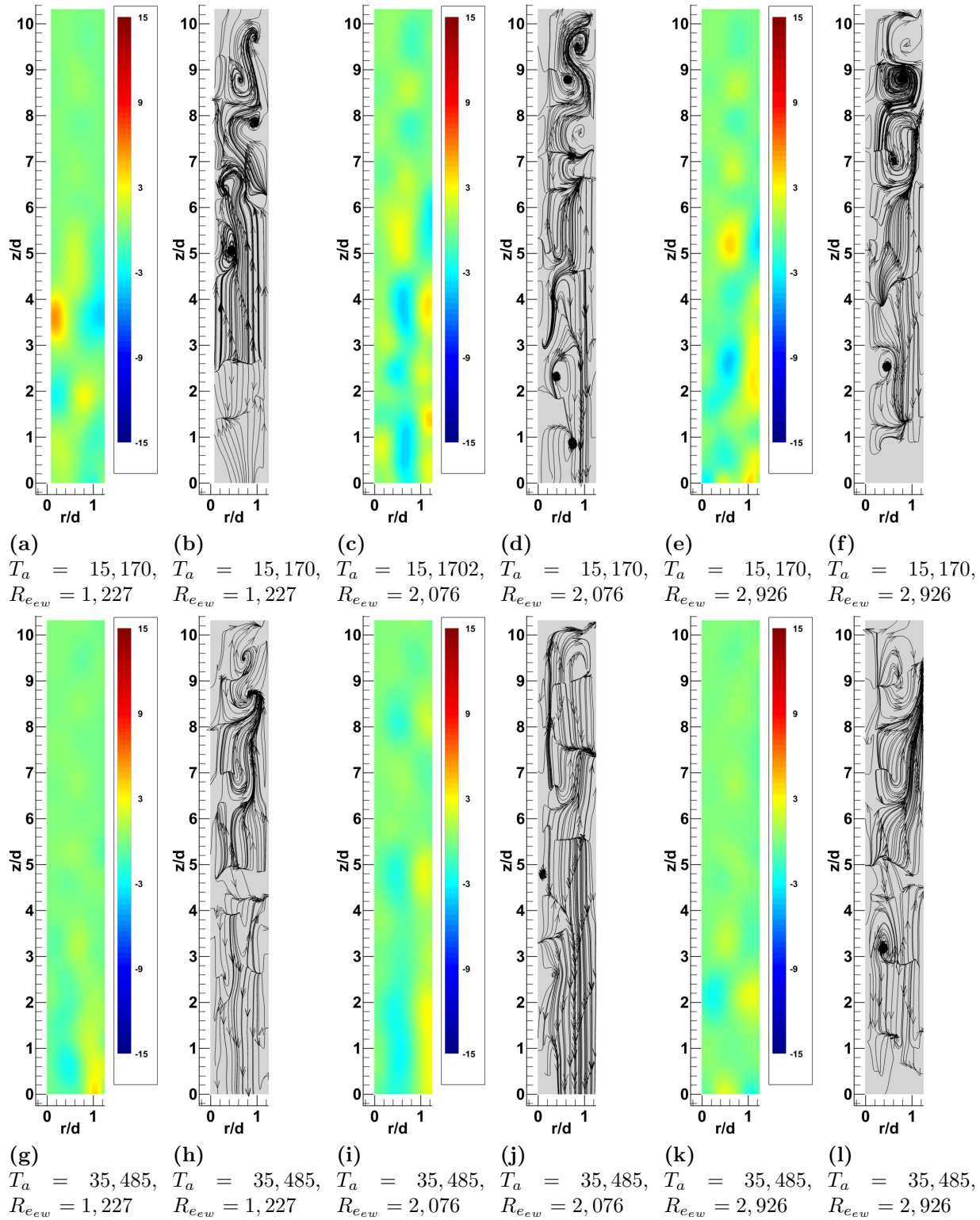

(a) $T_a = 15,170$, $R_{e_{ew}} = 1,227$ **(b)** $T_a = 15,170$, $R_{e_{ew}} = 1,227$ **(c)** $T_a = 15,1702$, $R_{e_{ew}} = 2,076$ **(d)** $T_a = 15,170$, $R_{e_{ew}} = 2,076$ **(e)** $T_a = 15,170$, $R_{e_{ew}} = 2,926$ **(f)** $T_a = 15,170$, $R_{e_{ew}} = 2,926$

(g) $T_a = 35,485$, $R_{e_{ew}} = 1,227$ **(h)** $T_a = 35,485$, $R_{e_{ew}} = 1,227$ **(i)** $T_a = 35,485$, $R_{e_{ew}} = 2,076$ **(j)** $T_a = 35,485$, $R_{e_{ew}} = 2,076$ **(k)** $T_a = 35,485$, $R_{e_{ew}} = 2,926$ **(l)** $T_a = 35,485$, $R_{e_{ew}} = 2,926$

Figure 3.79: Counter-rotational annular mean flow, non-dimensionalized vorticity $[\frac{\omega \hat{\mathbf{d}}}{2\Omega_I R_I}]$ & streamlines, for varying $R_{e_{ew}}$ at $\Gamma_{ew} = 1.5$

driven circulation in the zone-2, resulting in an increased positive axial force drawing fluid upward from the annulus.

Increases in Taylor number beyond the initial onset at $3,360$ resulted in similar effects as described above, increasing in magnitude as T_a was increased. However for all rotational rates above the initial onset, vortices in the lower half of the annulus were seen to be unstructured and extremely chaotic. This deformation of Taylor vortices was noted to occur much sooner than either the co-rotation or TCF cases. Most interestingly though was the stability of TVs in the upper half of the annulus between $z/\hat{d} \approx 6 - 11.5$. While similar conditions were seen to occur at the co-rotational state, the disparity in vortex structure and vorticity between the two halves in the current case was of a much greater magnitude. The exact cause of these differences between the upper and lower annular regions was not entirely clear. One possibility is that it resulted from some form of limited axial flow penetration occurring in an oscillatory fashion. The radial shifts in the Taylor vortices eventually resulted in counter rotating pairs being directly beside one-another in a sawtooth like pattern a seen in Figure 3.78 (e); and increased in length for increases in either T_a of $R_{e_{ew}}$. These extremely elongated sawtooth vortices were found to be remarkably similar to flow structures described by Lopez, Marques, and Shen, for the case of Taylor-Couette flow with harmonic axial oscillations of the inner cylinder [36]. This comparison seemed to indicate that flow with in the system was in-fact oscillatory in nature, and was to some extend for all other test cases, with the notable exception of the $\Gamma_{ew} = 0$ TCF case. This gives a semblance of reasoning for the increased stability and reduced vorticity of TVs in the upper half of the annulus. Vortices in the upper portion experienced greater axial flow which increased the critical Taylor number and thus reduced their relative vorticity. Additionally since the upper most vortices for all test cases had an opposing slope of vortical fluid exchange, (velocity contours), to those formed in the lower half of the annulus any influences caused by flow conditions in the zone-2 could result in differing effects in these two regions.

Higher modal POD results for the $\Gamma_{ew} = 1.5$ counter-rotational case are presented in Figures C.9 - C.12 (zone-2 plots) and Figures D.4 - D.6 (annular plots). Streamlines displayed in Figures C.9 - C.12 show an increased number of vortical structures when compared to mean flow results. As with $\Gamma_{ew} = 1$ counter-rotation results these additional zone-2 vortices were found to be much more sporadically positioned within the domain relative to co-rotation results at the same aspect ratio. Additionally these recirculating regions were typically found to appear on either side of the rational axis opposed to the on axis core recirculation's seen at co-rotational conditions. Mode-1 streamlines presented in Figure C.5 show flow interactions between the zone-2 and annulus to be more dynamic than $\Gamma_{ew} = 0.5$ & 1 results, showing positive axial flow reversals typically found in mode-3 results and higher at lower aspect ratios. Mode 1 and 3 results in Figures C.9 and A.11 display what appears to be a progressive movement of Taylor vortices form the annulus into the zone-2, similar to the pattern noted in mean flow results, showing a chain of small vortical structures directly above the annuls between $z/\hat{d} \approx 11.5 - 16.5$ (vorticity plots C.9 (h) and A.11 (h)). zone-2 cylinder driven vortices appeared to become increasingly displaced radially inward at higher Taylor numbers and was noted to begin at the same conditions that positive TV movement into the zone-2 first began ($\approx 15,170$). Unlike the counter-rotational mode-1 results of $\Gamma_{ew} = 0.5$ & 1 increases in $R_{e_{ew}}$ were not found to result in increased annular flow penetration, on the contrary flow was found to generally display some form of positive axial flow form the the annulus into the zone-2 as seen in the streamlines of Figure C.10 in the area between $z/\hat{d} \approx 9 - 14$ and $r/d \approx 0 - 1$. Mode-3 results at $T_a = 15,170$ for increases in $R_{e_{ew}}$, Figure C.12, are not as consistent in displaying this positive axial flow instead showing slight negative axial flows at the top of the annulus for $R_{e_{ew}} > 2,076$; indicating that as with other co and counter-rotational results fluid movements within the system were most likely of an oscillatory nature.

Annular results for $\Gamma_{ew} = 1.5$ counter-rotation at modes 1 & 3 were found to display chaotic yet slightly more structured flow than that at TCF and co-rotational conditions.

Figures D.5 (a-f) of mode-1 show a progressive distortion of Taylor vortex structure at increased Taylor numbers, predominantly in the lower portions of the annulus between $z/\hat{d} \approx 0 - 5$; similar to mean flow results. However streamlines are seen to display much more identifiable Taylor vortices at these higher modes than the other two rotational cases. It was also noted that vorticity levels at mode-1 were much higher than TCF and co-rotation $\Gamma_{ew} = 1.5$ mode-1 results, showing levels that are orders of magnitude larger in Figures D.5 (a) and (c). Similarly mode-3 results of Figure D.6 (g) displays elevated vorticity levels to those of TCF and co-rotational results, beyond $T_a = 3,360$ however vorticity was found to drop and became relatively comparable to the results of the other two rotational conditions.

Chapter 4

Conclusions

Investigations of the effects of a varying end-wall heights on the bifurcation and stability of secondary steady state flows within the annular gap of a Taylor-Couette cell were conducted. End-wall aspect ratios of $\Gamma_{ew} = 0, 0.5, 1, 1.5$ were tested. For the latter three ratios, co-rotation, counter-rotation, and stationary rotational conditions for the upper end-wall were investigated. At Taylor numbers between $1,312 - 35,485$ for inner cylinder rotation; and a Reynolds number range of $944 - 2,926$ for co- and counter-rotational end-wall conditions.

Formation of Taylor vortices was found to occur at $T_a \approx 3,360$ for all test cases. From the TCF baseline case of $\Gamma_{ew} = 0$ these initial vortices were found to have already undergone a secondary bifurcation and were thus of a wavy form at initial observation. Increases in Γ_{ew} were found to attenuate both the structural stability and vorticity of Taylor vortices. Such effects were found to decrease as distance form the annular gap and zone-2 interface increased, in the negative axial direction.

Changes in vortex stability and vorticity were found to result primarily from oscillatory axial flow within the annulus. This flow was produced by circulatory flow conditions that were found to occur in zone-2, between the cylinder and end-wall. While recirculating flow, similar to a vortex breakdown bubble, was seen to occur in the central core at $\Gamma_{ew} = 1$ and $\Gamma_{ew} = 1.5$ these recirculating zones were of a highly distorted form when compared to the breakdown bubble seen in the $\Gamma_{ew} = 1.5$ Escudier case [24]. Additionally the presence of such recirculating zones were not found to have any overt influence on Taylor vortex stability; where core recirculation was seen to occur at conditions for both stable and unstable Taylor vortices.

Axial flow within the annulus was found to increase with increasing Γ_{ew}. At the onset of Taylor vortex distortion a positive axial displacement was seen to occur, this was typically accompanied by some axial or radial displacement in the vortical loci at the top of the annular gap. These shifts were found to increase the amount fluid exchange between the annulus and zone-2, and appeared to increase axial oscillation magnitude. While the specific change in oscillatory frequency was beyond the scope of the present work, results indicated that such effects were enhanced by additional rotation of the upper end-wall and were found to be greatest for the counter-rotational case. This was due to the adversarial nature of flow produced by the cylinder and upper end-wall, such that each acted as a pump drawing fluid towards their rotating surfaces in opposing directions.

In the case of counter-rotation the adversarial nature of flow with in the central core region was enhanced due to the equivalent rotational direction which allowed for greater fluid vacillation between the end-wall and cylinder. Such vacillating flow resulted in the earliest found occurrences of mean flow Taylor vortex deformation, which was initially seen at $T_a = 6,352$ for $\Gamma_{ew} = 1.5$. For co-rotational cases such effects were found to be dampened by the opposing rotational direction of end-wall and cylinder central cores; resulting in a larger core region with a semblance of solid body rotation. This larger core region was found to actually enhance the stability of Taylor vortices within the annulus when compared to count-rotational or stationary end-wall conditions for $\Gamma_{ew} > 0$ and $T_a > 3,360$. Where for $\Gamma_{ew} = 1.5$ destabilization was delayed all the way out to $T_a \approx 27,769$. It also allowed for the formation of stacked counter rotating vortices to form within the core. However, at $\Gamma_{ew} = 0.5$ & 1 for $T_a = 3,360$ co-rotation was found to result in Taylor vortices with a less coherent structure and lower vorticity when compared to the counter-rotation and stationary cases; effects which were greatest at $\Gamma_{ew} = 1$. And although Taylor vortex destabilization at $\Gamma_{ew} = 1.5$ was found to be significantly delayed by the co-rotational condition it also resulted in extremely low vorticity levels, when compared to counter-rotation and stationary

$\Gamma_{ew} = 1.5$ conditions. Indicating that co-rotation had some effect in delaying the on set of Taylor vortex formation.

Increases in $R_{e_{ew}}$ were found to typically result in increased negative axial compression of Taylor vortices. This compression was seen to continue until the rotational rate of the end-wall became large enough to over power the zone-2 circulatory flow produced by the inner cylinder. At such a point bulk momentum of the fluid was seen to shift in the positive axial direction, and caused increases in axial flow within the annulus. However $R_{e_{ew}}$ was found to be a secondary cause in Taylor vortex degradation, which primarily resulted form the combined effects of increases in Γ_{ew} and T_a. As such the effects of increases in $R_{e_{ew}}$ on Taylor vortex stability were found to decrease with increasing Taylor number.

Bibliography

[1] Acheson, D. J. *Elementary Fluid Dynamics.* New York, Ny: Oxford University Press, 1990.

[2] Andereck, C. David., Liu, S. S., and Swinney, Harry L., "Flow Regimes in a Circular Couette System with Independently Rotating Cylinders" *Journal of Fluid Mechanics,* Vol. 164, 1986: 155-183.

[3] Andereck, C. D., Dickman, R. & Swinney, H. L., "New Flows in a Circular Couette System with Co-Rotating Cylinders" *Physics of Fluids.* Vol. 26, (1395). 1983

[4] Anderson, John D. *Fundamentals of Aerodynamics.* Fourth Edition. New York, NY: McGraw-Hill, 2007.

[5] Benjamin, T. B., "Bifurcation Phenomena in Steady Flows of a Viscous Fluid II. Experiments." *Proceedings of the Royal Society of London, A.* Vol. 359, No. 1696, 1978: 27-43

[6] Biage, M., Harris, Scott R., Lempert, W. R., & Smits, A. J., "Visualization Study of Taylor-Couette Flow: a Description of the Transition to Turbulence." *27th AIAA Fluid Dynamics Conference June, 1996. New Orleans, LA.* Princeton, NJ: AIAA, 1996.

[7] Børns, M., Voigt, L. K. & Sørensen, J. N., "Streamline Topology of Steady Axisymmetric Vortex Breakdown in a Cylinder with Co- and Counter-Rotating End-Covers" *Journal of Fluid Mechanics* Vol. 401, 1999: 275-292.

[8] Brown, G. L., & Lopez J. M., "Axisymmetric Vortex Breakdown Part 2. Physical Mechanisms." *Journal of Fluid Mechanics.* Vol. 221, 1990: 553-576.

[9] Cabeza, C., Sarasúa, G., Martí, A. C., & Bove, I., "A Simple Mechanism for Controlling Vortex Breakdown in a Closed Flow" *arXiv:physics/0512248v2* 2006.

[10] Cazemier, W., *"Proper Orthogonal Decomposition and Low Dimensional Models for Turbulent Flows."* Diss. University of Groningen, 1997.

[11] Chandrasekhar, S., *Hydrodynamic and Hydromagnetic Stability.* New York, Ny: Oxford University Press, 1961.

[12] Chandrasekhar, S., "The Stability of Viscous Flow Between Rotating Cylinders in the Presence of a Magnetic Field." *Proceedings of the Royal Society of London, A.* Vol. 216, No. 1126, 1953: 293-309.

[13] Chatterjee, A., "An Introduction to the Proper Orthogonal Decomposition." *Current Science.* Vol. 78, No. 7, 2000: 808-817

[14] Cole, J. A., "Taylor-Vortex Instability and Annulus-Length Effects." *Journal of Fluid Mechanics.* Vol. 75, part 1, 1976: 1-15.

[15] Coles, D. "Transition in Circular Couette Flow" *Journal of Fluid Mechanics.* Vol. 21, 1965: 385-425

[16] Coles, D., "A Note on Taylor Instability in Circular Couette Flow." *Journal of Applied Mechanics.* Sep, 1967: 529-534.

[17] Czarny, O., Serre, E., Bontoux, P. & Lueptow, R. M., "Interaction Between Ekman Pumping and the Centrifugal Instability in Taylor-Couette Flow." *Physics of Fluids.* Vol. 15, No. 2, 2003: 467-477

[18] Davidson, P. A. *Turbulence: An Introduction for Scientists and Engineers.* Second Edition. New York, Ny: Oxford Univesity Press, 2015.

[19] Davey, A., Di Prima R. C., & Stuart, J. T., "On the Instability of Taylor Vortices." *Journal of Fluid Mechanics.* Vol. 31, Part 1, Great Britain, 1968: 17-52.

[20] Donelly, R. J., Ozima, M., "Experiments on the Stability of Flow Between Rotating Cylinders in the Presence of a Magnetic Field." *Proceedings of the Royal Society of London, A.* Vol. 266, No. 1325, 1962: 272-286.

[21] Donnelly, R. J. & Schwarz, K. W., "Experiments on the Stability of Viscous Flow Between Rotating Cylinders: IV. Finite-Amplitude Experiments." *Proceedings of the Royal Society A.* Vol. 283, London, 1965: 531-556.

[22] Donnelly, Russell J. "Taylor-Couette Flow the Early Days" *Physics Today.* November 1991: pp. 32-39.

[23] Edwards, W. S., Beane, S. R., Varma, S., "Onset of Wavy Vortices in the Finite-Length Couette–Taylor Problem." Physics of Fluids. Vol. 3(6), 1991: 1510-1518.

[24] Escudier, M. P., "Observations of the Flow Produced in a Cylindrical Container by a Rotating Endwall." *Experiments in Fluids.* Vol. 2, 1984: 189-196.

[25] Gelfgat, A. Yu., Bar-Yoseph, P. Z., Solan, A., "Stability of Confined Swirling Flow with and without Vortex Breakdown." *Journal of Fluid Mechanics* Vol. 311, 1996: 1-36.

[26] Harvery, J. K., "Some Observations of the Vortex Breakdown Phenomenon." *Journal of Fluid Mechanics.* Vol. 14, 1962: 585-592.

[27] Helmholtz, H., "LXII. On Integrals of the Hydrodynamical Equations, which Express Vortex-Motion." *Philosophical Magazine Series 4.* Vol. 33, No. 226, 1867: 485-512.

[28] Hoffmann, C., Altmeyer, S., Heise, M., Abshagen, .J, & Pfister, G., "Axisymmetric Propagating Vortices in Centrifugally Stable Taylor-Couette Flow." *Journal of Fluid Mechanics.* Vol. 728, 2003: 458-470.

[29] Ikeda, E., & Maxworthy, T., "Spatially Forced Co-rotating Taylor-Couette Flow." *Physical Review, E.* Vol. 49, No. 6, 1994.

[30] Jones, C. A., "The Transition to Wavy Taylor Vortices." *Journal of Fluid Mechanics.* Vol. 157, 1984: 135-162.

[31] Jørgensen, B. H., Sørensen J. N., Aubry, N., "Control of Vortex Breakdown in a Closed Cylinder with a Rotating Lid" *Theoretical and Computational Fluid Dynamic.* Vol. 24, 2010: 483-496

[32] Krueger, E. R., Gross, A. G. & Di Prima, R. C. "On the Relative Importance of Taylor-Vortex and Non-Axisymmetric Modes in Flow Between Rotating Cylinders." *Journal of Fluid Mechanics.* Vol. 24, 1966: 521-538.

[33] Lalaoua, A., "Effect of a Pulsating Radial Motion of the Outer Cylinder on the Onset of Taylor Vortices in Finite-Length Geometry." *Topical Problems of Fluid Mechanics.* Prague, February 2015: 105-116.

[34] Lopez, J. M., "Axisymmetric Vortex Breakdown in an Enclosed Cylinder Flow." *Lecture Notes in Physics. 11th International Conference on Numerical Methods in Fluid Dynamic; 1989.* Vol. 323, Berlin: Springer-Verlag, 1989: 384-388.

[35] Lopez, J. M. "Axisymmetric Vortex Breakdown Part 1. Confined Swirling Flow." *Journal of Fluid Mechanics.* Vol. 221, 1990: 533-552.

[36] Lopez, J. M., Marques, F., Shen, J., "Endwall effects in a Periodically Forced Centrifugally Unstable Flow." *Fluid Dynamics Research.* Vol. 27, 2000: 91-108.

[37] Lueptow, R., "Taylor-Couette Flow." *Scholarpedia.* Vol. 4(11), 2009: 6389. Web. 18 Aug. 2015.

[38] Moussa, N. A., Poncet, S., Ghezal, A., & Lounis, M., "Effect of Radius Ration on the Stability of Co- and Counter- Taylor Couette Flow." *Proceedings of the International Conference on Heat Transfer and Fluid Flow, August, 2014.* Prague, Czech Republic, 2104: Paper No. 203.

[39] Mudkavi, Vidyadhar Y. "The Phenomenon of Vortex Breakdown." *Proceedings of Fluid Dynamics Symposium.* National Aerospace Laboratories, July 1993: 123-135.

[40] Mullin, T., Tavener, S. J., Cliffe, K. A., "On the Creation of Stagnation Points in a Rotating Flow." *Journal of Fluids Engineering.* Vol. 120-4, 1998: 685-689.

[41] Mununga, L., Lo Jacono, D., Sorensen, J.N., Leweke, T., Thompson, M.C., & Hourigan, K., "Control of Confined Vortex Breakdown with Partial Rotating Lids." *Journal of Fluid Mechanics.* Vol. 738, 2013: 5-33.

[42] Mutabazi, I., Abcha, N., Crumeyrolle, O., Ezersky, A., "Application of the Particle Image Velocimetry to the Couette-Taylor Flow." *The Particle Image Velocimetry-Characteristics, Limits and Possible Applications.* Ed: Cavazzini, G., *InTech.* DOI: 10.5772/45644. 2012.

[43] Niklas, M., "Influence of Magnetic Fields on Taylor Vortex Formation in Magnetic Fluids." *Zeitschrift Für Physik, B.* Vol. 68, 1987:493-501.

[44] Noui-Mehidi, M. N., Ohmura, N., & Kataoka, K., "An Experimental Investigation of Flow Mode Selection in a Conical Taylor-Couette System." *International Journal of Fluid Dynamics.* Vol. 5, Art. 1, 2001: 1-16.

[45] Peckham, D. H., & Atkinson, S. A., "Preliminary Results of Low-Speed Wind Tunnel Tests on Gothic Wing of Aspect Ratio 1.0." *Aeronautical Research Council.* Technical Report C.P., No. 508, London, 1957.

[46] Schwarz, K. W., Springett, B. E. & Donnelly, R. J. "Modes of Instability in Spiral Flow Between Rotating Cylinders." *Journal of Fluid Mechanics.* Vol. 20, 1964: 281-289.

[47] Serre, E., Sprague, M. A., Lueptow, R. M., " Stability of Taylor-Couette Flow in a Finite-Length Cavity with Radial Throughflow." *Physics of Fluids.* Vol. 20, 034106, 2008: 1-10.

[48] Sirovich, L., "Turbulence and the Dynamics of Coherent Structures Part 1: Coherent Structures." *Quarterly of Applied Mathmatics* Vol. XLV, Num. 3, October 1987: 561-571

[49] Snyder, H. A. & Karlsson, S. K. "Non-Axisymmmetric Modes of Secondary Flows." *Bulletin of American Physical Society.* Vol. 10, 1965.

[50] Sparrow, E. M., Munro, W. D., & Jonsson, V. K., "Instability of the Flow Between Rotating Cylinders: The Wide Gap Problem." *Journal of Fluid Mechanics.* Vol. 20, 1964: 35-46.

[51] Sprague, M. A., Weidman, P. D., Macumber, S., & Fischer, P. F., "Tailored Taylor Vortices." *API |Physics of Fluids.* Vol. 20, January 2008.

[52] Taylor, G. I., "Stability of a Viscous Liquid Contained Between Two Rotating Cylinders." *Philosophical Transactions of the Royal Society A.* Vol. 223, London, 1923: 289-343.

[53] White, Frank M. *Viscous Fluid Flow.* Third Edition. New York, Ny: McGraw-Hill, 2006.

[54] Willis, A. P., Barenghi, C. F., "Hydromagnetic Taylor-Couette Flow: Numerical Formulation and Comparison with Experiment." *Journal of Fluid Mechanics.* Vol. 463, 2002: 361-375.

[55] Willis, A. P., Barenghi, C. F., "Hydromagnetic Taylor-Couette Flow: Wavy Modes." *Journal of Fluid Mechanics.* Vol. 472, 2002: 399-410.

[56] Wimmer, M., "An Experimental Investigation of Taylor Vortex Flow Between Conical Cylinders." *Journal of Fluid Mechanics.* Vol. 292, 1995: 205-227.

[57] Valentine, D. T., Jahnke, C. C., "Flows Induced in a Cylinder with Both End Walls Rotating." *Physics of Fluids.* Vol. 6, 2702, 1994.

[58] Vogel, H. U.,"Experimentelle Ergebnisse über die laminare Stroömung in einem zylindrischen Gehäuse mit darin rotierender Scheibe." *Max-Planck-Institut für Strömungsforschung.* Technical Report Bericht 6, 1968.

Appendices

Appendix A

Co-rotational supplemental figures (zone-2)

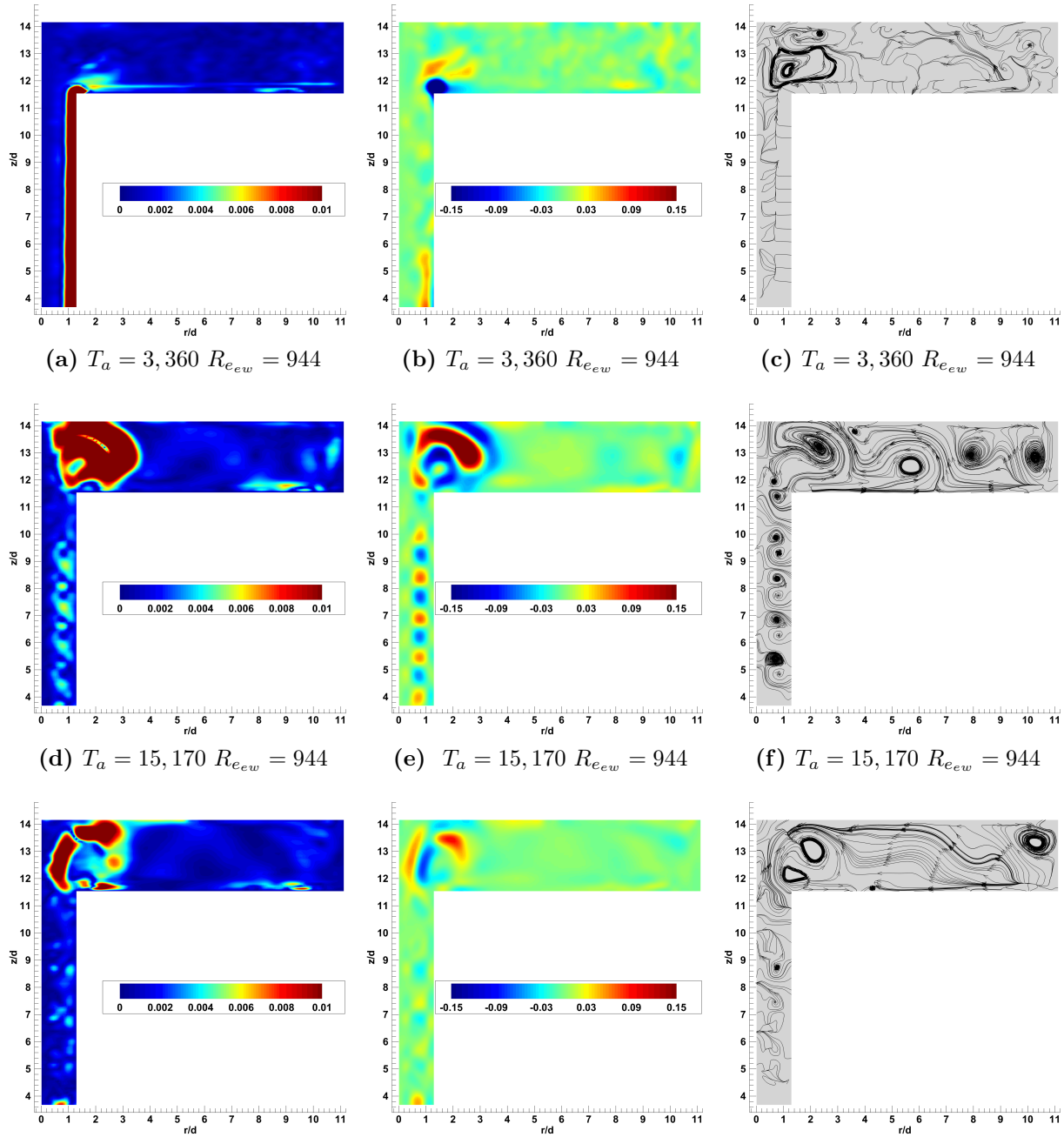

(a) $T_a = 3,360$ $R_{e_{ew}} = 944$ **(b)** $T_a = 3,360$ $R_{e_{ew}} = 944$ **(c)** $T_a = 3,360$ $R_{e_{ew}} = 944$

(d) $T_a = 15,170$ $R_{e_{ew}} = 944$ **(e)** $T_a = 15,170$ $R_{e_{ew}} = 944$ **(f)** $T_a = 15,170$ $R_{e_{ew}} = 944$

(g) $T_a = 35,485$ $R_{e_{ew}} = 944$ **(h)** $T_a = 35,485$ $R_{e_{ew}} = 944$ **(i)** $T_a = 35,485$ $R_{e_{ew}} = 944$

Figure A.1: Co-rotation at POD mode-1, velocity profile (left), non-dimensionalized vorticity $[\frac{\omega \hat{\mathbf{d}}}{2\Omega_I R_I}]$ (middle), streamlines (right), for varying T_a at $\Gamma_{ew} = 0.5$

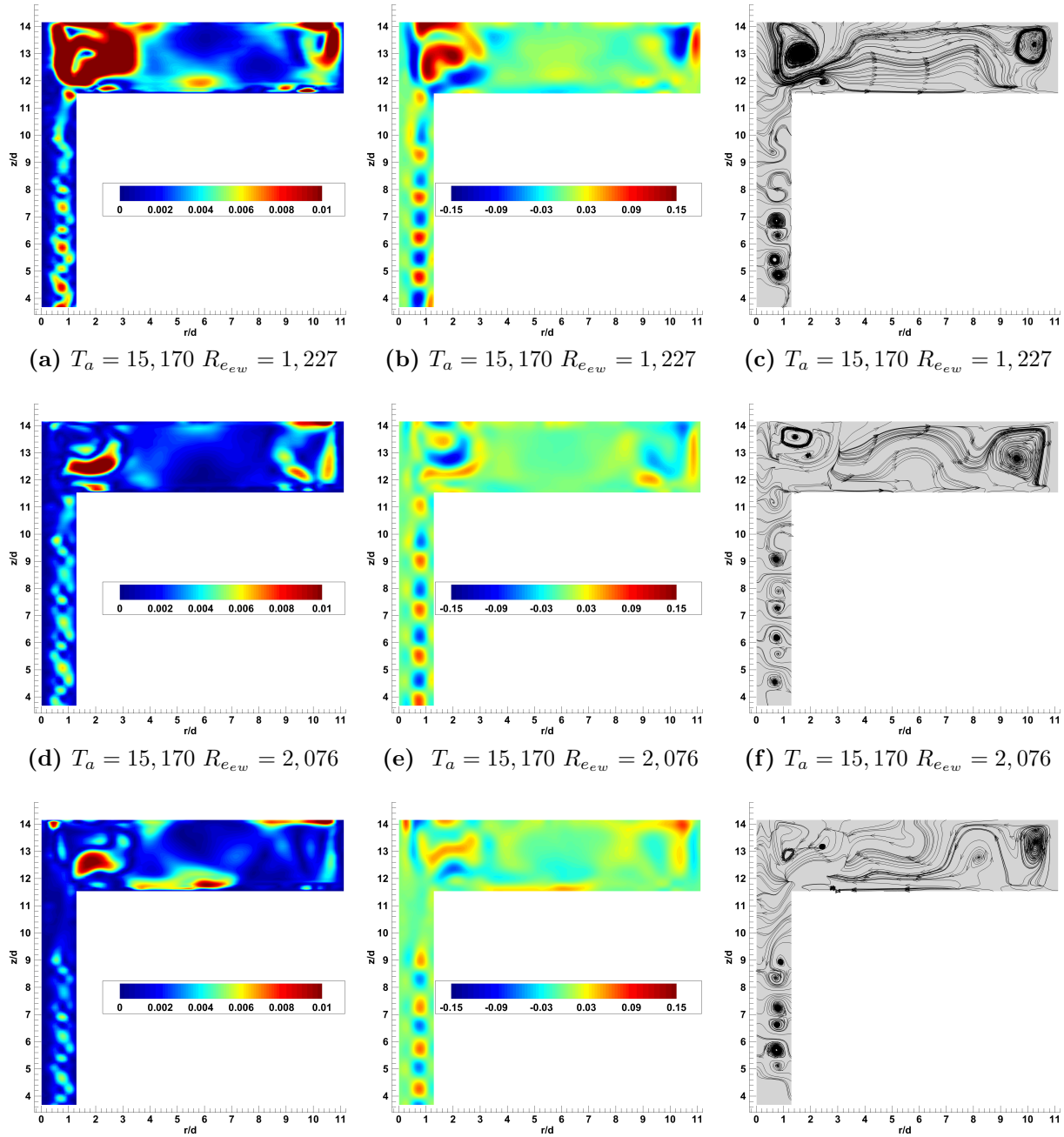

(a) $T_a = 15,170$ $R_{e_{ew}} = 1,227$ **(b)** $T_a = 15,170$ $R_{e_{ew}} = 1,227$ **(c)** $T_a = 15,170$ $R_{e_{ew}} = 1,227$

(d) $T_a = 15,170$ $R_{e_{ew}} = 2,076$ **(e)** $T_a = 15,170$ $R_{e_{ew}} = 2,076$ **(f)** $T_a = 15,170$ $R_{e_{ew}} = 2,076$

(g) $T_a = 15,170$ $R_{e_{ew}} = 2,926$ **(h)** $T_a = 15,170$ $R_{e_{ew}} = 2,926$ **(i)** $T_a = 15,170$ $R_{e_{ew}} = 2,926$

Figure A.2: Co-rotation at POD mode-1, velocity profile (left), non-dimensionalized vorticity $[\frac{\omega \hat{\mathbf{d}}}{2\Omega_I R_I}]$ (middle), streamlines (right), for varying R_{eew} at $\Gamma_{ew} = 0.5$

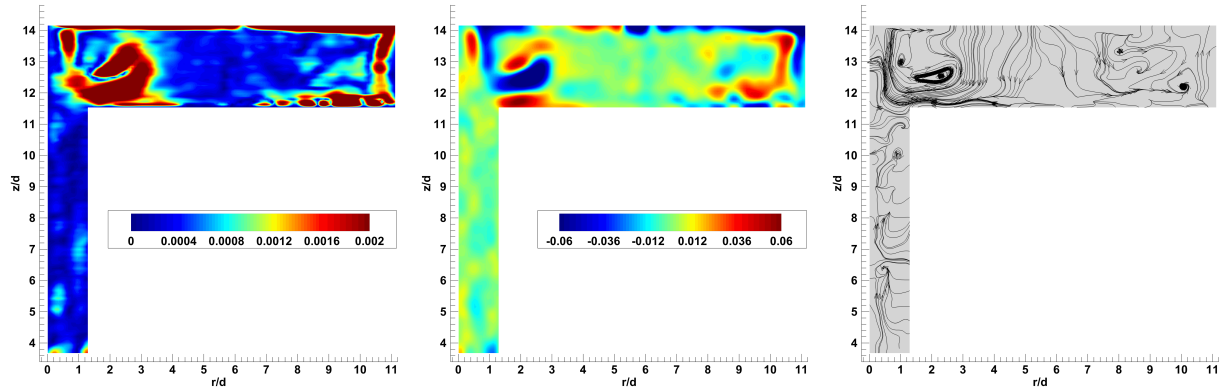

(a) $T_a = 3,360$ $R_{e_{ew}} = 944$ **(b)** $T_a = 3,360$ $R_{e_{ew}} = 944$ **(c)** $T_a = 3,360$ $R_{e_{ew}} = 944$

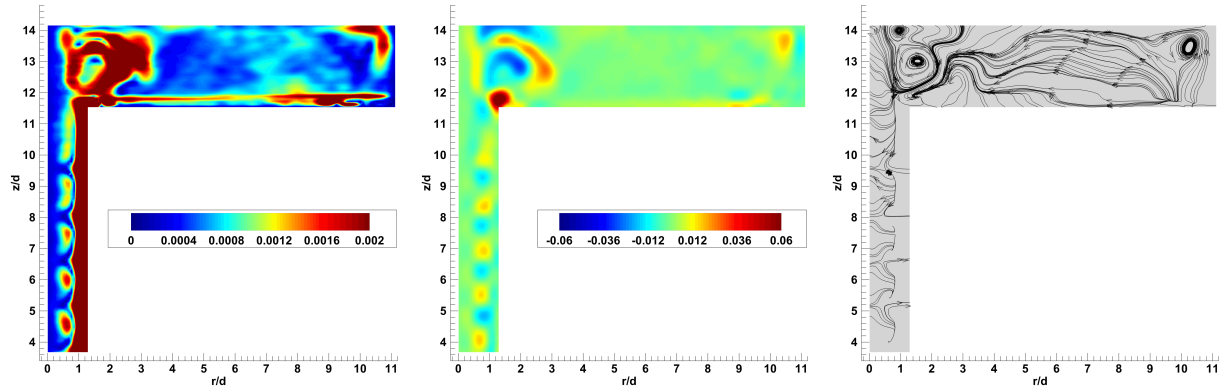

(d) $T_a = 15,170$ $R_{e_{ew}} = 944$ **(e)** $T_a = 15,170$ $R_{e_{ew}} = 944$ **(f)** $T_a = 15,170$ $R_{e_{ew}} = 944$

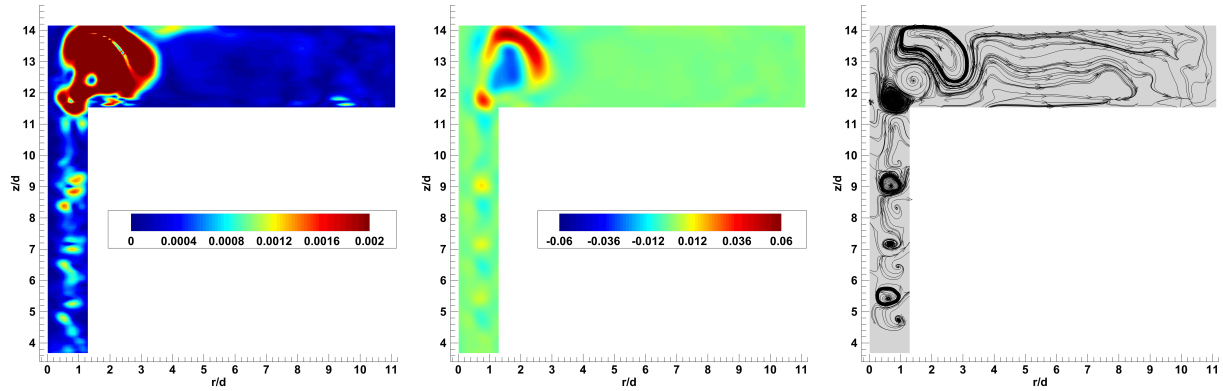

(g) $T_a = 35,485$ $R_{e_{ew}} = 944$ **(h)** $T_a = 35,485$ $R_{e_{ew}} = 944$ **(i)** $T_a = 35,485$ $R_{e_{ew}} = 944$

Figure A.3: Co-rotation at POD mode-3, velocity profile (left), non-dimensionalized vorticity $[\frac{\omega \hat{\mathbf{d}}}{2\Omega_I R_I}]$ (middle), streamlines (right), for varying T_a at $\Gamma_{ew} = 0.5$

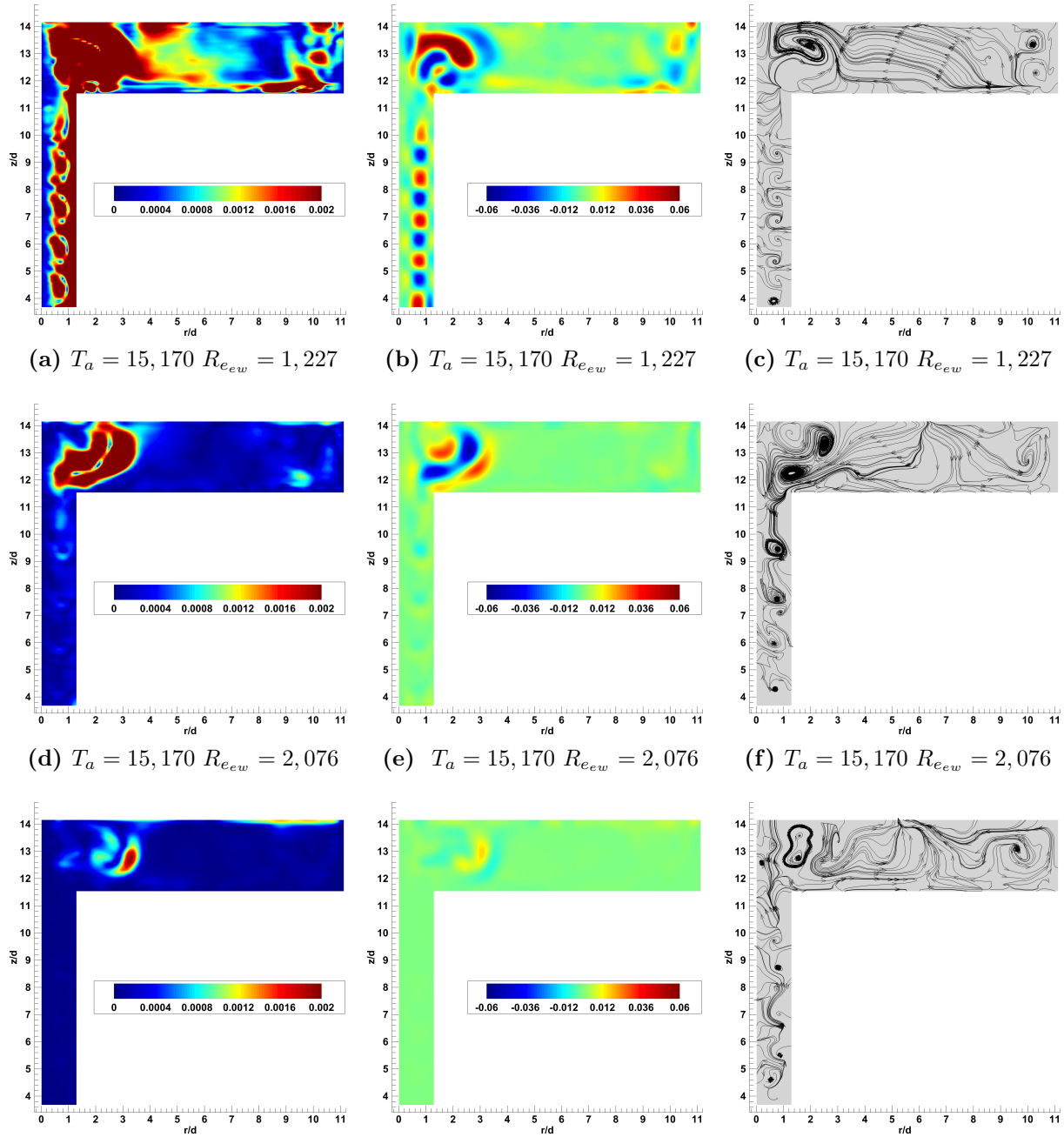

(a) $T_a = 15,170\ R_{e_{ew}} = 1,227$ **(b)** $T_a = 15,170\ R_{e_{ew}} = 1,227$ **(c)** $T_a = 15,170\ R_{e_{ew}} = 1,227$

(d) $T_a = 15,170\ R_{e_{ew}} = 2,076$ **(e)** $T_a = 15,170\ R_{e_{ew}} = 2,076$ **(f)** $T_a = 15,170\ R_{e_{ew}} = 2,076$

(g) $T_a = 15,170\ R_{e_{ew}} = 2,296$ **(h)** $T_a = 15,170\ R_{e_{ew}} = 2,296$ **(i)** $T_a = 15,170\ R_{e_{ew}} = 2,296$

Figure A.4: Co-rotation at POD mode-3, velocity profile (left), non-dimensionalized vorticity $[\frac{\omega \hat{\mathbf{d}}}{2\Omega_I R_I}]$ (middle), streamlines (right), for varying R_{eew} at $\Gamma_{ew} = 0.5$

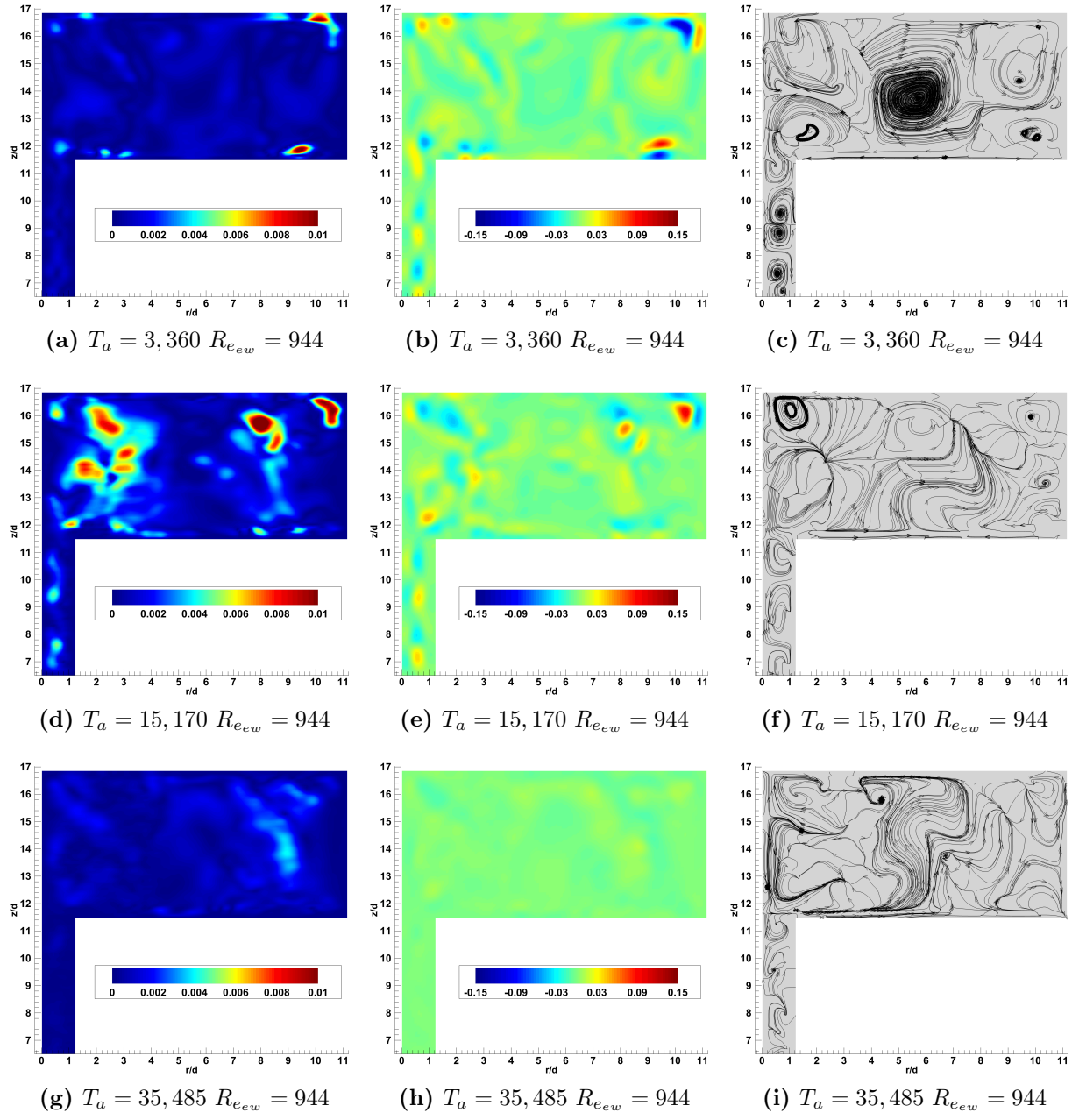

(a) $T_a = 3,360$ $R_{e_{ew}} = 944$ **(b)** $T_a = 3,360$ $R_{e_{ew}} = 944$ **(c)** $T_a = 3,360$ $R_{e_{ew}} = 944$

(d) $T_a = 15,170$ $R_{e_{ew}} = 944$ **(e)** $T_a = 15,170$ $R_{e_{ew}} = 944$ **(f)** $T_a = 15,170$ $R_{e_{ew}} = 944$

(g) $T_a = 35,485$ $R_{e_{ew}} = 944$ **(h)** $T_a = 35,485$ $R_{e_{ew}} = 944$ **(i)** $T_a = 35,485$ $R_{e_{ew}} = 944$

Figure A.5: Co-rotation at POD mode-1, velocity profile (left), non-dimensionalized vorticity $[\frac{\omega \hat{\mathbf{d}}}{2\Omega_I R_I}]$ (middle), streamlines (right), for varying T_a at $\Gamma_{ew} = 1$

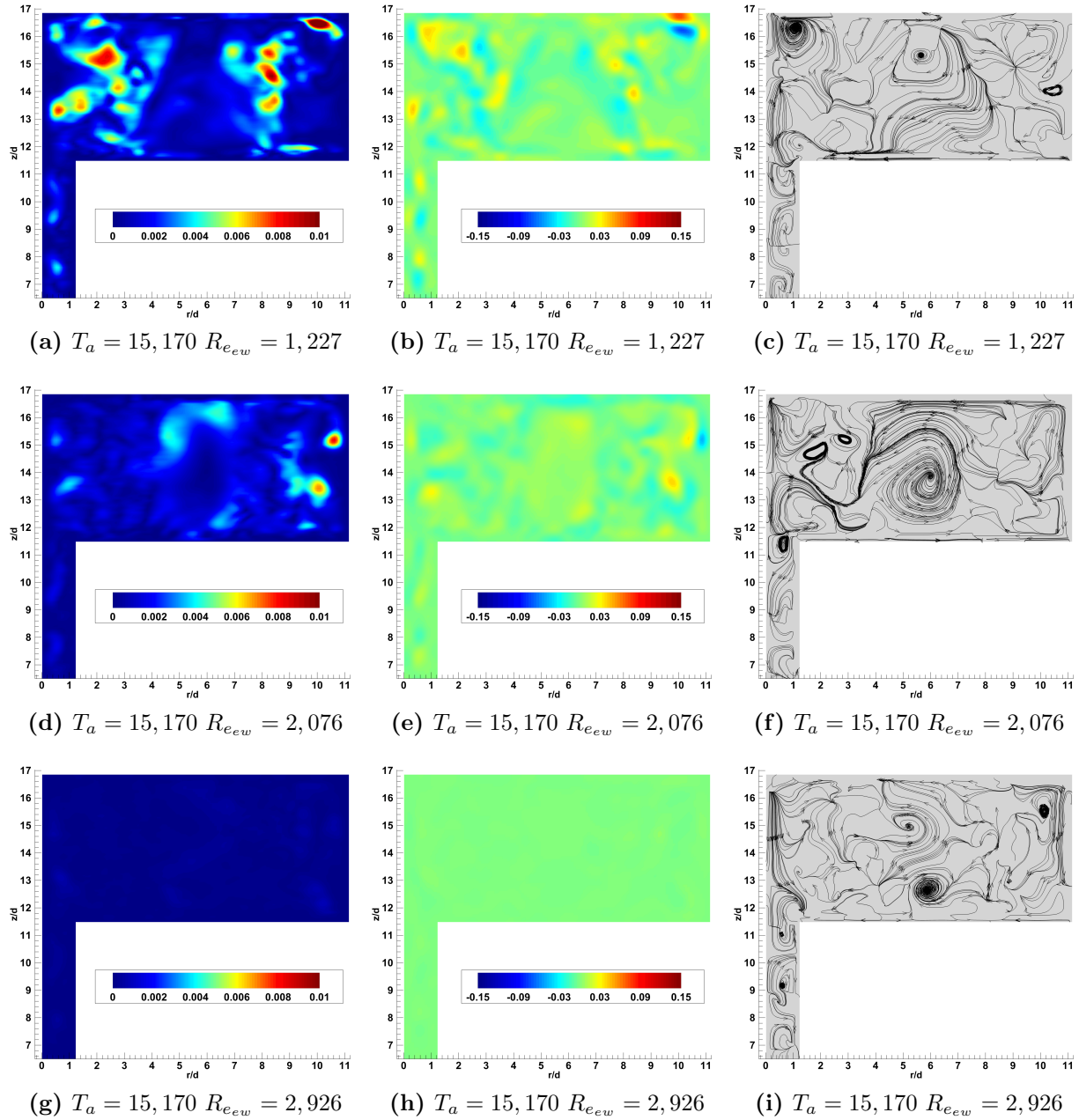

(a) $T_a = 15,170$ $R_{e_{ew}} = 1,227$ **(b)** $T_a = 15,170$ $R_{e_{ew}} = 1,227$ **(c)** $T_a = 15,170$ $R_{e_{ew}} = 1,227$

(d) $T_a = 15,170$ $R_{e_{ew}} = 2,076$ **(e)** $T_a = 15,170$ $R_{e_{ew}} = 2,076$ **(f)** $T_a = 15,170$ $R_{e_{ew}} = 2,076$

(g) $T_a = 15,170$ $R_{e_{ew}} = 2,926$ **(h)** $T_a = 15,170$ $R_{e_{ew}} = 2,926$ **(i)** $T_a = 15,170$ $R_{e_{ew}} = 2,926$

Figure A.6: Co-rotation at POD mode-1, velocity profile (left), non-dimensionalized vorticity $[\frac{\omega \hat{\mathbf{d}}}{2\Omega_I R_I}]$ (middle), streamlines (right), for varying $R_{e_{ew}}$ at $\Gamma_{ew} = 1$

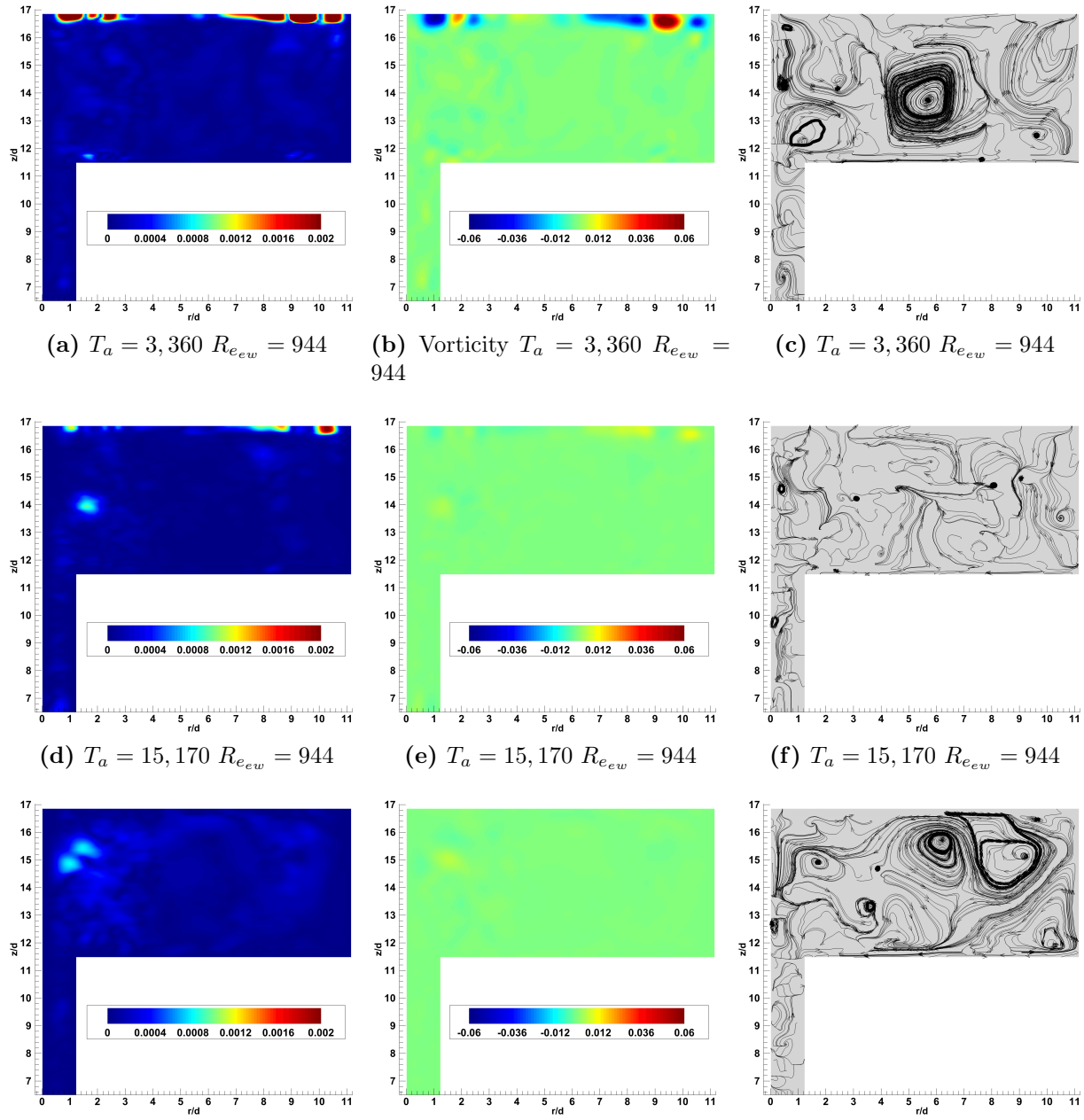

(a) $T_a = 3,360$ $R_{e_{ew}} = 944$ **(b)** Vorticity $T_a = 3,360$ $R_{e_{ew}} = 944$ **(c)** $T_a = 3,360$ $R_{e_{ew}} = 944$

(d) $T_a = 15,170$ $R_{e_{ew}} = 944$ **(e)** $T_a = 15,170$ $R_{e_{ew}} = 944$ **(f)** $T_a = 15,170$ $R_{e_{ew}} = 944$

(g) $T_a = 35,485$ $R_{e_{ew}} = 944$ **(h)** $T_a = 35,485$ $R_{e_{ew}} = 944$ **(i)** $T_a = 35,485$ $R_{e_{ew}} = 944$

Figure A.7: Co-rotation at POD mode-3, velocity profile (left), non-dimensionalized vorticity $[\frac{\omega \hat{\mathbf{d}}}{2\Omega_I R_I}]$ (middle), streamlines (right), for varying T_a at $\Gamma_{ew} = 1$

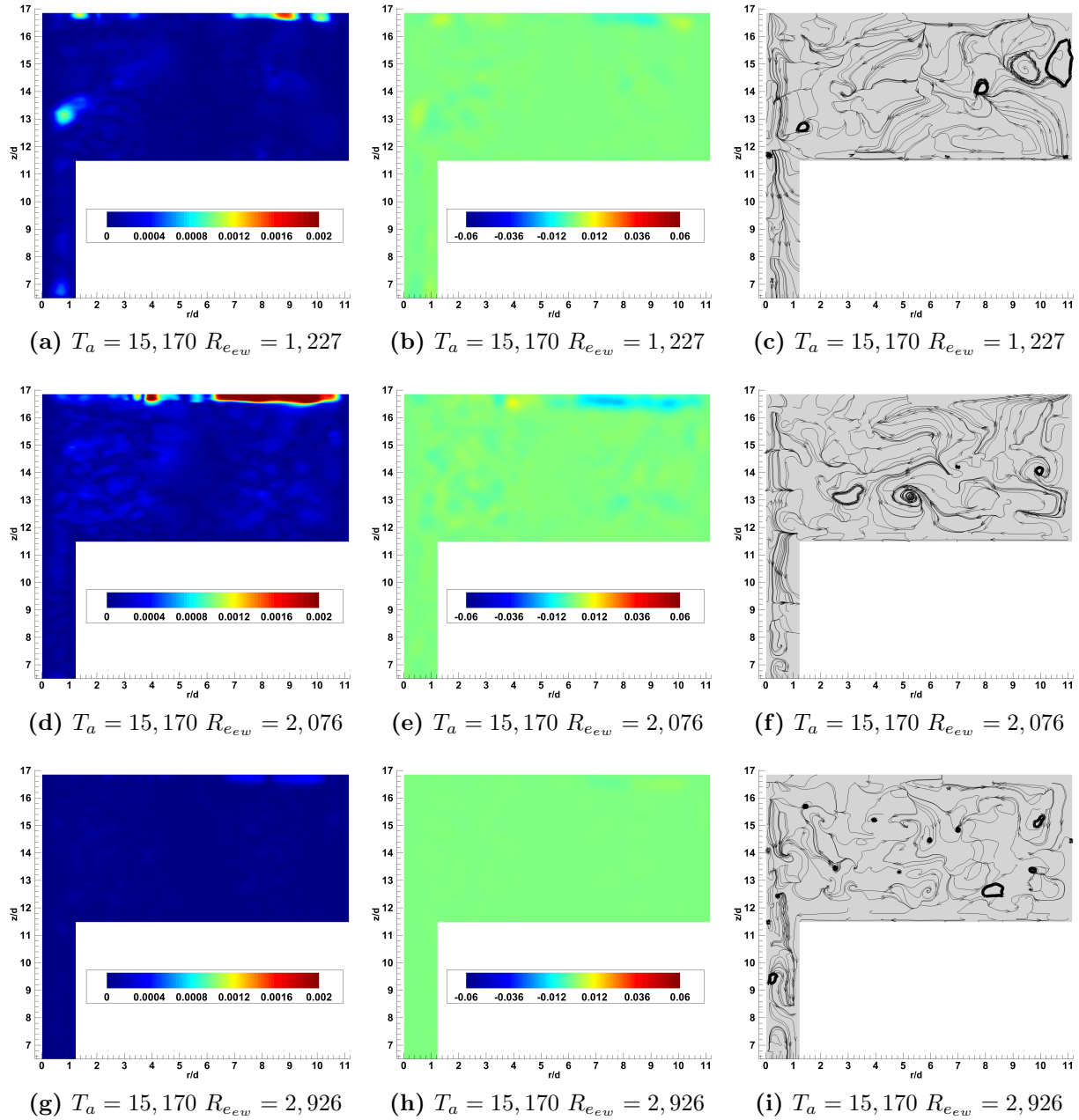

(a) $T_a = 15,170$ $R_{e_{ew}} = 1,227$ **(b)** $T_a = 15,170$ $R_{e_{ew}} = 1,227$ **(c)** $T_a = 15,170$ $R_{e_{ew}} = 1,227$

(d) $T_a = 15,170$ $R_{e_{ew}} = 2,076$ **(e)** $T_a = 15,170$ $R_{e_{ew}} = 2,076$ **(f)** $T_a = 15,170$ $R_{e_{ew}} = 2,076$

(g) $T_a = 15,170$ $R_{e_{ew}} = 2,926$ **(h)** $T_a = 15,170$ $R_{e_{ew}} = 2,926$ **(i)** $T_a = 15,170$ $R_{e_{ew}} = 2,926$

Figure A.8: Co-rotation at POD mode-3, velocity profile (left), non-dimensionalized vorticity $[\frac{\omega \hat{\mathbf{d}}}{2\Omega_I R_I}]$ (middle), streamlines (right), for varying $R_{e_{ew}}$ at $\Gamma_{ew} = 1$

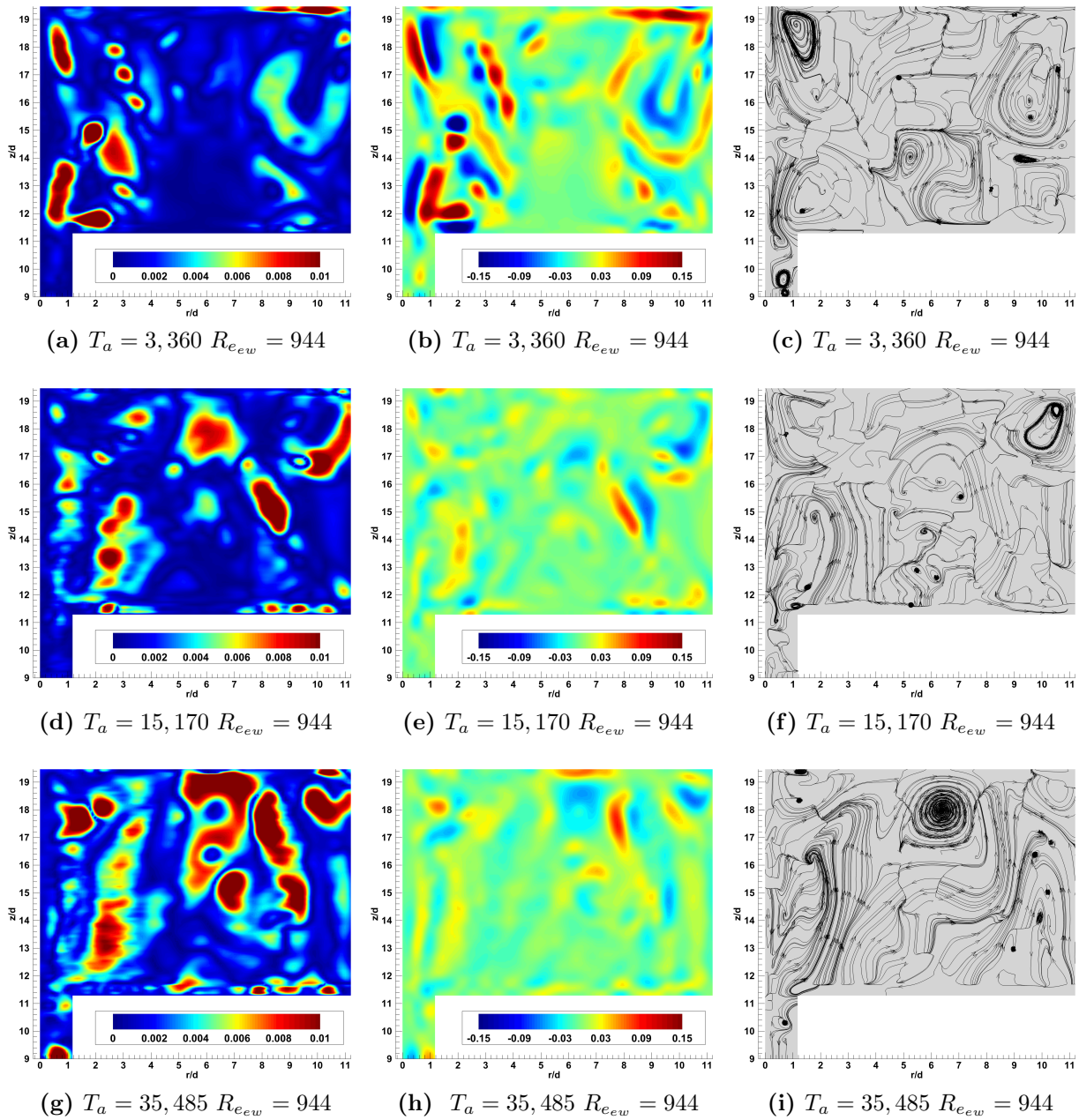

(a) $T_a = 3,360$ $R_{e_{ew}} = 944$ **(b)** $T_a = 3,360$ $R_{e_{ew}} = 944$ **(c)** $T_a = 3,360$ $R_{e_{ew}} = 944$

(d) $T_a = 15,170$ $R_{e_{ew}} = 944$ **(e)** $T_a = 15,170$ $R_{e_{ew}} = 944$ **(f)** $T_a = 15,170$ $R_{e_{ew}} = 944$

(g) $T_a = 35,485$ $R_{e_{ew}} = 944$ **(h)** $T_a = 35,485$ $R_{e_{ew}} = 944$ **(i)** $T_a = 35,485$ $R_{e_{ew}} = 944$

Figure A.9: Co-rotation at POD mode-1, velocity profile (left), non-dimensionalized vorticity $[\frac{\omega \hat{\mathbf{d}}}{2\Omega_I R_I}]$ (middle), streamlines (left), for varying T_a at $\Gamma_{ew} = 1.5$

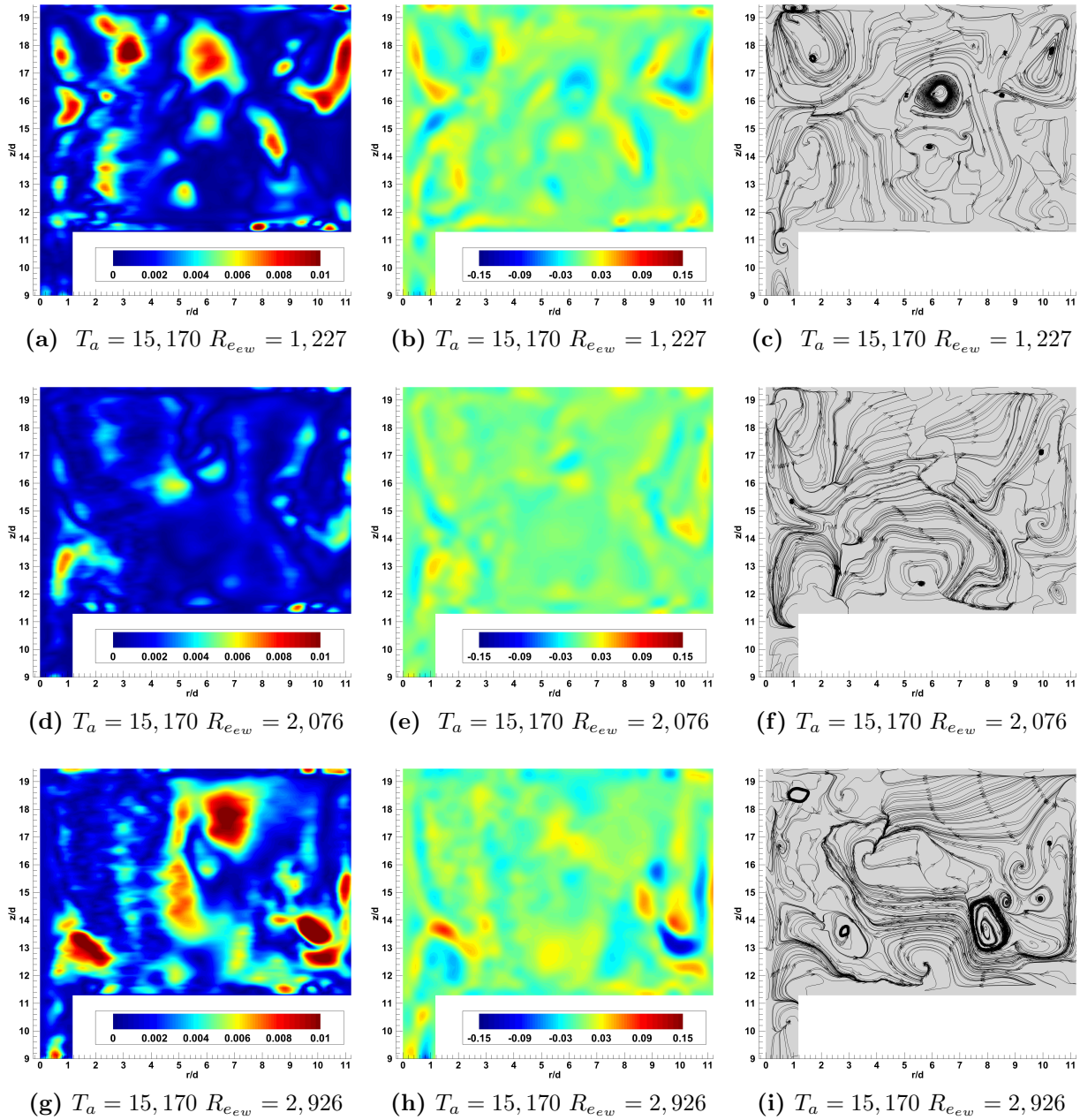

(a) $T_a = 15,170$ $R_{e_{ew}} = 1,227$ **(b)** $T_a = 15,170$ $R_{e_{ew}} = 1,227$ **(c)** $T_a = 15,170$ $R_{e_{ew}} = 1,227$

(d) $T_a = 15,170$ $R_{e_{ew}} = 2,076$ **(e)** $T_a = 15,170$ $R_{e_{ew}} = 2,076$ **(f)** $T_a = 15,170$ $R_{e_{ew}} = 2,076$

(g) $T_a = 15,170$ $R_{e_{ew}} = 2,926$ **(h)** $T_a = 15,170$ $R_{e_{ew}} = 2,926$ **(i)** $T_a = 15,170$ $R_{e_{ew}} = 2,926$

Figure A.10: Co-rotation at POD mode-1, velocity profile (left), non-dimensionalized vorticity $[\frac{\omega \hat{\mathbf{d}}}{2\Omega_I R_I}]$ (middle), streamlines (right), for varying $R_{e_{ew}}$ at $\Gamma_{ew} = 1.5$

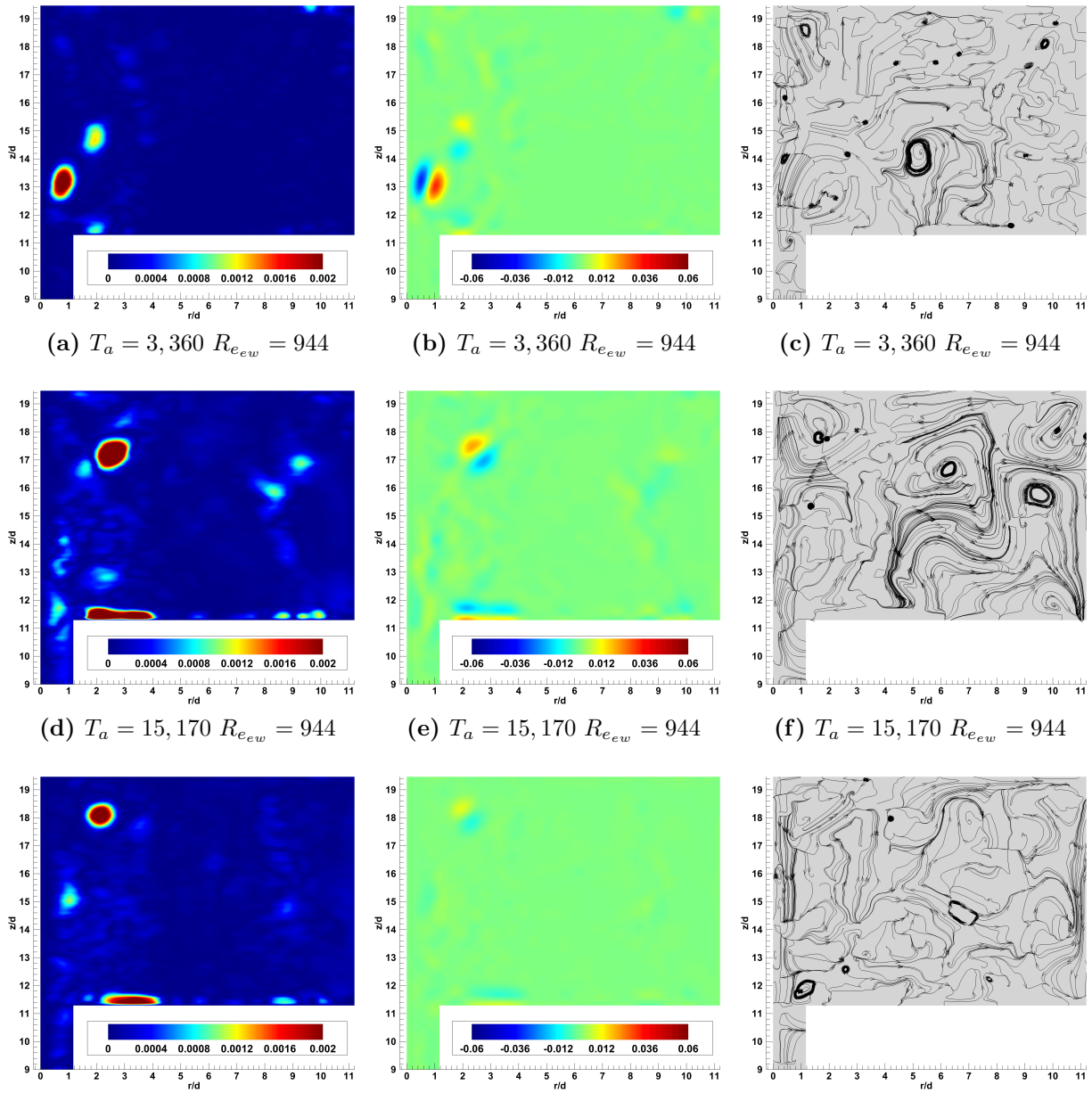

(a) $T_a = 3,360$ $R_{e_{ew}} = 944$ **(b)** $T_a = 3,360$ $R_{e_{ew}} = 944$ **(c)** $T_a = 3,360$ $R_{e_{ew}} = 944$

(d) $T_a = 15,170$ $R_{e_{ew}} = 944$ **(e)** $T_a = 15,170$ $R_{e_{ew}} = 944$ **(f)** $T_a = 15,170$ $R_{e_{ew}} = 944$

(g) $T_a = 35,485$ $R_{e_{ew}} = 944$ **(h)** $T_a = 35,485$ $R_{e_{ew}} = 944$ **(i)** $T_a = 35,485$ $R_{e_{ew}} = 944$

Figure A.11: Co-rotation at POD mode-3, velocity profile (left), non-dimensionalized $[\frac{\omega \hat{\mathbf{d}}}{2\Omega_I R_I}]$ (middle), streamlines (left), for varying T_a at $\Gamma_{ew} = 1.5$

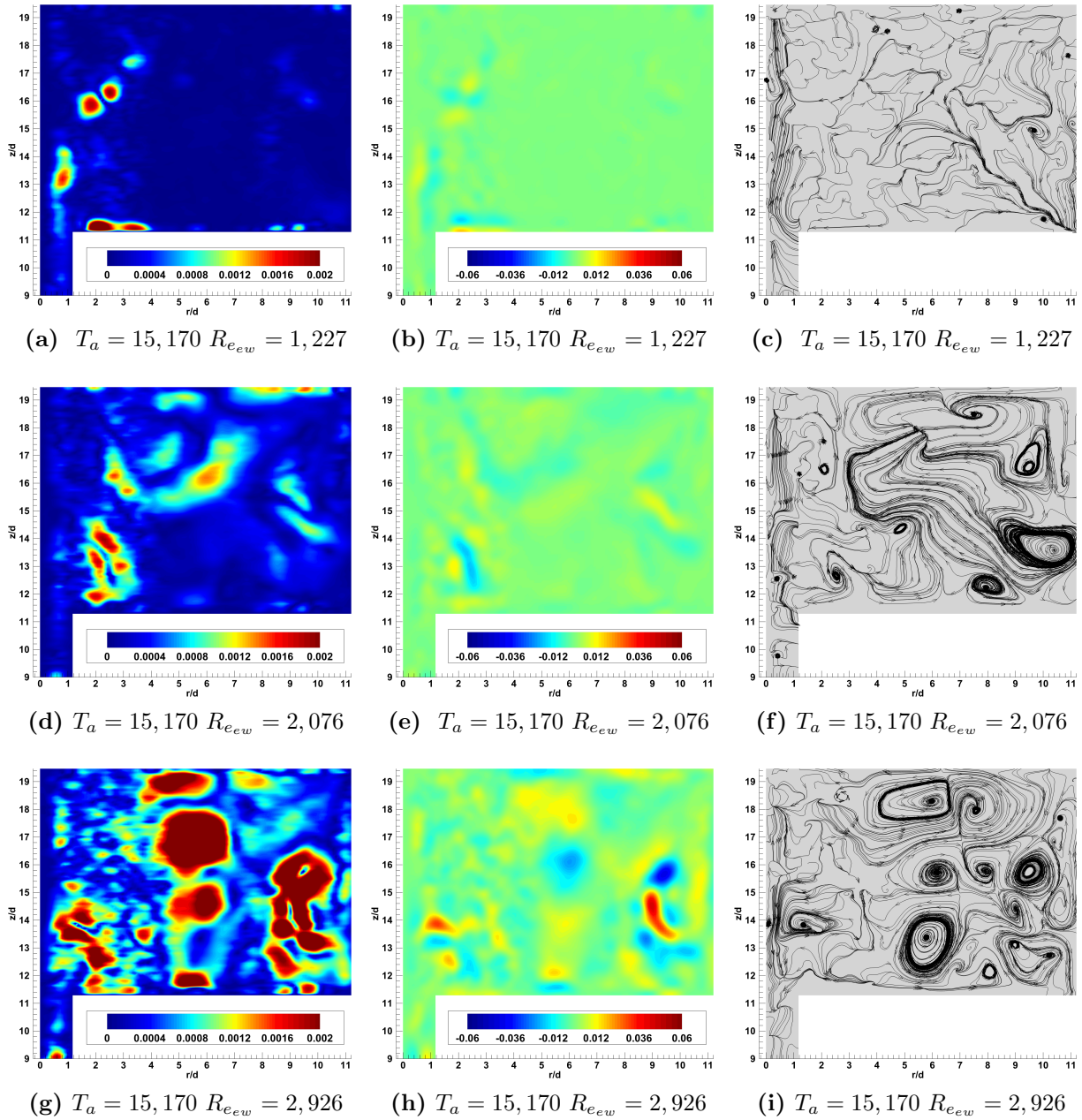

(a) $T_a = 15,170$ $R_{e_{ew}} = 1,227$ **(b)** $T_a = 15,170$ $R_{e_{ew}} = 1,227$ **(c)** $T_a = 15,170$ $R_{e_{ew}} = 1,227$

(d) $T_a = 15,170$ $R_{e_{ew}} = 2,076$ **(e)** $T_a = 15,170$ $R_{e_{ew}} = 2,076$ **(f)** $T_a = 15,170$ $R_{e_{ew}} = 2,076$

(g) $T_a = 15,170$ $R_{e_{ew}} = 2,926$ **(h)** $T_a = 15,170$ $R_{e_{ew}} = 2,926$ **(i)** $T_a = 15,170$ $R_{e_{ew}} = 2,926$

Figure A.12: Co-rotation at POD mode-3, velocity profile (left), non-dimensionalized vorticity $[\frac{\omega \hat{\mathbf{d}}}{2\Omega_I R_I}]$ (middle), streamlines (right), for varying $R_{e_{ew}}$ at $\Gamma_{ew} = 1.5$

Appendix B

Co-rotational supplemental figures (annular domain)

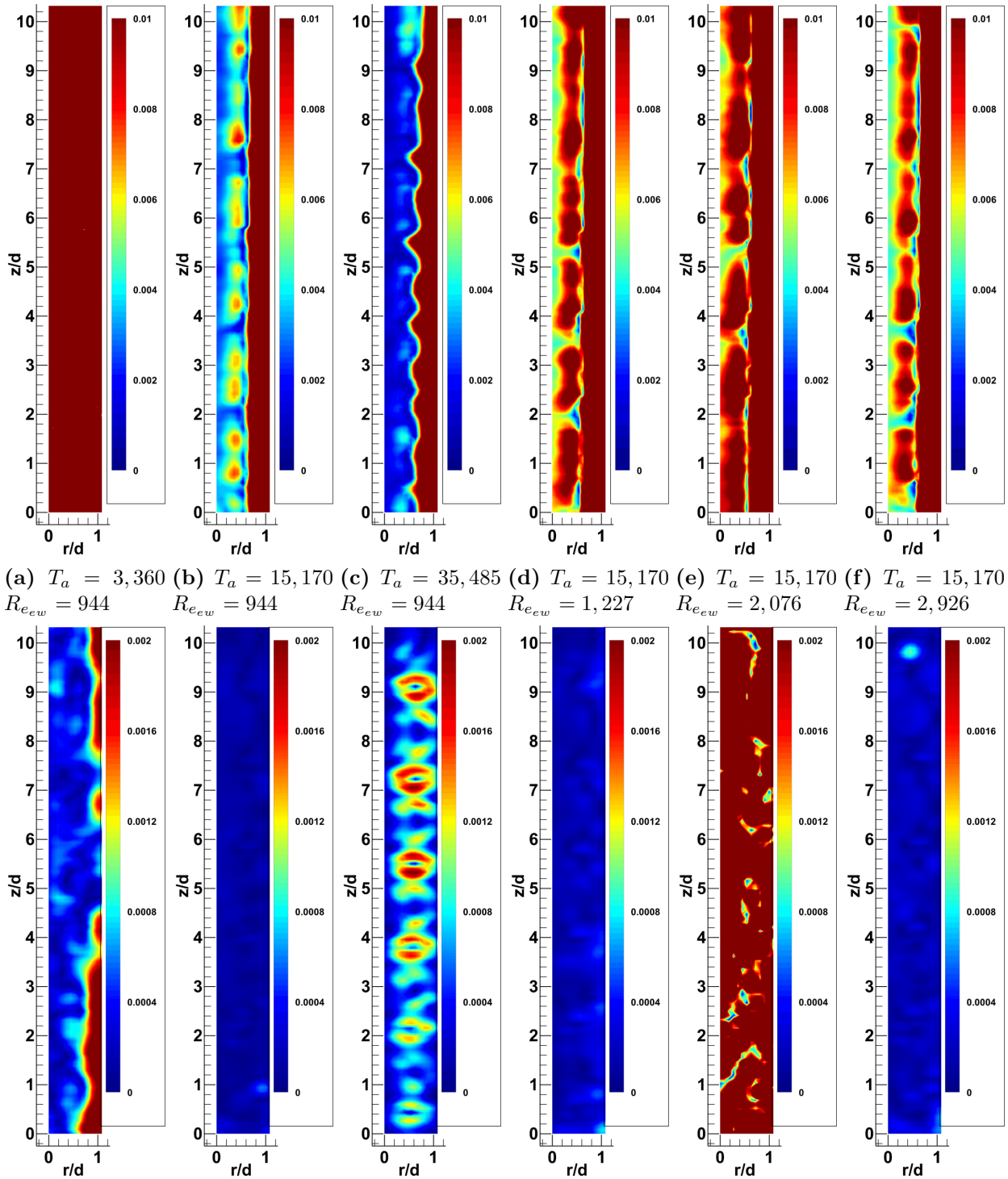

(a) $T_a = 3,360$ $R_{e_{ew}} = 944$ (b) $T_a = 15,170$ $R_{e_{ew}} = 944$ (c) $T_a = 35,485$ $R_{e_{ew}} = 944$ (d) $T_a = 15,170$ $R_{e_{ew}} = 1,227$ (e) $T_a = 15,170$ $R_{e_{ew}} = 2,076$ (f) $T_a = 15,170$ $R_{e_{ew}} = 2,926$

(g) $T_a = 3,360$ $R_{e_{ew}} = 944$ (h) $T_a = 15,170$ $R_{e_{ew}} = 944$ (i) $T_a = 35,485$ $R_{e_{ew}} = 944$ (j) $T_a = 15,170$ $R_{e_{ew}} = 1,227$ (k) $T_a = 15,170$ $R_{e_{ew}} = 2,076$ (l) $T_a = 15,170$ $R_{e_{ew}} = 2,926$

Figure B.1: Co-rotational annular flow at POD mode-1 (top) and mod-3 (bottom), velocity profile for varying T_a (left) & for varying $R_{e_{ew}}$ (right) at $\Gamma_{ew} = 1$

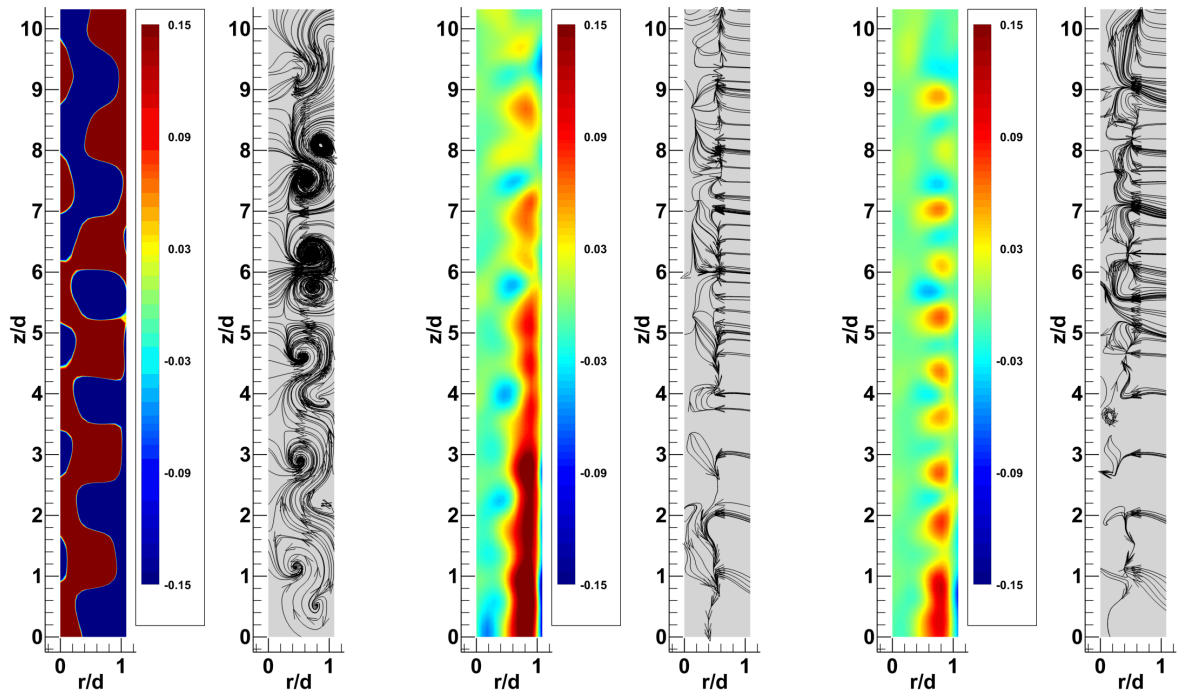

(a) $T_a = 3,360$ $R_{e_{ew}} = 944$ (b) $T_a = 3,360$ $R_{e_{ew}} = 944$ (c) $T_a = 15,170$ $R_{e_{ew}} = 944$ (d) $T_a = 15,170$ $R_{e_{ew}} = 944$ (e) $T_a = 35,485$ $R_{e_{ew}} = 944$ (f) $T_a = 35,485$ $R_{e_{ew}} = 944$

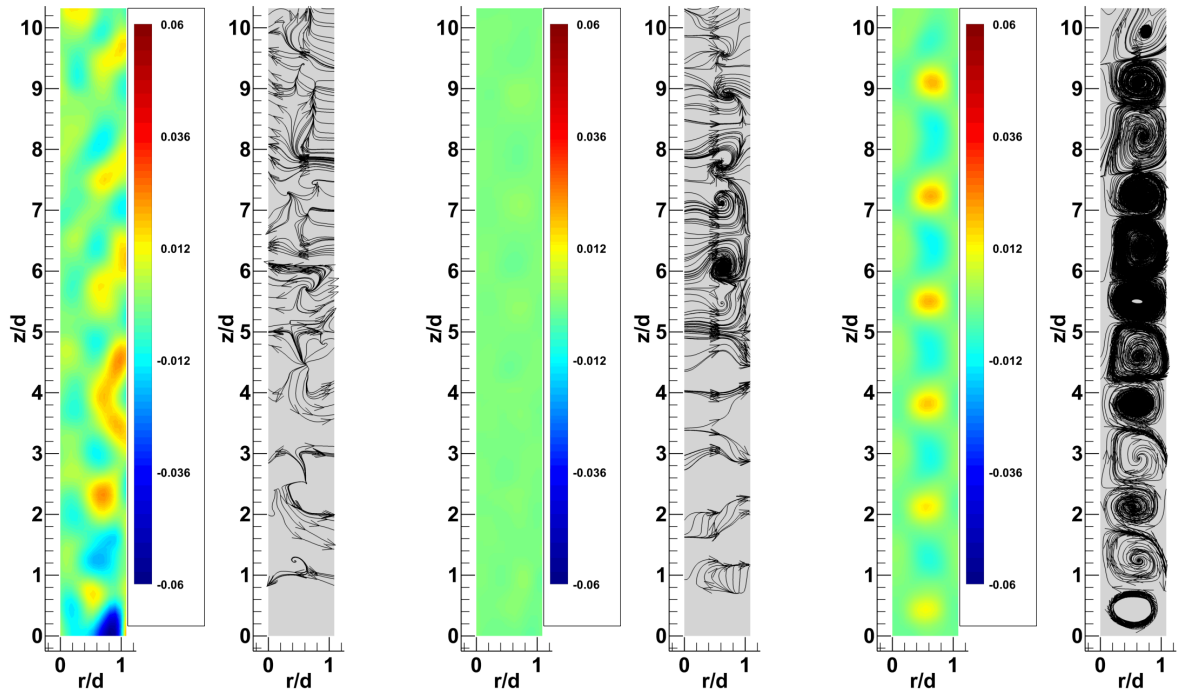

(g) $T_a = 3,360$ $R_{e_{ew}} = 944$ (h) $T_a = 3,360$ $R_{e_{ew}} = 944$ (i) $T_a = 15,170$ $R_{e_{ew}} = 944$ (j) $T_a = 15,170$ $R_{e_{ew}} = 944$ (k) $T_a = 35,485$ $R_{e_{ew}} = 944$ (l) $T_a = 35,485$ $R_{e_{ew}} = 944$

Figure B.2: Co-rotation annular flow at POD mode-1 (top) and mode-3 (bottom), non-dimensionalized vorticity $[\frac{\omega \hat{\mathbf{d}}}{2\Omega_I R_I}]$ & streamlines, for varying T_a at $\Gamma_{ew} = 1$

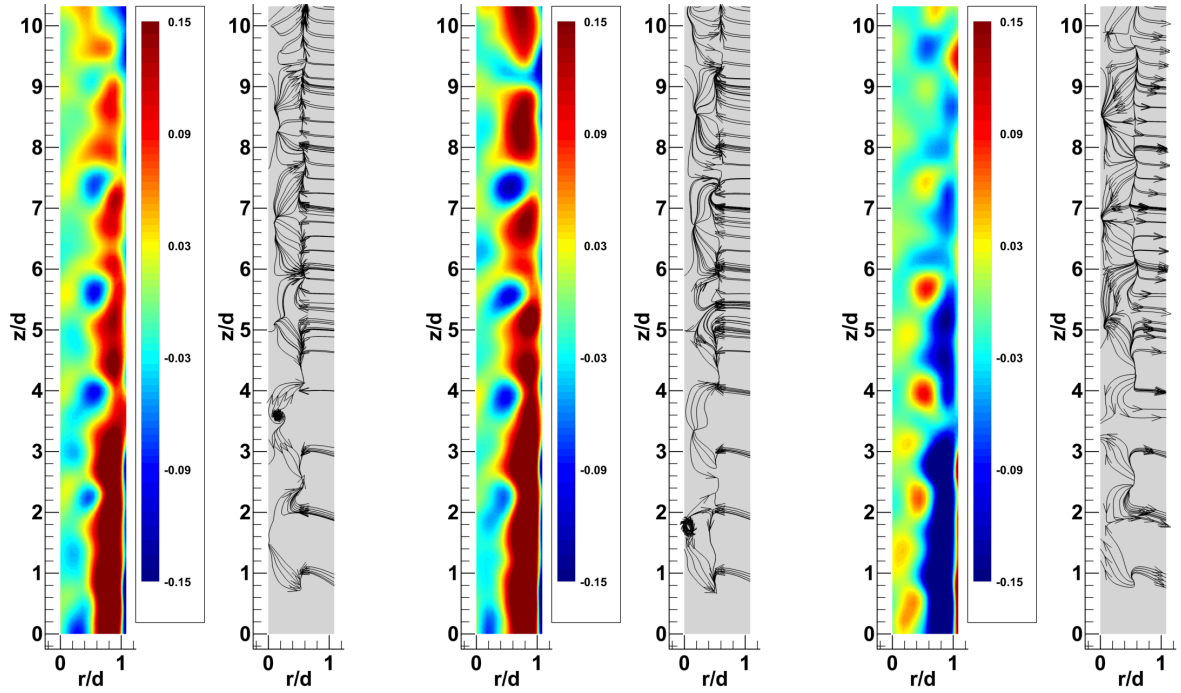

(a) $T_a = 15,170$ $R_{e_{ew}} = 1,227$ **(b)** $T_a = 15,170$ $R_{e_{ew}} = 1,227$ **(c)** $T_a = 15,170$ $R_{e_{ew}} = 2,076$ **(d)** $T_a = 15,170$ $R_{e_{ew}} = 2,076$ **(e)** $T_a = 15,170$ $R_{e_{ew}} = 2,926$ **(f)** $T_a = 15,170$ $R_{e_{ew}} = 2,926$

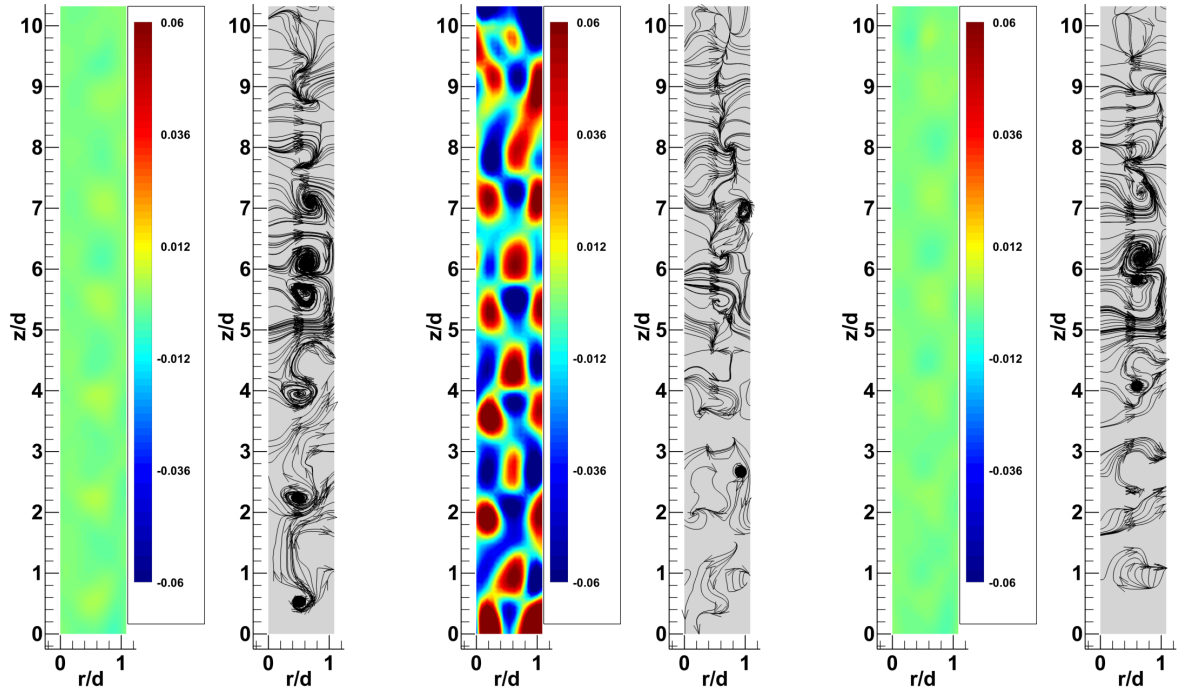

(g) $T_a = 15,170$ $R_{e_{ew}} = 1,227$ **(h)** $T_a = 15,170$ $R_{e_{ew}} = 1,227$ **(i)** $T_a = 15,170$ $R_{e_{ew}} = 2,076$ **(j)** $T_a = 15,170$ $R_{e_{ew}} = 2,076$ **(k)** $T_a = 15,170$ $R_{e_{ew}} = 2,926$ **(l)** $T_a = 15,170$ $R_{e_{ew}} = 2,926$

Figure B.3: Co-rotation annular flow at POD mode-1 (top) and mode-3 (bottom), non-dimensionalized vorticity $[\frac{\omega \hat{\mathbf{d}}}{2\Omega_I R_I}]$ & streamlines, for varying $R_{e_{ew}}$ at $\Gamma_{ew} = 1$

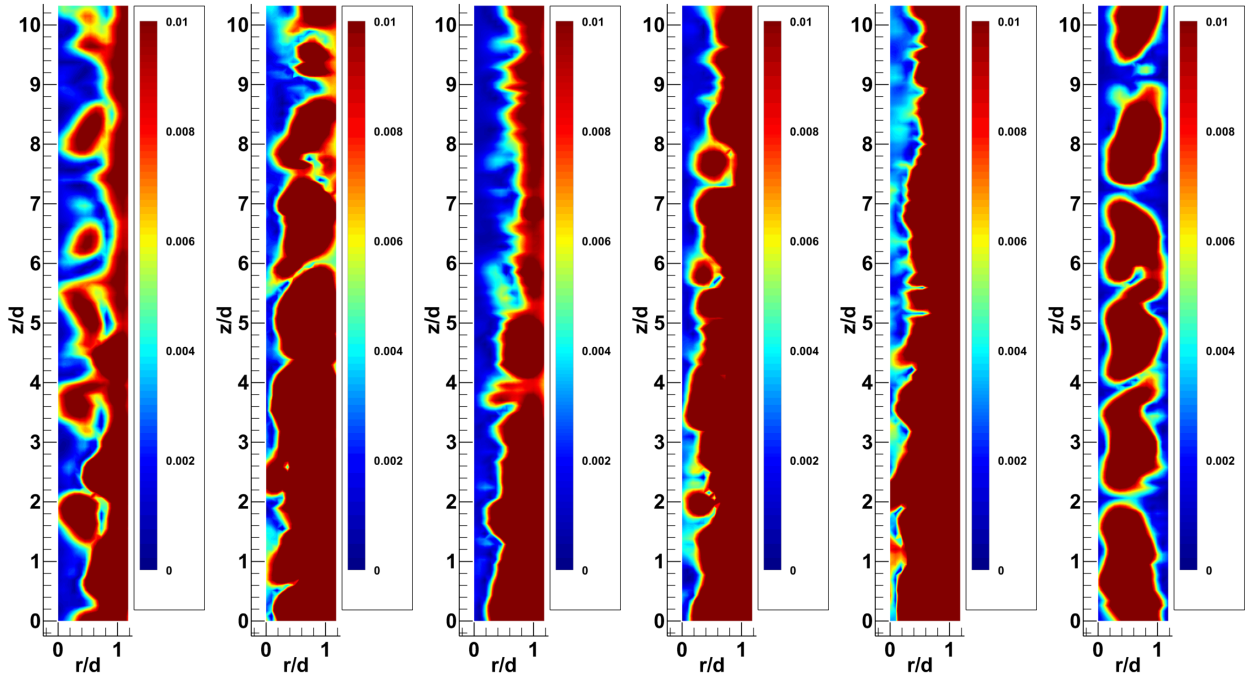

(a) $T_a = 3,360$ $R_{e_{ew}} = 944$ **(b)** $T_a = 15,170$ $R_{e_{ew}} = 944$ **(c)** $T_a = 35,485$ $R_{e_{ew}} = 944$ **(d)** $T_a = 15,170$ $R_{e_{ew}} = 1,227$ **(e)** $T_a = 15,170$ $R_{e_{ew}} = 2,076$ **(f)** $T_a = 15,170$ $R_{e_{ew}} = 2,926$

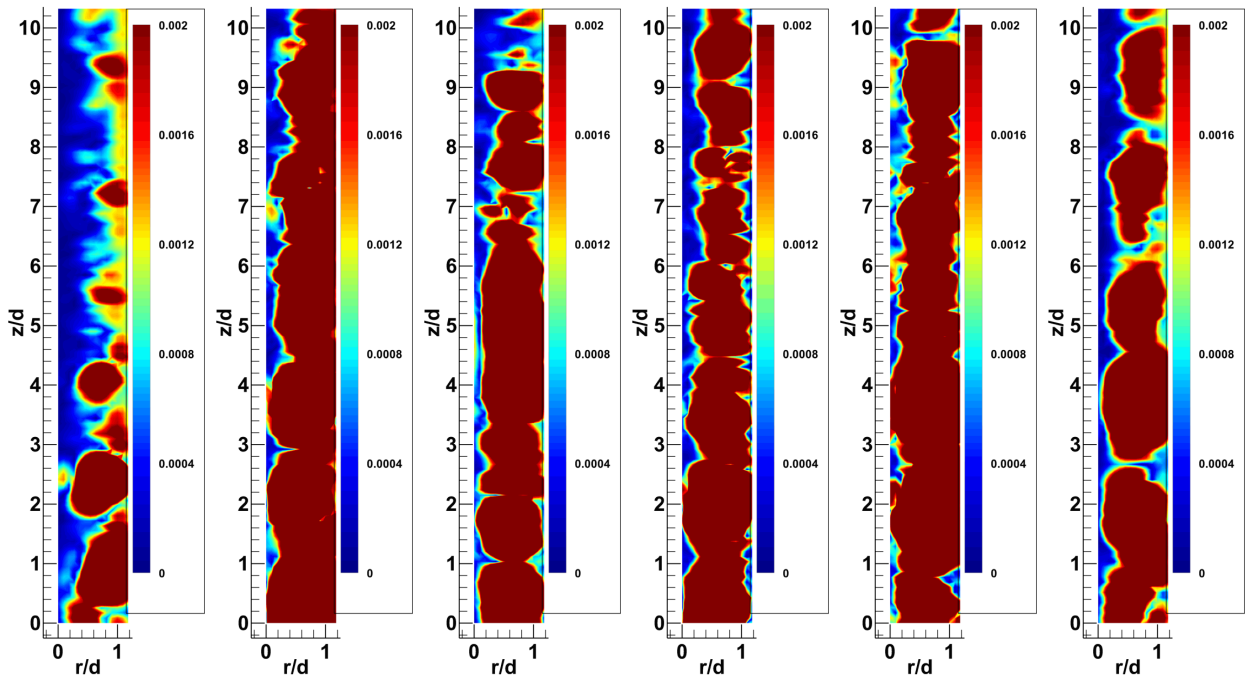

(g) $T_a = 3,360$ $R_{e_{ew}} = 944$ **(h)** $T_a = 15,170$ $R_{e_{ew}} = 944$ **(i)** $T_a = 35,485$ $R_{e_{ew}} = 944$ **(j)** $T_a = 15,170$ $R_{e_{ew}} = 1,227$ **(k)** $T_a = 15,170$ $R_{e_{ew}} = 2,076$ **(l)** $T_a = 15,170$ $R_{e_{ew}} = 2,926$

Figure B.4: Co-rotational annular flow at POD mode-1 (top) and mod-3 (bottom), velocity profile for varying T_a (left) and for varying $R_{e_{ew}}$ (right), at $\Gamma_{ew} = 1.5$

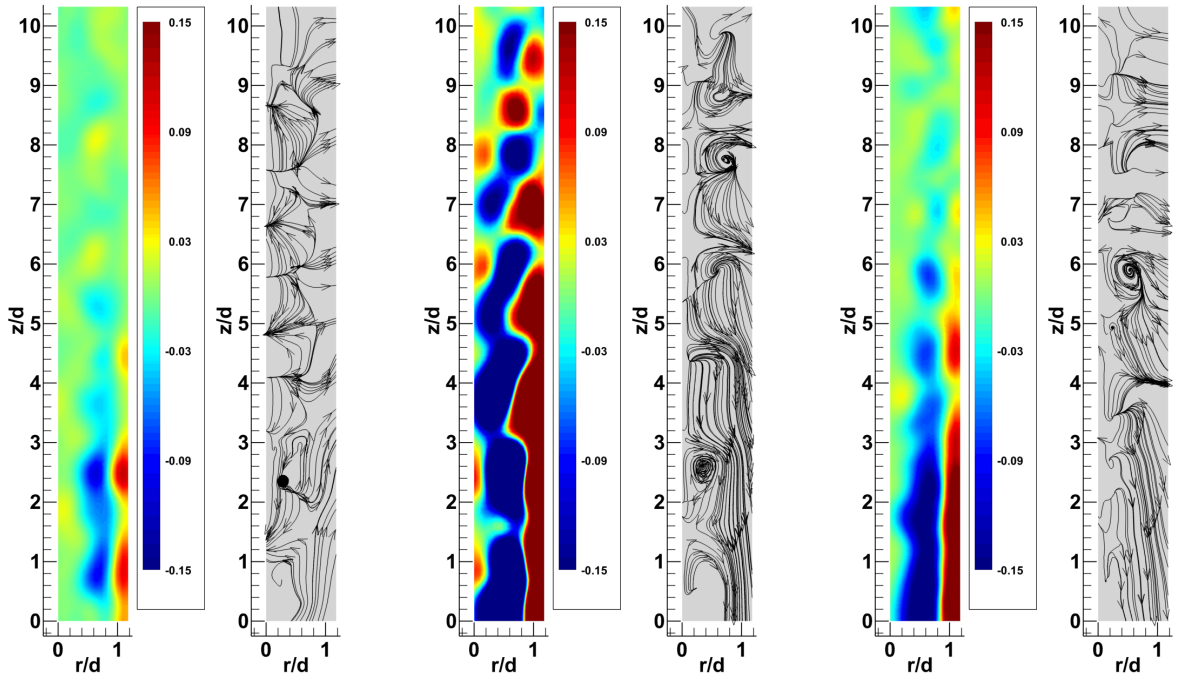

(a) $T_a = 3,360$ $R_{e_{ew}} = 944$ (b) $T_a = 3,360$ $R_{e_{ew}} = 944$ (c) $T_a = 15,170$ $R_{e_{ew}} = 944$ (d) $T_a = 15,170$ $R_{e_{ew}} = 944$ (e) $T_a = 35,485$ $R_{e_{ew}} = 944$ (f) $T_a = 35,485$ $R_{e_{ew}} = 944$

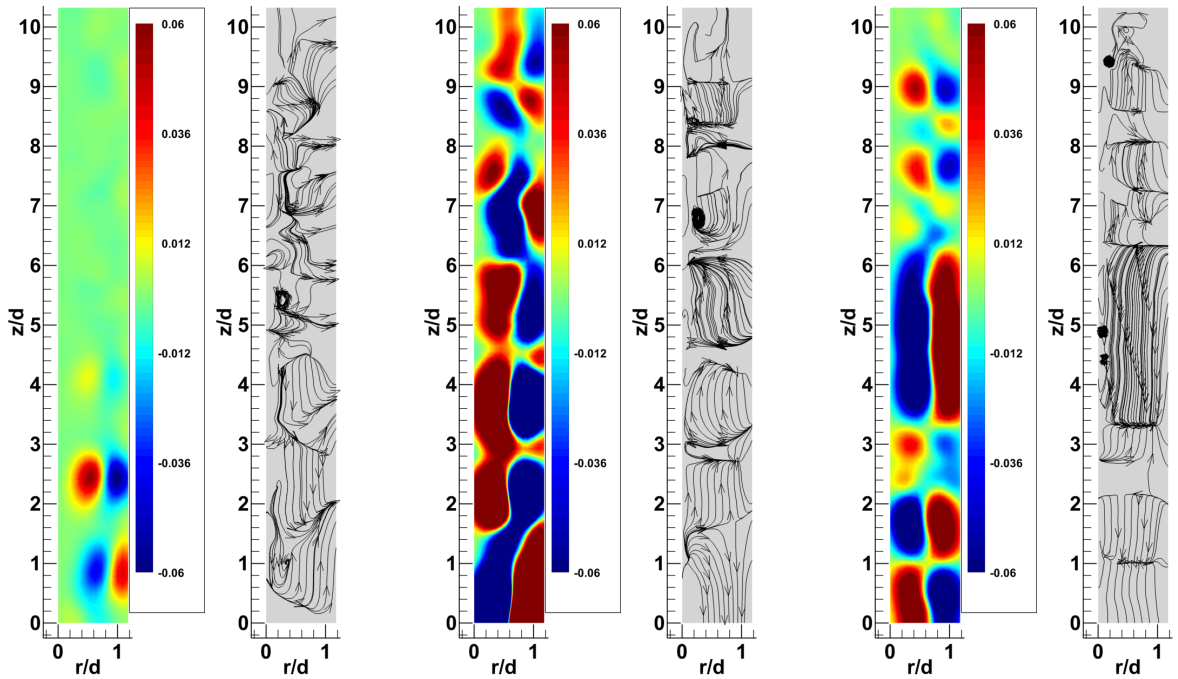

(g) $T_a = 3,360$ $R_{e_{ew}} = 944$ (h) $T_a = 3,360$ $R_{e_{ew}} = 944$ (i) $T_a = 15,170$ $R_{e_{ew}} = 944$ (j) $T_a = 15,170$ $R_{e_{ew}} = 944$ (k) $T_a = 35,485$ $R_{e_{ew}} = 944$ (l) $T_a = 35,485$ $R_{e_{ew}} = 944$

Figure B.5: Co-rotation annular flow at POD mode-1 (top) and mode-3 (bottom), non-dimensionalized vorticity $[\frac{\omega \hat{\mathbf{d}}}{2\Omega_I R_I}]$ & streamlines, for varying T_a at $\Gamma_{ew} = 1.5$

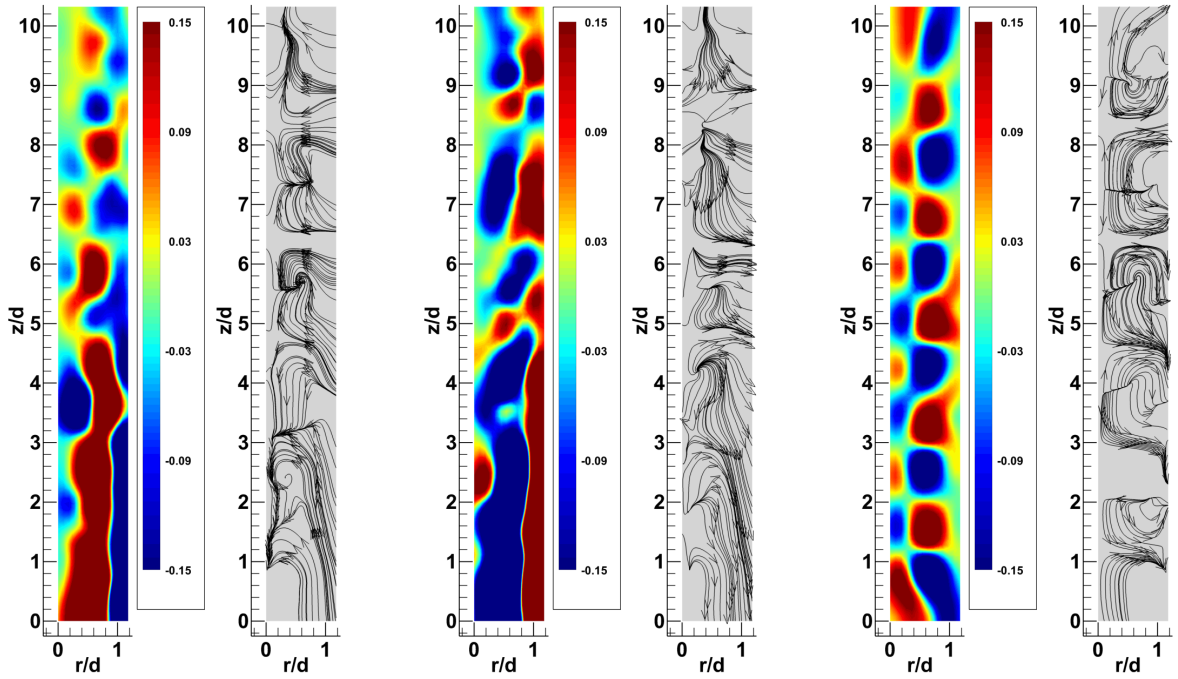

(a) $T_a = 15,170$ $R_{e_{ew}} = 1,227$ **(b)** $T_a = 15,170$ $R_{e_{ew}} = 1,227$ **(c)** $T_a = 15,170$ $R_{e_{ew}} = 2,076$ **(d)** $T_a = 15,170$ $R_{e_{ew}} = 2,076$ **(e)** $T_a = 15,170$ $R_{e_{ew}} = 2,926$ **(f)** $T_a = 15,170$ $R_{e_{ew}} = 2,926$

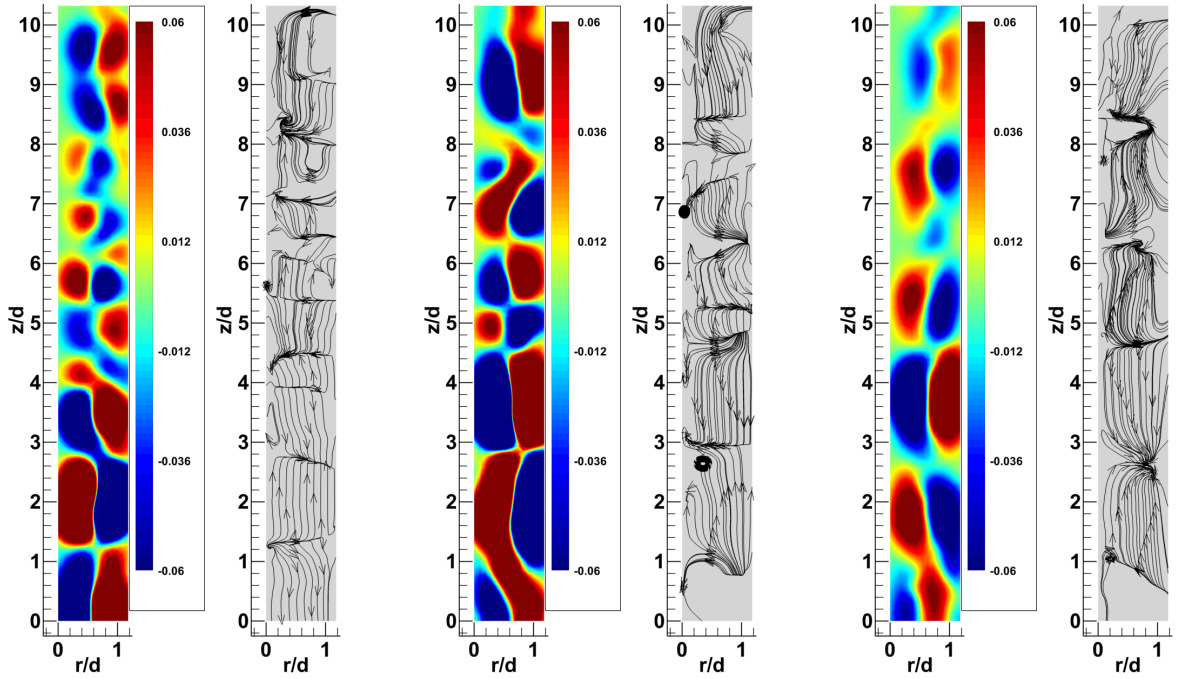

(g) $T_a = 15,170$ $R_{e_{ew}} = 1,227$ **(h)** $T_a = 15,170$ $R_{e_{ew}} = 1,227$ **(i)** $T_a = 15,170$ $R_{e_{ew}} = 2,076$ **(j)** $T_a = 15,170$ $R_{e_{ew}} = 2,076$ **(k)** $T_a = 15,170$ $R_{e_{ew}} = 2,926$ **(l)** $T_a = 15,170$ $R_{e_{ew}} = 2,926$

Figure B.6: Co-rotation annular flow at POD mode-1 (top) and mode-3 (bottom), non-dimensionalized vorticity $[\frac{\omega \hat{\mathbf{d}}}{2\Omega_I R_I}]$ & streamlines, for varying $R_{e_{ew}}$ at $\Gamma_{ew} = 1.5$

Appendix C

Counter-rotational supplemental figures (zone-2)

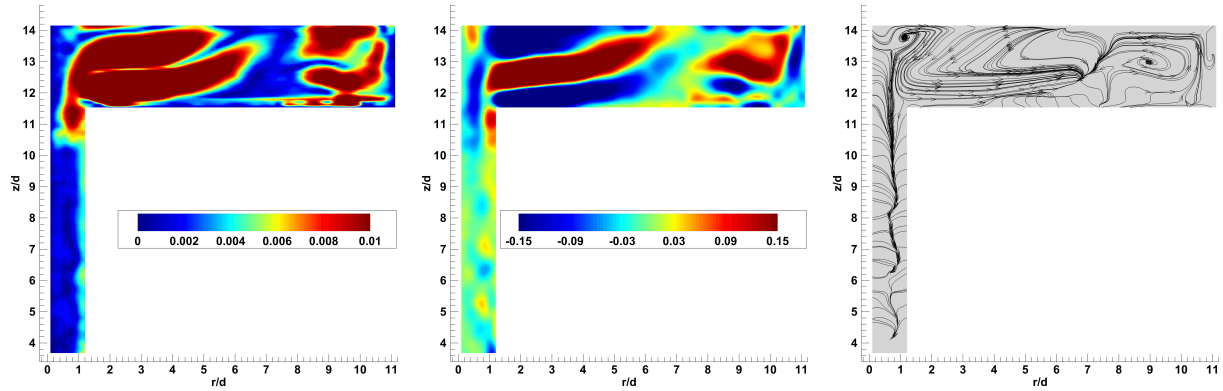

(a) $T_a = 3,360$ $R_{e_{ew}} = 944$ **(b)** $T_a = 3,360$ $R_{e_{ew}} = 944$ **(c)** $T_a = 3,360$ $R_{e_{ew}} = 944$

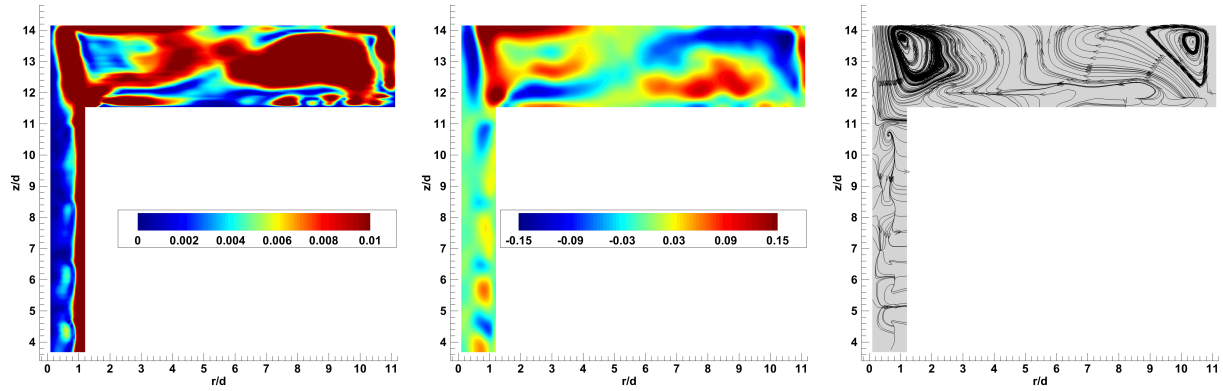

(d) $T_a = 15,170$ $R_{e_{ew}} = 944$ **(e)** $T_a = 15,170$ $R_{e_{ew}} = 944$ **(f)** $T_a = 15,170$ $R_{e_{ew}} = 944$

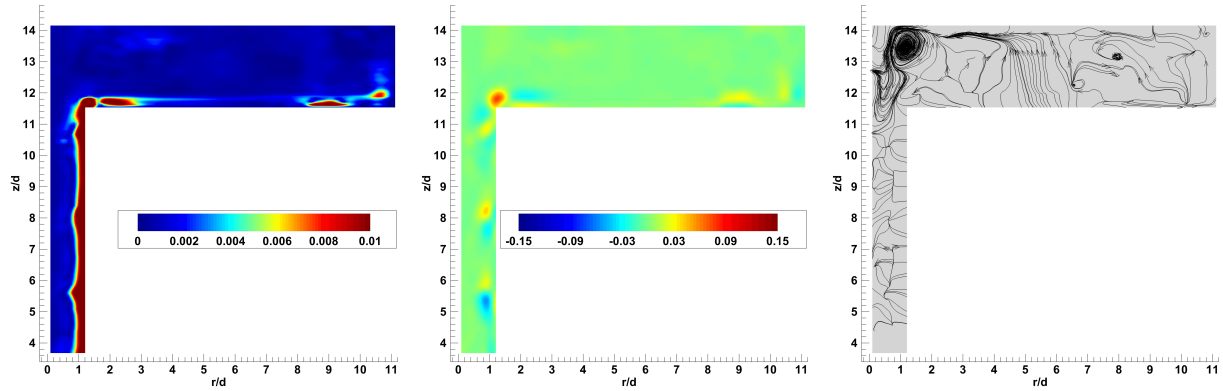

(g) $T_a = 35,485$ $R_{e_{ew}} = 944$ **(h)** $T_a = 35,485$ $R_{e_{ew}} = 944$ **(i)** $T_a = 35,485$ $R_{e_{ew}} = 944$

Figure C.1: Counter-rotation at POD mode-1, velocity profile (left), non-dimensionalized vorticity $[\frac{\omega \hat{\mathbf{d}}}{2\Omega_I R_I}]$ (middle), streamlines (right), for varying T_a at $\Gamma_{ew} = 0.5$

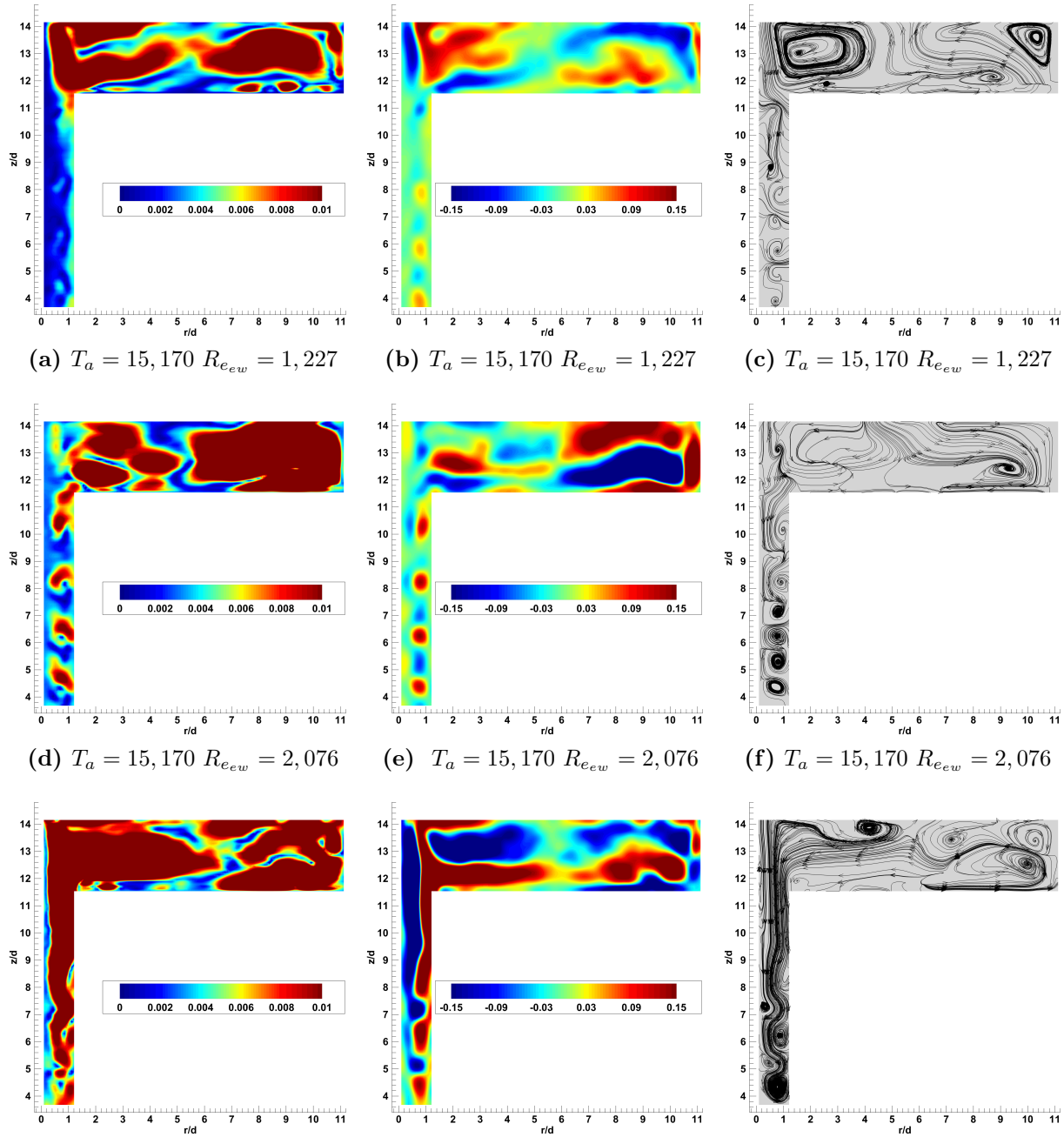

(a) $T_a = 15,170\ R_{e_{ew}} = 1,227$ **(b)** $T_a = 15,170\ R_{e_{ew}} = 1,227$ **(c)** $T_a = 15,170\ R_{e_{ew}} = 1,227$

(d) $T_a = 15,170\ R_{e_{ew}} = 2,076$ **(e)** $T_a = 15,170\ R_{e_{ew}} = 2,076$ **(f)** $T_a = 15,170\ R_{e_{ew}} = 2,076$

(g) $T_a = 15,170\ R_{e_{ew}} = 2,926$ **(h)** $T_a = 15,170\ R_{e_{ew}} = 2,926$ **(i)** $T_a = 15,170\ R_{e_{ew}} = 2,926$

Figure C.2: Counter-rotation at POD mode-1, velocity profile (left), non-dimensionalized vorticity $[\frac{\omega \hat{\mathbf{d}}}{2\Omega_I R_I}]$ (middle), streamlines (right), for varying R_{eew} at $\Gamma_{ew} = 0.5$

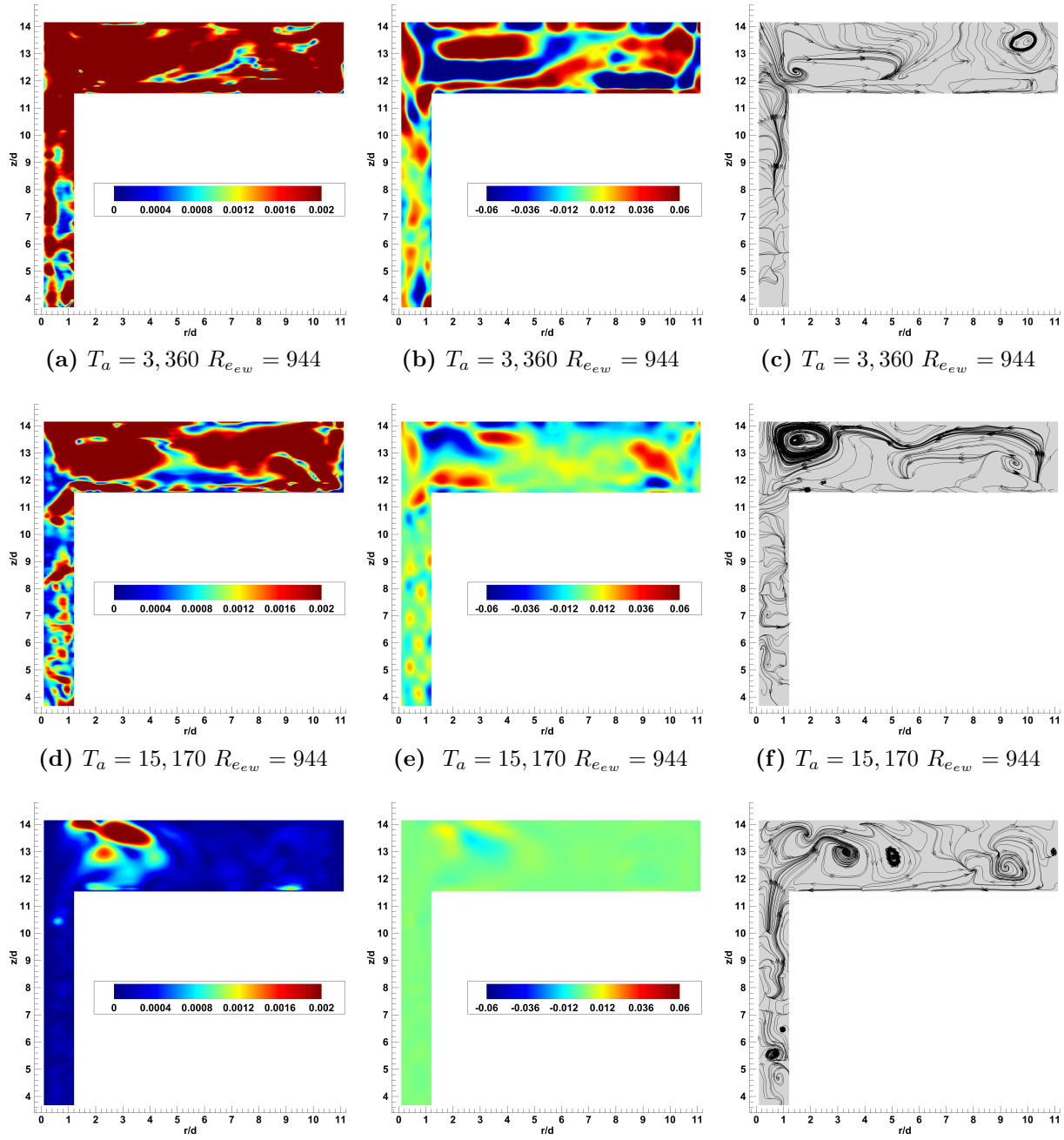

(a) $T_a = 3,360$ $R_{e_{ew}} = 944$ **(b)** $T_a = 3,360$ $R_{e_{ew}} = 944$ **(c)** $T_a = 3,360$ $R_{e_{ew}} = 944$

(d) $T_a = 15,170$ $R_{e_{ew}} = 944$ **(e)** $T_a = 15,170$ $R_{e_{ew}} = 944$ **(f)** $T_a = 15,170$ $R_{e_{ew}} = 944$

(g) $T_a = 35,485$ $R_{e_{ew}} = 944$ **(h)** $T_a = 35,485$ $R_{e_{ew}} = 944$ **(i)** $T_a = 35,485$ $R_{e_{ew}} = 944$

Figure C.3: Counter-rotation at POD mode-3, velocity profile (left), non-dimensionalized vorticity $[\frac{\omega \hat{\mathbf{d}}}{2\Omega_I R_I}]$ (middle), streamlines (right), for varying T_a at $\Gamma_{ew} = 0.5$

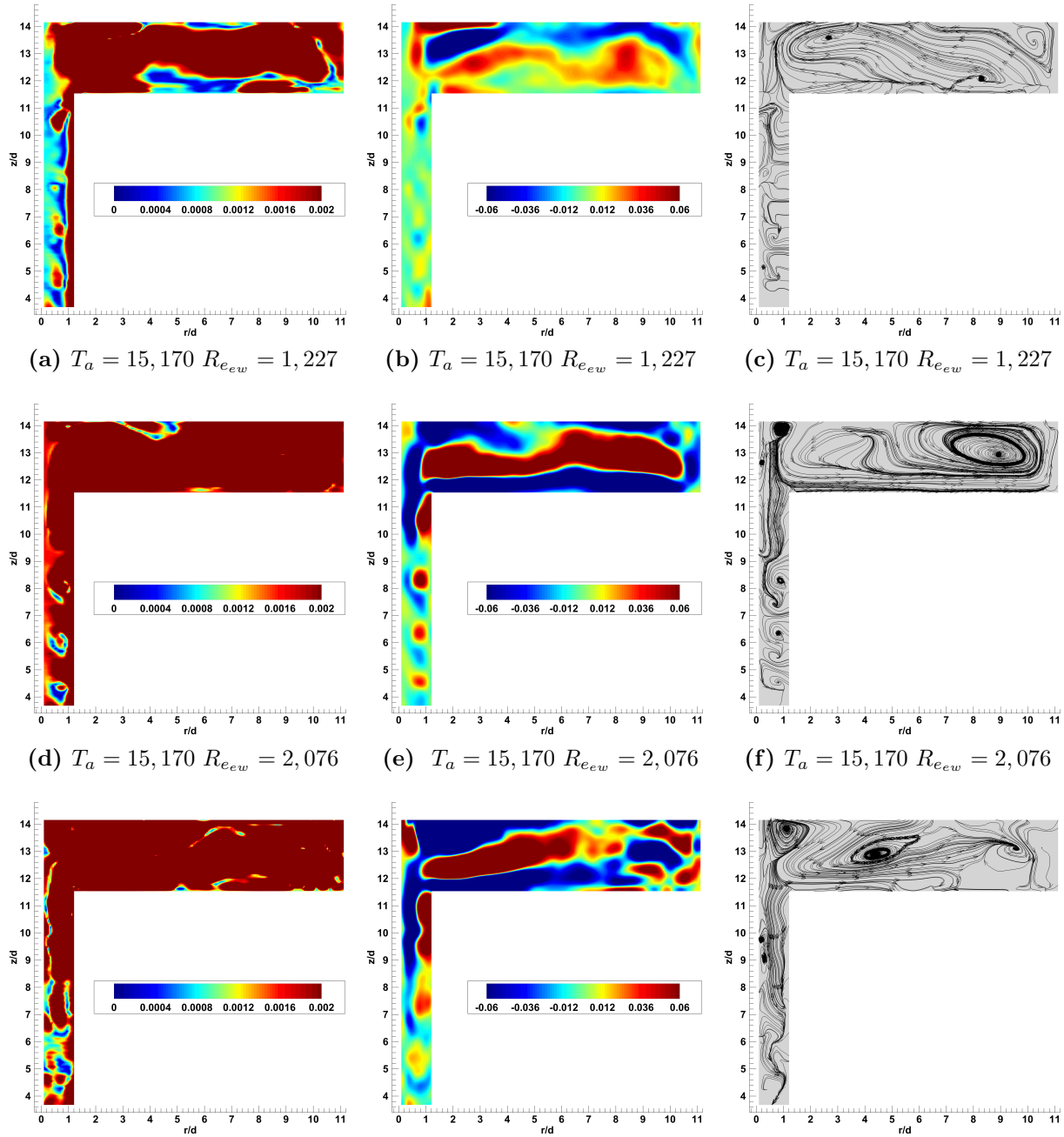

(a) $T_a = 15,170$ $R_{e_{ew}} = 1,227$ **(b)** $T_a = 15,170$ $R_{e_{ew}} = 1,227$ **(c)** $T_a = 15,170$ $R_{e_{ew}} = 1,227$

(d) $T_a = 15,170$ $R_{e_{ew}} = 2,076$ **(e)** $T_a = 15,170$ $R_{e_{ew}} = 2,076$ **(f)** $T_a = 15,170$ $R_{e_{ew}} = 2,076$

(g) $T_a = 15,170$ $R_{e_{ew}} = 2,296$ **(h)** $T_a = 15,170$ $R_{e_{ew}} = 2,296$ **(i)** $T_a = 15,170$ $R_{e_{ew}} = 2,296$

Figure C.4: Counter-rotation at POD mode-3, velocity profile (left), non-dimensionalized vorticity $[\frac{\omega \hat{\mathbf{d}}}{2\Omega_I R_I}]$ (middle), streamlines (right), for varying R_{eew} at $\Gamma_{ew} = 0.5$

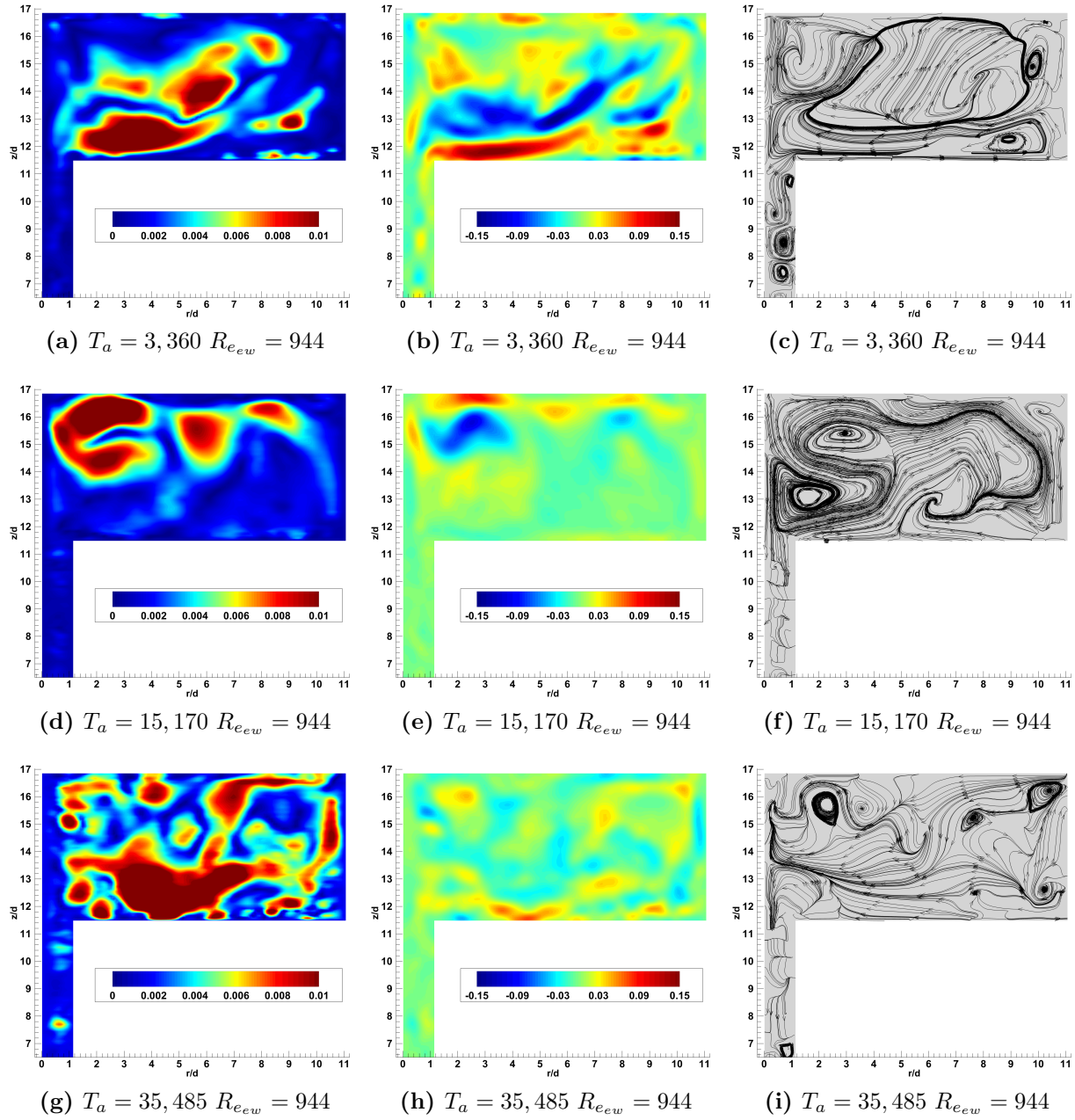

(a) $T_a = 3,360$ $R_{e_{ew}} = 944$ **(b)** $T_a = 3,360$ $R_{e_{ew}} = 944$ **(c)** $T_a = 3,360$ $R_{e_{ew}} = 944$

(d) $T_a = 15,170$ $R_{e_{ew}} = 944$ **(e)** $T_a = 15,170$ $R_{e_{ew}} = 944$ **(f)** $T_a = 15,170$ $R_{e_{ew}} = 944$

(g) $T_a = 35,485$ $R_{e_{ew}} = 944$ **(h)** $T_a = 35,485$ $R_{e_{ew}} = 944$ **(i)** $T_a = 35,485$ $R_{e_{ew}} = 944$

Figure C.5: Counter-rotation at POD mode-1, velocity profile (left), non-dimensionalized vorticity $[\frac{\omega \hat{\mathbf{d}}}{2\Omega_I R_I}]$ (middle), streamlines (right), for varying T_a at $\Gamma_{ew} = 1$

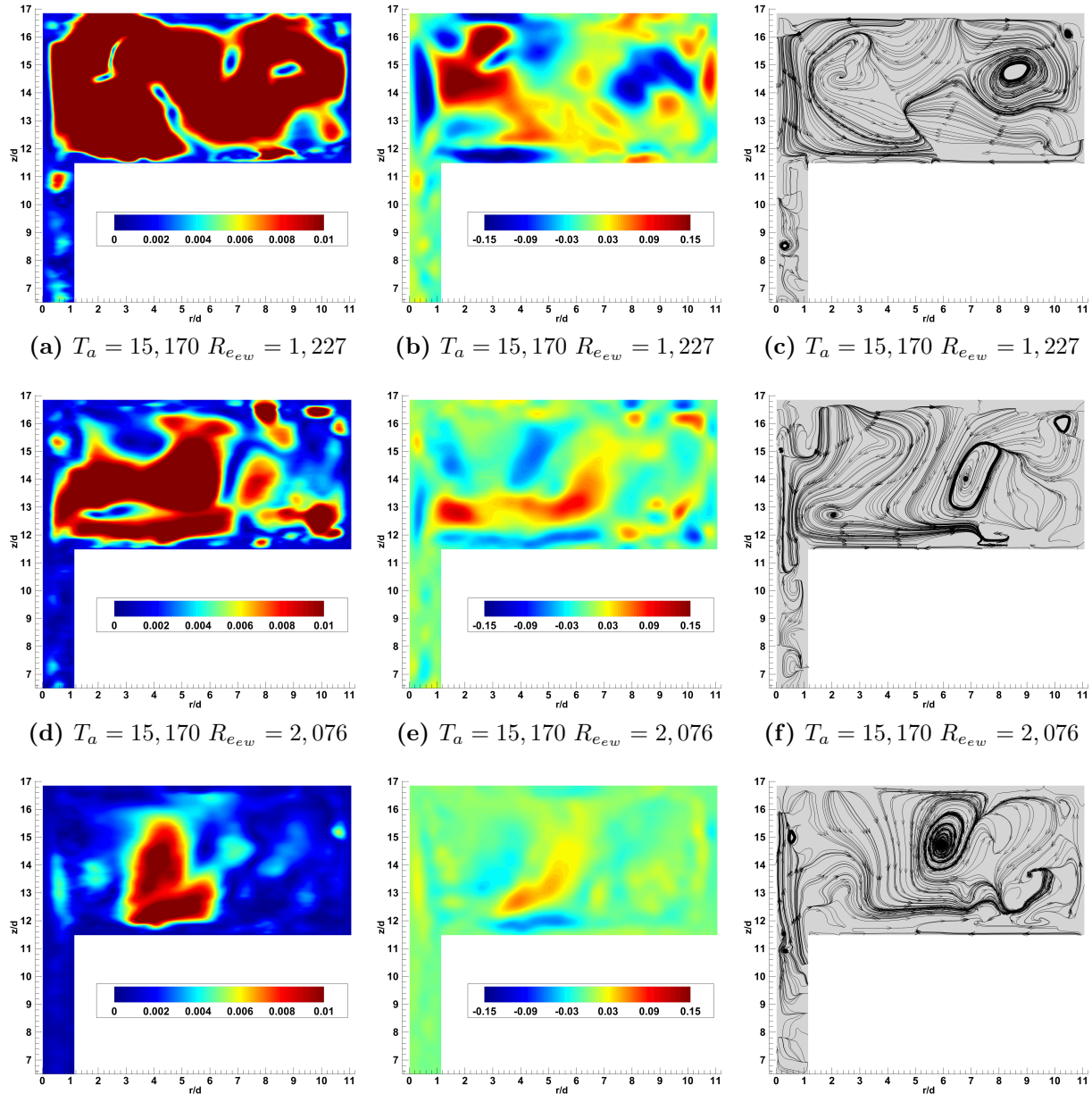

(a) $T_a = 15,170$ $R_{e_{ew}} = 1,227$ **(b)** $T_a = 15,170$ $R_{e_{ew}} = 1,227$ **(c)** $T_a = 15,170$ $R_{e_{ew}} = 1,227$

(d) $T_a = 15,170$ $R_{e_{ew}} = 2,076$ **(e)** $T_a = 15,170$ $R_{e_{ew}} = 2,076$ **(f)** $T_a = 15,170$ $R_{e_{ew}} = 2,076$

(g) $T_a = 15,170$ $R_{e_{ew}} = 2,926$ **(h)** $T_a = 15,170$ $R_{e_{ew}} = 2,926$ **(i)** $T_a = 15,170$ $R_{e_{ew}} = 2,926$

Figure C.6: Counter-rotation at POD mode-1, velocity profile (left), non-dimensionalized vorticity $[\frac{\omega \hat{\mathbf{d}}}{2\Omega_I R_I}]$ (middle), streamlines (right), for varying $R_{e_{ew}}$ at $\Gamma_{ew} = 1$

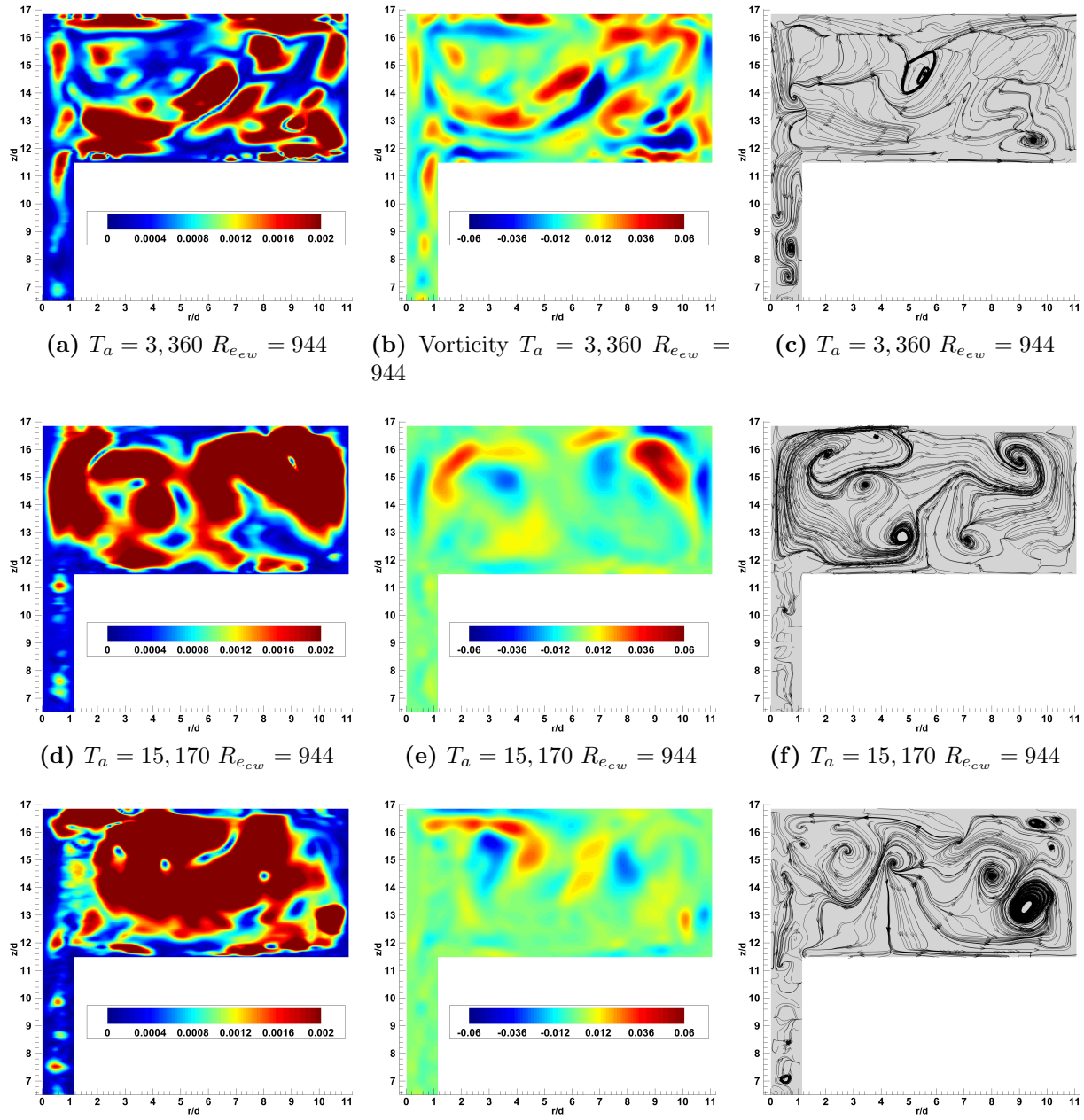

(a) $T_a = 3,360$ $R_{e_{ew}} = 944$ **(b)** Vorticity $T_a = 3,360$ $R_{e_{ew}} = 944$ **(c)** $T_a = 3,360$ $R_{e_{ew}} = 944$

(d) $T_a = 15,170$ $R_{e_{ew}} = 944$ **(e)** $T_a = 15,170$ $R_{e_{ew}} = 944$ **(f)** $T_a = 15,170$ $R_{e_{ew}} = 944$

(g) $T_a = 35,485$ $R_{e_{ew}} = 944$ **(h)** $T_a = 35,485$ $R_{e_{ew}} = 944$ **(i)** $T_a = 35,485$ $R_{e_{ew}} = 944$

Figure C.7: Counter-rotation at POD mode-3, velocity profile (left), non-dimensionalized vorticity $[\frac{\omega \hat{\mathbf{d}}}{2\Omega_I R_I}]$ (middle), streamlines (right), for varying T_a at $\Gamma_{ew} = 1$

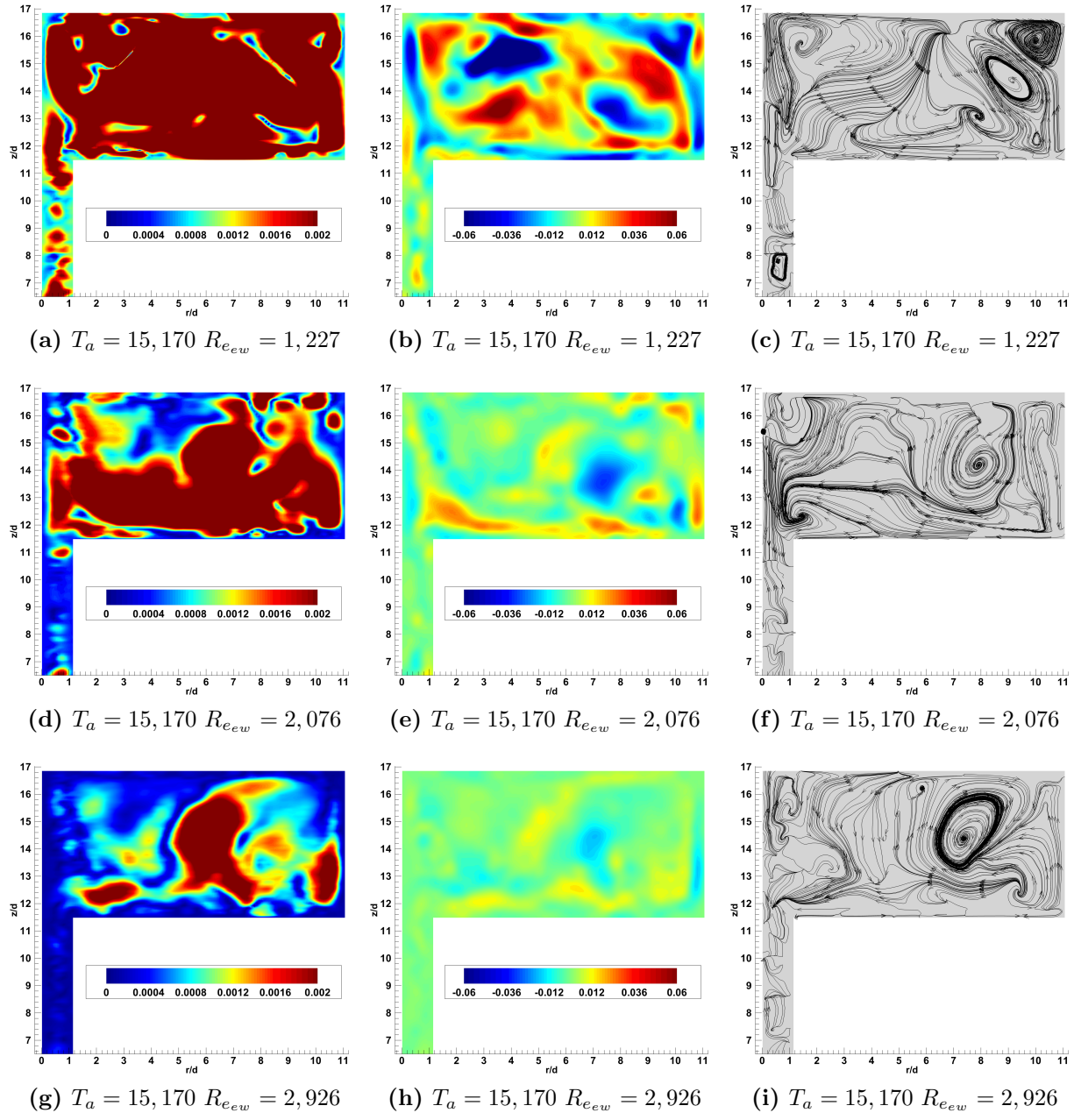

(a) $T_a = 15,170$ $R_{e_{ew}} = 1,227$ **(b)** $T_a = 15,170$ $R_{e_{ew}} = 1,227$ **(c)** $T_a = 15,170$ $R_{e_{ew}} = 1,227$

(d) $T_a = 15,170$ $R_{e_{ew}} = 2,076$ **(e)** $T_a = 15,170$ $R_{e_{ew}} = 2,076$ **(f)** $T_a = 15,170$ $R_{e_{ew}} = 2,076$

(g) $T_a = 15,170$ $R_{e_{ew}} = 2,926$ **(h)** $T_a = 15,170$ $R_{e_{ew}} = 2,926$ **(i)** $T_a = 15,170$ $R_{e_{ew}} = 2,926$

Figure C.8: Counter-rotation at POD mode-3, velocity profile (left), non-dimensionalized vorticity $[\frac{\omega \hat{\mathbf{d}}}{2\Omega_I R_I}]$ (middle), streamlines (right), for varying $R_{e_{ew}}$ at $\Gamma_{ew} = 1$

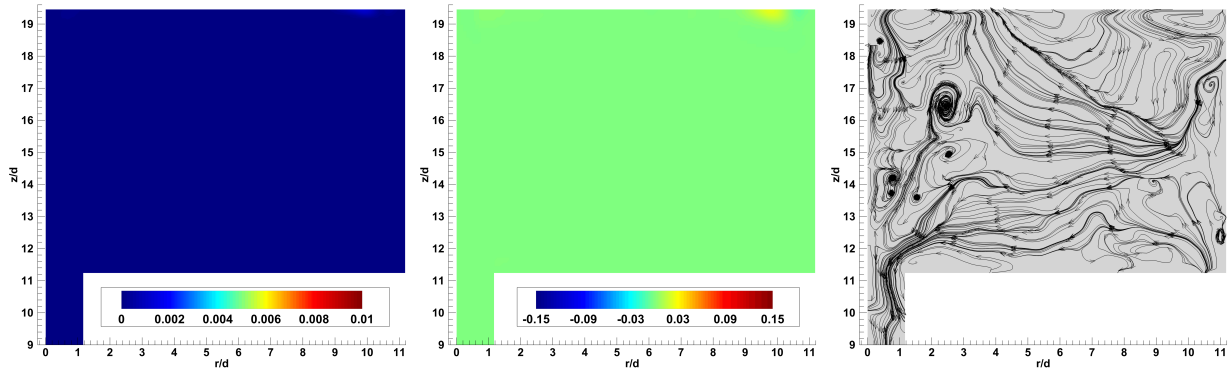

(a) $T_a = 3,360$ $R_{e_{ew}} = 944$ **(b)** $T_a = 3,360$ $R_{e_{ew}} = 944$ **(c)** $T_a = 3,360$ $R_{e_{ew}} = 944$

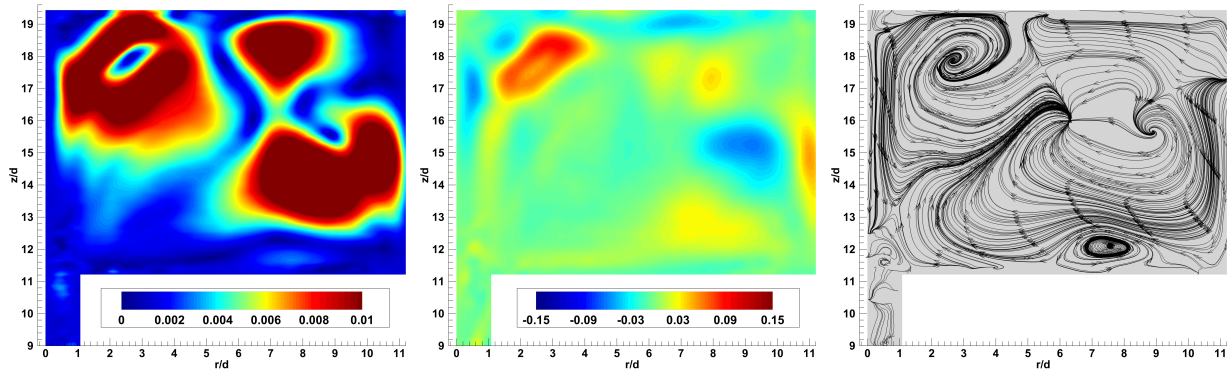

(d) $T_a = 15,170$ $R_{e_{ew}} = 944$ **(e)** $T_a = 15,170$ $R_{e_{ew}} = 944$ **(f)** $T_a = 15,170$ $R_{e_{ew}} = 944$

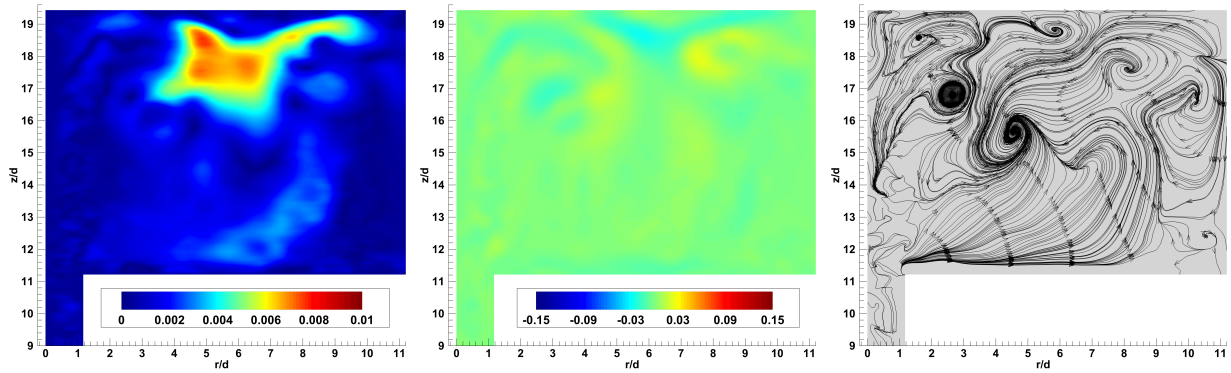

(g) $T_a = 35,485$ $R_{e_{ew}} = 944$ **(h)** $T_a = 35,485$ $R_{e_{ew}} = 944$ **(i)** $T_a = 35,485$ $R_{e_{ew}} = 944$

Figure C.9: Counter-rotation at POD mode-1, velocity profile (left), non-dimensionalized vorticity $[\frac{\omega \hat{\mathbf{d}}}{2\Omega_I R_I}]$ (middle), streamlines (left), for varying T_a at $\Gamma_{ew} = 1.5$

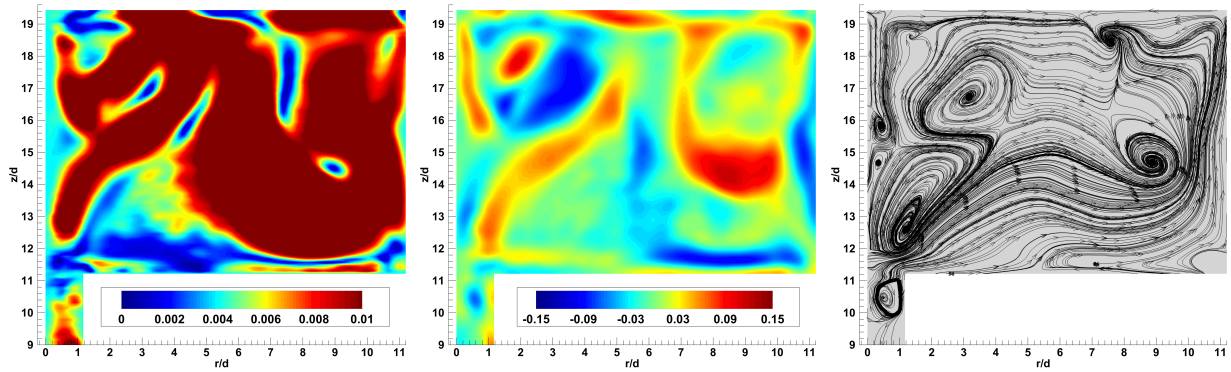

(a) $T_a = 15,170\ R_{e_{ew}} = 1,227$ **(b)** $T_a = 15,170\ R_{e_{ew}} = 1,227$ **(c)** $T_a = 15,170\ R_{e_{ew}} = 1,227$

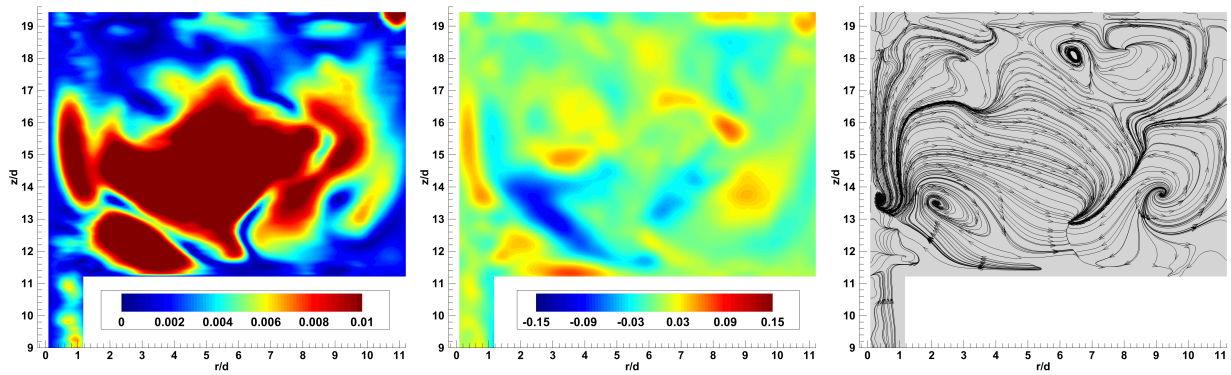

(d) $T_a = 15,170\ R_{e_{ew}} = 2,076$ **(e)** $T_a = 15,170\ R_{e_{ew}} = 2,076$ **(f)** $T_a = 15,170\ R_{e_{ew}} = 2,076$

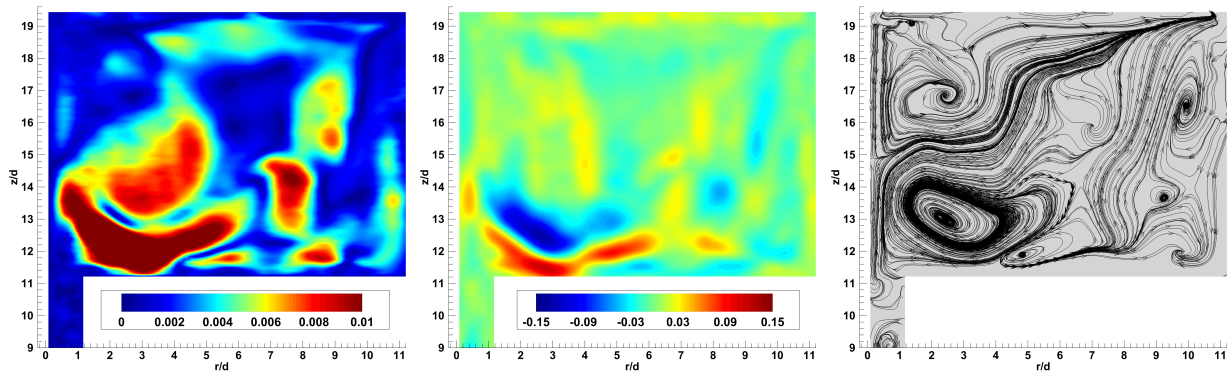

(g) $T_a = 15,170\ R_{e_{ew}} = 2,926$ **(h)** $T_a = 15,170\ R_{e_{ew}} = 2,926$ **(i)** $T_a = 15,170\ R_{e_{ew}} = 2,926$

Figure C.10: Counter-rotation at POD mode-1, velocity profile (left), non-dimensionalized vorticity $[\frac{\omega \hat{\mathbf{d}}}{2\Omega_I R_I}]$ (middle), streamlines (right), for varying $R_{e_{ew}}$ at $\Gamma_{ew} = 1.5$

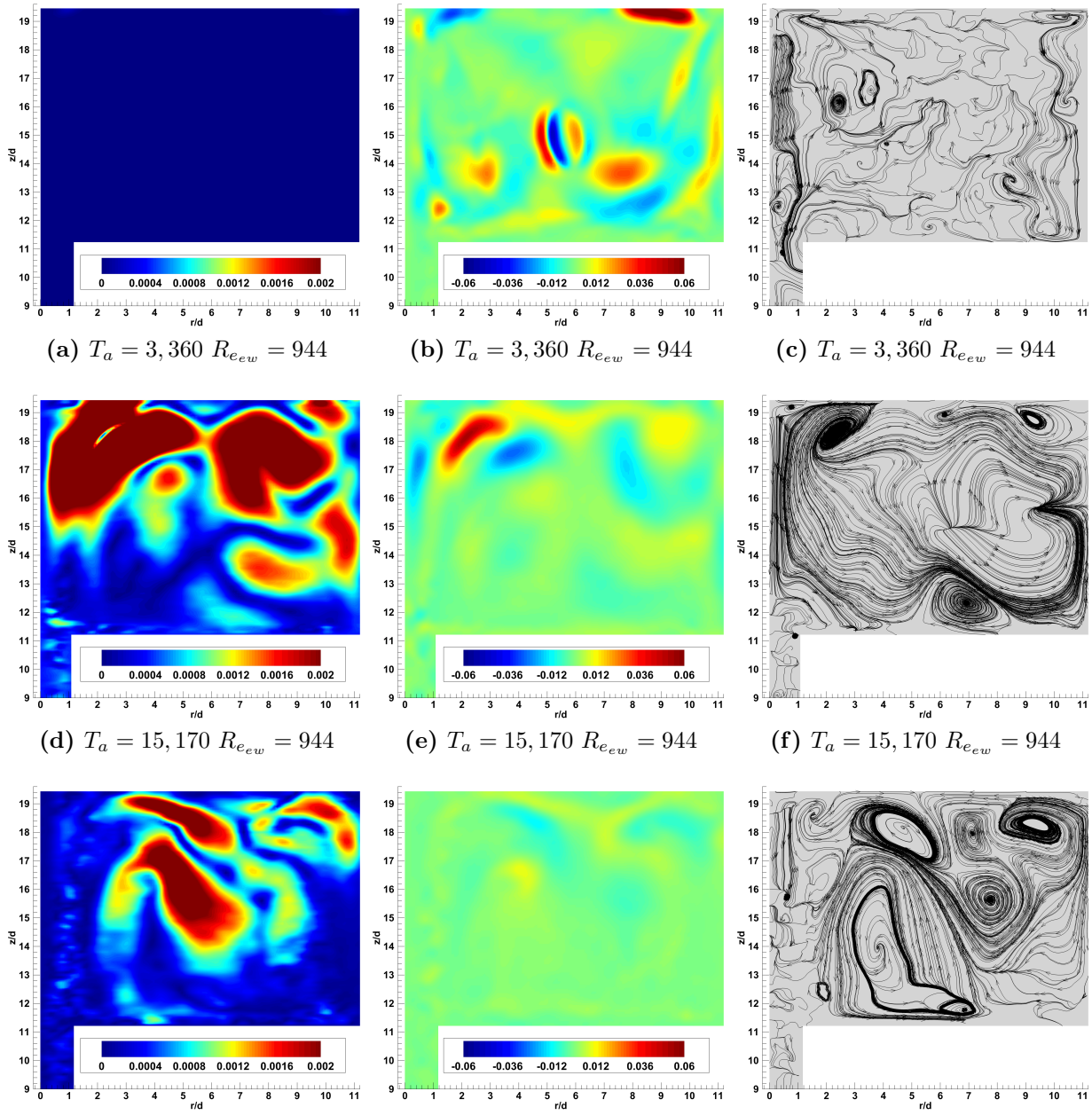

(a) $T_a = 3,360$ $R_{e_{ew}} = 944$ **(b)** $T_a = 3,360$ $R_{e_{ew}} = 944$ **(c)** $T_a = 3,360$ $R_{e_{ew}} = 944$

(d) $T_a = 15,170$ $R_{e_{ew}} = 944$ **(e)** $T_a = 15,170$ $R_{e_{ew}} = 944$ **(f)** $T_a = 15,170$ $R_{e_{ew}} = 944$

(g) $T_a = 35,485$ $R_{e_{ew}} = 944$ **(h)** $T_a = 35,485$ $R_{e_{ew}} = 944$ **(i)** $T_a = 35,485$ $R_{e_{ew}} = 944$

Figure C.11: Counter-rotation at POD mode-3, velocity profile (left), non-dimensionalized vorticity $[\frac{\omega \hat{\mathbf{d}}}{2\Omega_I R_I}]$ (middle), streamlines (left), for varying T_a at $\Gamma_{ew} = 1.5$

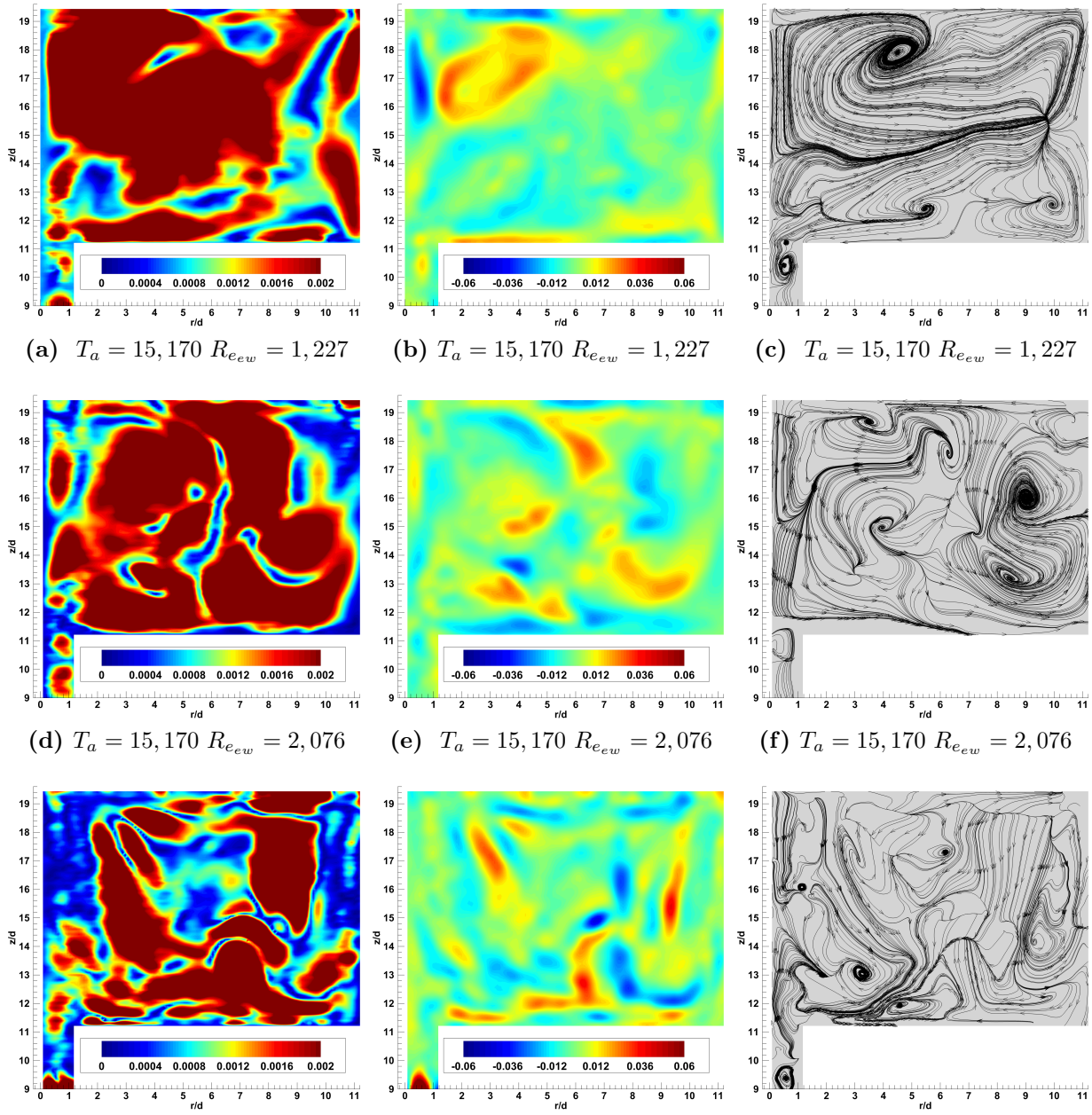

(a) $T_a = 15,170\ R_{e_{ew}} = 1,227$ **(b)** $T_a = 15,170\ R_{e_{ew}} = 1,227$ **(c)** $T_a = 15,170\ R_{e_{ew}} = 1,227$

(d) $T_a = 15,170\ R_{e_{ew}} = 2,076$ **(e)** $T_a = 15,170\ R_{e_{ew}} = 2,076$ **(f)** $T_a = 15,170\ R_{e_{ew}} = 2,076$

(g) $T_a = 15,170\ R_{e_{ew}} = 2,926$ **(h)** $T_a = 15,170\ R_{e_{ew}} = 2,926$ **(i)** $T_a = 15,170\ R_{e_{ew}} = 2,926$

Figure C.12: Counter-rotation at POD mode-3, velocity profile (left),non-dimensionalized vorticity $[\frac{\omega \hat{\mathbf{d}}}{2\Omega_I R_I}]$ (middle), streamlines (right), for varying $R_{e_{ew}}$ at $\Gamma_{ew} = 1.5$

Appendix D

Counter-rotational supplemental figures (annular domain)

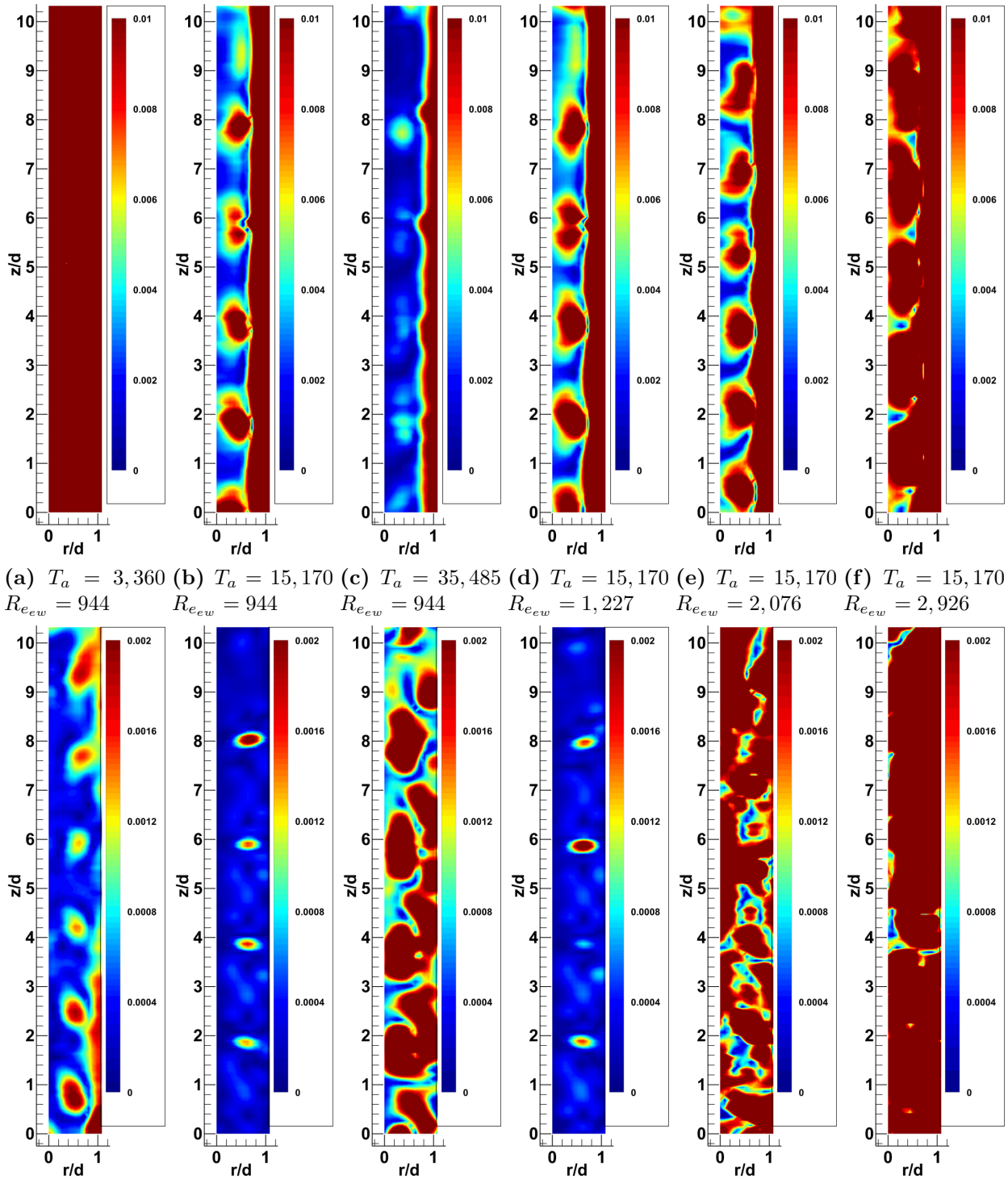

(a) $T_a = 3,360$ $R_{e_{ew}} = 944$ **(b)** $T_a = 15,170$ $R_{e_{ew}} = 944$ **(c)** $T_a = 35,485$ $R_{e_{ew}} = 944$ **(d)** $T_a = 15,170$ $R_{e_{ew}} = 1,227$ **(e)** $T_a = 15,170$ $R_{e_{ew}} = 2,076$ **(f)** $T_a = 15,170$ $R_{e_{ew}} = 2,926$

(g) $T_a = 3,360$ $R_{e_{ew}} = 944$ **(h)** $T_a = 15,170$ $R_{e_{ew}} = 944$ **(i)** $T_a = 35,485$ $R_{e_{ew}} = 944$ **(j)** $T_a = 15,170$ $R_{e_{ew}} = 1,227$ **(k)** $T_a = 15,170$ $R_{e_{ew}} = 2,076$ **(l)** $T_a = 15,170$ $R_{e_{ew}} = 2,926$

Figure D.1: Counter-rotational annular flow at POD mode-1 (top) and mod-3 (bottom), velocity profile for varying T_a (left), & varying $R_{e_{ew}}$ (right), at $\Gamma_{ew} = 1$

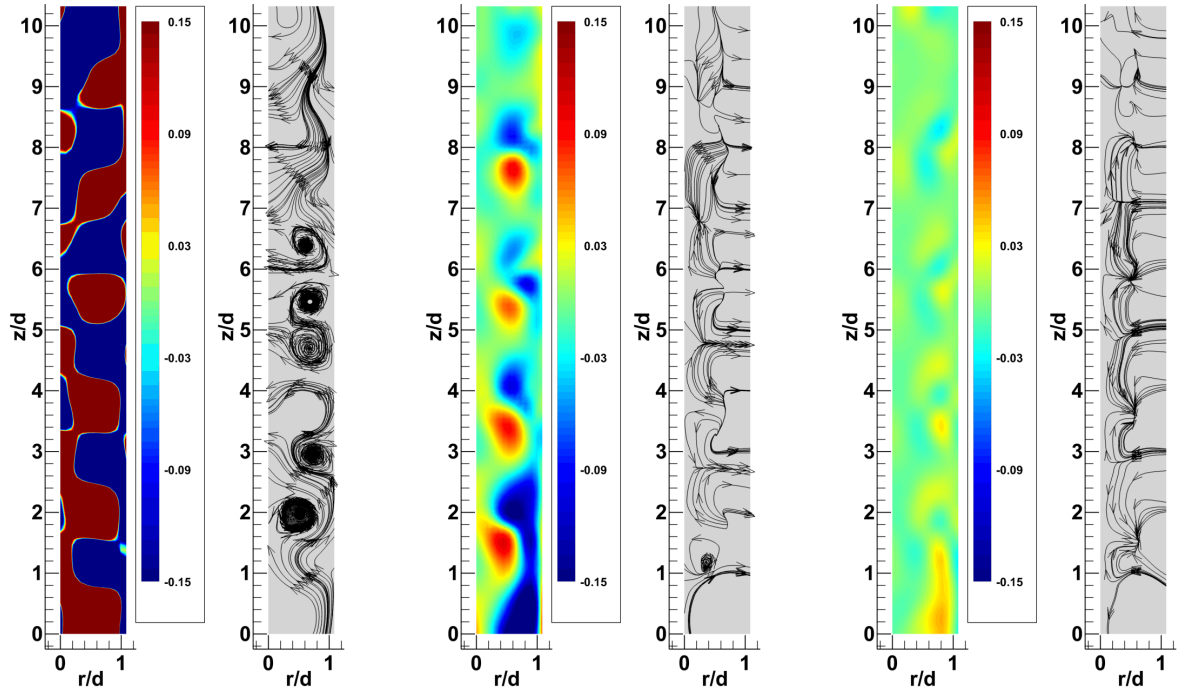

(a) $T_a = 3,360$ $R_{e_{ew}} = 944$ (b) $T_a = 3,360$ $R_{e_{ew}} = 944$ (c) $T_a = 15,170$ $R_{e_{ew}} = 944$ (d) $T_a = 15,170$ $R_{e_{ew}} = 944$ (e) $T_a = 35,485$ $R_{e_{ew}} = 944$ (f) $T_a = 35,485$ $R_{e_{ew}} = 944$

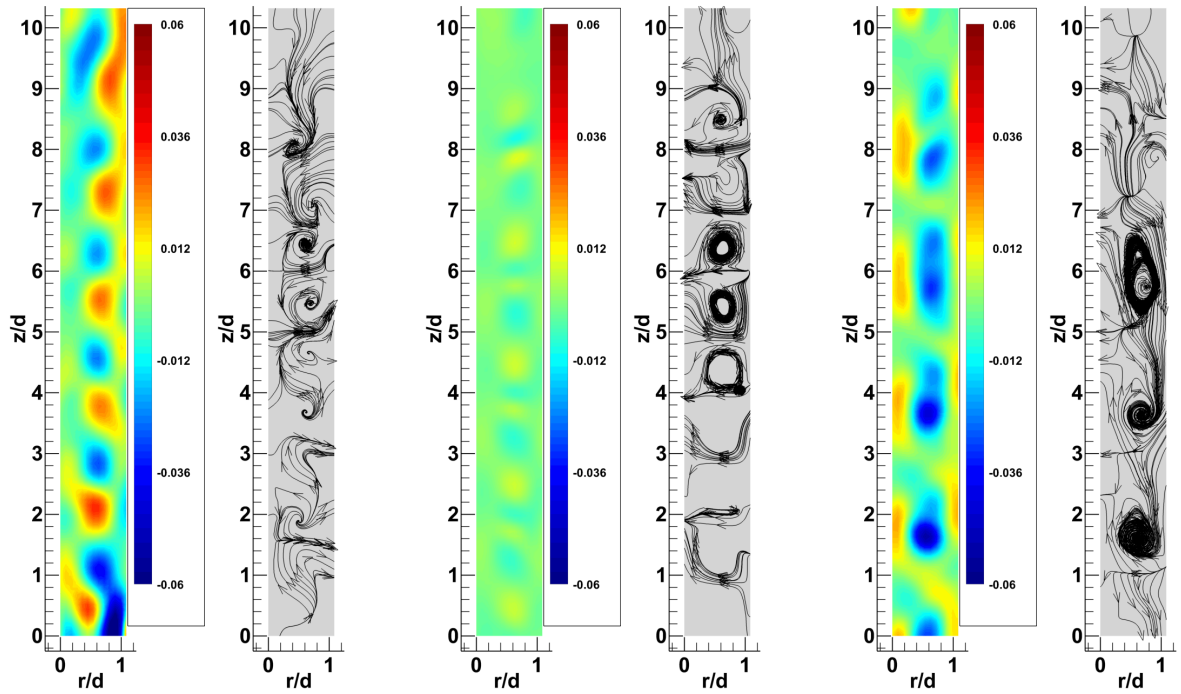

(g) $T_a = 3,360$ $R_{e_{ew}} = 944$ (h) $T_a = 3,360$ $R_{e_{ew}} = 944$ (i) $T_a = 15,170$ $R_{e_{ew}} = 944$ (j) $T_a = 15,170$ $R_{e_{ew}} = 944$ (k) $T_a = 35,485$ $R_{e_{ew}} = 944$ (l) $T_a = 35,485$ $R_{e_{ew}} = 944$

Figure D.2: Counter-rotation annular flow at POD mode-1 (top) and mode-3 (bottom), non-dimensionalized vorticity $[\frac{\omega \hat{\mathbf{d}}}{2\Omega_I R_I}]$ & streamlines, for varying T_a at $\Gamma_{ew} = 1$

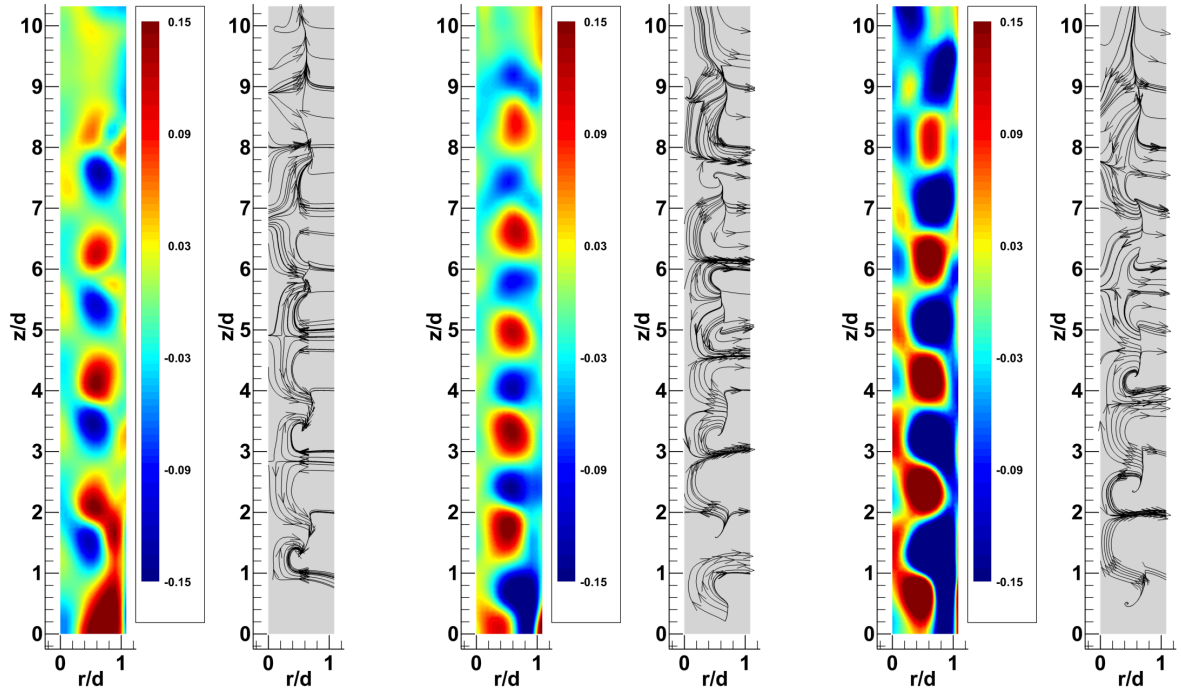

(a) $T_a = 15,170$ $R_{e_{ew}} = 1,227$ **(b)** $T_a = 15,170$ $R_{e_{ew}} = 1,227$ **(c)** $T_a = 15,170$ $R_{e_{ew}} = 2,076$ **(d)** $T_a = 15,170$ $R_{e_{ew}} = 2,076$ **(e)** $T_a = 15,170$ $R_{e_{ew}} = 2,926$ **(f)** $T_a = 15,170$ $R_{e_{ew}} = 2,926$

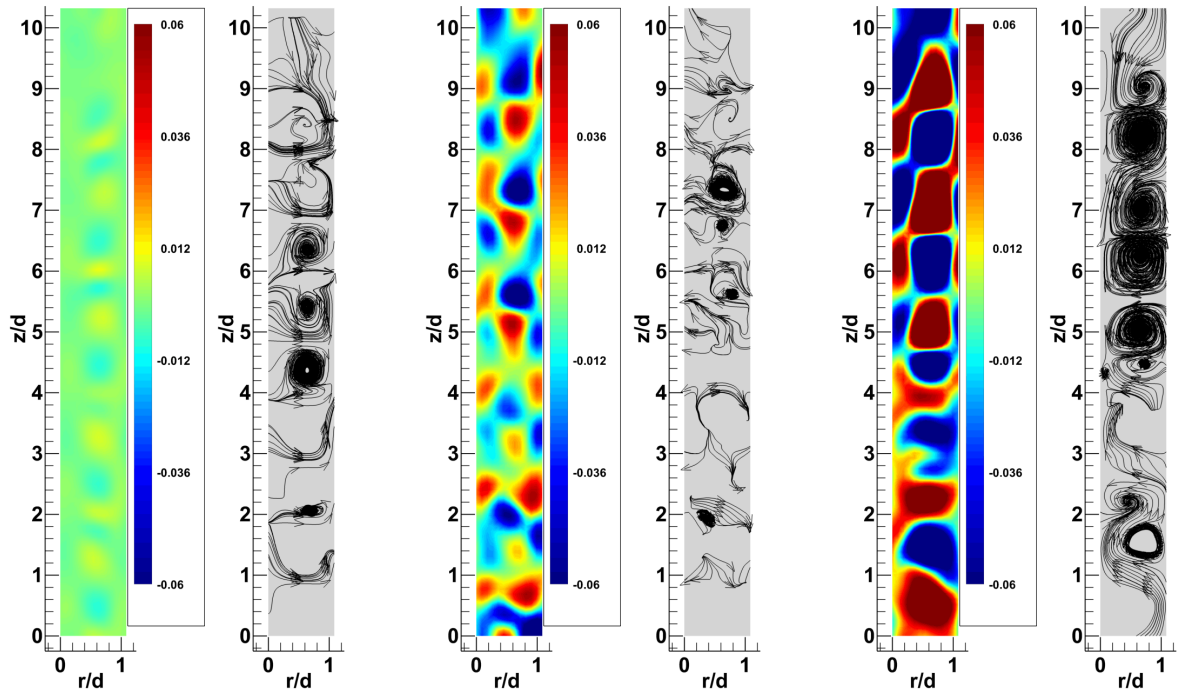

(g) $T_a = 15,170$ $R_{e_{ew}} = 1,227$ **(h)** $T_a = 15,170$ $R_{e_{ew}} = 1,227$ **(i)** $T_a = 15,170$ $R_{e_{ew}} = 2,076$ **(j)** $T_a = 15,170$ $R_{e_{ew}} = 2,076$ **(k)** $T_a = 15,170$ $R_{e_{ew}} = 2,926$ **(l)** $T_a = 15,170$ $R_{e_{ew}} = 2,926$

Figure D.3: Counter-rotation annular flow at POD mode-1 (top) and mode-3 (bottom), non-dimensionalized vorticity $[\frac{\omega \hat{\mathbf{d}}}{2\Omega_I R_I}]$ & streamlines, for varying $R_{e_{ew}}$ at $\Gamma_{ew} = 1$

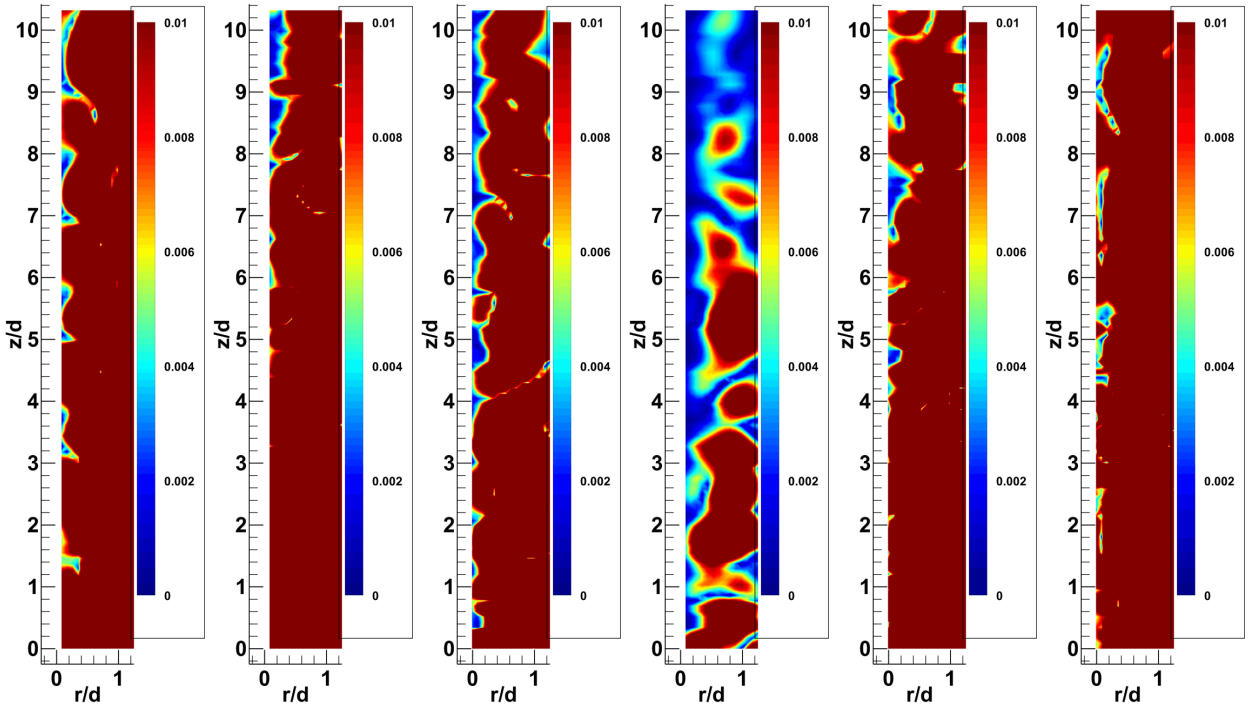

(a) $T_a = 3,360$ $R_{e_{ew}} = 944$ **(b)** $T_a = 15,170$ $R_{e_{ew}} = 944$ **(c)** $T_a = 35,485$ $R_{e_{ew}} = 944$ **(d)** $T_a = 15,170$ $R_{e_{ew}} = 1,227$ **(e)** $T_a = 15,170$ $R_{e_{ew}} = 2,076$ **(f)** $T_a = 15,170$ $R_{e_{ew}} = 2,926$

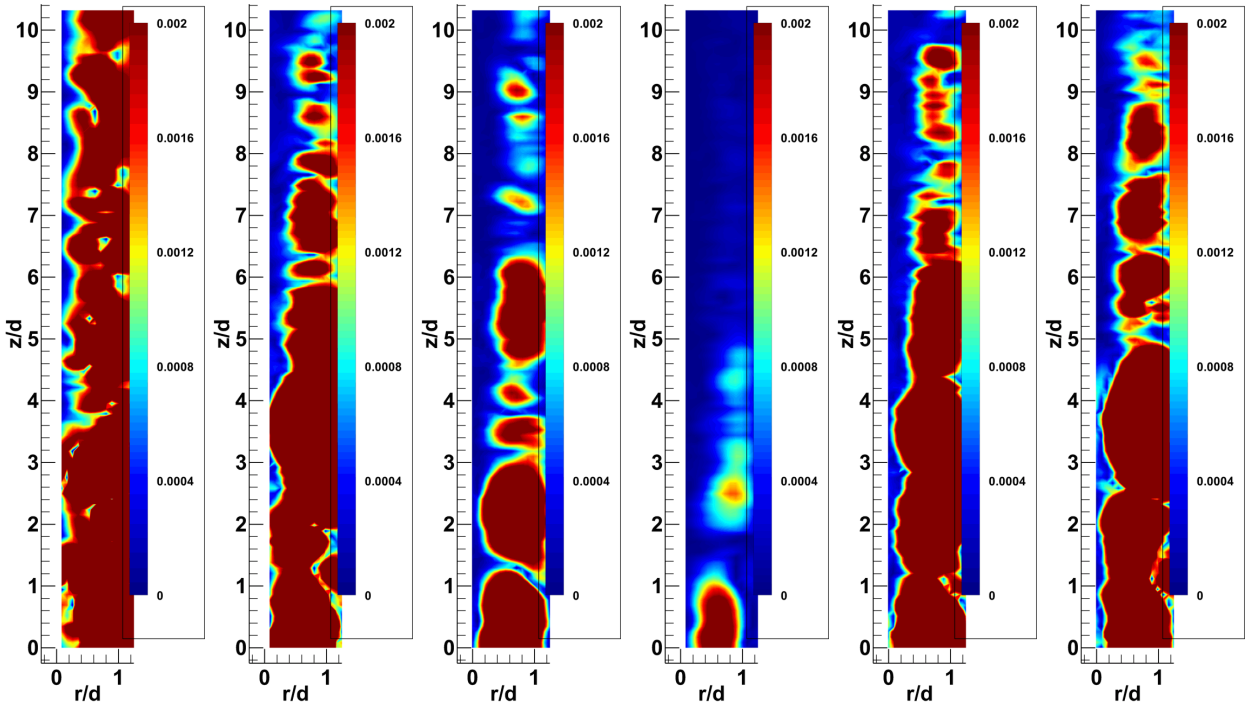

(g) $T_a = 3,360$ $R_{e_{ew}} = 944$ **(h)** $T_a = 15,170$ $R_{e_{ew}} = 944$ **(i)** $T_a = 35,485$ $R_{e_{ew}} = 944$ **(j)** $T_a = 15,170$ $R_{e_{ew}} = 1,227$ **(k)** $T_a = 15,170$ $R_{e_{ew}} = 2,076$ **(l)** $T_a = 15,170$ $R_{e_{ew}} = 2,926$

Figure D.4: Counter-rotational annular flow at POD mode-1 (top) and mod-3 (bottom), velocity profile velocity profile for varying T_a (left), & varying $R_{e_{ew}}$ (right), at $\Gamma_{ew} = 1.5$

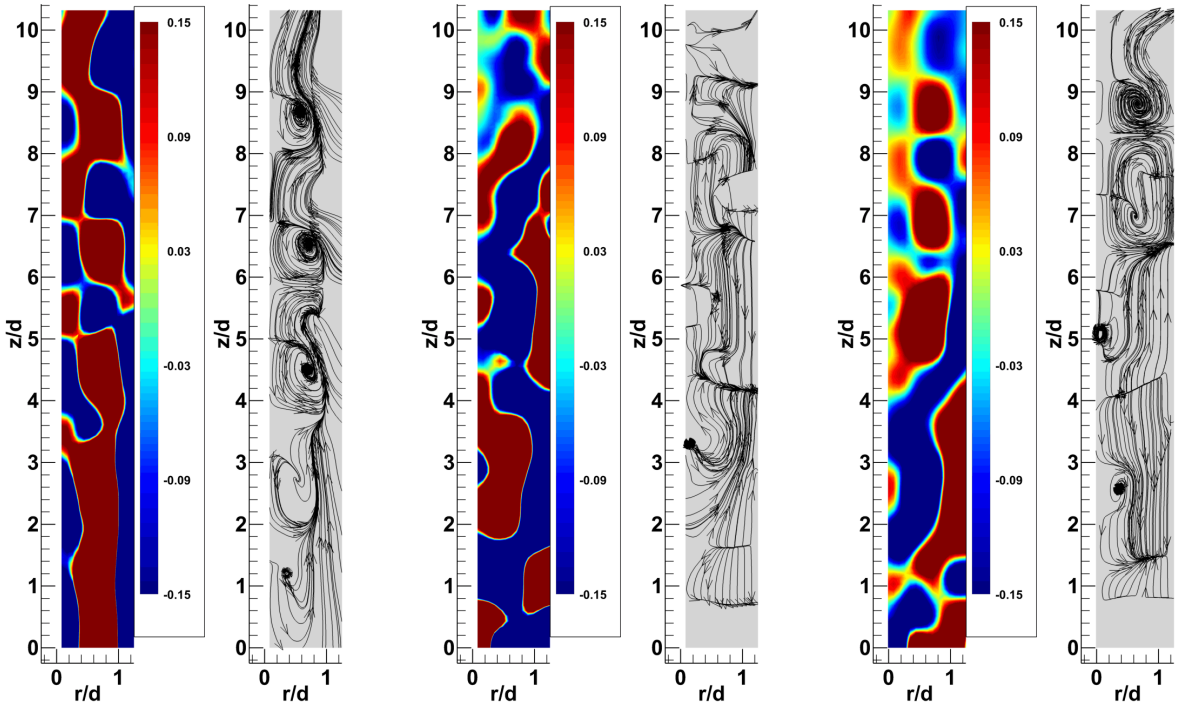

(a) $T_a = 3,360$ $R_{e_{ew}} = 944$ (b) $T_a = 3,360$ $R_{e_{ew}} = 944$ (c) $T_a = 15,170$ $R_{e_{ew}} = 944$ (d) $T_a = 15,170$ $R_{e_{ew}} = 944$ (e) $T_a = 35,485$ $R_{e_{ew}} = 944$ (f) $T_a = 35,485$ $R_{e_{ew}} = 944$

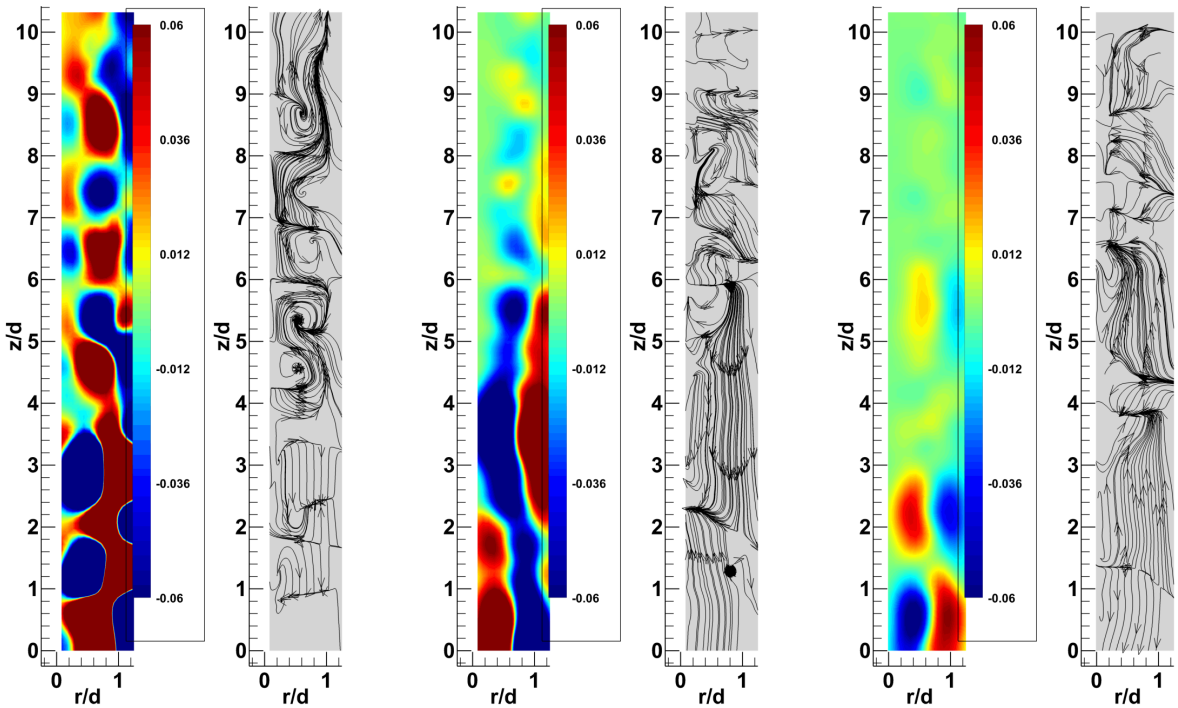

(g) $T_a = 3,360$ $R_{e_{ew}} = 944$ (h) $T_a = 3,360$ $R_{e_{ew}} = 944$ (i) $T_a = 15,170$ $R_{e_{ew}} = 944$ (j) $T_a = 15,170$ $R_{e_{ew}} = 944$ (k) $T_a = 35,485$ $R_{e_{ew}} = 944$ (l) $T_a = 35,485$ $R_{e_{ew}} = 944$

Figure D.5: Counter-rotation annular flow at POD mode-1 (top) and mode-3 (bottom), non-dimensionalized vorticity $[\frac{\omega \hat{\mathbf{d}}}{2\Omega_I R_I}]$ & streamlines, for varying T_a at $\Gamma_{ew} = 1.5$

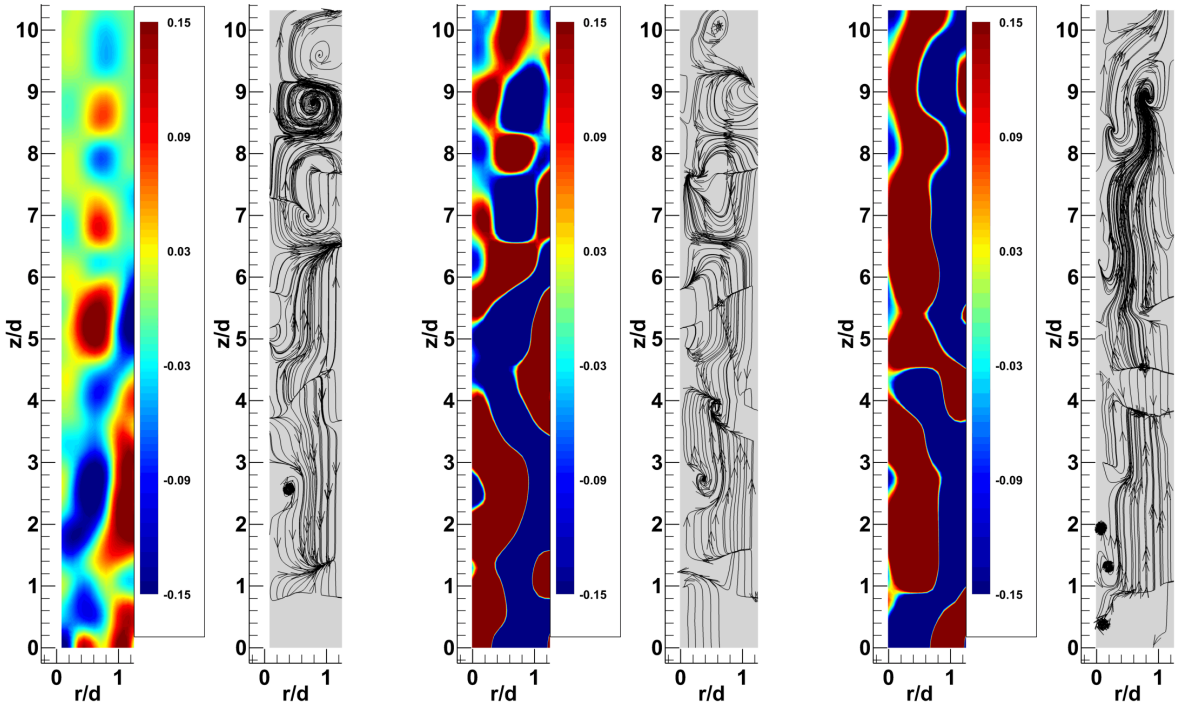

(a) $T_a = 15,170$ $R_{e_{ew}} = 1,227$ **(b)** $T_a = 15,170$ $R_{e_{ew}} = 1,227$ **(c)** $T_a = 15,170$ $R_{e_{ew}} = 2,076$ **(d)** $T_a = 15,170$ $R_{e_{ew}} = 2,076$ **(e)** $T_a = 15,170$ $R_{e_{ew}} = 2,926$ **(f)** $T_a = 15,170$ $R_{e_{ew}} = 2,926$

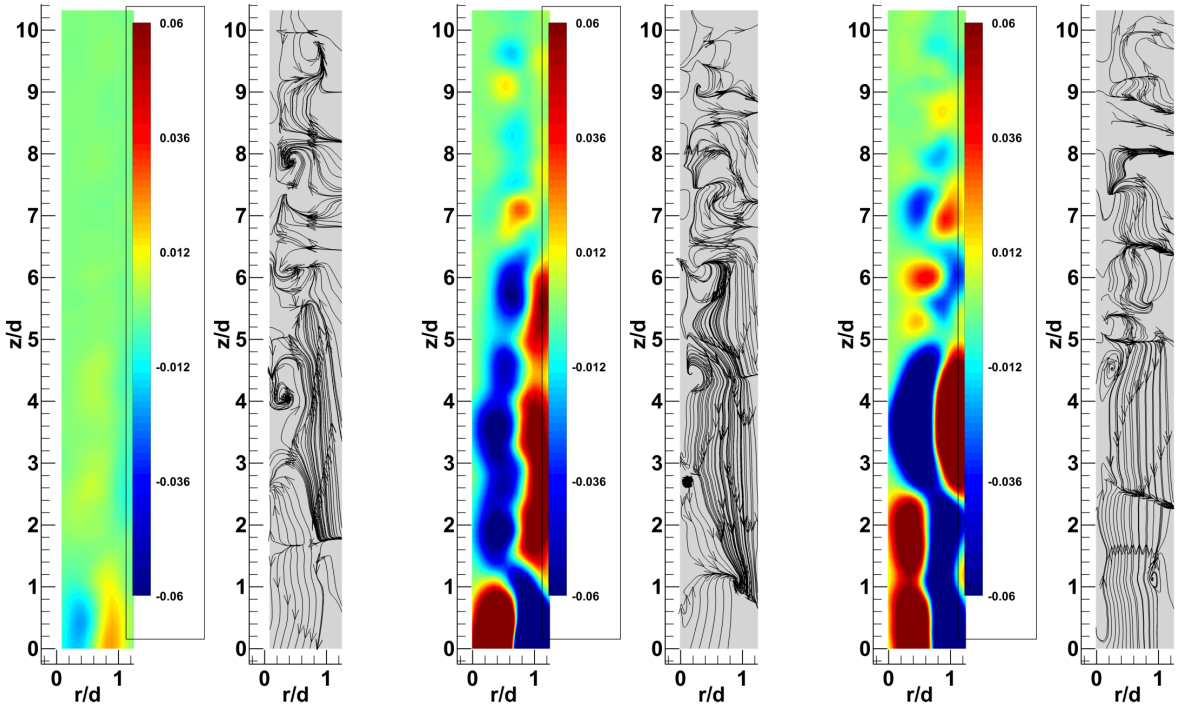

(g) $T_a = 15,170$ $R_{e_{ew}} = 1,227$ **(h)** $T_a = 15,170$ $R_{e_{ew}} = 1,227$ **(i)** $T_a = 15,170$ $R_{e_{ew}} = 2,076$ **(j)** $T_a = 15,170$ $R_{e_{ew}} = 2,076$ **(k)** $T_a = 15,170$ $R_{e_{ew}} = 2,926$ **(l)** $T_a = 15,170$ $R_{e_{ew}} = 2,926$

Figure D.6: Counter-rotation annular flow at POD mode-1 (top) and mode-3 (bottom), non-dimensionalized vorticity $[\frac{\omega \hat{\mathbf{d}}}{2\Omega_I R_I}]$ & streamlines, for varying $R_{e_{ew}}$ at $\Gamma_{ew} = 1.5$